INSTITUT FÜR ANGEWANDTE PHYSIK
TECHNISCHE UNIVERSITÄT DARMSTADT

Assessment of a Rubidium ESFADOF Edge-Filter as Receiver for a Brillouin-Lidar Capable of Remotely Measuring Oceanic Temperature Profiles

Vom Fachbereich Physik
der Technischen Universität Darmstadt

zur Erlangung des Grades
eines Doktors der Naturwissenschaften
(Dr. rer. nat.)

genehmigte
Dissertation

von

Dipl.-Phys. Alexandru Lucian Popescu
aus Bukarest

Darmstadt 2010
D17

Referent:	Prof. Dr. Thomas Walther
Koreferent:	Prof. Dr. Gerhard Birkl
Tag der Einreichung:	26. Januar 2010
Tag der Prüfung:	17. Februar 2010

Abstract

Global and local climate changes affect nature and mankind. Forecasts of these processes on global and local scales rely on a thorough understanding of the underlying physics through accurate data. In this context, the knowledge of the temperature profile of the upper–ocean mixed layer is relevant in oceanography, weather forecasts and climate studies and can be correlated to other parameters, such as concentrations of nutrients, oxygen and CO_2. Currently, only in–situ techniques are available, such that a remote sensing application for the measurement of oceanic temperature profiles is highly desirable. Such a system would deliver accurate, cost effective and area wide data, which could be used to improve current models and forecasts within many domains of oceanography and climatology. However, only recent progress in laser and receiver technology made a remote sensing solution feasible. When employing the lidar principle, an airborne compatible system based on the detection of the temperature dependent frequency shift of the Brillouin–scattering becomes feasible.

Laser pulses are fired into the ocean and the Brillouin–scattering imprints the temperature information on the backscattered light. An appropriate detector on board an aircraft extracts the temperature and correlates it to the time of flight of the laser pulses. As a result, a three–dimensional temperature profile of the upper–ocean mixed layer is extracted. Measuring the very small frequency shift of the Brillouin–scattering is the main challenge of this project. The shift varies from 6.8 GHz–7.8 GHz for water temperatures between 0°C and 40°C, when injecting laser pulses at a wavelength of 543 nm. The employment of spectrally narrow edge–filters converts the frequency measurement into an intensity measurement. As compact, robust and light weight devices, these filters are in particular suited for an airborne implementation. This work demonstrates that Excited State Faraday Anomalous Dispersion Optical Filters (ESFADOFs) are such high resolution optical edge–filters. They deliver the desired edge–filter characteristics, when operated around the Rubidium $5P_{3/2} \rightarrow 8D_{5/2}$ transition (543 nm), and transmission changes of up to 24% within a few GHz were demonstrated. In addition, fundamental investigations of the ESFADOF transmissions are presented. They result in distinct operational limits, due to radiation trapping, energy–pooling and plasma formation. Together with the scalability of these devices, their implementation as the Brillouin–lidar detector is addressed.

Zusammenfassung

Globale und lokale Klimaveränderungen haben seit jeher Mensch und Natur beeinflußt. Globale als auch lokale Prognosen basieren auf ein sorgfältiges Verständnis der bestimmenden Physik, die durch präzise Daten erworben wird. In diesem Zusammenhang profitieren Ozeanographie, Wettervorhersagen und Klimaforschung von der ortsaufgelösten Kenntnis des ozeanischen Temperaturprofils der Durchmischungszone. Die Kenntnis dieses Profils läßt Schlußfolgerungen auf weitere Parameter wie den Nährstoff–, Sauerstoff– und CO_2–Gehalt zu. Da zur Zeit nur kontaktbasierte Methoden zur Verfügung stehen, würde in diesem Zusammenhang eine Fernerkundungsmethode zur kostengünstigen Bestimmung des maritimen Temperaturprofils wertvolle Daten für bestehende Modelle und Prognosen in vielen Bereichen der Ozeanographie und Klimaforschung liefern. Erst durch neue Entwicklungen in der Laser– und Detektortechnologie rückt die Vermessung der Brillouin-Streuung als optischer Temperaturindikator mittels eines Lidar–Systems in greifbare Nähe.

Eingestrahlte Laserpulse werden im Wasser inelastisch gestreut. Die dem Streulicht aufgeprägte Temperaturinformation läßt sich aus einem Flugzeug oder einem Hubschrauber messen und über die Flugzeit der Laserpulse mit der Tiefe korrelieren. Als Ergebnis wird ein dreidimensionales Temperaturprofil extrahiert. Die zentrale Herausforderung besteht in der genauen Bestimmung der temperaturabhängigen Frequenzverschiebung der Brillouin-Streuung. Diese liegt für Wassertemperaturen von 0°C–40°C bei einer eingestrahlten Laserwellenlänge von 543 nm zwischen 6,8 GHz und 7,8 GHz. Der Einsatz eines schmalbandigen Kantenfilters transformiert die notwendige Frequenzmessung in eine Intensitätsmessung. Durch ihren kompakten, leichten und robusten Aufbau sind diese Filter besonders für ein flugzeuggestütztes System von Vorteil. Wie in dieser Arbeit gezeigt wird, lassen sich solche hochauflösenden und schmalbandigen Filter auf Basis eines *Excited State Faraday Anomalous Dispersion Optical Filter* (ESFADOF) aufbauen. Ferner wird gezeigt, daß der entwickelte Aufbau in der Lage ist die notwendigen Transmissionscharakteristika an der atomaren $5P_{3/2} \rightarrow 8D_{5/2}$ Resonanz (543 nm) bereitzustellen. Transmissionsänderungen von bis zu 24% innerhalb weniger GHz werden gezeigt. Zusätzlich werden fundamentale Untersuchungen der ESFADOF–Transmission präsentiert. Diese definieren Betriebsgrenzen, die durch *radiation–trapping*, *energy–pooling* und die Induktion eines Plasmas bestimmt werden. Zusammen mit der Skalierbarkeit dieser Filter wird der Einsatz als Brillouin–Lidar–Detektor diskutiert.

Pentru Alexandru şi Florina

Contents

1

Introduction

The world oceans cover over 70% of the earth's surface and accumulate the majority of all water resources. They gave birth to life and are the largest biological habitat of our planet. Their endless immensity makes them one of the predominant factors of the earth's climate. They store and transport heat, gases and nutrients on global scales and contribute via a continuous exchange with the atmosphere to the climate and weather of entire continents [1, 2]. Thus, it is not surprising that mankind has been fascinated by the seas from the very beginning of civilization. However, only the extensive research of the last centuries begin to reveal the processes which drive global climate and climate changes [3]. Nevertheless, the modeling and forecasting of the earth's climate remains one of the most challenging attempts of mankind. A thorough understanding of the global and local climate is essential for the existence of civilizations on long time scales. One example is the decline of the Maya civilization, which occupied wide areas of Central America. Recent research attributes this decline to the occurrence of a century-scale decrease in rainfall and intense multiyear droughts combined with local social stresses. Regardless of whether the Maya civilization contributed to some extent to their decline, the impact of the local climate change was severe [4].

The fact, that mankind is facing the realm of global warming is nowadays undoubted and the emission of anthropogenic green house gases is held responsible for this climate change [3, 5, 6]. However, as the underlying strongly coupled Earth's climate is hard to predict, it is not surprising, that throughout the scientific community there is disagreement with respect to the dimension, the time scales and the direct consequences of the anticipated global warming [7–9]. This disagreement sharpened within the *Lomborg debate* and is based on the book of Bjørn Lomborg [7], whose positive assessment of the outcomings of global climate change is very controversly discussed throughout the literature [8, 9].

However, it is as well undoubted, that the data base and climate models upon which the debate on climate change is hinged, has to be permanently improved [3, 5, 6]. This holds true in particular for the effects of the ocean upper mixed layer, which is strongly coupled to the atmosphere. This mixed layer typically exhibits a thickness of 10–200 m and links the atmosphere and the deep ocean. It directly affects the air–sea exchange of heat, momentum and gases [10]. Hence, it influences weather and climate on global scales, when for example area

wide sea currents act as global conveyor belts of heat. A predominant example is the Gulf Stream, which transports heat from the warm waters of the Gulf of Mexico to the north of the Atlantic ocean. This is the cause of Europe's mild climate [2, 11]. Another, more dramatic coupling between the ocean upper mixed layer and the atmosphere causes hurricanes. They extract their energy from evaporating oceanic waters and their impact on the costal zone might be devastating [1, 2, 12–15]. Hurricane forecasting and the prediction of their trajectories is highly desirable in view of the immense damages, which hurricanes may cause. Such forecast rely on the knowledge of the heat content of the upper mixed layer, which is linked to the temperature profile of the ocean upper mixed layer.

But, currently only *in situ* techniques are available and contact based instruments extract the water temperature profile. This fact restricts the data aquisition to fixed buoys, ships, drifters or deployable sensors such as expandable bathythermographs [6]. Thus, an airborne based remote sensing technique is highly desireable, as it would considerably increase the available amount of data and allow for flexible, area wide and extended surveys. In addition, such a technique would lead to an enormous cost benefit.

The Brillouin–lidar project is dedicated to the development of such an airborne compatible system, which will be capable of remotely extracting the temperature profile of the upper mixed layer by employing the *Light Detection and Ranging*–technique [16]. Estimates of the maximum penetration depths of such a system result in 50–100 m [17], when operating within the absorption minimum of water (380–550 nm) [18]. The working principle can be summarized as follows: (1) Laser pulses are fired into the ocean. (2) There, they interact with the water column and spontaneous Brillouin–scattering imprints the temperature information on the backscattered light. (3) An appropriate detector extracts this temperature information from the backscatter and correlates it to the time of flight of the laser pulses, which delivers the depth information.

The present thesis is embedded within this project and discusses the development and the thorough assessment of an edge–filter receiver, which will allow to extract the temperature profile of the water column of the ocean upper mixed layer. The edge–filter is based on the employment of an *Excited State Faraday Anomalous Dispersion Optical Filter* (ESFADOF). They are very well suited for an airborne compatible application, as this work demonstrates. Of course, the development of this receiver can not be uncoupled from the overall requirements of the measurement principle and of the Brillouin–lidar implementation. Chapter 2 gives an overview of the Brillouin–lidar working principle and summarizes the requirements of an airborne compatible implementation. Particular emphasis is put on the receiver system. As the Brillouin–lidar employs an active direct detection scheme, an additional pulsed transmitter is required. This transmitter has been discussed extensively within the PhD-Thesis of Kai Schorstein [19] and is therefore not subject of this work. Chapter 3 presents the working principle of the ESFADOF based edge–filter together with an theoretical approach to these devices, which is based on preliminary works [16, 20, 21]. In addition, an ex-

perimental setup has been developed. It allows the measurement of the transmission characteristics of the ESFADOF receiver with yet unreported accuracy in frequency and transmission. Chapter 4 discusses this setup and the measurement scheme in detail. Chapter 5 presents the outcome of an extensive survey upon the transmission characteristics of the developed Rubidium based ESFADOF devices and this work finishes in chapter 6, which discusses the prospects of the presented results.

2

Remote Sensing of the Water Column: The Brillouin-Lidar

Remote sensing methods exhibit a number of advantages compared to *in situ* techniques. In particular, they allow for fast and accurate observations, which are potentially inaccessible to direct methods. The possibility of their use on mobile platforms considerably extends the observation regions and introduces an important cost benefit compared to direct sampling. Remote sensing techniques in general can be separated into two categories: (1) Passive techniques, which exploit natural sources, such as sunlight or thermal radiation and (2) active techniques, which require an additional source. A very widely spread overview on active and passive remote sensing techniques and systems can be found in the book of Cracknell and Hayes [22] and the book of Fujii and Fukuchi extensively addresses active systems based on laser remote sensing techniques [23].

The Brillouin-lidar concept is based on an active technique, which allows the extraction of the temperature profile of the water column. It would enrich currently available *in situ* techniques, such as expandable bathythermographs, glider and drifter or fixed buoys [6]. All of these systems, which are available to this date, require the direct contact of a thermocouple to the water column. In addition, satellite based passive remote sensing systems have been employed since the 1980s. They explore the thermal blackbody radiation of the sea surface and make area-wide observations of the sea-surface temperature (SST) available [22]. However, these satellite based systems are limited in spatial resolution and to the sea-surface temperature. Hence, an airborne based remote sensing technique, capable of resolving the temperature profile, is highly desireable and would close the gap between the area-wide satellite observation of the SST and the localized temperature profiles from *in situ* techniques. However, such a remote sensing technique has to be operated from mobile platforms, while satisfying two conditions: (1) The measurement principle has to explore a remotely accessible temperature tracer and (2) has to ensure sufficiently high penetration depths in order to obtain a temperature profile.

By employing the *Light Detection and Ranging*–technique (Lidar-technique) such a remote sensing application becomes feasible. Its measurement scheme is similar to the more widely known Radar-technique (*Radio Detection and Ranging*), which actively employs radio frequencies in order to determine the

distance of objects from the observer. However, the employment of optical frequencies increases the spatial resolution, but allows also to correlate other observables with the time dependent return signal. The working principle is as follows: (1) light-pulses are emitted and (2) their interaction with the surrounding medium and/or targets results in a time dependent return signal; (3) by collecting and evaluating this signal a profile of the interaction processes results [24]. By investigating the return signal which emerges from the Brillouin– or Raman–scattering of the injected light pulses inside the water column, an optically accessible interaction is found. Both processes rely on the inelastic scattering of light and exhibt a clear temperature dependance. Hence, by incorporating these processes into an active lidar measurement scheme, a remote sensing technique results, which extracts the temperature profile from the water column. Briefly speaking, the Raman-scattering process probes properties on a molecular scale, such as the temperature dependent concentration of the monomer and polymer forms of water [25, 26], while Brillouin-scattering explores the water properties on a larg scale, such as the temperature dependent speed of sound, which emerges from inelastic scattering of light on permanently available density fluctuations [27–31]. Both scattering processes result in a frequency shift of the backscattered signal, which can be exploited as temperature tracer [32–34]:

1. **Raman–scattering:** The Raman–scattering imprints a large Stokes–shift of about 3350 cm^{-1} with respect to the injected light pulses on the backscattered signal [33]. This potentially shifts the backscattered signal out of the narrow spectral absorption minimum of water (380–550 nm [18]), when employing green laser light. This fact limits the achievable penetration depth of such a lidar system [26, 33]. In addition, the measurement principle relies crucially on a highly accurate spectral discrimination of the contributions from the monomer and polymer forms of water. The latter includes also contributions from hydrogen bonds to the rovibrational spectra of water, whereas the former emerges from the bare water molecule. As the monomer– and the polymer–contributions cover a large frequency span of 2800-3900 cm^{-1}, they can be discriminated by selecting two different observation wavelengths. This method is known as the two-color technique [26, 33]. But, as the Raman–spectrum is susceptible to daylight, parasitic fluorescence and selective absorption due to Chlorophyll or dissolved organic matter, a significant reduction in achievable measurement accuracy results [25, 26, 33]. For the sake of completeness, it has to be mentioned that the monomer and polymer forms of water show different amounts of depolarization of the injected polarized laser pulses. This can be exploited in order to determine their corresponding concentrations and hence the water temperature [26, 33]. This approach, known as the depolarization technique, does not require two explicit wavelength discriminations.
2. **Brillouin–scattering:** The Brillouin-scattering imprints a temperature dependent frequency shift of approx. $\pm$7–8 GHz symmetrically located around the injected light pulses on the backscattered signal, when employing green laser light [30]. This small frequency shift assures high penetration depths, when operating near the absorption minimum of water [35], but also requires a

highly accurate frequency discrimination, in order to separate the Brillouin–signal, which carries the temperature information, from additional Rayleigh–scattering of hydrosols. The aim of this thesis is the development and the assessment of a receiver system capable of measuring this small frequency shift. Thus, a more detailed description will be given below.

Hence, when taking the mentioned disadvantages of the Raman–scattered signal into consideration, it becomes clear why the Raman–scattering approach has been abandoned since the 1980s, in particular as the accuracy of both temperature tracers depend on the number of backscattered and collected photons [17, 26]. However, within a well controlled laboratory test-frame the Raman-technique is still of importance [36], but for field applications it is rather more advantageous to explore Brillouin–scattering.

2.1 Measurement Principle

Guagliardo *et al.* suggested Brillouin scattering as a temperature tracer in 1980 [30]. Since then several different approaches have been investigated. Hickman *et al.* were the first, who discussed a Brillouin-lidar system in detail in 1991 [35]. The working principle is depicted in Fig. 2.1 and can be understood similar to already established bathymetric lidars [37, 38]:

1. **Transmitter:** An appropriate transmitter produces high energy ns-laser pulses of high spectral quality, whose emission wavelength is close to the absorption minimum of water [18]. These pulses are fired into the ocean. The temporal pulse width correlates with the spatial resolution of the lidar, the pulse energy with the maximum penetration depth, the repetition rate with the signal-to-noise-ratio and the spectral quality with the potential temperature resolution.
2. **Brillouin-scattering:** As soon as the laser pulses pentrate the water surface, they undergo spontaneous Brillouin-scattering on permanently present density fluctuations. A spectral investigation of the backscattered light reveals a doublet structure symmetrically located around the injected laser wavelength (indicated by the red and blue colored arrows in Fig. 2.1). The doublet originates from the symmetry of the scattering process. However, the frequency shift of the scattered signal is temperature dependent and can therefore be exploited as a temperature tracer.
3. **Receiver:** An appropriate receiver system collects the backscattered signal and correlates it with the time of flight of the laser pulses, which delivers the depth information. It is advantageous to explore the symmetric doublet structure of the backscattered Brillouin-signal in order to increase the signal-to-noise-ratio.
4. **Post-processing:** Depending on the implemented receiver technology, different raw signals have to be processed in order to extract the time dependent frequency shift. However, through a prior calibration and validation these signals can be transformed into the coresponding temperature profile.

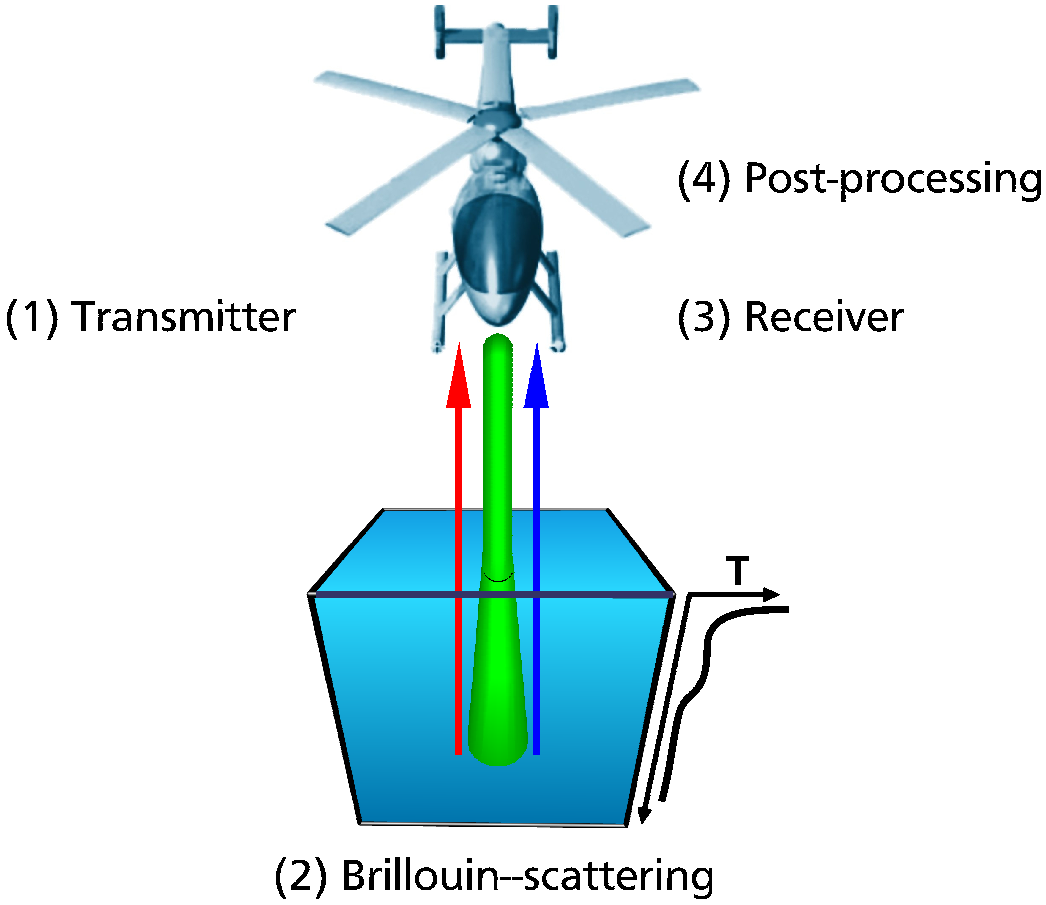

Fig. 2.1: Working principle of the Brillouin-lidar: (1) The transmitter generates green ns laser pulses, which are fired into the ocean. (2) There, the laser pulses undergo spontaneous Brillouin-scattering, which returns a temperature dependent frequency shifted signal. This Brillouin-signal consists of two spectral components, which are symetrically located around the injected laser wavelength (indicated by the red and blue colored arrows). The frequency shift carries the temperature information and the time of flight of the response correlates to the penetration depth of the laser pulses. (3) A telescope collects the backscattered signal and an appropriate receiver system extracts the time dependent frequency shift. (4) The temperature profile is extracted from the recorded signals through a prior calibration process.

Fry and coworkers demonstrated first laboratory versions of the measurement principle [17, 39–42]. Recently, within the PhD thesis of Kai Schorstein, who took part in the Brillouin–lidar project of Prof. Th. Walther *et al.*, a first range resolved temperature profile has been reported [19, 43, 44]. He employed a pulsed fiber amplifier accompanied with a second harmonic generation as the light source. So far his transmitter delivers up to 131 μJ of green pulse energy with a repetition rate of up to 5 kHz. The receiver was a scanning Fabry-Perot interferometer equipped with a photomultiplier tube [43, 44]. The laboratory test frame allowed the employment of a scanning interferometer, which delivered the entire Brillouin-backscattered spectrum and clearly demonstrated the feasibility of such a system. However, for mobile platforms and in particular on board an aircraft a better suited receiver in terms of light gathering power and stability than the employed interferometer is required.

Promising approaches for a suitable receiver setup are heterodyne techniques [45] and static edge-filters [46]. In the latter, the transmission characteristics of a filter are designed such that sharp transmission edges occur at the typical separation of the Brillouin shifted lines. Thus, small frequency shifts are converted to large changes in transmission. i.e. the frequency measurement is transformed into a transmission measurement. It is desirable that the edges are steep, symmetrically located and exhibit a transmission as high as possible.

Several proposals exist to implement such a system:

1. Fry and coworkers developed a high power frequency doubled Nd:YAG laser system as the light source and a receiver system based on an Iodine edge-filter. I_2 is of particular interest, as the outer edges of a pair of its molecular absorption lines lie within the region of interest, i.e. $\pm$7–8 GHz around the 532 nm emission wavelength of the frequency doubled Nd:YAG laser [17, 39]. The filter relies on an accidental overlap of two iodine absorption lines with the spectral requirements of the edge filter.
2. Th. Walther *et al.* proposed a system based on a frequency doubled, high repetition rate fiber amplifier and an excited state Faraday anomalous dispersion optical filter (ESFADOF) as the edge-filter receiver [16, 20, 47, 48]. The ESFADOF is a mechanically stable, high resolution edge filter capable of resolving small frequency shifts with high accuracy. Moreover, the transmission characteristics can be tailored to the specific needs of the problem.
3. Dahe and coworkers proposed a detection scheme based on stimulated Brillouin-scattering [49, 50]. However, this technique does not provide single shot profiling, for either sound speed nor determination of the depth of submerged objects.

This thesis follows the proposal of Th. Walther *et al.* and discusses the ESFADOF filter characteristics towards a practical implementation of the receiver device.

2.2 System Requirements

A remote sensing technique, which explores the temperature dependent Brillouin-scattering, requires two key components: (1) A transmitter, which emits laser pulses near the absorption minimum of water and (2) a receiver system, which is capable of resolving the temporal variations of the Brillouin-shift on a ns scale.

Since operation from a mobile platform is intended, the complete sensor system has to fulfill rather stringent specifications:

1. The entire setup has to be compact, insensitive to vibrations and energy efficient. Similar to already operational airborne lidars, such as the helicopter-borne laser Methane detection system [51] or the SHOALS airborne lidar bathymetry system [38], the proposed Brillouin-lidar has to comply within 300 kg of available payload and 2 kW of electrical power.
2. In order to resolve the Brillouin shift, the laser source has to produce high energy ns-pulses, preferentially close to the Fourier transform limit.
3. The wavelength of the laser radiation should be close to the absorption minimum of water, i.e. between 380 and 550 nm [18].
4. The receiver unit must exhibit a high light gathering power, and have the ability to resolve the Brillouin-shift on a ns time scale.

The following subsections discuss the advantages of a pulsed fiber amplifier transmitter as well as the Brillouin–scattering in order to gain more evidence on the system requirements. Finally, they end with a discussion about the appropriate receiver technology, which can meet these requirements.

2.2.1 Transmitter

As proposed and discussed in earlier publications [16, 20, 43, 47, 48, 52–54] a light source which is compatible with the above specifications is a pulsed fiber amplifier. It is composed of a master oscillator (seed) which defines the spectral and temporal properties of the laser pulses. Then in a power amplifier these pulses are amplified and since there is no need for any resonant optics, the system is intrinsically insensitive to vibrations.

Recent progress in fiber laser and amplifier technology enable the extension to other operational wavelengths apart from the telecom spectral region. High power systems have been realized by the introduction of large mode area fibers [55]. Fiber lasers and amplifiers have already proven their large versatility delivering cw or pulsed radiation and pulse lengths from femto- to nanoseconds [56–58]. Recently, within the Brillouin-lidar project, a three stage Yb–doped fiber amplifier, which can be operated between 1020 nm-1100 nm when pumped at 976 nm [59], has been developed [19, 54]. The large operation range of the fiber amplifier makes it easier to match the emission wavelength of the transmitter with the demands of the proposed receiver system based on an atomic edge filter [16, 47]. Compared to a Nd:YAG laser, a fiber amplifier is advantageous considering sensitivity to vibration, efficiency, weight, physical dimensions and

operating wavelength region. Currently, when seeding the fiber amplifier with 10 ns long, nearly Fourier–limited pulses, output energies of up to 516 μJ at a wavelength of 1064 nm have been demonstrated [19, 54]. These pulses are frequency converted by a second harmonic generation within a nonlinear Potassium titanyl phosphate crystal (KTP) to the green spectral region. Up to 131 μJ at 532 nm of near Fourier transform limited green pulse energies with a repetition rate of up to 5 kHz are available so far. Fourier transform limited pulses are necessary in order to accurately measure the peak positions of the Brillouin lines. This can be guaranteed by the employed seeding technique [60].

Energy scaling in this operating regime is in general limited by nonlinear effects. The high peak intensities inside the fiber core, the long interaction lengths and the small bandwidth promote the occurrence of stimulated Brillouin scattering (SBS) inside the fiber, which may lead to the destruction of the fiber ends [61, 62]. The onset of SBS can be prevented or at least shifted to higher energies by: (1) increasing the diameter of the fiber core thus reducing peak intensity, (2) reducing fiber length, (3) decreasing pulse length and (4) increasing bandwidth. Clearly, (3) and (4) are not applicable options for the Brillouin-lidar transmitter, as they would considerably decrease the accuracy of the temperature measurement. Hence, a thorough optimization of the entire 3 stage fiber amplifier is mandatory in order to achieve the described specifications, while operating below the damage thresholds. This is of particular importance for the third amplification stage, where the highest output energies are obtained. There, highly doped and relatively short fibers prove to be advantageous [19]. The employment of an active photonic crystal fiber will considerably increase the converted output energy in the near future [63].

However, in order to reach penetration depths of >50 m pulse energies of at least 1 mJ are required. Considerably deeper penetrations are limited due to the exponential absorption inside the water column [17]. Hence, the operating wavelength has to be close to the absorption minimum of water [18]. The employment of an injection seeded fiber amplifier with a consecutive frequency conversion unit potentially offers the desired pulse energies, while being robust and versatile. Thus, operations from mobile platforms are possible. In addition, the broad spectral bandwidth of the fiber amplifier allows to simultaneously satisfy the wavelength requirements of the receiver.

The depth information x is obtained by simultaneously measuring the time of flight information of the laser pulses through [24]

$$x = \frac{t}{2}\frac{c}{n_{H_2O}}. \tag{2.1}$$

$t = \tilde{t} - t_0$ denotes the difference between the time when the laser pulse penetrates the water surface t_0 and the total elapsed time of the scattering response $\tilde{t}$ with respect to the pulse injection. The factor of 1/2 accounts for the round trip of the laser pulses, c is the speed of light and $n_{H_2O} = 1.33$ is the refractive index of water [64]. The spatial resolution of the lidar is then given by

$$\Delta x = \sqrt{\left(\frac{c}{2n_{H_2O}}\Delta t\right)^2 + \left(\frac{t\,c}{2n_{H_2O}^2}\Delta n_{H_2O}\right)^2} \tag{2.2}$$

$$= \sqrt{\left(\frac{c}{2n_{H_2O}}\Delta t\right)^2 + \left(x\,\frac{\Delta n_{H_2O}}{n_{H_2O}}\right)^2}, \tag{2.3}$$

where Δt represents the longest time uncertainty in the signal processing chain and Δn_{H_2O} the uncertainty in refractive index. State-of-the-art signal processing is available on a ns time scale [38], so that the dominant temporal uncertainty can be reduced to the pulse length τ. The last term of Eq. 2.2 accounts for the temperature and salinity dependence of the refractive index, which themselves are bound to uncertainties. However, it can be neglected for principal considerations, but has to be included in the final implementation of the signal post-processing, as its contribution increases with increasing penetration depth x.

A pulse length of $\tau = 10$ ns has been chosen in order to satisfy the tradeoff between the spatial resolution of the profile measurement and the accompanied accuracy limitations of the temperature measurement [17]. On the one hand, the pulse length defines the resolution cell beneath the water surface, which can be computed to $\Delta x = 1.13$ m, when neglecting the refractive index contribution. But on the other hand, as the spectral width of the laser pulses are connected through the Fourier transform limit to their pulse length, they define the amount of additional spectral broadening of the Brillouin–scattering. Shorter pulse lengths would certainly increase the spatial accuracy of the depth profile, but would artificially broaden the spectral response of the Brillouin-scattering through the Fourier transform limit and hence decrease the accuracy of the temperature measurement (cf. Sec. 2.2.3).

2.2.2 Brillouin–Scattering

As already mentioned in Sec. 2.1, the proposed Brillouin–lidar explores spontaneous Brillouin–scattering as the temperature tracer. It takes advantage of permanently available density fluctuations, which propagate with the speed of sound inside the medium. The latter is temperature dependent. Specifically, light propagating in water is inelastically scattered off these moving density fluctuations, where a momentum transfer to or from the sound waves occurs (cf. Fig. 2.2). First descriptions of the underlying physics have been independently given by Mandel'shtam in 1918 [27] and by Brillouin in 1921 [28]. A good overview on this topic can be found in the books of Fabelinskii [31] and Berne and Pecora [65].

The density fluctuations result in a modulation of the dielectric constant, which can be decomposed into two terms: (1) The first term originates from isentropic density fluctuations, which propagate at the speed of sound in all directions. They are responsible for the inelastic Brillouin–scattering. (2) The isobar fluctuations of the entropy do not propagate and result in the elastic Rayleigh–scattering [31, 65]. Thus, the Brillouin–scattering is sensitive to the local velocity of sound.

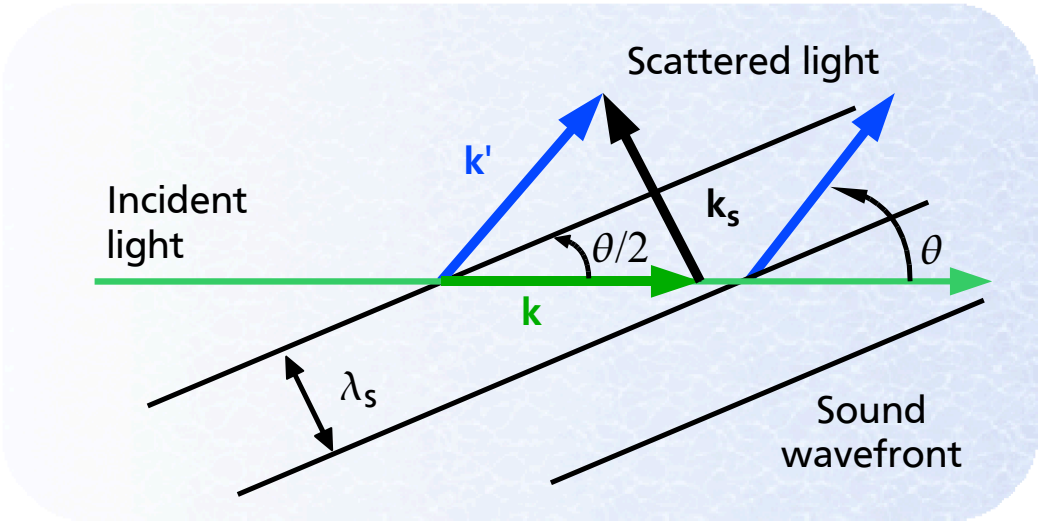

Fig. 2.2: Schematic drawing of the Brillouin-scattering: The incident light is inelastically scattered off permanently available density fluctuations, where the conservation of momentum translates into the depicted Bragg–condition. Due to the symmetry of the process, both propagation direction of the sound waves have to be considered, though only the blue shifted case, which results into a momentum transfer from the water to the light wave, is depicted. The isotropic scattering process covers the whole polar and azimuthal angles, ϕ and θ respectively.

By decomposing the density fluctuations into Fourier components, it is possible to extract the resulting frequency shift ν_B from the conservation of energy and momentum (cf. Fig. 2.2). Let $\mathbf{k}$ and ω denote the wavevector and the angular frequency of the incident light wave. Then, the scattered light wave, denoted by $\mathbf{k}'$ and ω' respectively, results from the conservation of energy and momentum

$$\omega' = \omega \pm \omega_S \tag{2.4}$$

$$\mathbf{k}' = \mathbf{k} \pm \mathbf{k_S}, \tag{2.5}$$

where $\mathbf{k_S}$ and ω_S denote the wavevector and the angular frequency of the involved sound wave respectively. The $\pm$ sign accounts for the different propagation directions of the sound wave. When considering the fact, that the scattered wave vector changes only little in absolute value, i.e. that $|\mathbf{k}'| \approx |\mathbf{k}| = \mathrm{k}$ is valid, the following relations hold for $\mathrm{k_S}$:

$$\mathrm{k_S^2} = \left|\mathbf{k}' - \mathbf{k}\right|^2 = \mathrm{k'^2} + \mathrm{k^2} - 2\mathbf{k}'\mathbf{k} = 4\mathrm{k^2}\sin^2\frac{\theta}{2} \tag{2.6}$$

$$\mathrm{k_S} = \pm 2\mathrm{k}\sin\frac{\theta}{2} = \pm\frac{4\pi\,\mathrm{n_{H_2O}}}{\lambda}\sin\frac{\theta}{2}. \tag{2.7}$$

It is obvious, that the scattered light wave undergoes a frequency change of ω_S due to the mentioned conservation of energy and momentum (cf. Eqs. 2.4 and 2.5).

Table 2.1: Expansion coefficients in the empirical expression for the speed of sound $v_S(T, S)$ as quoted by Del Grosso [66].

$c_0 = 1402.392$	$c_1 = 5.01109398873$
$c_2 = -0.0550946843172$	$c_3 = 0.00022153596924$
$c_4 = 1.32952290781$	$c_5 = 0.000128955756844$
$c_6 = -0.012562783426$	$c_7 = 0.000096840315641$

Hence, by inserting $k_S = \omega_S / v_S$, which relates the absolute wavevector k_S to the speed of sound v_S, in Eq. 2.7

$$\omega_S = \pm \frac{4\pi n_{H_2O} v_S}{\lambda} \sin \frac{\theta}{2} \tag{2.8}$$

results and obtaining the commonly used Brillouin–shift $\nu_B = \omega_S / 2\pi$ is straight forward:

$$\nu_B = \pm 2 \frac{n_{H_2O} v_S}{\lambda} \sin \frac{\theta}{2}. \tag{2.9}$$

Thus, the Brillouin–shift ν_B is sensitive to the local velocity of sound $v_S(x)$ and the local refractive index $n_{H_2O}(x)$. Both entities depend on the local temperature T(x) and the local salinity S(x) [64, 66–69]:

$$v_S = v_S(x) = v_S(T(x), S(x), p(x)) \tag{2.10}$$

$$n_{H_2O} = n_{H_2O}(x) = n_{H_2O}(T(x), S(x), \lambda, p(x)). \tag{2.11}$$

The dependency of the water pressure p(x) on the penetration depth x is well known. In addition, Leroy and Parthiot published in 1998 relationships which connect pressure and depth in the oceans and seas [70] (an erratum has been recently published [71]). However, due to this well known dependency it will be neglected for the upcoming discussion, as it can always be easily included.

Del Grosso published in 1974 an empirical relation, which relates the speed of sound $v_S(T, S)$ to the water temperature T and salinity S [66]:

$$\begin{aligned} v_S(T, S, p) = c_0 + c_1 T + c_2 T^2 + c_3 T^3 + \\ c_4 S + c_5 S^2 + c_6 TS + c_7 T^2 S + f(S, T, p). \end{aligned} \tag{2.12}$$

The expansion coefficients c_i are summarized in Tab. 2.1 and f(S, T, p) accounts for the mentioned pressure dependency. Although Eq. 2.12 is still of practical use, successive enhancements have been performed through the last decades. They include local variations and can be found in the corresponding literature [67, 69]. However, due to its simplicity and high accuracy, Eq. 2.12 has been used in this work.

In addition, Quan and Fry published an empirical relation for the index of refraction of seawater $n_{H_2O}(T(x), S(x), \lambda)$ [64]:

$$\begin{aligned} n_{H_2O}(T,S,\lambda) = n_0 + S(n_1 + n_2 T + n_3 T^2) + n_4 T^2 + \\ \frac{n_5 + n_6 S + n_7 T}{\lambda} + \frac{n_8}{\lambda^2} + \frac{n_9}{\lambda^3} \end{aligned} \tag{2.13}$$

Table 2.2: Expansion coefficients in the empirical expression for the index of refraction of seawater $n_{H_2O}(T,S,\lambda)$ as quoted by Quan and Fry [64].

$n_0 = 1.31405$	$n_1 = 1.779 \times 10^{-4}$
$n_2 = -1.05 \times 10^{-6}$	$n_3 = 1.6 \times 10^{-8}$
$n_4 = -2.02 \times 10^{-6}$	$n_5 = 15.868$
$n_6 = 0.01155$	$n_7 = -0.00423$
$n_8 = -4382$	$n_9 = 1.1455 \times 10^{6}$

and Tab. 2.2 summarizes the corresponding expansion coefficients. Eqs. 2.12 and 2.13 are important results, as they connect the speed of sound and the index of refraction with the temperature T and the salinity S of the water sample. Hence, the 5 parameters ν_B, n_{H_2O}, v_S, S and T are interconnected through Eqs. 2.9, 2.12 and 2.13, so that by measuring ν_B it is possible to extract the water temperature T, when the salinity S is known. However, although the salinity S is not a priori known, extensive studies of Fry *et al.* showed that the salinity parameter S has a minor effect on the deduction of the water temperature T by a measurement of the Brillouin–shift ν_B [72]. Precisely speaking, Fry *et al.* showed, that whenever the salinity S is known, an uncertainty of 1 MHz in the measurement of the Brillouin–shift ν_B results in an uncertainty of the deduced temperature T of 0.06°C. If the salinity S is equipped with an uncertainty of 1‰, a temperature uncertainty of 0.4°C results. In addition, the studies of Fry *et al.* showed that the uncertainty in salinity S does not extend 1‰ within 92% of the world oceans, even though S is subject to well known seasonal periodicities. Hence, by extracting the salinity S from historical data its uncertainty can be reduced to less than 1‰ and thus it is possible to extract the water temperature T from the measurement of the Brillouin–shift ν_B with an uncertainty of less than 0.4°C. These results have to be emphasized again, as they allow accurate measurements of the temperature profile. Whenever the salinity S is known or subject to independent measurements an increase of the measurement accuracy results.

Typical values for the index of refraction and the speed of sound are $n_{H_2O} = 1.33$ and $v_S = 1500$ m/s respectively. For the proposed Brillouin–lidar implementations only a scattering angle of $\theta = 180^\circ$ is of importance, so that a Brillouin–shift of the order of $\nu_B = 7.5$ GHz has to be expected for a laser wavelength of $\lambda = 532$ nm. However, the quoted relations for the speed of sound and the index of refraction (cf. Eqs. 2.12 and 2.13) allow a more accurate estimation. Typical oceanic temperatures lie between 0°C and 40°C, and the salinity varies between 30‰ and 40‰ [72]. Hence, by inserting these acceptance boundaries into the above relations, a Brillouin-shift of 7–8 GHz results for an operation wavelength of $\lambda = 532$ nm. This result is of importance for the lidar system, which has been proposed by Fry, as its transmitter employs a frequency doubled Nd:YAG laser [17]. As this work follows the proposal of Walther *et al.*, whose transmitter employs a frequency doubled fiber amplifier together with an ESFADOF edge-filter, a different output wavelength of $\lambda = 543$ nm has to be considered [16].

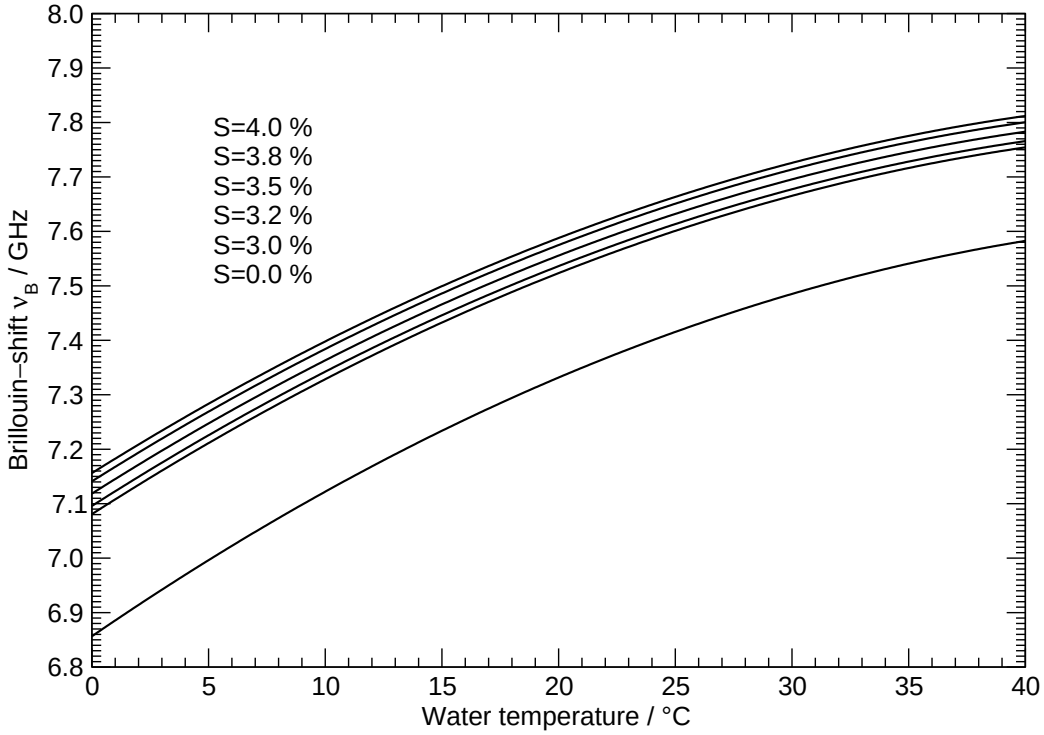

Fig. 2.3: Temperature dependence of the Brillouin–shift ν_B for different salinities S, $\theta = 180°$ and $\lambda = 543$ nm: The plots have been calculated by inserting Eqs. 2.12 and 2.13 into Eq. 2.9. Whenever the salinity is known a clear relationship between the Brillouin-shift and the temperature exists.

Hence, Brillouin-shifts between 6.8–7.8 GHz occur, as depicted in Fig. 2.3 for different salinities.

For the sake of completeness it has to be mentioned, that the literature discusses also a lidar system based on stimulated Brillouin–scattering [49, 50]. However, it is of minor importance for a practical remote sensing application of oceanic temperature profiles, as it does not allow single shot profiling or the detection of submerged objects. Briefly speaking, the description of stimulated Brillouin–scattering is based on the described spontaneous Brillouin–scattering, where the incident light wave induces itself density fluctuations inside the scattering medium. They are responsible for the stimulated Brillouin–scattering through a self enhancing effect. A detailed treatment of the stimulated Brillouin–scattering can be found in the corresponding literature [31, 62, 73].

2.2.3 Spectral Profile of the Backscatter

As stated above, the temperature information is encoded in the spectral profile of the scattered light. The part, which is redirected under $\theta = 180°$ back to the aircraft is of particular importance and its spectral profile can be decomposed into 2 principal components (cf. Fig. 2.4):

1. Rayleigh–scattering: Rayleigh-scattering occurs due to the presence of dissolved hydrosols. The elastic nature of this process reproduces the spectral profile of the injected laser pulses [31]:

$$S_R(\Delta\nu) = I_R\, S_L(\Delta\nu, \delta\nu_L). \tag{2.14}$$

Here $\Delta\nu$ represents the frequency shift from the injected Brillouin-lidar laser wavelength and I_R represents the total integrated intensity, such that

$$\int S_L(\Delta\nu, \delta\nu_L)\mathrm{d}\Delta\nu = 1 \tag{2.15}$$

holds for the normalized spectral profile of the laser $S_L(\Delta\nu, \delta\nu_L)$, which can be described as a normalized Lorentz–profile for cw lasers:

$$S_L(\Delta\nu, \delta\nu_L) = L(\Delta\nu, \delta\nu_L) = C\frac{(\delta\nu_L/2)^2}{\Delta\nu^2 + \left(\frac{\delta\nu_L}{2}\right)^2}. \tag{2.16}$$

$\delta\nu_L$ is the spectral width of the laser emission and by setting $C = \frac{2}{\pi\delta\nu_L}$ a normalization with respect to the integrated intensity of $L(\Delta\nu, \delta\nu_L)$ results; otherwise by setting $C = 1$ a normalization with respect to the peak intensity can be obtained. However, the spectral profile of a laser pulse can be different from the Lorentz–profile. In general, the spectral profile reflects the temporal characteristics of the laser pulse through its Fourier–transformation [74]. The proposed Brillouin-lidar transmitter injects 10 ns near Fourier–limited laser pulses into the water column [16]. From the Gaussian temporal profile a Gaussian spectral profile results and S_L transforms into:

$$S_L(\Delta\nu, \delta\nu_L) = G(\Delta\nu, \delta\nu_L) = \frac{1}{\sqrt{2\pi}\,\delta\nu_L} e^{-\frac{\Delta\nu^2}{2\delta\nu_L^2}}. \tag{2.17}$$

A more thorough treatment has to take the actual temporal profile into account. However, for a 10 ns long pulse, near Fourier limited operation has been demonstrated and the Gaussian approximation is valid. The spectral width of the 7 ns long frequency converted output pulse has been measured to $\delta\nu_L = 62.9$ MHz, which is only a factor of 1.01(7) broader than the theoretical lower limit for a pure Gaussian pulse [19].

However, the absence of hydrosols, which is the case for most of the oceanic waters, leads to an almost total suppression of the Rayleigh–scattering. Its contribution to the spectral profile follows the Landau–Placzek ratio, which relates the intensity of the Rayleigh–scattering I_R to the total intensity of the Brillouin–scattering $2\,I_B$ by

$$\frac{I_R}{2\,I_B} = \gamma_c, \tag{2.18}$$

where γ_c represents the ratio of specific heats [75–77]. However, particularly turbid waters near the costal zone exhibit a strong Rayleigh–component. It has

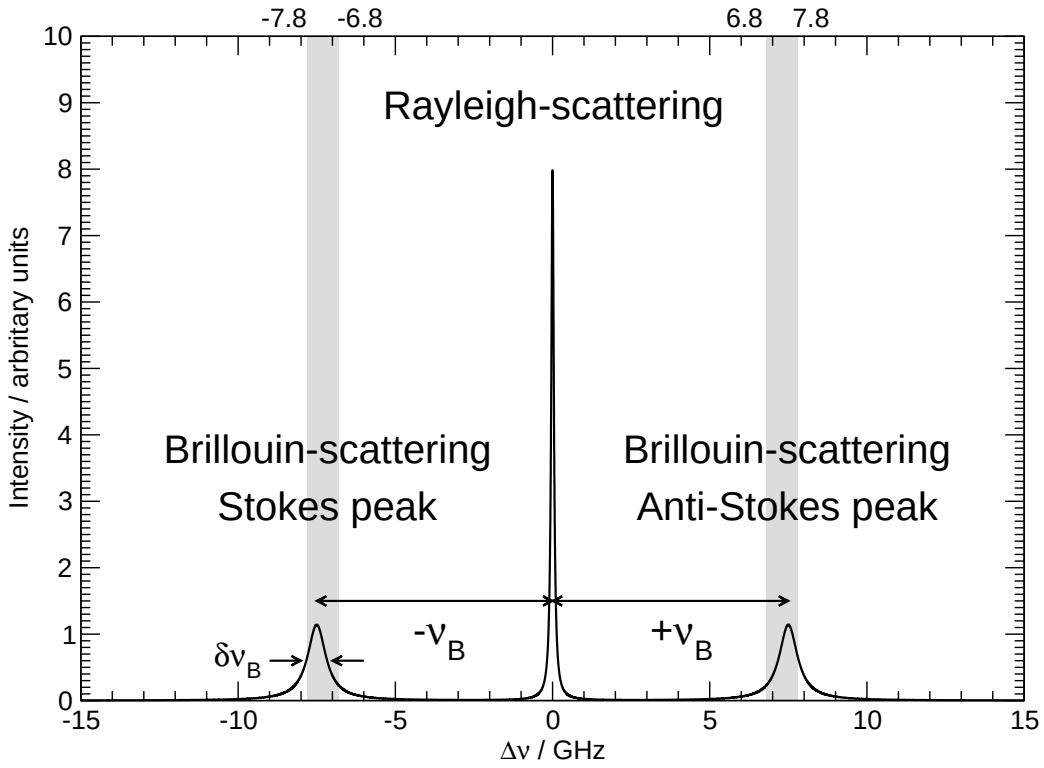

Fig. 2.4: Simulated backscattered spectrum: The spectral profile of the backscatter can be decomposed into the Rayleigh–scattering, which emerges due to elastic scattering on hydrosols, and into inelastic Brillouin-scattering on permanently available density fluctuations. The doublet–structure is a result of the symmetry of the Brillouin–scattering. The gray areas mark the region of interest, where the temperature dependent frequency shift ν_B of the Brillouin–scattering has to be expected for oceanic water temperatures of interest (0°C–40°C) when probing the Brillouin–scattering with laser pulses at 543 nm. The plot shows a simulated spectrum for $\nu_B = \pm 7.5$ GHz, $\theta = 180°$ and a considerable amount of hydrosols, which lead to the pronounced Rayleigh–scattering.

to be excluded from the backscattered spectrum prior to the evaluation by the receiver system, in order to exclude any unwanted crosstalks or side–effects. Narrow atomic or molecular absorption lines are suitables candidates for this task. The system of Fry *et al.* employs Iodine and/or Bromine molecular absorption cells [17, 39–42].

2. Brillouin–scattering: The wave–picture of the scattering process allows the interpretation of Eqs. 2.5 and 2.7 as a Bragg–condition, which guarantees constructive interference of the scattered light waves (cf. Fig. 2.2). Here, the periodic sound wavefronts act as moving reflectors, which result in a Doppler shift of ν_B of the scattered light waves; the factor of 2 accounts for the movement of the reflectors and the $\pm$ sign for both propagation directions. Employing this picture it follows that the sound waves, which experience an exponential damping Γ_S, imprint statistical phase fluctuations on the scattered light

wave. The latter result in a Lorentz–profile, when spectrally resolving the scattered light [31, 65]. Hence the spectral profile of the Brillouin–scattering $S_B(\Delta\nu, \nu_B, \delta\nu_B)$ can be decomposed into two symmetrically located Lorentz–profiles:

$$\begin{aligned} S_B(\Delta\nu, \nu_B, \delta\nu_B) &= I_B\,(L(\Delta\nu - \nu_B, \delta\nu_B) + L(\Delta\nu + \nu_B, \delta\nu_B)) \\ &= I_B\,C\left(\frac{(\delta\nu_B/2)^2}{(\Delta\nu - \nu_B)^2 + \left(\frac{\delta\nu_B}{2}\right)^2} + \frac{(\delta\nu_B/2)^2}{(\Delta\nu + \nu_B)^2 + \left(\frac{\delta\nu_B}{2}\right)^2}\right). \end{aligned} \tag{2.19}$$

ν_B denotes the temperature dependent Brillouin-shift and $\delta\nu_B$ the spectral width of the Lorentz–profile $L(\Delta\nu - \nu_B, \delta\nu_B)$. Again, by setting $C = \frac{2}{\pi\delta\nu_B}$ a normalization with respect to the integrated intensity $2\,I_B$ is achieved. The red shifted component is referred to as the Stokes peak and the blue shifted one as the anti-Stokes peak.

Due to the fact that the Brillouin–scattering is always probed with light sources of finite spectral width an additional broadening of the Lorentz–profile results. This holds true in particular when employing short but spectrally broad laser pulses. Hence, $S_B(\Delta\nu, \nu_B, \delta\nu_B)$ has to be replaced by the convolution of S_B with the spectral profile of the probe laser S_L:

$$S_B^L(\Delta\nu, \nu_B, \delta\nu_B, \delta\nu_L) =$$

$$\int S_B(\Delta\nu, \nu_B, \delta\nu_B)\, S_L(\Delta\nu - \Delta\nu', \delta\nu_L)\, d\Delta\nu'. \tag{2.20}$$

This is the reason for the efforts in delivering Fourier transform limited probe pulses. In view of the above discussion (cf. Sec. 2.2.4), 7 ns long Fourier transform limited probe pulses allow a spatial resolution of approx. 1 m, while they contribute only with $\delta\nu_L = 62.9$ MHz to the additional spectral broadening of eq. 2.20. Compared to the spectral width of the Brillouin–lines, which will be discussed below, this contribution has a minor effect on the determination of the Brillouin–shift, but has to be included for a proper calibration of the receiver system.

The Lorentz–character of the spectral profile of the Brillouin–scattering reflects the lifetime of the involved sound waves via

$$\delta\nu_B = \frac{\Gamma_S}{2}\left(\frac{4\pi\, n_{H_2O}}{\lambda}\sin\frac{\theta}{2}\right)^2. \tag{2.21}$$

The exponential damping of the sound waves Γ_S depends on

$$\Gamma_S = \frac{1}{\rho}\left(\frac{3}{4}\eta + \eta' + \frac{\kappa}{C_p}(\gamma_c - 1)\right)^2, \tag{2.22}$$

where ρ is the density of water, η is the shear viscosity, η' is the bulk viscosity, κ is the thermal conductivity and $\gamma_c = \frac{C_p}{C_v}$ is the ratio of specific heats of

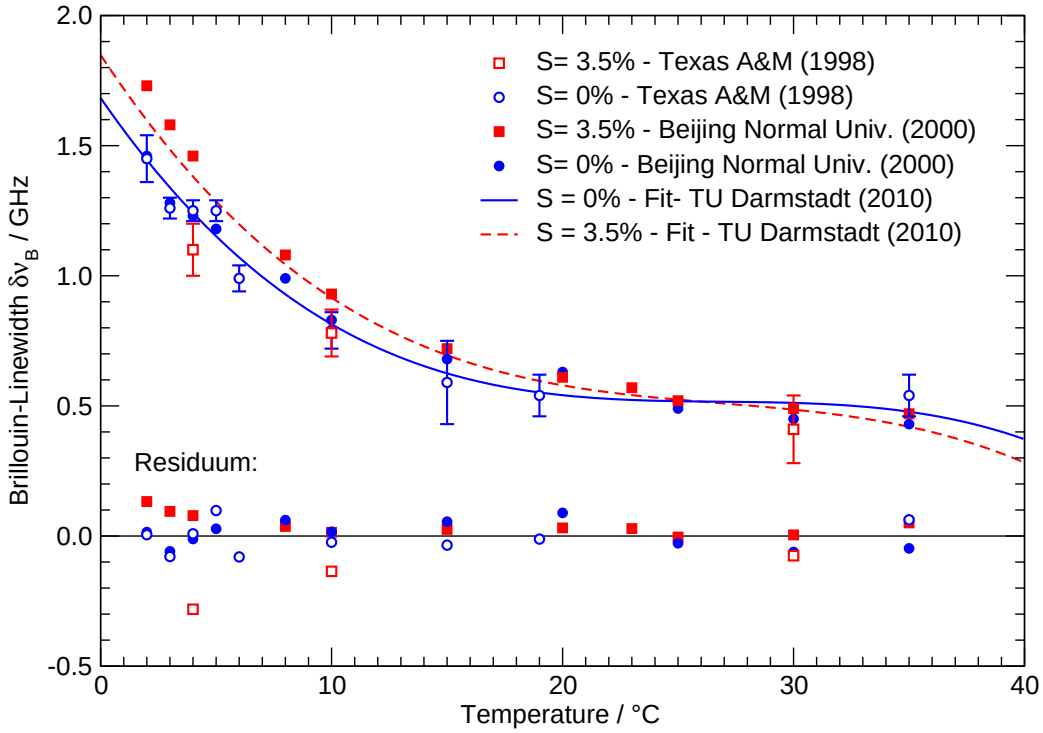

Fig. 2.5: Temperature dependence of the Brillouin–linewidth $\delta\nu_B$ for two different salinities S and $\theta = 180°$: The data points have been extracted from Ref. [41]. The Brillouin–linewidth $\delta\nu_B$ decreases from 1.73 GHz to 0.41 GHz with increasing temperature. The data also suggests a dependency on the salinity S, which has been implemented in the polynomial fit. However, the residuum indicates a poor accuracy of <0.2 GHz for >95% of the data points.

water [31, 41]. Data for the thermal conductivity κ, the density ρ, the shear viscosity η and the ratio of specific heats γ_c are available in the literature [78]. Hence, a measurement of the Brillouin–linewidth $\delta\nu_B$ can be used to determine the temperature dependence of the bulk viscosity of water, which has been performed by Rouch *et al.* in 1976 [77]. Fry *et al.* succeeded in measuring the temperature dependence of $\delta\nu_B$ for two different salinities [41]. The results of these measurements are depicted in Fig. 2.5. The probing wavelength was $\lambda_1 = 532$ nm and the Brillouin–backscatter ($\theta = 180°$) has been evaluated by a scanning high finesse Fabry–Perot interferometer. The Brillouin–linewidth $\delta\nu_B$ decreases from 1.73 GHz to 0.41 GHz with increasing temperature. The data also suggest a dependency on the salinity S, which is bound to the structure of the water solution [79]. Tao *et al.* measured in 1988 Brillouin spectra of LiCl aqueous solutions as a function of concentration. They showed that the Brillouin–linewidth is subject to the dynamics of the hydration shell and their suggested model derived characteristic relaxation times on a ps time scale (e.g. 24 ps at 36 mol % LiCl) [80]. In 2002 Erokhin reviewed several methods in determining the water structure. Among them, he suggested ultrafast nonlinear pump probe experiments [79]. However, re-

cent progress in ultrafast infrared pump probe experiments revealed the dynamics of the hydrogen-bond formation [81] and the molecular reorientation dynamics of pure liquid water [82], as well as the dynamics of the hydration shell [83, 84]. Fayer and coworkers recently published the direct observation of the characteristic timescales for a hydrogen bond to switch from the ion to a water molecule and vice versa [84]. The first process takes the order of 7 ps and is independent from the ion concentration. In other words, it is representative of the residence time of water in the hydration shell. The reverse process was determined to take 24 ps, while being dependent on concentration; it increases with decreasing salt concentration [83, 84]. The agreement between both independent methods of Tao *et al.* and Fayer *et al.* is striking.

In conclusion, a highly accurate Brillouin–lidar remote sensing technique has to take the ion–water dynamics into consideration. For a thorough assessment of the detection system within the framework of this study, the temperature and salinity dependence of the Brillouin–width $\delta\nu_B$ has been approximated through a polynomial fit to the data of Ref. [41]. An elementary model, which exhibits the smallest residuum is given by

$$\delta\nu_B = a_0 + a_1 T + a_2 T^2 + a_3 T^3 + a_4 S + a_5 S T. \qquad (2.23)$$

As data for two salinities have been measured, only a linear ansatz in S makes sense. Tab. 2.3 summarizes the corresponding expansion coefficients and the result of Eq. 2.23 together with the corresponding residuum are included in Fig. 2.5. The validity of the model is restricted to the temperature range of 2°C to 35°C, where data is available. In addition the change in operation wavelength has to be considered. The data of Fig. 2.5 has been measured with the help of a frequency doubled Nd:YAG laser and a calibrated scanning high–finesse Fabry–Perot interferometer. The probing wavelength was $\lambda_1 = 532$ nm [41]. As the operating wavelength of this work is $\lambda_2 = 543$ nm, Eq. 2.23 has to be corrected according to Eq. 2.21 by a factor of $(\frac{\lambda_1}{\lambda_2})^2 = 0.96$. Although this correction lies well within the accuracy of the residuum, it has to be applied in order to exclude this systematic error. However, it is highly desirable that future investigations increase the accuracy of the mentioned measurements of the Brillouin–width, upon which the quoted polynomial fit relies. This would considerably increase the measurement accuracy of the Brillouin–lidar and resolve potential ambiguities due to the poor knowledge of the salinity dependence.

Fry *et al.* already suggested in 2002 the simultaneous measuremend of the Brillouin–linewidth as an additional relationship, which would complete the system of equations [41]. Hence, the 5 a priori unknown parameters ν_B, v_S, n_{H_2O}, S and T are fully determined by Eqs. 2.9, 2.12, 2.13, 2.23 and the measurement of ν_B and $\delta\nu_B$, so that the temperature and salinity profile can be extracted with high accuracy without the need of introducing historical data. However, in view of the required accuracy for the measurement of $\delta\nu_B$, which has to extend the so far achieved accuracy, such a system faces huge difficulties. In particular when regarding high penetration depths, from where only

Table 2.3: Expansion coefficients in the empirical expression for the Brillouin–linewidth $\delta\nu_B$.

$a_0 = 1.683(57)$	$a_1 = -0.128(15)$
$a_2 = 0.0047(10)$	$a_3 = -6(2) \times 10^{-5}$
$a_4 = 0.0047(14)$	$a_5 = -1.82(78) \times 10^{-4}$

few photons reach the detector, this method seems unlikely to yield the desired high accuracies.

2.2.4 Receiver

The discussion showed, how the Brillouin–scattering can be explored as a temperature tracer within a remote sensing technique. Compared to the Raman–technique, which requires the determination of the spectral contributions from the monomer– and polymer–configuration of the water molecules, the Brillouin–shift is not susceptible to daylight, parasitic fluorescence and selective absorption due to Chlorophyll or dissolved organic matter, as the temperature information is encoded in the Brillouin–shift ν_B and not in the intensity of the signal. In other words, the measurement principle is highly robust against external distortions, due to the high spectral brightness of the Brillouin–signal, when compared to spectral broad contributions as daylight, parasitic fluorescence or selective absorption. The latter influences only the signal to noise ratio and hence the maximum achievable observation depth.

In order to resolve the Brillouin–shift, different detection schemes are conceivable (cf. Fig. 2.6):

1. **Scanning Fabry–Perot interferometer:** The employment of a high finesse scanning Fabry-Perot interferometer in combination with a photomultiplier tube delivers the entire Brillouin–spectrum, when the mirror distance of the interferometer is scanned by a piezoelectric transducer. The so recorded spectra are similar to the one depicted in Fig. 2.4 and the Brillouin-shift ν_B as well as the spectral width $\delta\nu_B$ can be extracted by fitting the discussed spectral profiles to the data (cf. Eqs. 2.14 and 2.19). Recently, by employing this technique, first range resolved measurements of the water temperature have been demonstrated. However, due to the mechanically controlled interference of the collected backscatter, this technique is suited for a well controlled laboratory test frame, but not for the noisy environment on board a mobile platform. In addition, this technique does not provide single shot profiling. In fact, the depth profile has been extracted by appropriately gating the detection electronics, which evaluate the signals from the photomultiplier tube, on a ns time scale [19, 44].
2. **Solid Fabry–Perot interferometer:** By employing a low finesse solid Fabry–Perot interferometer, it is possible to implement an edge–filter technique [45, 85–87]. In contrast to the previous detection scheme, a mechanical scanning of the mirror distances is not required any more. The idea is to pass

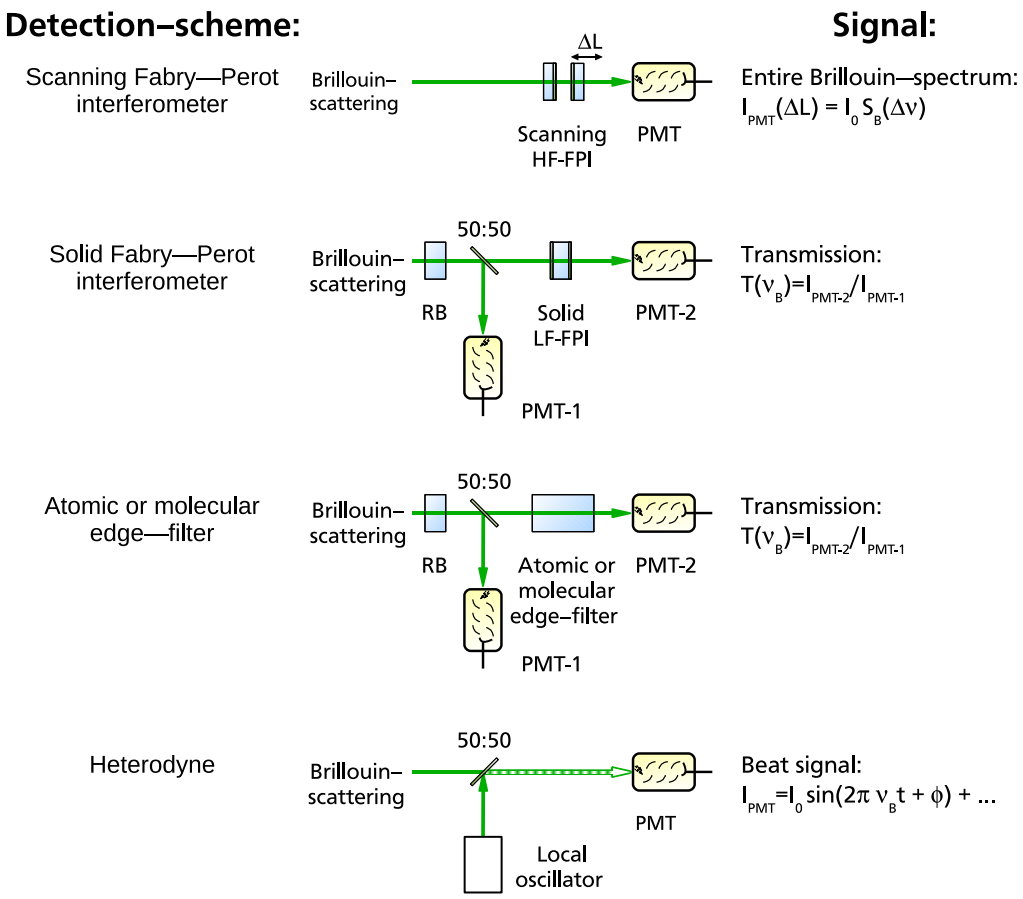

Fig. 2.6: Schematic overview of the discussed detection–schemes: Photomultiplier tube or equivalent photodetector (PMT), 50:50 beam splitter (50:50). The Rayleigh–blocker (RB) extracts the elastic component from the backscatter. Othewise, a trustworthy ratio of the recorded intensity signals $I_{PMT\text{-}2}/I_{PMT\text{-}1}$ is not possible. The resulting signals depend on the employed detection scheme, but are always a function of the Brillouin–shift ν_B, which allows the deduction of the water temperature.

the backscattered light through the solid Fabry–Perot interferometer. Due to interference effects within the interferometer only a fraction of the collected light passes through. As the amount of light, which passes the interferometer, depends on the frequency shift of the return signal it is possible to deduce the frequency shift through a former performed calibration, provided that the free spectral range of the interferometer covers the dynamic range of the Brillouin–scattering process, e.g. the $\pm$7–8 GHz for 532 nm light, and that the interferometer offers a sufficiently low finesse, such that the dynamic range of the interferometer's transmission covers itself the mentioned spectral region of interest of $\pm$7–8 GHz around the injected laser pulses. However, the setup has to hold the distance between the two mirrors fixed by all means. Practical implementations employ a solid substrate of appropriate thickness, whose highly parallel front facets are equipped with appropriate coatings. Neverthe-

less, as the free spectral range and the finesse of the interferometer depend on the mirror distance and their surface quality respectively, they are always subject to environmental distortions, which can not be fully excluded. Thus, this method requires extremely stable operating conditions and/or repeated calibrations in order to deliver reliable data. Another issue is the lack in light gathering power, which is a consequence of the poor finesse of the interferometer. This effect considerably reduces the signal to noise ratio together with the discrimination of the signal. Thus, high pulse intensities in combination with an additional narrow spectral bandpass, which filters the backscattered light from the unwanted broad background spectrum, are required in order to increase the signal to noise ratio. However, this method has been widely employed for wind lidars [45] and is of particular importance for the satellite based wind–lidar ADM-Aeolus [85–87]. These systems extract the wind velocity field from the backscattered light through the Doppler–shift, which is imprinted by the Rayleigh– or Mie–scattering. Hence, employing UV probe laser pulses is advantageous in order to increase the Doppler–shift and thus simultaneously the velocity discrimination [85]. However, systems relying on infrared and visible radiations have been realized as well [45]. Due to the solid setup of the interferometer single shot profiling is always possible.

3. **Atomic or molecular edge–filters:** The detection scheme described under point 2 can be established also by other means. A possible implementation takes advantage of the spectral transmission characteristics of atomic or molecular absorption lines. By replacing the solid Fabry–Perot interferometer with an atomic or molecular absorption cell, the same detection scheme results, provided that the dynamic range of the scattering process can be resolved by the edges of the involved absorption line. The measurement of the frequency shift is then reduced again to the measurement of the filter transmission. In addition, these filters offer considerably steeper transmissions–edges in general and hence increase the discrimination of the signal. When employing such filters, the problem is reduced to the employment of a suitable probe laser, whose operating wavelength suits or can be tailored to the needs of the atomic or molecular edge–filter, or vice versa. Such systems have been implemented as detectors for wind–lidars [45, 46], but are also of importance for the Brillouin–lidar implementation of the proposed system of Fry *et al.* [17, 39–42]. Their system employs a frequency doubled Nd:YAG laser and an edge–filter receiver based on molecular Iodine absorption cells. I_2 is of particular interest, as the outer edges of a pair of its molecular absorption lines lie within the region of interest, i.e. $\pm$7–8 GHz around the 532 nm emission wavelength of the transmitter. In addition, Th. Walther *et al.* proposed a Brillouin–lidar transceiver based on a frequency doubled fiber amplifier and an ESFADOF detector [16, 47, 48]. The ESFADOF device is an atomic edge–filter, whose transmission characteristics can be tailored to the needs of the Brillouin–lidar measurement principle. The transmission characteristics of the ESFADOF device is the subject of this work. The employment of a frequency doubled fiber amplifier based transmitter is mandatory, as it allows to tailor the emission wavelength of the Brillouin–lidar to the needs of the ESFADOF detector.

Both the Iodine as well as the ESFADOF edge–filter allow single shot profiling and offer a considerably increased light gathering power, as their working principle does not rely on interference effects.

4. **Heterodyne detection scheme:** The working principle of a heterodyne detection scheme is as follows: (1) The backscattered light wave is superimposed with the light wave of a local oscillator, whose emission wavelength is precisely known. The emission wavelength of the local oscillator can, but does not have to be identical to the emission wavelength of the transmitter. (2) The superposition of both light waves is guided to a sufficiently fast photodetector. (3) The photodetector records a beat–signal, due to interference effects between both light waves. The carrier frequency of the beat–signal corresponds to the sum of both frequencies and the envelope to their difference. However, the fast carrier frequency can not be resolved by the detector, which records only the considerably lower envelope frequency. (4) By evaluating this beat–signal using appropriate electronic devices, like an electrical spectrum analyzer, a measurement of the frequency difference between both light waves is possible [45]. This detection scheme has been successfully employed in Doppler wind–lidar systems [45, 88]. A heterodyne detection system, which extracts the Brillouin–shift from the backscattered signal might be possible, though it has not been investigated to the best knowledge of the author yet. The demands on such a system are rather stringent: (a) An additional local oscillator is required. It has to emit narrowband cw laser light, whose emission wavelength matches the wavelength of the injected laser pulses. (b) The detector, which records the beat–signal, has to be able to follow the beat–signal of approx. 7–8 GHz with high accuracy, when employing green laser pulses. (c) In addition, the bandwidth of the employed electronics must allow the resolution of the large Brillouin–shift with an accuracy of 1 MHz, in order to achieve the desired temperature accuracies. (d) Single shot profiling can only be achieved if the electronics extract the frequency shift on a ns time scale. Otherwise an electrical gating technique is required.

   The cw output of the master oscillator of the fiber amplifer can be used in order to generate the local oscillator radiation. The operating scheme of the transmitter cuts ns pulses from the cw output of the master oscillator. Only these pulses are injected into the fiber amplifier. Hence, for all other times the cw laser light of this master oscillator can be used in order to seed a second fiber amplifier. The second fiber amplifier increases the laser power, so that by an additional second harmonic generation the required cw green laser light is produced. The green cw output matches then the frequency of the injected laserpulses and can be used as a local oscillator for the heterodyne detection scheme.

   Alternatively, it is possible to weaken the mentioned requirements by shifting the operating wavelength of the local oscillator to the center of the region of interest of the Stokes or anti–Stokes Brillouin–peak (cf. Fig. 2.4). This considerably reduces the bandwidth of the heterodyne signal, which has to be resolved by the employed detector and electronics, to the spectral width of

the Brillouin-peaks. However, a second master oscillator is required then. Its emitted radiation has to be amplified and frequency converted as described. But, as the frequency of the local oscillator has to be known and held fixed on a MHz scale with respect to the frequency of the injected laser pulses, an additional locking–mechanism is required, which considerably increases the complexity of the detection scheme.

A promising alternative to actively shifting the emission wavelength of the local oscillator is the employment of a temperature and salinity controlled water sample on board the aircraft. This makes the need of a second master oscillator obsolete, in case the cw output of the initial master oscillator is amplified and frequency converted. By injecting this green cw output into the calibrated water sample, the spontaneous Brillouin–scattering inside the water sample can be exploited, as it is presicely known. The so generated known Brillouin–scattering can be successively mixed with the unknown Brillouin–scattering signal from the ocean. The resulting beat–signal on the photodetector, can be evaluated as above in order to extract the temperature profile of the oceanic water column.

In addition to the Brillouin–shift, the heterodyne technique delivers also the width of the Brillouin–lines, so that the above mentioned temperature and salinity dependency of the Brillouin–width (cf. Eq. 2.23) can be explored.

Schemes 2 and 3 are referred to as direct detection schemes and scheme 4 as heterodyne or coherent detection scheme and a thorough comparison of these schemes can be found in Ref. [45]. There it is shown that, regardless whether scheme 2 or 3 is employed as edge-filter, the accuracies of the direct and coherent detection scheme are nearly equivalent, when employing state-of-the-art technologies. They almost reach the shot–noise limit for a wide range of signal intensities and the accuracy is dominated by the spectral width and the intensity of the return signal. The two intensity extrema are of particular interest: Coherent–lidars profit from an enhancement of the beat–signal due to the presence of the local oscillator, so that they are advantageous for low intensities. Direct detection lidars are superior when high return intensities lead to disturbing coherent speckle–formation [45].

In conclusion, as a practical receiver system has to measure the Brillouin–shift ν_B on a ns time scale, while being able to reliably operate within the harsh environment on board an aircraft, only direct detection schemes, which employ edge-filters, or the heterodyne technique are accurate and fast enough, while they are sufficiently insensitive to vibrations. However, in view of the discussed complexity of the heterodyne technique, when regarding the measurement of the Brillouin–shift, a direct detection scheme seems more advantageous. This work is embedded in the framework of the proposal of Th. Walther *et al.* and investigates the employment of an excited state Faraday anomalous dispersion optical filter (ESFADOF) as edge–filter within the direct detection scheme. This approach offers several advantages: (1) The employment of an ESFADOF allows to tailor the edge-filter characteristics to the needs of the measurement, so that the symmetry

of the Brillouin–backscatter can be exploited, which increases the signal/noise–ratio considerably. (2) The system is insensitive to vibrations, as resonators are not required, and exhibits a high light gathering power. (3) The signal processing allows single shot profiling on a ns time scale, while keeping the complexity reasonable.

2.3 Ideal Edge–Filter

The previous section discussed the system requirements towards a practical Brillouin–lidar remote sensing technique of oceanic temperature profiles. Particular focus has been spent on the Brillouin–scattering and the spectral profile of the backscatter, which can be explored as a temperature tracer. Different detection schemes are conceivable in order to extract the Brillouin–shift and hence the temperature information (cf. Sec. 2.2.4 and Fig. 2.6). This subsection is dedicated to the direct detection scheme, which is one of the most promising techniques. Suitable edge-filters are excited state Faraday anomalous dispersion optical filters (ESFADOFs). Their working principle, their implementation and assessment are the subject of this work. However, a thorough investigation of the ideal edge–filter reveals important insight for an optimized system design.

The symmetric square well transmission spectrum, is the ideal edge–filter, as the dynamic range of the Brillouin–shift ν_B barely extends to twice the Brillouin–width $\delta\nu_\mathrm{B}$ for water temperatures of interest (0°C–40°C; compare Figs. 2.3–2.5). The symmetry cancels small frequency fluctuations of the probe laser. The transmission spectrum of this ideal edge–filter follows

$$\begin{aligned}\mathrm{F}(\Delta\nu) = &\left\{\Theta(-(\Delta\nu-\Delta\nu_\mathrm{Edge}))-\Theta(-(\Delta\nu-2\Delta\nu_\mathrm{Edge}))\right\}+\\ &\left\{\Theta(\Delta\nu-\Delta\nu_\mathrm{Edge})-\Theta(\Delta\nu-2\Delta\nu_\mathrm{Edge})\right\}\end{aligned} \tag{2.24}$$

and is depicted in the inset of Fig. 2.7. $\Theta(\Delta\nu)$ represents the Heaviside unit step function [89] and the terms in curly brackets correspond to boxcar functions, such that the overall transmission beyond the region of interest of $[-2\Delta\nu_\mathrm{Edge}, 2\Delta\nu_\mathrm{Edge}]$ vanishes. The position of the transmission edges has been chosen to $\Delta\nu_\mathrm{Edge} = 7.5$ GHz, which lies well within the region of interest of $\pm 6.8 - 7.8$ GHz and delivers the steepest transmission signal with respect to a temperature change.

According to Fig. 2.6, the signal of the direct detection scheme, which employs an edge–filter, is the ratio between the transmitted and collected intensity $\mathrm{S}_1 = \mathrm{T}(\nu_\mathrm{B}) = \mathrm{I}_\mathrm{PMT\text{-}2}/\mathrm{I}_\mathrm{PMT\text{-}1}$. Any corrections, as e.g. the sensitivities of the employed photomultiplier tubes, have been omitted for clarity. They can be easily integrated [45]. However, any photomultiplier tube spectrally integrates the recorded intensity and the signal S_1 becomes

$$\mathrm{S}_1(\mathrm{T,S}) = \frac{1}{2\,\mathrm{I}_\mathrm{B}} \int \mathrm{F}(\Delta\nu)\; \mathrm{S}_\mathrm{B}^\mathrm{L}(\Delta\nu, \nu_\mathrm{B}(\mathrm{T,S}), \delta\nu_\mathrm{B}(\mathrm{T,S}), \delta\nu_\mathrm{L})\; \mathrm{d}\Delta\nu. \tag{2.25}$$

$\delta\nu_\mathrm{L} = 63$ MHz accounts, according to Eq. 2.20, for the spectral width of the probe laser pulses. $\nu_\mathrm{B}(\mathrm{T,S})$ and $\delta\nu_\mathrm{B}(\mathrm{T,S})$ follow Eqs. 2.9, 2.12, 2.13 and 2.21

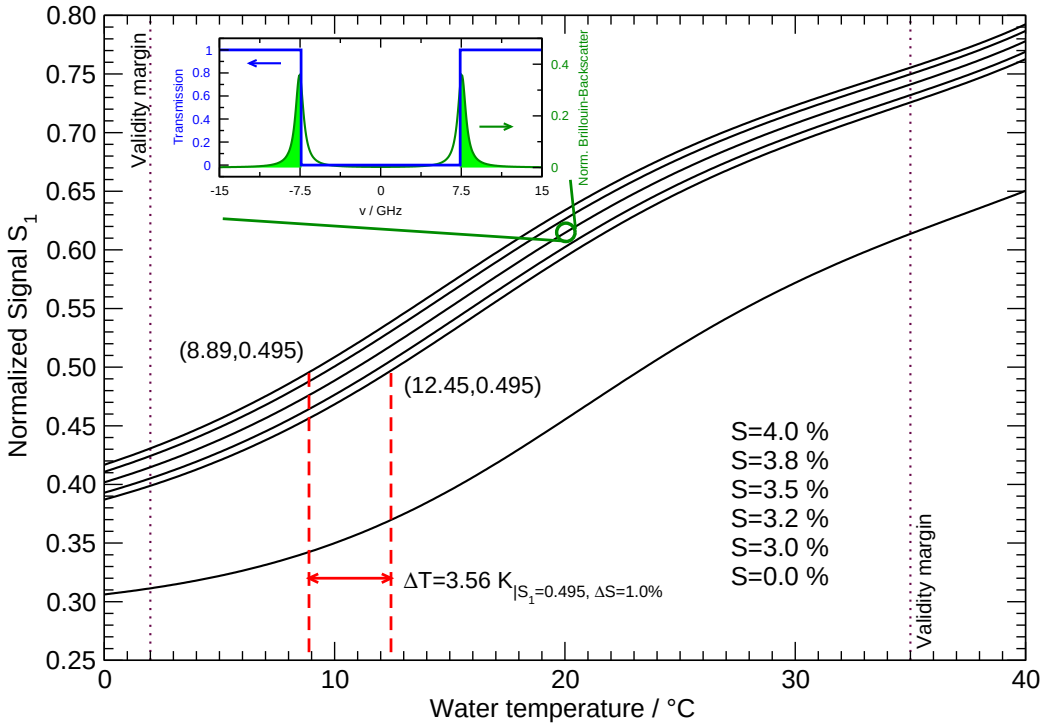

Fig. 2.7: Simulated characteristic curves of the Brillouin–lidar receiver, based on the ideal square well edge–filter: The inset shows the ideal square well transmission spectrum together with the Brillouin–doublet and its transmission through the edge–filter for $\theta = 180°$, $\lambda = 543$ nm, T$=$ 20°C and S$=$ 35‰. The filled area of the Brillouin–doublet corresponds to the intensity, which passes the edge–filter. When normalizing this intensity with respect to the integrated intensity of the Brillouin–doublet, the circled data point in the main graph results. A variation of the temperature T and the salinity S leads to the depicted normalized signals S_1. The dotted lines mark the validity margins inbetween the tailor expansion of the Brillouin–width (Eq. 2.23) is valid. A monotonous relationship between the normalized signal S_1 and the water temperature is apparent. The broken lines mark an example concerning the uncertainty of the temperature deduction, when the salinity of the water column is insufficiently known. As worldwide ocean waters exhibit salinities between 30 ‰ and 40 ‰, an uncertainty of ΔS $= 10$ ‰ results in an uncertainty of the temperature deduction of ΔT $= 3.56$ K within this example. However, local salinity uncertainties hardly extend ΔS $= 1$ ‰, which increases the accuracy of the temperature deduction to better than 0.5°C [72]. Nevertheless, this example again emphasizes the importance of the salinity knowledge.

respectively. The Brillouin–doublet as well as the integrand of Eq. 2.25 are included in the inset of Fig. 2.7 for T= 20°C and S= 35 ‰. In addition, Fig. 2.7 compiles the temperature dependency of the signal S_1(T,S) for different salinities. A monotonous relationship between the normalized signal S_1 and the water temperature is apparent.

The uncertainty in the deduction of the temperature from the normalized signal S_1 depends also on the knowledge of the salinity of the water column, as indicated in the plot by the broken lines. Oceanic waters exhibit salinities, which range from 30 ‰ to 40 ‰ [1, 90], such that the ignorance of the salinity parameter S results in a huge temperature error, which corresponds to the difference between the projections of the signal S_1 on the temperature scale for the two salinity extrema:

$$\Delta T = |T(S_1, S = 40‰) - T(S_1, S = 30‰)| . \tag{2.26}$$

$T(S_1, S)$ corresponds to the inversion of Eq. 2.25 with respect to the temperature T. Fortunately, as the discussion of Sec. 2.2.2 emphasized, such a huge uncertainty in the salinity parameter S is not to be expected. The studies of Fry *et al.* showed that uncertainties of the salinity parameter S of the order of $\Delta S = 1‰$ can be expected, when relying on localized historical data and considering seasonal variations. Hence, a measurement error of better than 0.5 K can be anticipated [72].

It is obvious, that the filter characteristics of a symmetric ideal square well transmission filter can not be realized experimentally. However, sufficiently steep transmission edges based on atomic or molecular absorption lines are available. Fry *et al.* implemented a receiver system based on Iodine or Bromine vapor cells, which accidentally offer suitable transmission edges due to a pair of their molecular absorption lines in the spectral region of interest, when employing a frequency doubled Nd:YAG laser ($\lambda = 532$ nm) as transmitter [17, 39, 40, 42]. However, any adjustment of the detection system to the needs of the application is impossible, due to the accidental correspondence of the molecular absorption lines.

As already stated above, the employment of an excited state Faraday anomalous dispersion optical filter offers the possibility to adjust the spectral transmission characteristics of the edge–filter to some extend, while offering symmetric transmission edges and an intrinsic daylight rejection. Their working principle, as well as a theoretical treatment of FADOFs in general will be the subject of the following chapter. The subsequent ones will focus on experimental implementations based on Rubidium vapor cells.

3

(Excited State) Faraday Anomalous Dispersion Optical Filters

A promissing approach in implementing an appropriate edge–filter receiver for the proposed Brillouin–lidar is the use of an *Excited State Faraday Anomalous Dispersion Optical Filter* (ESFADOF). Its working principle is equivalent to that of a ground state based *Faraday Anomalous Dispersion Optical Filter* (FADOF), while it operates between two excited states, as the nomenclature indicates. Thus, ESFADOFs require an external pump source, which populates the lower ESFADOF state. This extends the choice of atomic transition lines and a suitable working wavelength can be found much easier for a particular application. The spectral width of the filter transmission is bound to the atomic transition line of interest. Hence, they act as extremely narrow spectral bandpass filters, when compared to Lyot– or interference–filters [91, 92]. Depending on the experimental conditions, typical spectral widths of a few GHz can be expected, while they exhibit contrasts of the order of $1 : 10^5$, which only depend on the extinction ratios of the employed polarizers. Thus, FADOFs and ESFADOFs provide inherently a good suppression of daylight. In addition, both systems are capable of producing steep transition edges at the desired frequency separations, which can therefore be used as optical edge–filters. The filter characteristics can be tuned over a wide range, such that a measurement of the Brillouin–shift with an accuracy of some MHz is potentially feasible, as this work demonstrates.

Generally speaking, FADOFs and their excited state counterparts (ESFADOFs) consist of an atomic vapor cell placed between two crossed polarizers in a homogeneous, constant magnetic field **B**. The magnetic field is applied parallel to the optical axis of the vapor cell (cf. Fig. 3.1). Due to the magnetic field and the Zeeman–splitting of the atomic transition lines nearly resonant, left and right circular polarized light will exhibit a difference in index of refraction, which results in a rotation of the polarization of the incident light. The degree of rotation is strongly wavelength dependent, due to the anomalous dispersion in the vicinity of the atomic absorption lines. This rotation is probed by the second polarizer, which is rotated by 90° with respect to the first one, such that the transmitted intensity depends on the degree of rotation of the polarization vector. The fact, that the anomalous dispersion is bound to the vicinity of the atomic absorption lines, results in a spectrally narrow transmission filter. As ESFADOFs operate between two excited states of the atomic vapor, they require a sufficiently high population of the lower ESFADOF state. Conveniently, this lower state is optically pumped

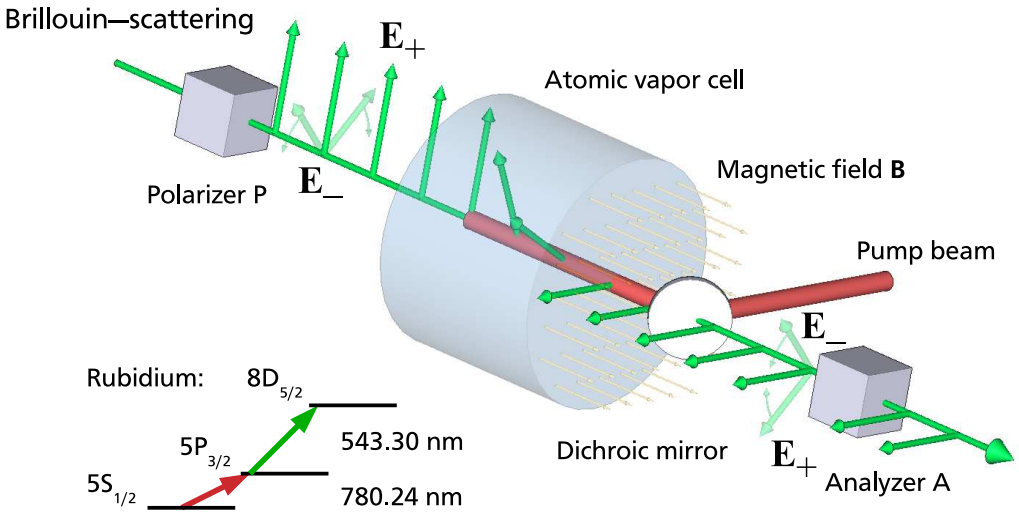

Fig. 3.1: Schematic drawing of an ESFADOF together with the relevant Rubidium transitions; with kind permission from Springer Science+Business Media [93]: P and A denote crossed polarizers, **B** an homogeneous magnetic field and the pump radiation is injected with the help of an dichroic mirror. The polarization vector experiences a rotation of its direction, when passed through the atomic vapor, due to the fact that its circular polarized components, $E_{\pm}$, are subject to different dispersions near the absorption lines of the atomic vapor, which itself is influenced by the magnetic field. The pump radiation populates the lower ESFADOF level, here the $5P_{3/2}$ level, such that the ESFADOF transition $5P_{3/2} \rightarrow 8D_{5/2}$ becomes accessible. In contrast, ground state FADOFs do not need this additional pump radiation. As long as transitions emerging from the ground state are accessible to the probing light, proper FADOF operation can be guaranteed.

by an additional laser source. The inset of Fig. 3.1 summarizes the relevant Rubidium transitions, upon which the experimental realization of the ESFADOF device relies. The implemented ESFADOF operates on the Rb $5P_{3/2} \rightarrow 8D_{5/2}$ transition (543.30 nm), while being optically pumped on the Rb D_2 transition $5S_{1/2} \rightarrow 5P_{3/2}$ (780.2405 nm). This choice has several advantages: (1) The ESFADOF transition wavelength is close to the absorption minimum of water [18]. (2) Radiation at this wavelength can be generated by second harmonic generation of the output of a compact Yb–doped fiber amplifier [54, 59]. (3) The lower ESFADOF-state $5P_{3/2}$ can be optically pumped on the $5S_{1/2} \rightarrow 5P_{3/2}$ transition by very efficient and robust semiconductor devices [94–100], making the employment of highly sophisticated solid state or dye lasers obsolete. The presentation of the experimental setup as well as a thorough discussion of the obtained results are the subject of the following chapters, where the current chapter focuses on the underlying physics of FADOFs and ESFADOFs.

3.1 Historical Overview

The following historical overview is intended to give a brief insight on the broad research field, concerning dispersive magnetic filters and their potential applications. It is not intended to be exhaustive and the author regrets having omitted any other important contribution.

The first observation of the enhancement of the Faraday–effect close to absorption lines was made by Macaluso and Corbino in 1898. They detected the magnetic rotation in the Sodium D-lines [101]. Later on, Wood discovered a similar effect in the band spectrum of Na_2 [102]. However, over 50 years later, Öhman implemented and explored a first experimental realization of a FADOF device in 1956 [103]. He modestly entitles his pioneering works

> "*A tentative monochromator for solar work based on the principle of selective magnetic rotation*" [103],

though it offers all the mentioned components which are essential for a FADOF: The atomic vapor cell placed in a homogeneous magnetic field and between two crossed polarizers. He demonstrated the working principle on the Sodium D-Lines in employing Sodium vapor and Sodium–flames inside the vapor cell. However, due to limitations concerning the optical quality of his setup, he was not able to operate his setup inside a telescope for solar observations, though he demonstrated the monochromatic band pass capabilities of this filter by imaging sunlight. It is obvious, that due to the lack of an appropriate narrow light source (Maiman invented the laser some years later in 1960 [104]), he was not able to record the spectral transmission characteristics of his device. Nevertheless, he was aware of the importance of this technique for astrophysics as a narrow bandpass filter. He stressed, the possibility of an enhanced investigation of the Hydrogen H_α line in employing his apparatus. In addition, he also emphasized the importance of the quality of the employed polarizers for the achievable contrast. However, successive works of Cacciani *et al.* implemented the proposals of Öhman in 1968 and succeeded in investigating the solar emission spectrum with spectral narrow bandpass filters based on the Faraday–effect and circular dichroism [105]. These instruments are known as *Magneto Optical Filter* (MOF) within the astrophysical community and have been predominantly used in investigating solar oscillations through the Doppler–shift of selected atomic emission lines (cf. e.g. Ref. [106] and references therein).

Roberts *et al.* investigated the Faraday effect and magnetic circular dichroism in atomic bismuth about 25 years later [107]. They implemented the first experimental setup, which allowed the measurement of the transmission spectrum of their implemented FADOF on a sub-GHz frequency scale. In addition, their publication presents a first theoretical description, which fits the presented data. Yeh published in 1981 a theoretical treatment of these dispersive magneto–optic filters, which is based on the fine–structure of the atomic Hamiltonian [108] and Chen *et al.* performed subsequent measurements on the Caesium D_2 transition line in 1987 [109]. The nomenclature *Faraday Anomalous Dispersion Optical Filter* with the acronym FADOF, which nowadays generally describes these kind

of optical filters, was introduced by Shay *et al.* in 1991 [110, 111]. Dick and Shay claim that they

> "*... demonstrated the operation of a new type of narrow–bandwidth optical filter, the Faraday anomalous dispersion optical filter (FADOF),* ..." [110],

though they have been aware [110, 111] of the work of Roberts *et al.* [107], Yeh [108] and hence of the work of Öhman [103]. However, Yin and Shay extended the theoretical treatment to the atomic hyperfine–structure and performed first measurements of a Rubidium based FADOF [111, 112]. Their theory reproduces the measured data with reasonable agreement. Chen *et al.* implemented a Sodium based FADOF in 1993 [113] and included it into a Sodium–lidar receiver in 1996 [114]. In addition, the author of the present work included some important modifications to the theoretical description of FADOFs in 2004 [16] and published a thorough comparison of the theoretical results with measured data in 2005 [20, 21]. Yin and Shay proposed, as a subsequent development to their previous work, the implementation of a *Stark Anomalous Dispersion Optical Filter* (SADOF), which includes the effects of an additional homogeneous electrical field to the FADOF operation in 1993 [115, 116]. The electrical field is applied perpendicular to the magnetic field, which is oriented parallel to the wavevector of the probing light. The electric field shifts, according to the Stark–effect, the position of the transition lines. Hence, this technique increases the tunability of the filter characteristics. Within their publication, Yin and Shay proposed the employment of a FADOF-device, which operates between two excited states and the lower FADOF state has to be pumped optically. This procedure extends the accessible transition lines considerably. In particular, they quote implementations, which employ transition lines of Potassium, Caesium and Rubidium. The central emission wavelength of selected lines of these elements are near to the frequency doubled emission of standard Nd–lasers, when embedding Nd in different host crystals [116]. However, the nomenclature *Excited State Faraday Anomalous Dispersion Optical Filter* (ESFADOF) for a FADOF filter, which operates between excited states, has been created by Billmers *et al.* in 1995 [117]. Although Yin and Shay published the working principle within their SADOF proposals, Billmers *et al.* received a patent on ESFADOFs in 1996 [118] on behalf of the US Navy. It should be emphasized, that Billmers *et al.* did not explicitly include electrical fields in their implementation. They succeeded in demonstrating the operation of such a device, though only pulsed pump radiation has been available [117, 119, 120]. Their experimental setup injects a pulsed pump laser of 84 kW/cm^2 in intensity within a pulse length of 10 ns into a Potassium based ESFADOF. The pulsed probe laser demonstrated ESFADOF filter characteristics of 4% in maximum transmission [117]. By increasing the pump intensity by a factor of 10 to 800 kW/cm^2, an increase by the same factor in ESFADOF transmission has been reported [119]. These values mark the highest so far reported pulsed ESFADOF transmissions. Ground state FADOFs can easily reach nearly 100% transmission [16, 20, 21, 111, 112].

However, the implementation of a continuously operating ESFADOF device, which exhibits comparably high transmissions, as it is advantageous for the proposed Brillouin–lidar, is more challenging, as similarly high pump intensities are required.

In addition to the above mentioned ones, several applications which employ MOFs, FADOFs or ESFADOFs have been proposed over the last decades. Generally speaking, they can be separated into two categories: (1) Most of them suggest the employment of these filters as narrow optical bandpass filters. The proposals or implementations cover Öhman's monochromator for solar work [103], optical bandpass filters for solar [105, 106] or lidar applications [114, 121, 122] and stress also the enhancement of optical free space or submerged communications by daylight rejection [108, 111, 116, 117]. (2) In addition to the employment as narrow bandpass filters, FADOFs and ESFADOF can be employed as high resolution edge–filters, which offers advantages in lidar–applications or as alternative measurement device, whenever high resolution interferometers can not be employed [16, 20]. However, to the best of the author's knowledge, only ground state FADOFs as narrow spectral bandpass filters have been implemented within lidar applications so far:

1. **Atmospheric temperature lidar:** Fricke and von Zahn implemented a lidar measurement scheme, which derives atmospheric temperatures by probing the hyperfine structure of the D_2 resonance line of the atmospheric Sodium layer in 1985 [123]. Since then the implementation of this instrument received several improvements. One of the most remarkable changes is the integration of FADOF based daylight rejection, which allowed the operation of the lidar during daytime by Chen *et al.* in 1996 [114]. Keeler received a patent on the technique in reducing optical noise by the employment of FADOFs in 1992 [124]. This instrument has been successfully extended to Potassium by Höffner *et al.* [121, 122, 125, 126]. The working principle is the following: (1) A strong tunable probe laser excites the D_1 transition of atmospheric Potassium between 80–105 km altitude. (2) The excited Potassium atoms emit characteristic fluorescence spectra, whose Doppler–broadening acts as a temperature tracer. (3) The Doppler–broadening is probed by tuning the probe laser around the K D_1 resonance line. The amount of backscattered light depends on the spectral overlap between the probe laser and the Doppler broadened atomic transition. (4) After collecting the backscattered response, it is passed through a Potassium FADOF, which blocks unwanted influences from other surrounding light sources. The employment of the FADOF bandpass increases the daylight suppression by 3 orders of magnitude and the signal to noise ratio by a factor of 2, compared to the first system design without the FADOF bandpass [125]. (5) A correlation of the extracted Doppler–width with the time of fight of the laser pulses delivers the temperature profile. The system is fully operational and delivers impressive atmospheric temperature profiles [122, 126].

2. Fire lidar: RL Associates Inc. sells a *Fire Lidar* application, whose purpose is to allow imaging through bright but spectrally broad light sources or scenes that are overexposed by these sources. The system aims to be particularly insensitive to light which is emitted by open fires or flames. Although it has been developed as a diagnostic tool for fire fighters, it gained in military importance [127]. The working principle is as follows: (1) A spectrally narrow but bright light source, preferably an eye safe laser system, illuminates the field of view of a camara, (2) whose imaging system is filtered by an appropriate spectral narrow FADOF system. (3) By matching the emission wavelength of the light source to the bandpass of the FADOF system, images of reasonable contrast result. The crossed polarizers of the FADOF device block the bright but spectrall broad light, which emerges from flames or other light sources.

Yin and Shay proposed and demonstrated such an imaging system already in 1994 [112]. However, Billmers *et al.* received a patent on this detection technique in 2004, again on behalf of the US Navy [128].

3.2 FADOF–Transmission

FADOFs and in some extent ESFADOFs have been discussed throughout the last century [16, 20, 21, 47, 93, 101, 103, 107–113, 115, 129]. The theoretical discussion, which follows, is based on Refs. [108, 111, 112] and has been partially published by the author [16, 20, 21, 47], whereas some important modifications with respect to the published work of Shay *et al.* [111, 112] have been included. In contrast to Refs. [111, 112], where only an average over the ground state levels is included, extensively more attention has to be paid to the Zeeman–splitting of the atomic transitions. In view of the fact, that the applied magnetic field **B** removes the degeneracy of the atomic levels or potentially causes new degeneracies, it is mandatory to individually add each contribution of the involved Zeeman splitted transitions to the polarizability of the atomic vapor. However, an introduction of the underlying fundamentals can be found in standard textbooks [130–133], though the theoretical description will be elaborated as detailed as it is required for the understanding of this work. Relevant constants of the Rb atom are summarized in Appendix A.

3.2.1 Homogeneous Magnetic Fields

By investigating the geometry of the setup (cf. Fig. 3.1), it is possible to deduce a relationship, which generally describes the overall transmission characteristics of FADOFs and ESFADOFs. For this purpose, it is advantageous to take the alignment of the wavevector of the incident light wave with respect to the constant and homogeneous magnetic field **B** into consideration. Hence, by defining a coordinate system, where $\mathbf{e}_z$, $\mathbf{e}_x$ and $\mathbf{e}_y$ denote perpendicular unit vectors, so that $\mathbf{e}_z$ is parallel to the wavevector of the incident light and to $\mathbf{B}_z$, it is possible to decompose the linearly polarized electric field $\mathbf{E}_{In}$, which is defined by the first polarizer P, into its circular components, by introducing the rotational basis

$$\begin{aligned} \mathbf{e}_+ &= \frac{1}{2}\left(\mathbf{e}_\mathrm{x} + i\,\mathbf{e}_\mathrm{y}\right) \\ \mathbf{e}_- &= \frac{1}{2}\left(\mathbf{e}_\mathrm{x} - i\,\mathbf{e}_\mathrm{y}\right) \\ \mathbf{e}_0 &= \mathbf{e}_\mathrm{z}. \end{aligned} \tag{3.1}$$

With this definition $\mathbf{E}_\mathrm{In} = \mathrm{E}\,\mathbf{e}_\mathrm{x}$ can be decomposed at the entry of the vapor cell into

$$\begin{aligned} \mathbf{E}_\mathrm{In}(\mathrm{z}=0) &= \mathbf{E}_+(0) + \mathbf{E}_-(0), \text{ with} \\ \mathbf{E}_+(0) &= \frac{\mathrm{E_{In}}}{2}\left(\mathbf{e}_\mathrm{x} + i\,\mathbf{e}_\mathrm{y}\right) \text{ and} \\ \mathbf{E}_-(0) &= \frac{\mathrm{E_{In}}}{2}\left(\mathbf{e}_\mathrm{x} - i\,\mathbf{e}_\mathrm{y}\right). \end{aligned} \tag{3.2}$$

$\mathbf{E}_\pm$ denote the electric field vectors of the right and left circular polarized light, respectively. The time dependence of the electric field vector can be neglected for the following discussion. In addition, it is assumed that the overall system is always in thermal equilibrium with its surroundings.

The homogeneous magnetic field $\mathbf{B} = \mathrm{B_z}\,\mathbf{e}_\mathrm{z}$, which is parallel to the wavevector of $\mathbf{E}_\mathrm{In}$, induces circular dichroism inside the vapor cell. Hence, the resulting anisotropy of the vapor is reflected by its complex index of refraction $\tilde{\mathbf{n}}$, which can be decomposed according to the circular basis of Eq. 3.1 into $\tilde{\mathbf{n}} = (\tilde{n}_+, \tilde{n}_-, \tilde{n}_0)$. The propagation of the electric field vector $\mathbf{E}$ through the vapor cell can be fully described by the knowledge of $\tilde{\mathbf{n}}$:

$$\mathbf{E}_\pm(\mathrm{z}) = \mathbf{E}_\pm(0)\,\mathrm{e}^{i\tilde{\mathrm{n}}_\pm(\omega)\frac{\omega}{\mathrm{c}}\mathrm{z}}\,. \tag{3.3}$$

c denotes the speed of light and ω the frequency of the light wave. Due to the circular dichroism, right and left circular polarized electric fields are absorbed differently and receive a phase difference, which results in the rotation of the polarization vector. Absorption and dispersion are frequency dependent and linked by the complex index of refraction. The real part of $\tilde{\mathrm{n}}_\pm$ describes the dispersion

$$\mathrm{n}_\pm(\omega) = Re\{\tilde{\mathrm{n}}_\pm(\omega)\} \tag{3.4}$$

and the imaginary part the absorption

$$\mathrm{k}_\pm(\omega) = \frac{2\omega}{\mathrm{c}}\,Im\{\tilde{\mathrm{n}}_\pm(\omega)\}\,. \tag{3.5}$$

Hence, the electric field amplitude $\mathrm{E_{Out}}$ after passing the vapor cell ($\mathrm{z} = \mathrm{L}$) and the second polarizer A, which is rotated by 90° with respect to the first one, results from the projection of $\mathbf{E}(\mathrm{L})$ on the basis of A:

$$\begin{aligned} \mathrm{E_{Out}} &= \mathbf{E}_+(\mathrm{L})\,\mathbf{e}_\mathrm{y} + \mathbf{E}_-(\mathrm{L})\,\mathbf{e}_\mathrm{y} \\ &= i\,\frac{\mathrm{E_{In}}}{2}\left(\mathrm{e}^{-\frac{1}{2}\mathrm{k}_+(\omega)\mathrm{L} + i\mathrm{n}_+(\omega)\frac{\omega}{c}\mathrm{L}} - \mathrm{e}^{-\frac{1}{2}\mathrm{k}_-(\omega)\mathrm{L} + i\mathrm{n}_-(\omega)\frac{\omega}{c}\mathrm{L}}\right). \end{aligned} \tag{3.6}$$

The rotation of the polarization vector with respect to the entry polarization $\mathbf{e}_\mathrm{x}$ is directly linked to the phase difference between both circular components of

the electric field vector **E** and the resulting frequency dependent Faraday rotation angle is given by

$$\phi(\omega) = \frac{\omega \mathrm{L}}{2\mathrm{c}} \left[\mathrm{n}_+(\omega) - \mathrm{n}_-(\omega)\right]. \tag{3.7}$$

Based on relations 3.6 and 3.7, it is possible to deduce the frequency dependent transmission of the FADOF device to

$$\begin{aligned} \mathrm{T}(\omega) &= \left|\frac{\mathrm{E}_{\mathrm{Out}}}{\mathrm{E}_{\mathrm{In}}}\right|^2 \\ &= \frac{1}{4}\Big\{\mathrm{e}^{-\mathrm{k}_+(\omega)\mathrm{L}} + \mathrm{e}^{-\mathrm{k}_-(\omega)\mathrm{L}} \\ &\quad -2\cos[2\phi(\omega)]\,\mathrm{e}^{-\frac{1}{2}(\mathrm{k}_+(\omega)+\mathrm{k}_-(\omega))\,\mathrm{L}}\Big\}. \end{aligned} \tag{3.8}$$

In conclusion, the full knowledge of the frequency dependent complex index of refraction $\tilde{\mathbf{n}}$ determines the FADOF transmission spectrum. Eq. 3.8 can be decomposed into the bare atomic absorption

$$\mathrm{a}(\omega) = \frac{1}{2}\Big\{\mathrm{e}^{-\mathrm{k}_+(\omega)\mathrm{L}} + \mathrm{e}^{-\mathrm{k}_-(\omega)\mathrm{L}}\Big\} \tag{3.9}$$

and the cosine–term, which describes, according to Malus–law [92], the projection of the electric field vector on the basis of the second polarizer A. It is obvious, that a removal of A transforms Eq. 3.8 into Eq. 3.9. However, the anisotropy of the index of refraction is based on the applied magnetic field. Thus, a fully isotropic vapor cell, which is either a consequence of a vanishing magnetic field or equal circular indices of refraction $\mathrm{n}_\pm$ far from atomic absorption lines, results in the disappearance of the Faraday rotation angle ϕ (cf. Eq. 3.7). As a result, the second polarizer A blocks the light wave, which explains the excellent daylight rejection of FADOF devices.

3.2.2 Inhomogeneities Along the Propagation

Constant but inhomogeneous complex refractive indices can be easily integrated in the above formalism. Such inhomogeneities result as a consequence of an inhomogeneous magnetic field, which affects the atomic transitions along the beam path. In addition, ESFADOFs are susceptible to develop strong inhomogenieties along the beam path, due to the necessity of optically pumping the lower ESFADOF state. The exponential decrease of the pump intensity along the pump beam trajectory (cf. Fig. 3.1) considerably affects the population of the lower ESFADOF state and hence the refractive indices. Sec. 3.3 discusses the connection between both entities and Sec. 3.6 extends the theoretical description to ESFADOFs.

Let $\tilde{\mathbf{n}}(\omega, \mathrm{z})$ denote the complex refractive indices along $\mathbf{e}_z$. Then, according to Eq. 3.3, any infinitesimal propagation of the electric field vector can be described as

$$\mathbf{E}_{\pm}(\mathrm{z}+\mathrm{dz}) = \mathbf{E}_{\pm}(\mathrm{z})\,\mathrm{e}^{i\tilde{\mathrm{n}}_{\pm}(\omega,\mathrm{z})\frac{\omega}{\mathrm{c}}\mathrm{dz}}. \tag{3.10}$$

A further propagation of the electric field vector through the vapor cell yields

$$\mathbf{E}_{\pm}(\mathrm{z}) = \mathbf{E}_{\pm}(0)\,\exp\left[i\frac{\omega}{\mathrm{c}}\int_0^{\mathrm{z}}\tilde{\mathrm{n}}_{\pm}(\omega,\mathrm{z}')\,\mathrm{dz}'\right], \tag{3.11}$$

which can be transferred again to the functional form of Eq. 3.3 by introducing effective complex refractive indices:

$$\tilde{\mathrm{n}}_{\pm}^{\mathrm{Eff}}(\omega) = \frac{1}{\mathrm{L}}\int_0^{\mathrm{L}}\tilde{\mathrm{n}}_{\pm}^{\mathrm{Eff}}(\omega,\mathrm{z}')\,\mathrm{dz}'. \tag{3.12}$$

This yields

$$\mathbf{E}_{\pm}(\mathrm{L}) = \mathbf{E}_{\pm}(0)\,\mathrm{e}^{i\tilde{\mathrm{n}}_{\pm}^{\mathrm{Eff}}(\omega)\frac{\omega}{\mathrm{c}}\mathrm{L}} \tag{3.13}$$

which is advantageous for a numeric implementation, as the complex refractive indices in Eqs. 3.4–3.9 can be replaced by the effective representation of Eq. 3.12.

3.3 Complex Refractive Indices

3.3.1 Atomic Polarizability

The knowledge of the complex refractive indices $\tilde{\mathbf{n}}$ enables the deduction of the FADOF transmission spectrum and as Eqs. 3.4–3.9 suggest, it is advantageous to introduce the circular basis of Eq. 3.1. The susceptibility tensor χ becomes diagonal within this basis and allows to relate the refractive indices to the atomic polarizability α via

$$\begin{aligned}&\alpha_{\mathrm{r}} = \varepsilon_0\,(\varepsilon_{\mathrm{r}}-1) = \varepsilon_0\,\chi_{\mathrm{r}} \quad \text{and}\\ &\mathrm{n}_{\mathrm{r}} = \sqrt{\varepsilon_{\mathrm{r}}\,\mu_{\mathrm{r}}}.\end{aligned} \tag{3.14}$$

As the permeability of the atomic vapor does not exceed $\mu_{\mathrm{r}} \approx 1$, only a dependency on the permittivity ε_{r} remains and it follows that

$$\mathrm{n}_{\mathrm{r}} = \sqrt{1+\chi_{\mathrm{r}}} \approx 1+\frac{1}{2}\chi_{\mathrm{r}}, \text{ where } r \in \{+,-,0\} \tag{3.15}$$

and $\chi_{\mathrm{r}} \ll 1$ has been used.

For the following discussion it is advantageous to employ the cgs–system, such that $\varepsilon_0 = 1/4\pi$. As the atomic polarizability α_{r} is governed by the atomic transitions, it is strongly wavelength dependent. Let ω denote the frequency of the incident lightwave and $\omega_{\gamma\gamma'}$ the central frequency of the atomic transition $\gamma \to \gamma'$, then

$$\alpha_{\mathrm{r}}^{\gamma}(\omega) = \frac{2}{3\hbar}\sum_{\gamma'}\frac{\mathrm{S}_{\mathrm{r}}^{\gamma\gamma'}}{\omega_{\gamma\gamma'}-\omega-i\frac{\mathrm{A}_{\mathrm{JJ'}}}{2}} \tag{3.16}$$

describes the atomic polarizability of one single atom in the vicinity of its atomic transitions ($|\omega_{\gamma,\gamma'} - \omega| \ll \omega_{\gamma,\gamma'}$). The sum over γ' includes all allowed transitions, which emerge from the lower level γ. $h = \hbar 2\pi$ denotes the Planck constant, $A_{JJ'}$ the Einstein coefficients and $S_r^{\gamma\gamma'}$ their line strengths. Eq. 3.16 is the complex representation of the Lorentz absorption profile, while the real part describes the dispersion and the imaginary part the absorption. They are linked through the Kramers–Kronig relation [133].

The probability $P(\gamma,\gamma')$ of exciting the transition $\gamma \rightarrow \gamma'$, when irradiating the atom with light of the frequency $\omega = \omega_{\gamma\gamma'}$, is linked via the oscillator strength $f(\gamma,\gamma')$ to the line strength $S_r^{\gamma\gamma'}$, as

$$P(\gamma,\gamma') = \frac{2\omega^2 e^2}{m_e c^3} \left| f(\gamma,\gamma') \right| \text{ and} \tag{3.17}$$

$$f(\gamma,\gamma') = \frac{2m_e}{3\hbar e^2} \frac{\omega_{\gamma,\gamma'}}{g_\gamma} S_{\gamma,\gamma'}. \tag{3.18}$$

e denotes the elementary charge, m_e the electron mass and g_γ the degeneracy of the lower level. Eq. 3.17 holds as long as the underlying dipole approximation is valid, i.e. as long as the wavelength of the exciting light wave exceeds the atomic dimensions. This assumpton is well satisfied, as optical frequencies exceed atomic dimensions by several orders of magnitude; e.g. the wavelengths of the atomic transitions of interest (780 nm and 543 nm; cf. Fig. 3.1) satisfy this assumption well, as the Rubidium atom does not exceed 5 Å in diameter.

By taking the degeneracies of the atomic transitions into account $S_r^{\gamma\gamma'}$ becomes

$$S_r^{\gamma\gamma'} = \sum_{MM'} \left| \langle \gamma M | \hat{d}_r | \gamma' M' \rangle \right|^2, \tag{3.19}$$

where M and M' index the degeneracies and $\hat{d}_r$ denotes the dipole operator, which links the atomic wavefunctions $|\gamma M\rangle$ and $|\gamma' M'\rangle$. Thus, $\langle \gamma M | \hat{d}_r | \gamma' M' \rangle$ is the transition matrix and the sum together with the factor of $1/g_\gamma$ in Eq. 3.18 results in an average over all γ sublevels. However, as the applied magnetic field lifts the degeneracies of the atomic levels, all sublevels have to be taken into account individually and the line strength $S_r^{\gamma\gamma'}$ becomes

$$S_r^{\gamma\gamma'} = \left| \langle \gamma | \hat{d}_r | \gamma' \rangle \right|^2 \tag{3.20}$$

and $g_\gamma = 1$. Hence, the total atomic polarizability $\alpha_r^{tot}(\omega)$ is achieved by summing over all ground state levels

$$\alpha_r^{tot}(\omega) = \sum_\gamma N(\gamma) \alpha_r^\gamma(\omega). \tag{3.21}$$

The number densities $N(\gamma)$ account for the population of the level γ and the sum over γ' in Eq. 3.16 refer to all upper state levels.

In addition to the above, the atomic motion due to the elevated temperature has to be taken into account. The resulting Doppler–shift of the atomic lines transfers $\omega_{\gamma,\gamma'}$ into $\omega_{\gamma,\gamma'}(1+\mathrm{v/c})$ and with the Maxwell–velocity distribution

$$\mathrm{f_v(v)dv} = \mathrm{N}(\gamma)\left(\frac{\mathrm{M}}{2\pi\,\mathrm{k_B T_{Cell}}}\right)^{1/2} \mathrm{e}^{-\frac{\mathrm{Mv}^2}{2\mathrm{k_B T_{Cell}}}}\,\mathrm{dv} \tag{3.22}$$

one obtains, after integrating over the entire velocity space the following total atomic polarizability:

$$\alpha_{\mathrm{r}}^{\mathrm{tot}}(\omega) = \frac{2}{3\hbar}\sum_{\gamma\gamma'}\mathrm{N}(\gamma)\mathrm{S_r^{\gamma\gamma'}}\int\frac{\mathrm{f_v(v)dv}}{\omega_{\gamma\gamma'}(1+\frac{\mathrm{v}}{\mathrm{c}})-\omega-i\frac{\mathrm{A_{JJ'}}}{2}}. \tag{3.23}$$

Eq. 3.23 is the complex representation of the Voigt–profile, which results when convoluting the natural Lorentz–profile of the atomic transition with the Gauss–profile of the Maxwell–velocity distribution. M is the atomic mass, $\mathrm{T_{Cell}}$ the temperature of the vapor cell and $\mathrm{k_B}$ the Boltzmann–constant. In conclusion, the spectral profile of the FADOF device is dominated by the Voigt–profile, due to the fact that important vapor densities require elevated cell temperatures.

In order to facilitate the discussion it is useful to introduce the Doppler–width as

$$\begin{aligned}\Delta\omega_{\mathrm{D}} &= \frac{\omega_{\gamma,\gamma'}}{\mathrm{c}}\sqrt{8\ln 2\ \mathrm{k_B T_{Cell}/M}}\ \text{ or}\\ \Delta\nu_{\mathrm{D}} &= \frac{\nu_{\gamma,\gamma'}}{\mathrm{c}}\sqrt{8\ln 2\ \mathrm{k_B T_{Cell}/M}},\end{aligned} \tag{3.24}$$

which allows to transfer Eq. 3.23 with the help of the transformation of the variables $\mathrm{t} = \sqrt{\frac{\mathrm{Mv}^2}{2\mathrm{k_B T_{Cell}}}}$ into

$$\alpha_{\mathrm{r}}^{\mathrm{tot}}(\omega) = \sum_{\gamma,\gamma'}\frac{1}{2\pi}\mathrm{C\,S_r^{\gamma,\gamma'}\,W}(\xi_{\gamma,\gamma'}). \tag{3.25}$$

$\mathrm{W}(\xi_{\gamma,\gamma'})$ describes the spectral lineshape of the Voigt–profile [74, 89], which follows

$$\mathrm{W}(\xi_{\gamma,\gamma'}) = \frac{1}{\sqrt{\pi}}\int_{-\infty}^{\infty}\frac{\mathrm{e}^{-\mathrm{t}^2}}{\mathrm{t}-\xi_{\gamma,\gamma'}}\,\mathrm{dt},\ \text{where} \tag{3.26}$$

$$\xi_{\gamma,\gamma'}(\omega) = \frac{\sqrt{\ln 2}}{\pi\Delta\nu_{\mathrm{D}}}(\omega-\omega_{\gamma,\gamma'}+i\frac{\mathrm{A_{JJ'}}}{2}). \tag{3.27}$$

The population of the lower level $\mathrm{N}(\gamma)$ together with some constants is included in

$$\mathrm{C} = \frac{2}{3}\frac{4\pi\sqrt{\ln 2}}{h\Delta\nu_{\mathrm{D}}}\mathrm{N}(\gamma). \tag{3.28}$$

FADOFs operate between the ground state γ and the excited state γ', thus $\mathrm{N}(\gamma)$ follows the Boltzmann–distribution

$$N(\gamma) = \frac{n(T_{Cell})\, e^{-E_\gamma / k_B T_{Cell}}}{\sum_{\tilde{\gamma}} e^{-E_{\tilde{\gamma}} / k_B T_{Cell}}}. \tag{3.29}$$

E_γ denotes the energy of the level γ and $n(T_{Cell})$ the temperature dependent number density of the atomic vapor. $n(T_{Cell})$ is a function of the vapor pressure for a uniformly heated Rb vapor cell (cf. Appendix A).

When dealing with ESFADOFs, the optical pumping process has to be considered. The population of the lower ESFADFOF state deviates from the Boltzmann–distribution and a careful treatment of the optical pumping, which populates the lower ESFADOF state γ, is required. Sec. 3.6 addresses this issue in more detail. However, the above developed deduction of the transmission characteristics remains valid, regardless of the exact process, which defines the population of the state γ.

This work investigates Rubidium based ESFADOFs. Therefore the natural abundance of the Rubidium isotopes ^{85}Rb and ^{87}Rb has to be included in order to correctly compute the transmission characteristics. Each isotope contributes a factor $\Delta\tilde{n}_\pm(\omega)$ according to its natural abundance to the total index of refraction:

$$\tilde{n}_\pm(\omega) = 1 + a_{85}\, \Delta\tilde{n}_\pm(\omega)\big|_{^{85}\mathrm{Rb}} + a_{87}\, \Delta\tilde{n}_\pm(\omega)\big|_{^{87}\mathrm{Rb}}, \tag{3.30}$$

where $a_{85} = 0.72$ and $a_{87} = 0.28$ denote the natural abundances of the Rubidium isotopes [78]. By combining Eq. 3.14 and 3.25, the $\Delta\tilde{n}_\pm(\omega)$ are calculated individually through

$$\Delta\tilde{n}_\pm(\omega) = \sum_{\gamma,\gamma'} C\, S_r^{\gamma,\gamma'}\, W(\xi_{\gamma,\gamma'}). \tag{3.31}$$

3.3.2 Atomic Eigenstates and Line strengths

The last section showed how the complex refractive indices separate into different terms. There are: (1) The number density $N(\gamma)$ of the lower FADOF state γ, which follows the Boltzmann–distribution for ground state FADOFs (cf. Eq. 3.29), (2) the lineshape $W(\xi_{\gamma,\gamma'})$ of the atomic transition $\gamma \to \gamma'$, which is dominated by the Voigt–profile (cf. Eq. 3.26) and (3) the corresponding line strengths $S_r^{\gamma,\gamma'}$, which are according to Eq. 3.20 the square of the absolute value of the entries of the dipole transition matrix:

$$S_r^{\gamma\gamma'} = \left| \langle \gamma | \hat{d}_r | \gamma' \rangle \right|^2.$$

Hence, the dependence on the magnetic field is included in the line strengths $S_r^{\gamma\gamma'}$ of the atomic transitions, as the eigenstates $|\gamma\rangle$ and the eigenvalues E_γ of the atomic Hamiltonian depend on the applied magnetic field. The underlying effect is the Zeeman–splitting of the transition lines, which causes a shift in the transition frequencies and strongly influences the line strengths. Hence, the complete Hamiltonian has to be solved. For this purpose it is useful to start with the

undisturbed atom in the coupled scheme. Its eigenstates can be described by the standard complete orthonormal basis $|\beta\rangle = |\mathrm{nLSJIFM}\rangle$ with a total orbital angular momentum **J**, nuclear spin **I**, total angular momentum $\mathbf{F} = \mathbf{J} + \mathbf{I}$, and its projection M along the direction of the external magnetic field. The eigenvalues and eigenstates of the Hamiltonian matrix can be extracted through its diagonalization after including all relevant perturbations. In other words, it is advantageous to start with the Hamiltonian of the atomic fine structure and then to include the hyperfine structure and the influence of the magnetic field as subsequent perturbations. The matrix elements of the Hamiltonian for each hyperfine component are given within the framework of this *Slater-Condon Ansatz* [132, 134, 135] by

$$\langle \mathrm{nLSJIFM}|\, H\, |\mathrm{nLSJIF'M'}\rangle = \mathrm{E_F} \;+\; \Delta \mathrm{E_{HF}}\, \delta_{\mathrm{F,F'}} \delta_{\mathrm{M,M'}} \;+\; \Delta \mathrm{E_z}, \qquad (3.32)$$

where $\mathrm{E_F}$ accounts for the fine structure, $\Delta \mathrm{E_{HF}}$ for the hyperfine structure and $\mathrm{E_z}$ for the Zeeman–splitting, respectively. The hyperfine contribution yields

$$\Delta \mathrm{E_{HF}} = \frac{\mathrm{h}}{2} \mathrm{AK} \;+\; \mathrm{hB} \left[\frac{\frac{3}{2}\mathrm{K(K+1)} - 2\mathrm{I(I+1)\,J\,(J+1)}}{2\mathrm{I(2I-1)\,2J\,(2J-1)}} \right], \qquad (3.33)$$

where $\mathrm{K} = \mathrm{F(F+1)} - \mathrm{J(J+1)} - \mathrm{I(I+1)}$; A and B are the magnetic dipole and electric quadrupole constants, respectively. The Zeeman–splitting is given by

$$\begin{aligned} \Delta \mathrm{E_z} = {} & \mu_0 \mathrm{B_z}\, (-1)^{\mathrm{M+J+I+1}} (\mathrm{g_J} - \mathrm{g_I}) \times \\ & \sqrt{\mathrm{J(J+1)(2J+1)(2F+1)(2F'+1)}} \times \\ & \left\{ \begin{array}{ccc} \mathrm{J} & 1 & \mathrm{J} \\ \mathrm{F'} & \mathrm{I} & \mathrm{F} \end{array} \right\} \left(\begin{array}{ccc} \mathrm{F} & 1 & \mathrm{F'} \\ -\mathrm{M} & 0 & \mathrm{M'} \end{array} \right) + \mu_0 \mathrm{B_z}\, \mathrm{g_I M}\, \delta_{\mathrm{F,F'}} \delta_{\mathrm{M,M'}} \end{aligned} \qquad (3.34)$$

and $\mathrm{B_z}$ denotes the magnetic field strength along the $\mathbf{e}_\mathrm{z}$–direction, μ_0 the Bohr magneton, $\mathrm{g_J}$ and $\mathrm{g_I}$ the gyromagnetic factors for the total angular momentum and the nuclear spin momentum, respectively. All spherical integrations are contained in the 3j- and 6j-symbols. The last term of Eq. 3.34 represents the coupling of the magnetic field to the nuclear spin. However, in view of the fact, that the nuclear magneton $\mu_0\, \mathrm{g_I}$ is a factor of $\mathrm{m_e}/\mathrm{m_p} \approx 1/2000$ less than the Bohr magneton ($\mathrm{m_p}$ is the proton mass), this term can be neglected.

In presence of the magnetic field the matrix representation of the Hamiltonian (cf. Eqs. 3.32–3.34) is no longer diagonal. A diagonalization of this matrix delivers the eigen–values E_γ and the eigen–vectors $\mathbf{Y}^\gamma$, which allow the expansion of the eigenstates of the fully perturbed Hamiltonian $|\gamma\rangle$ into the standard basis $|\beta\rangle = |\mathrm{nLSJIFM}\rangle$:

$$|\gamma\rangle = \sum_\beta |\beta\rangle \langle \beta\, |\, \gamma\rangle = \sum_\beta \mathrm{Y}_\beta^\gamma\, |\beta\rangle\,. \qquad (3.35)$$

Finally, the desired line strengths are obtained from the overlap of the atomic dipole operator $\widehat{\mathbf{d}}$ with the eigen–states of the atomic transition

$$\mathrm{S_r^{\gamma,\gamma'}} = \left| \langle \gamma |\, \widehat{\mathrm{d}}_\mathrm{r}\, | \gamma' \rangle \right|^2 = \left| \sum_{\beta,\beta'} \mathrm{Y}_\beta^\gamma\, \langle \beta |\, \widehat{\mathrm{d}}_\mathrm{r}\, | \beta' \rangle\, \mathrm{Y}_{\beta'}^{\gamma'} \right|^2 . \qquad (3.36)$$

This equation is of particular importance, as it allows to introduce the expansion of the dipole operator within the standard basis $|\beta\rangle$ into its spherical components and by applying the Wigner-Eckart Theorem [130–132] the following results follow:

$$\langle\beta|\,\widehat{\mathrm{d}}_{\mathrm{r}}\,|\beta'\rangle = (-1)^{\mathrm{F-M}} \begin{pmatrix} \mathrm{F} & 1 & \mathrm{F}' \\ -\mathrm{M} & \mathrm{r} & \mathrm{M}' \end{pmatrix} \langle\beta \parallel \widehat{\mathrm{d}} \parallel \beta'\rangle\,, \tag{3.37}$$

$$\langle\beta \parallel \widehat{\mathrm{d}} \parallel \beta'\rangle = (-1)^{\mathrm{J+I+F+1}} \sqrt{(2\mathrm{F}+1)(2\mathrm{F}'+1)} \times \begin{Bmatrix} \mathrm{J} & \mathrm{I} & \mathrm{F} \\ \mathrm{F}' & 1 & \mathrm{J}' \end{Bmatrix} \langle \mathrm{J} \parallel \widehat{\mathrm{d}} \parallel \mathrm{J}'\rangle \text{ and} \tag{3.38}$$

$$\langle \mathrm{J} \parallel \widehat{\mathrm{d}} \parallel \mathrm{J}'\rangle^2 = \frac{3\mathrm{h}\lambda^3}{64\pi^4}(2\mathrm{J}'+1)\mathrm{A}_{\mathrm{JJ'}}, \tag{3.39}$$

where $\mathrm{r} \in \{+1,-1,0\}$. The last term is called the reduced matrix element, as it belongs to all hyperfine components of the $\mathrm{J} \rightarrow \mathrm{J}'$ transition, and λ denotes its wavelength.

Finally, it has to be emphasized, that the employed semi-empirical *Slater-Condon Ansatz* in diagonalizing the Hamiltonian of Eq. 3.32 requires, that the matrix representation in the chosen basis $|\beta\rangle$ adequately describes the underlying physics.

This is not generally fulfilled when regarding arbitrary atoms. Therefore, additional corrections, e.g. as the mixing of configurations for multi-electron atoms, have to be included [132]. However, Rubidium with its single valence electron and the completely filled inner electronic shells can be approximated well within the described theoretical approach [130] and the deduced estimations of the line strength reach an accuracy of about 10% [132].

3.4 Transmission Characteristics of a Simplified FADOF

The presented theoretical description allows to compute the transmission characteristics of FADOF devices in general. Some fundamental insight on the principal behavior of FADOF systems can be obtained in investigating the case of an atomic system without a hyperfine structure, i.e. when $\mathbf{I} = 0$. This case reduces the computational effort and the contribution of Eq. 3.33 vanishes.

Figs. 3.2 and 3.3 have been computed by employing the above developed theoretical approach to a ground state FADOF, which operates between the $\mathrm{S}_{1/2} \rightarrow \mathrm{P}_{3/2}$ atomic fine structure. The inserted atomic parameters correspond to Rb, though $\mathbf{I} = 0$ has been set for simplicity. All other parameters are annotated. Fig. 3.2 compiles the absorption coefficients $\mathrm{k}_{\pm}$, the index of refraction $\mathrm{n}_{\pm}$ and the Faraday rotation angle ϕ. The circular absorption components completely separate for the chosen magnetic field strength. Together with the high number density of the Rb vapor (cf. Appendix A), which leads to a considerable absorption and dispersion throughout the vapor cell, high Faraday rotation angles result. Within the cell length L a rotation of up to 6π occurs. By inserting these results

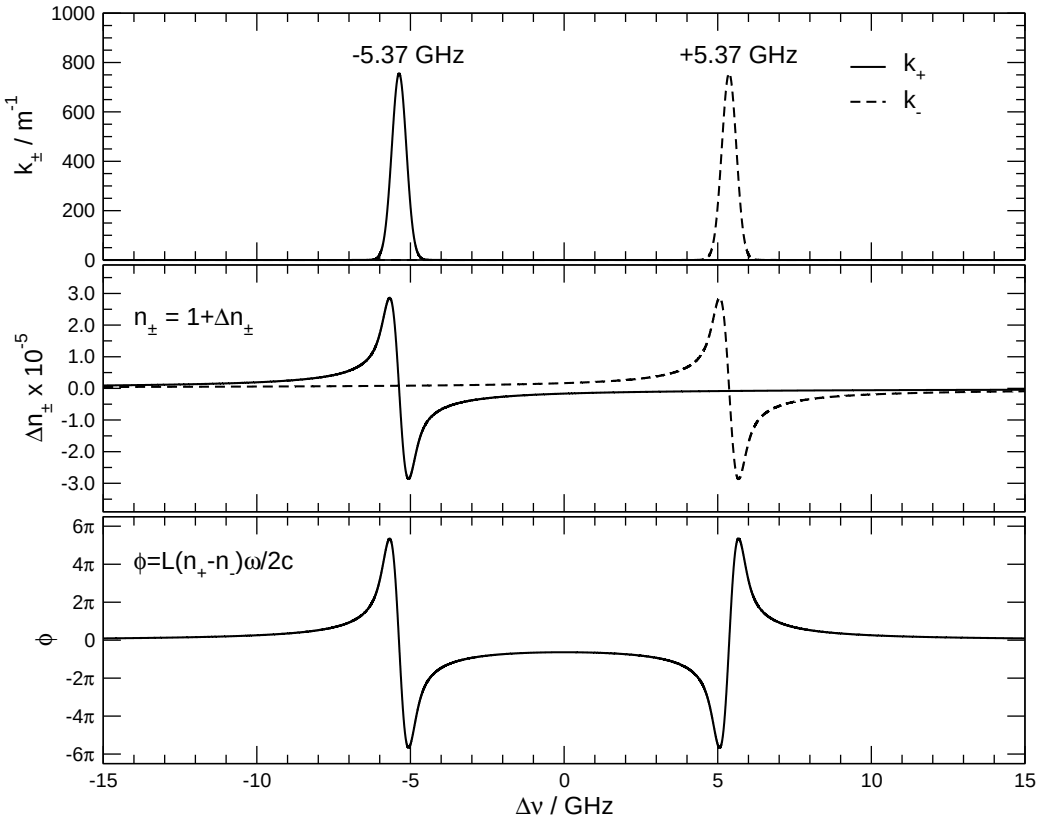

Fig. 3.2: Simulated frequency dependence of $k_{\pm}$, $n_{\pm}$ and ϕ for a simplified ($\mathbf{I} = 0$) FADOF, which operates on the $S_{1/2} \rightarrow P_{1/2}$ transition: A magnetic field strength of $B_z = 230$ mT, a cell temperature of $T_{Cell} = 70°C$ and a cell length of $L = 15$ mm have been chosen. All other parameters correspond to the Rb atom. The separation of the circular absorption components due to the presence of the magnetic field is apparent. This affects also the dispersion, which corresponds to the real part of the complex index of refraction, and the resulting Faraday rotation angle reaches values of up to 6π. The quoted parameter values have been chosen, in order to shift the central frequency of the circular absorption components to the annotated value, which is advantageous for the FADOF transmission spectrum of Fig. 3.3.

into Eq. 3.8, the FADOF transmission spectrum can be computed. This is depicted in the upper part of Fig. 3.3. The inserted parameters have been chosen in order to deliver symmetric and steep transmission edges in the region of interest of the Brillouin–lidar and these filter characteristics compare well to the discussed ones of the ideal edge–filter (cf. Sec. 2.3). The filled curve of the upper graph corresponds to the transmitted intensity signal of the Brillouin–backscatter through the depicted FADOF transmission characteristics. By performing the same evaluation as described in Sec. 2.3, the lower part of Fig. 3.3 has been obtained. The circled data point corresponds to the integrated normalized intensity of the transmitted Brillouin–backscatter, which corresponds to the filled area in the upper graph and to a water temperature of 20 °C and a salinity of S = 35‰. Thus, the area of the

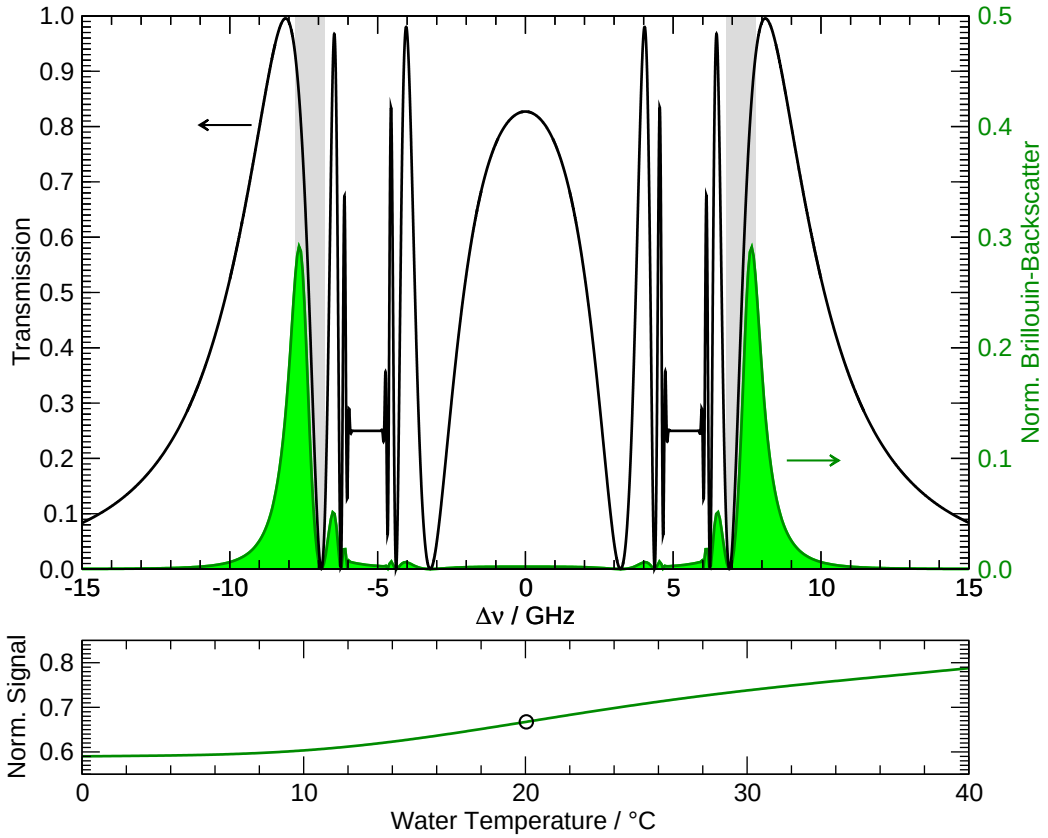

Fig. 3.3: Simulated transmission characteristics of a simplified ($\mathbf{I} = 0$) FADOF edge–filter, which operates on the $S_{1/2} \rightarrow P_{1/2}$ transition: The upper part shows the FADOF transmission, which results when inserting the simulated complex refractive indices, which are compiled in Fig. 3.2, into Eq. 3.8, together with the transmitted intensity of the Brillouin–backscatter. The latter has been computed according to the discussion of Sec. 2.3 for a water temperature of $T = 20°C$ and a salinity of $S = 35‰$. It has been normalized to the total intensity of the Brillouin–backscatter, so that its area corresponds to the normalized transmission signal of the FADOF edge-filter. A variation of the water temperature leads to the characteristic curve of the Brillouin–lidar, which is the lower part of the figure. The circled data point corresponds to the spectral integral of the transmitted and normalized Brillouin–backscatter of the upper part. In conclusion, FADOFs potentially deliver the desired steep transmission edges within the region of interest (grayed areas in the upper graph). They can be employed as edge-filter receiver.

filled curve in the upper graph corresponds to the normalized transmission signal of the FADOF edge-filter. The normalization has been performed with respect to the total integrated intensity of the Brillouin–doublet.

By performing this procedure for different water temperatures, it follows that the presented FADOF filter characteristics are suited as edge–filter receiver for the Brillouin–lidar. The lower part of Fig. 3.3 reveals a clear dependency of the normalized signal on the water temperature. In conclusion, FADOFs potentially

deliver the desired steep and symmetric edge–filter characteristics within the region of interest and are therefore a very promissing development towards an operational Brillouin–lidar. The next section touches on the extension towards real systems.

3.5 Rubidium Ground State FADOF

First investigations of the author within the Brillouin–lidar project concentrated on ground state FADOFs. These works theoretically and experimentally investigated a Rubidium based FADOF system, which operates on the $5S_{1/2} \rightarrow 5P_{3/2}$ ground state transition. The obtained results have been published [16, 20, 21] prior to this work and are not the purpose of this thesis. However, they experimentally and theoretically prove that FADOFs are able to deliver steep and symmetrical transmission edges. An excellent agreement between the experimental data and the theoretical description has been demonstrated. Fig. 3.4 shows a comparison of the experimental data with the presented theory. The figure is intended to prove the mentioned excellent agreement between the experiment and the theoretical approach without any further discussion of the experimental details. They can be found in the cited works.

Furthermore, Fig. 3.4 shows that real FADOF systems are capable of delivering steep and symmetric transmission edges.

According to the discussion of the last section, the steep and symmetric transmission edges of FADOF or ESFADOF devices can be employed as high resolution edge-filters. In addition, these edges are tunable within a few GHz around the central frequency of the employed transition by adjusting the magnetic field strength and/or the number density of the atomic vapor. The former influences $S_r^{\gamma,\gamma'}$ and the latter $N(\gamma)$.

3.6 Extension to Excited State FADOFs: ESFADOFs

The presented theoretical framework can be applied to excited state Faraday anomalous dispersion optical filters as well. This work investigates Rubidium based ESFADOFs on the $5P_{3/2} \rightarrow 8D_{5/2}$ transition (cf. Fig. 3.1). Consequently, $\gamma \rightarrow \gamma'$ refer to all possible transitions within the corresponding Zeeman–multiplets. In addition, as the ESFADOF operating transition becomes accessible through the external optical pumping process, which populates the lower ESFADOF state, the number density of the lower ESFADOF state $N(\gamma)$ can not be described any more by a Boltzmann–distribution (cf. Eq. 3.29). In fact, $N(\gamma)$ is strongly correlated to the exact spatial and spectral pump geometry.

As Eqs. 3.25 and 3.28 indicate, a strongly populated lower ESFADOF state $N(\gamma)$ increases the signal strength of the transmitted light. Thus, high pump intensities as well as high opacities of the vapor are advantageous. On the other hand, high power lasers increase the complexity of the system considerably. They

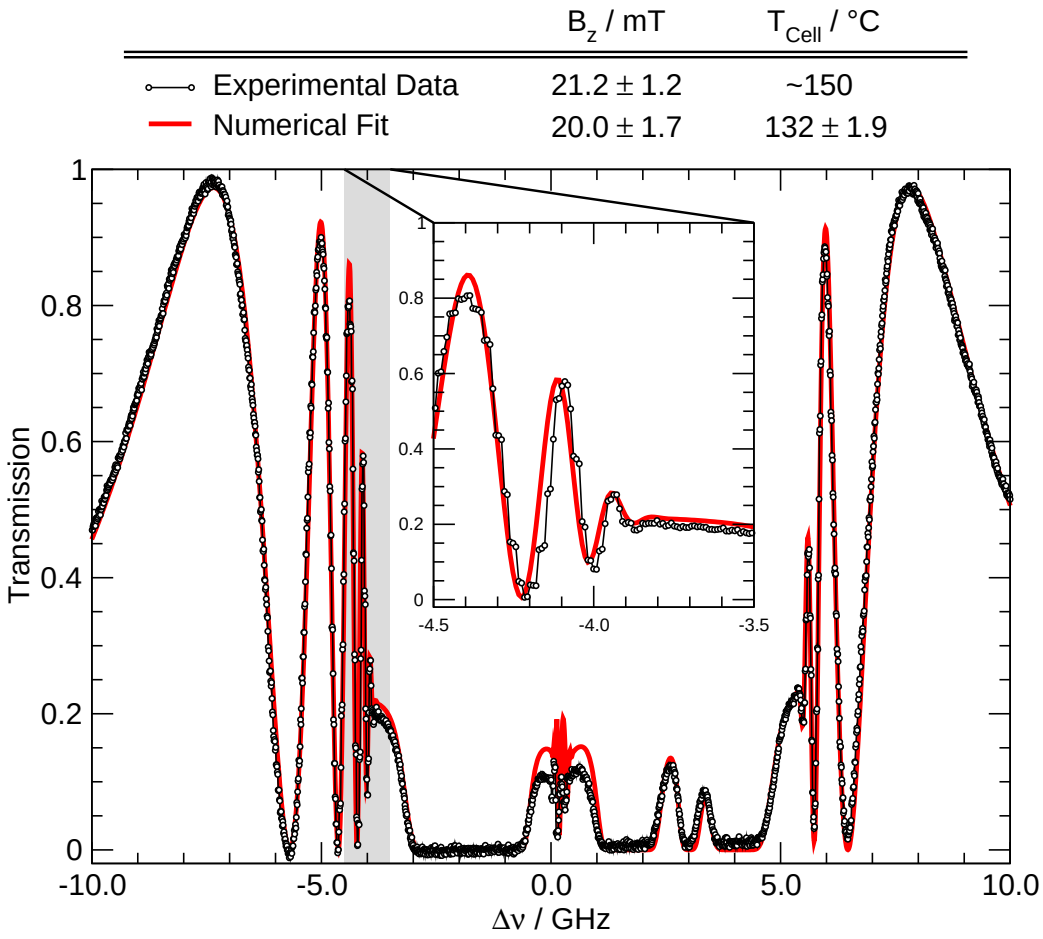

Fig. 3.4: Transmission characteristics of a Rubidium based ground state FADOF: The abscissa shows the frequency detuning of the probe laser from the center of the investigated Rb $5S_{1/2} \rightarrow 5P_{3/2}$ transition ($\lambda = 780.24\,\text{nm}$), while the ordinate shows the transmission of the FADOF device. The experimental parameters as well as the results of a numerical fit to the data are annotated in the figure. The fit has been performed by a custom developed evolutionary algorithm [136], which delivers the start parameters for the Levenberg–Marquardt least squares fit [137]. The measured temperature has been obtained on the vapor cell surface, which explains the deviation from the fit result. However, the agreement between theory and experiment is excellent. This proves the general applicability of the described theoretical approach. The inset highlights the rotation of the polarization angle, as the Faraday angle subtends an angle of π within each oscillation (cf. Eq. 3.7). In conclusion, FADOFs are capable of delivering steep and symmetric transmission edges, which are tunable within a few GHz around the central frequency of the employed transition. More details, in particular on the experimental setup, can be found in Refs. [16, 20, 21].

have to comply with the same specifications such as weight and ruggedness as the rest of the Brillouin–lidar setup. However, as already discussed above, currently available semiconductor devices deliver high pump powers, while being compact, insensitive to vibrations and highly efficient. Furthermore, a non–uniform distribution of the excited state atoms throughout the atomic vapor cell must be included in a thorough theoretical treatment, which certainly extends standard rate equation models. This fact lifts in particular the spatial homogeneity of the refractive indices. Thus, the computation of the ESFADOF transmission must follow the discussion of Sec. 3.2.2.

Briefly speaking, theoretically predicting $\mathrm{N}(\gamma)$ requires the consideration of (1) the optical pumping process, (2) radiation trapping [138, 139] and (3) quenching processes, as for example energy pooling [140] and fine structure mixing collisions.

In conclusion, a proper treatment of the pumping process, which populates the lower ESFADOF state, exceeds standard rate equation models and has to be included in order to complete the theoretical description. Regardless of the fact that pulsing the external pump radiation could be employed as an additional temporal gating technique, which might increase the signal/noise ratio, as it switches the ESFADOF transmission on and off, the following discussion treats the cw pumped case only. However, solving the complexity of the Zeeman–multiplets for both Rb isotopes, with the high degree in nonlinearity of the underlying problem exceeds the purpose of this work. Hence, the discussion is rather intended as hinting towards a complete model and should not be regarded as complete.

3.6.1 Optical Pumping

The optimal pumping scheme overlaps the radiation of an additional pump laser, whose wavelength is tuned close to the center of the pump transition, with the beam of the incident Brillouin–scattering (cf. Fig. 3.1). Hence, the highest number densities of the lower ESFADOF state $\mathrm{N}(\gamma)$ can be expected near the entry window of the vapor cell. As already mentioned above, $\mathrm{N}(\gamma) = \mathrm{N}(\gamma, \mathbf{r})$ depends on the exact position inside the vapor cell and exponentially decreases due to the Lambert–Beer law [74]. The optical pumping process can be described by rate equations, which balance the transfer rates to and from each involved level [141]. Fig. 3.5 depicts a schematic of the involved atomic transitions, which will be indexed in the following discussion according to this figure. It already includes refinements of the model, which will be discussed below.

First of all, it is intuitive to consider only the atomic fine structure ($\mathbf{I} = 0$) and to reduce the problem to a two level system. Let $\mathrm{N}_0 = \tilde{\mathrm{N}}_0/\mathrm{N}$ and $\mathrm{N}_0 = \tilde{\mathrm{N}}_1/\mathrm{N}$ denote the relative population of the involved two level system, where $\mathrm{N} = \mathrm{n}(\mathrm{T}_{\mathrm{Cell}})$ denotes the total number density of the atomic vapor. When neglecting the presence of the magnetic field, the optical pumping process on the Rb $5\mathrm{S}_{1/2} \rightarrow 5\mathrm{P}_{3/2}$ transition can be approximated by the following two level rate equations:

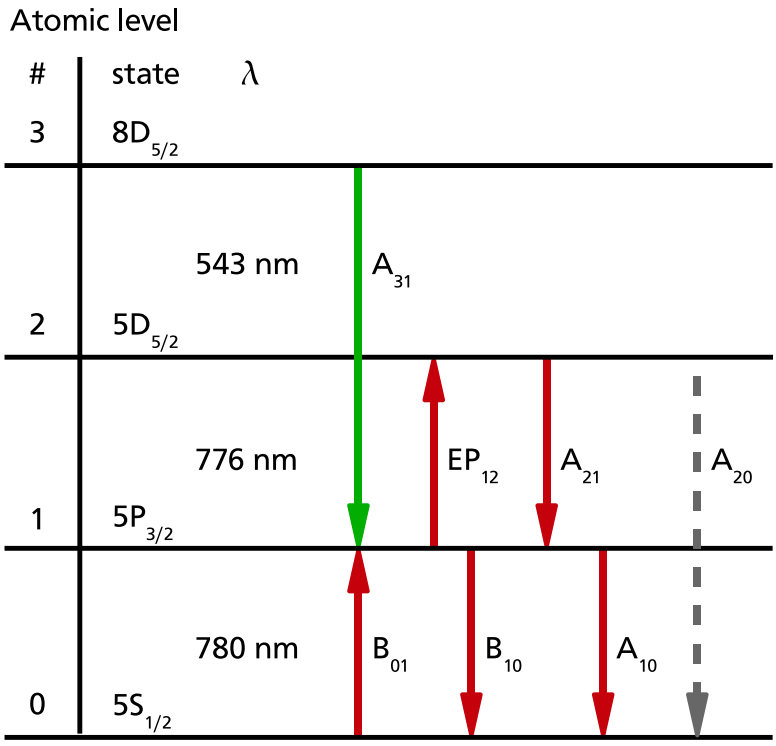

Fig. 3.5: Schematic of the involved atomic transitions, which dominate the modeling of the Rubidium ESFADOF: Only the atomic fine structure is indicated, though the applied magnetic field strength lifts the degeneracy and shifts the Zeeman–sublevels. A and B correspond to the Einstein–coefficients of the indexed transition and EP_{21} denotes the energy-pooling transfer rate. The Einstein coefficient A_{20} compiles the decay pathways from level 2 to level 0 via other intermediate levels. They are not indicated in the figure for clarity. Details are given in the text.

$$\frac{\mathrm{d}}{\mathrm{dt}}\mathrm{N}_0(\mathbf{r}) = \underbrace{\mathrm{A}_{10}\mathrm{N}_1(\mathbf{r})}_{\text{Spont. decay}} - \underbrace{\int \mathrm{d}\omega \frac{\mathrm{I}_{\mathrm{Pump}}(\nu,\mathbf{r})}{\mathrm{h}\nu_{\mathrm{P}}}\sigma_{01}(\omega)\left[\mathrm{N}_0(\mathbf{r}) - \frac{\mathrm{g}_1}{\mathrm{g}_0}\mathrm{N}_1(\mathbf{r})\right]}_{\text{Absorption and stim. emission}}, \tag{3.40}$$

$$\frac{\mathrm{d}}{\mathrm{dt}}\mathrm{N}_1(\mathbf{r}) = \underbrace{-\mathrm{A}_{10}\mathrm{N}_1(\mathbf{r})}_{\text{Spont. decay}} + \underbrace{\int \mathrm{d}\omega \frac{\mathrm{I}_{\mathrm{Pump}}(\nu,\mathbf{r})}{\mathrm{h}\nu_{\mathrm{P}}}\sigma_{01}(\omega)\left[\mathrm{N}_0(\mathbf{r}) - \frac{\mathrm{g}_1}{\mathrm{g}_0}\mathrm{N}_1(\mathbf{r})\right]}_{\text{Absorption and stim. emission}}, \tag{3.41}$$

$$\sum_{\mathrm{i}} \mathrm{N}_{\mathrm{i}} = 1 \quad \text{Normalization.} \tag{3.42}$$

This linear system of equation has its well known steady state solution ($\frac{\mathrm{d}}{\mathrm{dt}}\mathrm{N_i}$=0, due to the cw pump radiation) [74]. Here, $\mathrm{A_{10}}$ is the Einstein coefficient for the spontaneous decay. $\mathrm{g_0}$ and $\mathrm{g_1}$ denote the degeneracies of the involved transitions. They depend on the Rb isotope: $\mathrm{g_0} = 12$, $\mathrm{g_1} = 24$ for ^{85}Rb and $\mathrm{g_0} = 8$ and $\mathrm{g_1} = 16$ for ^{87}Rb. It is convenient to treat each isotope individually and to combine the results afterwards. $\sigma_{01}(\omega)$ is the spectral profile of the absorption cross section and $\mathrm{I_{Pump}}(\nu, \mathbf{r})$ the spectral profile of the pump laser intensity. The dependencies on the local position $\mathbf{r}$ indicate that spatial variations of the pump intensity translate also into spatial variations of the number densities. As a first approximation, it is convenient to reduce the problem to one dimension along the $\mathbf{e}_\mathrm{z}$ direction. This approximation is appropriate as long as the diameter of the pump laser exceeds the diameter of the incident Brillouin–scattered beam and as long as radiation trapping is neglected (see below). In a second step the exponential decay of the pump intensity has to be considered. For that purpose, it is useful to divide the vapor cell into infinitesimally thin slices along the propagation of the pump beam. The system of equations can be solved independently for each slice, where the spectral pump intensity profile decreases from slice to slice according to the photon scattering rate of a pure two level system [74]

$$\Gamma_{\mathrm{Ph}}^{\gamma,\gamma'} = \frac{\mathrm{s}_0^{\gamma,\gamma'}\Gamma_{\gamma,\gamma'}/2}{1+\mathrm{s}_0^{\gamma,\gamma'}+(2\delta/\Gamma_{\gamma,\gamma'})^2}. \tag{3.43}$$

$\Gamma_{\gamma,\gamma'}$ represents the natural linewidth of the involved $\gamma \rightarrow \gamma'$ transition, $\mathrm{s}_0^{\gamma,\gamma'}$ the saturation parameter $\mathrm{s}_0^{\gamma,\gamma'} = \mathrm{I_{Pump}}/\mathrm{I_S^{\gamma,\gamma'}}$, $\mathrm{I_S^{\gamma,\gamma'}} = \frac{\hbar\omega}{\sigma_{01}(\omega)}$ the saturation intensity and $\delta = \omega - \omega_{\gamma,\gamma'}$ the detuning from the line center. The photon scattering rate $\Gamma_{\mathrm{Ph}}^{\gamma,\gamma'}$ converges to $\Gamma_{\gamma,\gamma'}/2$ and the population of the two level system equilibrates, due to the hard pumping on the Rb D2 absorption line; typical values are $\delta \approx 0$, $\mathrm{s}_0^{5\mathrm{S}_{1/2},5\mathrm{P}_{3/2}} \gg 1$ for $\mathrm{I_S^{5S_{1/2},5P_{3/2}}} = 3.17$ mW/cm^2 and $\mathrm{I_{Pump}} > 100$ W/cm^2.

The attenuation of the laser beam intensity along the beam direction can be described as

$$\frac{\mathrm{d}}{\mathrm{dz}}\mathrm{I_{Pump}}(\mathbf{r},\omega) = \mathrm{h}\omega_\mathrm{P}\,\Gamma_{\mathrm{Ph}}^{01}(\mathbf{r},\omega)\,\mathrm{N}\,[\mathrm{N_0}(\mathbf{r}) - \mathrm{N_1}(\mathbf{r})]\,. \tag{3.44}$$

In order to describe the ESFADOF transmission spectra adequately, it is mandatory to include the hyperfine structure and the different isotopes. Hence, the introduced two level pumping scheme must be extended to the full problem. This is particularly challenging, as the magnetic field lifts the degeneracies of the involved atomic levels. Thus, each Zeeman–substate has to be treated individually. Nevertheless the basic idea of the discussion remains valid.

Let γ and γ' index the Zeeman–substates of the $5\mathrm{S}_{1/2}$ atomic ground level (denoted as level 0) and $5\mathrm{P}_{3/2}$ pump level (denoted as level 1) respectively. As the hyperfine structure and the magnetic field lift all degeneracies, all possible transitions between the Zeeman–sublevels of level 0 and level 1 have to be considered.

According to Eqs. 3.40–3.42, the following system of equations balance the contributions of these transitions:

$$\sum_{\gamma'} \mathrm{I}_{\gamma\gamma'} \left[\mathrm{N}_{\gamma'} - \mathrm{N}_{\gamma}\right] + \sum_{\gamma'} \mathrm{A}_{\gamma\gamma'} \mathrm{N}_{\gamma'} = 0 \quad \mathrm{g}_1 \text{ equations for the upper levels,} \tag{3.45}$$

$$-\sum_{\gamma} \mathrm{I}_{\gamma\gamma'} \left[\mathrm{N}_{\gamma'} - \mathrm{N}_{\gamma}\right] - \sum_{\gamma} \mathrm{A}_{\gamma\gamma'} \mathrm{N}_{\gamma'} = 0 \quad \mathrm{g}_0 \text{ equations for the lower levels,} \tag{3.46}$$

$$\sum_{\gamma} \mathrm{N}_{\gamma} + \sum_{\gamma'} \mathrm{N}_{\gamma'} = 1 \quad \text{normalization.} \tag{3.47}$$

The $\mathrm{A}_{\gamma\gamma'}$ correspond to the transition rates of the spontaneous emission and the $\mathrm{I}_{\gamma\gamma'}$ to the pump rates for the $\gamma \rightarrow \gamma'$ transition. The spectral profile of the linear polarized pump laser is incorporated into the pump rates $\mathrm{I}_{\gamma\gamma'}$, as

$$\mathrm{I}_{\gamma\gamma'} = \frac{1}{\hbar\omega_{\gamma\gamma'}} \int \mathrm{d}\omega \left[\sigma_{+}^{\gamma\gamma'}(\omega) + \sigma_{-}^{\gamma\gamma'}(\omega)\right] \frac{\mathrm{I}_{\mathrm{Pump}}(\omega)}{2} \,. \tag{3.48}$$

The spectral profile of the absorption cross section $\sigma_{+}^{\gamma\gamma'}(\omega)$ can be embedded into the framework of Sec. 3.3.2 through the following relation

$$\sigma_{\mathrm{r}}^{\gamma\gamma'}(\omega) = \frac{2}{3} \frac{\omega_{\gamma\gamma'}}{\mathrm{c}} \frac{4\pi}{\mathrm{h}} \frac{\sqrt{\ln 2}}{\Delta\nu_{\mathrm{D}}} \mathrm{S}_{\mathrm{r}}^{\gamma\gamma'} Im\left\{W(\xi_{\gamma\gamma'}, \omega)\right\}. \tag{3.49}$$

Although the complexity of the description of the pumping process increases significantly, Eqs. 3.45–3.47 remain linear and the system can be represented by an algebraic equation. For this purpose, it is useful to compile the number density into a vector representation $\mathbf{N} = (\mathrm{N}_{\gamma}, \mathrm{N}_{\gamma'})$, such that the system of equations translate into

$$\mathsf{A}\mathbf{N} = \begin{pmatrix} 0 \\ \vdots \\ 0 \\ 1 \end{pmatrix} . \tag{3.50}$$

The normalization (Eq. 3.47) has been added to the last row of the matrix A, which compiles the transition rates between the sublevels. In other words Eq. 3.50 is the matrix representation of Eq. 3.45–3.47. This algebraic equation can be solved by standard methods, as the Gauss–algorithm or the LU–decomposition [142]. The absorption of the pump beam has to be included according to the above described approach by dividing the vapor cell in infinitesimal thin slices. For each slice Eq. 3.50 has to be solved and the scattered pump radiation has to be extracted from the incident pump intensity before it is passed to the next slice. Thus, the computational effort increases rapidely in order to achieve accurate estimations.

3.6.2 Quenching Processes

The focus of the last section was the development of a rate equation model, which describes the optical pumping process of the vapor cell. Although the fully lifted

degeneracies have been included, several other important mechanisms, which significantly influence the population of the ESFADOF levels have been omitted so far. This section is devoted to quenching processes, which have to be included due to the elevated temperature of the vapor cell. Generally speaking, the collision of excited Rb atoms with other excited or ground state atoms lead to the transfer of excitation through different processes. There are: (1) Spin-Exchange collisions; they lead to a redistribution of the population within the same fine structure multiplet, while conserving the total spin. (2) Energy-pooling collisions; they must occur between two excited atoms and extract population from the excited states, as one atom is lifted to an even higher excitation level and the other is de–excited to the ground state [140].

Both processes have been extensively investigated in Rb vapor [140, 143]. A very detailed overview on optical pumping and the accompanied spin exchange, which leads among other processes to a randomization of the atomic polarization, can be found in the review article of Happer [141]. Briefly speaking, atomic collisions lead to an exchange of their spins, while conserving the total spin. The effect of this process redistributes the excitation among different polarizations of the same atomic level and leads to small corrections. This holds in particular true, when regarding high pump intensities, which have the ability to strongly polarize the atomic vapor. However, as the following section shows, the atomic vapor depolarizes nevertheless to some extent, but this is mainly a consequence of the frequency redistribution of the trapped radiation.

In contrast to the first process, the energy-pooling process extracts population from the pumped lower ESFADOF state. Therefore, it is required to treat this process in more detail. It can be described by the following reaction:

$$\mathrm{Rb}^{*}(5\mathrm{P}_{3/2}) + \mathrm{Rb}^{*}(5\mathrm{P}_{3/2}) + \Delta\mathrm{E}_{\mathrm{EP}} \rightarrow \mathrm{Rb}^{**} + \mathrm{Rb}(5\mathrm{S}_{1/2}), \tag{3.51}$$

where Rb^{**} denotes an even higher excited state, e.g. the $5\mathrm{D}_{3/2}$ or the $5\mathrm{D}_{5/2}$ level. But, depending on the temperature of the atomic vapor, other atomic levels might be reached as well (cf. also Sec. 5.3.2 and Fig. 5.18). The energy gap ΔE is extracted from the thermal energy of the vapor. The inverse process is called energy–transfer and results by simple time reversal of Eq. 3.51:

$$\mathrm{Rb}^{**} + \mathrm{Rb} \rightarrow \mathrm{Rb}^{*} + \mathrm{Rb}^{*}. \tag{3.52}$$

In order to present the general idea, it is sufficient to restrict the discussion to the predominant energy–pooling process, which transfers excitation to the 5D state [140]. As Fig. 3.5 indicates, the implications of the energy–pooling process are rather dramatic. The energy–pooling process extracts two atoms from the lower ESFADOF state, which therefore affects the ESFADOF transmission through Eq. 3.28. This process can be included in the rate equations 3.45–3.47 by introducing the energy–pooling quenching rate EP_{12}. It is convenient to restrict the treatment again to the fine structure. An extension to the complete problem can be accomplished in the same manner as it was the case for the optical pumping process.

The energy–pooling quenching rate EP_{12} follows

$$EP_{12} = \sigma_{12}^{EP} v_{RMS} N_1 N \,, \tag{3.53}$$

where $\sigma^{EP}_{5P_{3/2}\leftrightarrow 5D} = 3\times 10^{-14}\mathrm{cm}^2$ denotes the energy–pooling cross section [140] and v_{RMS} is the root mean square velocity of the colliding atoms. It is obvious that EP_{12} must depend on the number density of the excited state $N_1 N$. Hence, the rate equations 3.40 and 3.41 have to be extended:

$$\begin{aligned}
\tfrac{d}{dt}N_0(\mathbf{r}) \;=\; & \underbrace{A_{10}N_1(\mathbf{r}) + A_{20}N_2(\mathbf{r})}_{\text{Spont. decay}} \\
& \underbrace{-\int d\omega \frac{I_{Pump}(\nu,\mathbf{r})}{h\nu_P}\sigma_{01}(\omega)\left[N_0(\mathbf{r}) - \frac{g_1}{g_0}N_1(\mathbf{r})\right]}_{\text{Absorption and stim. emission}} \\
& \underbrace{+EP_{12}\left[N_1(\mathbf{r}) - \frac{g_1}{g_0}e^{\frac{\Delta E_{EP}}{k_B T}}N_2(\mathbf{r})\right]}_{\text{Energy–pooling + energy transfer}}
\end{aligned} \tag{3.54}$$

$$\begin{aligned}
\tfrac{d}{dt}N_1(\mathbf{r}) \;=\; & \underbrace{A_{21}N_2(\mathbf{r}) - A_{10}N_1(\mathbf{r})}_{\text{Spont. decay}} \\
& \underbrace{+\int d\omega \frac{I_{Pump}(\nu,\mathbf{r})}{h\nu_P}\sigma_{01}(\omega)\left[N_0(\mathbf{r}) - \frac{g_1}{g_0}N_1(\mathbf{r})\right]}_{\text{Absorption and stim. emission}} \\
& \underbrace{-2\,EP_{12}\left[N_1(\mathbf{r}) - \frac{g_1}{g_0}e^{\frac{\Delta E_{EP}}{k_B T}}N_2(\mathbf{r})\right]}_{\text{Energy–pooling}}
\end{aligned} \tag{3.55}$$

$$\tfrac{d}{dt}N_2(\mathbf{r}) \;=\; \underbrace{-(A_{21}N_2(\mathbf{r}) + A_{20}N_2(\mathbf{r}))}_{\text{Spont. decay}} + \underbrace{EP_{12}\left[N_1(\mathbf{r}) - \frac{g_1}{g_0}e^{\frac{\Delta E_{EP}}{k_B T}}N_2(\mathbf{r})\right]}_{\text{Energy–pooling}} \tag{3.56}$$

$$\sum_i N_i \;=\; 1 \quad \text{Normalization.} \tag{3.57}$$

The energy–transfer process has been included by the principle of detailed balance, i.e. that the energy–pooling quenching rate has to be modified for the upward directed reaction in order to account for the energy-gap, which is provided by or released to the thermal bath. This explains the Bolzmann–term in the rate equations.

A_{20} compiles all other possible transition pathways, wich emerge from level 2 and end in the ground state 0. It is clearly understood that the direct transition $2 \rightarrow 0$ is forbidden. The exact problem requires the individual treatment of each possible decay pathway. Extending the rate equations for that purpose is not complicated. However, it would only increase the conceptual effort, but would not

deliver more insight. Approximating these processes by the effective transfer rate A_{20} is accurate enough for the current disccussion. Hence A_{20} is a function of the transition rates of all possible decay pathways $2 \rightarrow \eta' \rightarrow \cdots \rightarrow \eta \rightarrow 0$, where the $2 \rightarrow 1 \rightarrow 0$ pathway is explicitly excluded. This yields:

$$A_{20} = \frac{1}{\frac{1}{A_{2\eta'}} + \cdots + \frac{1}{A_{\eta 0}}} + \cdots \tag{3.58}$$

By inserting data from the Kurucz atomic line database [144] $A_{20} = 2$ MHz results.

Moreover, after inserting the expression for the energy–pooling transfer rate (Eq. 3.53) into the system of rate equations 3.54–3.57, the nonlinear character of this process becomes visible. Mixed and quadratic terms of the number densities appear. These terms suspend the linear behavior of the rate equations. In addittion, the complexity considerably increases, when extending the description to the complete Zeeman–splitted case. Hence, estimations can only be computed by numerical solutions. However, restricting the model to the fine structure only, allows to estimate the effect of the energy–pooling quenching. Fig. 3.6 has been obtained by numerically solving the system of the rate equations 3.54–3.57 based on Rb atoms, while neglecting the spatial dependency. A typical cell temperature of $T_{Cell} = 170^{\circ}C$ has been assumed. The saturation of the vapor is clearly visible and the energy–pooling quenching of the excited atoms binds 6% of the total vapor density to the higher excited level 2. This result is of particular importance for Sec. 5.3.2.

3.6.3 Radiation Trapping

Radiation trapping is always an issue when optically pumping atomic vapor. The pump radiation, which is scattered off the pump beam by the atomic vapor, does not leave the atomic vapor directly. In fact, there always exists a non–vanishing probability that the scattered photons are reabsorbed by the atomic vapor prior to leaving the vapor. These photons are re–emitted afterwards and can undergo a cycle of absorptions and re–emissions, before they eventually leave the vapor. Thus, radiation trapping increases the number density of excited state atoms, as there is also an important probability that these photons re–enter the primary pumped regions. Theoretical descriptions of this phenomenon go back to the pioneering works of Holstein, who published in 1947 a description based on an integro–differential equation, known as the Holstein–equation [138]:

$$\frac{d}{dt} n(\mathbf{r}, t) = -A\, n(\mathbf{r}, t) + A \int_V n(\mathbf{r}', t)\, G(\mathbf{r}, \mathbf{r}')\, d\mathbf{r}' . \tag{3.59}$$

A is the Einstein coefficient, $n(\mathbf{r})$ is the number density of the excited state and $\int_V G(\mathbf{r}, \mathbf{r}')\, d\mathbf{r}'$ is the radiation trapping operator.

Since 1947, radiation trapping has been the subject to extensive research throughout the years and it is still a fascinating research–field today [139]. A comprehensive introduction to this subject together with an exhausting survey of this

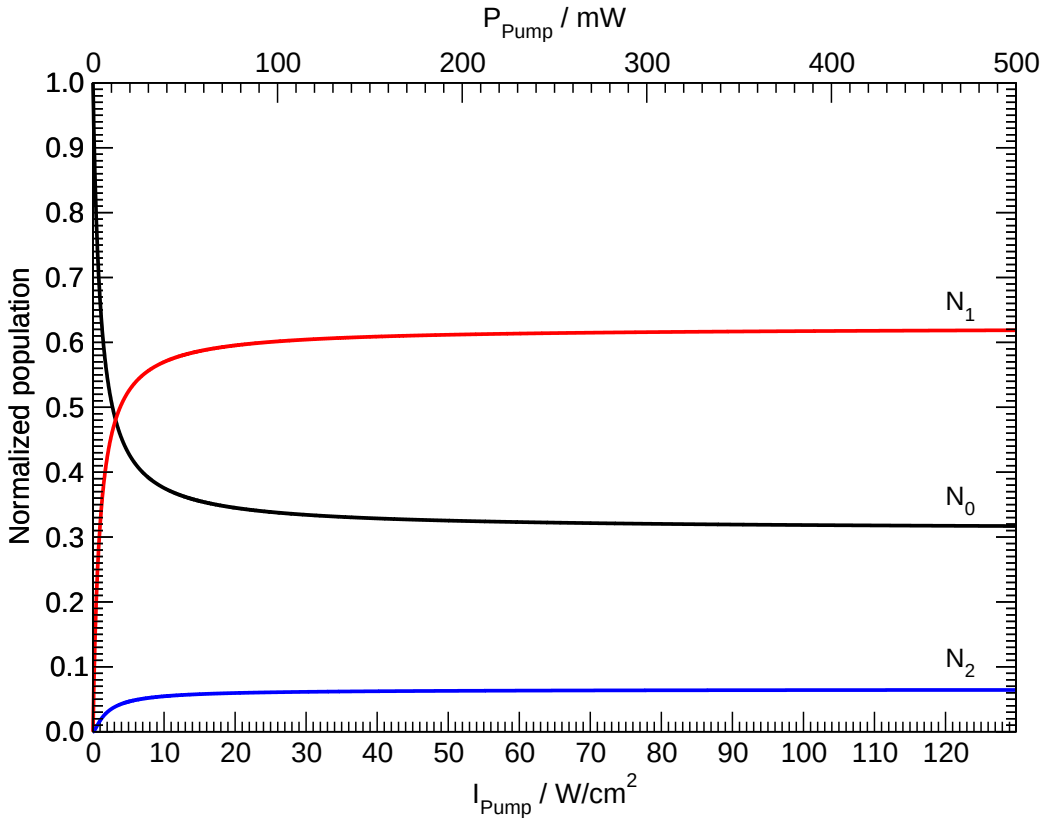

Fig. 3.6: Simulated distribution of the level populations, when including the energy–pooling quenching: The pump intensity has been chosen to follow the experimentally available intensities. The maximum available pump power of $P_{Pump} = 500$ mW translates into a maximum pump intensity of approx. 130 W/cm^2. The spatial decrease of the pump intensity has been neglected and the depicted behavior is only valid near the entry window of the pump laser. The saturation of the vapor is clearly visible and the energy–pooling quenching of the excited atoms binds 6% of the total vapor density to the higher excited level 2.

field is given by the book of Molisch and Oehry [139]. Remarkable are also the series of analytical solutions of the Holstein–equation, which were published by Van Trigt [145–148]. However, these analytical solutions are restricted to very simplified geometries, which allowed the analytical solution of the Holstein-equation. They are not universally applicable and reliable solutions of the radiation trapping problem for arbitrary geometries have to be obtained numerically. This holds also true for the steady state problem, which arises when optically pumping the ESFADOF device with a cw laser beam. In that case, radiation trapping must be included in the above described optical pumping. Hence, the number densities of the pumped state then follows

$$\frac{\mathrm{d}}{\mathrm{dt}}\mathrm{n}(\mathbf{r},\mathrm{t}) \;=\; 0 = -\mathrm{A}_{10}\,\mathrm{n}(\mathbf{r},\mathrm{t}) \;+\; \mathrm{E}(\mathbf{r}) \;+\; \mathrm{A}_{10}\int_{\mathrm{V}} \mathrm{n}(\mathbf{r}',\mathrm{t})\,\mathrm{G}(\mathbf{r},\mathbf{r}')\,\mathrm{d}\mathbf{r}' \;. \quad (3.60)$$

The first term represents the losses due to spontaneous emission of atoms located at point $\mathbf{r}$. The second term, $E(\mathbf{r})$, is the spatial excitation of the vapor atoms, which is dominated by the pump laser. Finally, the last term describes the increase of the number density at point $\mathbf{r}$ due to the reabsorption of photons which have been emitted at point $\mathbf{r}'$. This contribution is averaged over the whole volume V by the integration. The kernel function $G(\mathbf{r},\mathbf{r}')$ describes the probability density that a photon emitted at point $\mathbf{r}'$ is reabsorbed at $\mathbf{r}$. Hence, the following relations hold:

$$G(\mathbf{r},\mathbf{r}') = -\frac{1}{4\pi\rho^2}\frac{\partial T(\rho)}{\partial \rho}, \tag{3.61}$$

$$T(\rho) = C_\nu \int k(\nu)\exp\left(-k(\nu)\rho\right)\mathrm{d}\nu \text{ and} \tag{3.62}$$

$$C_\nu = \frac{1}{\int k(\nu)\mathrm{d}\nu}. \tag{3.63}$$

The interpretation of $T(\rho)$ is straight forward; it describes the frequency-averaged probability that a photon emitted at point $\mathbf{r}'$ traverses a distance $\rho = |\mathbf{r}-\mathbf{r}|$ without being absorbed. C_ν is a normalization factor, and $k(\nu)$ is the absorption line shape of the pump transition.

At this point it has to be emphasized, that Eq. 3.60 is only valid under the following assumptions [139]: (1) Only two levels of the atomic structure are relevant for the radiation trapping process, (2) the density of ground state atoms is much larger than the density of upper-state atoms, (3) the spatial distribution of lower-state atoms is uniform, (4) all photons arriving at the walls leave the cell, (5) the time of flight of the photons is negligible compared to the natural life time of the excited atoms, (6) the atoms are stationary during an absorption and reemission cycle, (7) the reemission of the photons leads to a complete frequency redistribution, and (8) the reemission occurs isotropically.

Clearly, assumptions (1), (2) and (3) are not fully valid for the description of the underlying radiation trapping problem:

(1) As the applied magnetic field lifts all degeneracies, this assumption can not hold anymore. In addition, the occurrence of quenching processes, as discussed in Sec. 3.6.2, considerably increases the complexity of the system, as they increase the number of involved states. High lying states, which are populated by the energy–pooling process generally de–excite via spontaneous emission. It is reasonably probable, that these photons are also trapped within the atomic vapor, due to the hard pumping beyond the saturation limit. Briefly speaking, each photon which emerges from a transition between a high lying state and the pumped level, e.g. the $2 \rightarrow 1$ transition in Fig. 3.5, can be trapped due to the hard pumping of the vapor cell. Hence, this fact results in a decrease of the lower ESFADOF level population and the complexity of the pumping process literally explodes.

(2) and (3) It is useful to distinguish between three regimes: (a) The hard pumping regime: The strong pump laser equilibrates the population of the

lower and upper levels and the medium becomes transparent. However, employing narrow semiconductor lasers, allows selective pumping along the broad absorption profile. Hence, only the directly affected overlap between the spectral profile of the pump laser and the spectral profile of the absorption line is saturated. Thus, the population of the lower ESFADOF state is dominated by the strong pump laser within the spectral overlapp. Transitions, which are not directly affected by the pump laser, behave differently. They profit from the frequency redistribution, due to the spontaneous emission of photons. The high amount of absorptions and re–emissions shifts a considerable amount of photons within the radiation trapping process to the line wings and therefore broadens the spectral profile of the complex refractive indices. (b) The intermediate pumping regime: The pump intensity reaches the saturation limit and decreases exponentially along the cell axis. The population of the pump states behave accordingly and the influence of the trapped radiation increases, which leads also to broadening of the spectral profile of the complex refractive indices. (c) The low pumping regime, where these assumptions are valid.

In addition to the above, particular care requires the depolarizing effects of the radiation trapping. In spite of the strong pump laser and the applied magnetic field, a considerable depolarization of the vapor results from the trapped radiation, as the spontaneously emitted photons are dephased and depolarized with respect to the pump laser [149]. This effect increases with the opacity of the vapor, as the number of absorptions and re–emissions increases exponentially [139]. However, this effect is rather advantageous for the Brillouin–lidar receiver. As the excitation of the lower ESFADOF level is widely spread over an increased number of sublevels, a broadened transmission spectrum of the ESFADOF device results.

In conclusion, extensive numerical models have to be employed to correctly estimate the number density of the excited state levels. Without the knowledge of the spatial distribution of this number density, a calculation of the expected ESFADOF transmission spectra is not meaningful for the operational conditions considered in this thesis. This is even more important, as the spatial distribution of the excited state atoms is subject to significant changes. The absorption of the pump intensity in combination with quenching processes and radiation trapping result in strong inhomogeneities along the pump beam path, which have to be included according to Sec. 3.2.2.

4

Experimental Investigations of the Rubidium ESFADOF

This chapter is dedicated to the experimental setup, which has been implemented in order to investigate the spectral transmission characteristics of the ESFADOF device. Extensive care has been taken to simultaneously measure the frequency scale and the transmission with high accuracies. Briefly speaking, the measurement principle can be summarized as follows: (1) A pump laser operating at 780 nm is injected into the ESFADOF vapor cell and populates the Rb $5P_{3/2}$ state. (2) An additional probe laser operating at the $5P_{3/2} \rightarrow 8D_{5/2}$ transition wavelength (543 nm) is overlapped with the pump laser and guided through the vapor cell. (3) The transmission spectrum of the ESFADOF device is recorded behind its exit polarizer by scanning the wavelength of the probe laser and evaluating both exit polarizations simultaneously by two photodiodes. (4) Additional frequency calibration units perform the measurement of the frequency scale with high accuracy. (5) The implemented electronics in combination with a computer aided measurement control and data acquisition yields high accuracies of the transmission measurement and allows a very precise averaging procedure, which is insensitive to any unavoidable long term frequency drift of the scanning laser.

In addition, the implementation of the ESFADOF device has to comply with the imposed requirements of the Brillouin-lidar (cf. Sec. 2.2), i.e. it has to provide steep transmission edges in the spectral region of interest, symmetrically located around the Brillouin-lidar's laser wavelength. The $\pm$6.8–7.8 GHz separation of the Brillouin-doublet requires high magnetic fields. Two different setups have been realized: *Vapor cell I* was used for detailed studies on the ESFADOF operational limits and *vapor cell II* demonstrated as a proof of concept measurement the desired separation of the transmission edges. Fig 4.1 illustrates all relevant subgroups, and the experiment has been divided into 6 main components:

1. **The ESFADOF device:** The ESFADOF consists of one fused silica Rb vapor cell kept in a selfmade Aluminum oven placed between two crossed polarizers (PBS-P and PBS-A). As alkali atoms are well known for their affinity to diffuse into low melting glasses, e.g. Borosilicate glasses [150], the employment of a fused silica vapor cell is advantageous at high temperatures. Temperatures of up to 200°C provide useful Rb vapor densities (cf. appendix A) and the temperature controlled oven is equipped with a heat pipe, which perma-

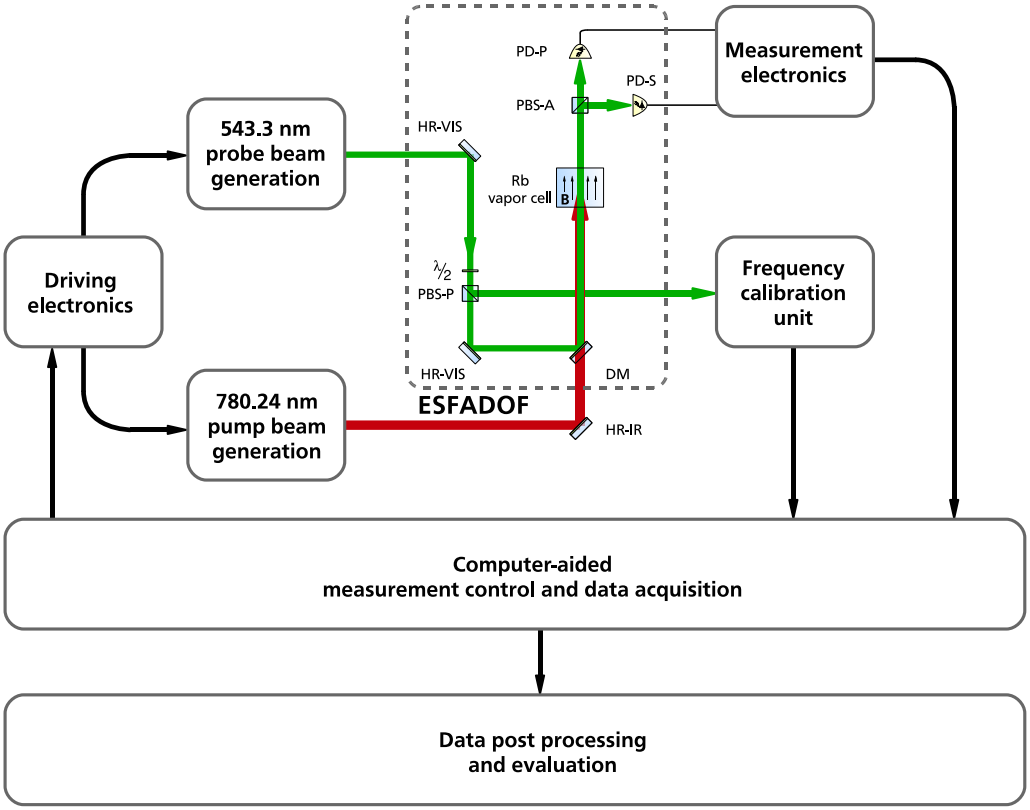

Fig. 4.1: Block diagram of the ESFADOF experimental procedure: The ESFADOF device is marked by the dashed frame and corresponds in principle to the schematic drawing of Fig. 3.1. High reflective dielectric mirrors for the visible spectral range (HR-VIS) and for the infrared spectral range (HR-IR) guide the probe and the pump beams through the experimental setup. The probe and the pump beam are overlapped with the help of a dichroic mirror (DM). A half–waveplate retarder ($\lambda/2$) adjusts the polarization of the probe beam, so that a small part of the radiation is extracted by the polarizing beam splitter cube PBS-P into the frequency calibration unit. The two crossed polarizers P and A of Fig. 3.1 correspond to the polarizing beam splitter cubes PBS-P and PBS-A. Two identical photodiodes (PD-S and PD-P) monitor the perpendicular polarization outputs of PBS-A and thus the ESFADOF transmission while scanning the wavelength of the probe laser.

nently extracts heat from a well defined region of the vapor cell. The heat pipe defines the coolest point of the setup and controls therefore the density of the Rb vapor, while keeping the front facets free from condensation. The magnetic field **B**, mandatory for FADOF operation, is provided by permanent high temperature ring magnets. The desired separation of the transmission edges require high magnetic field strengths of 500 mT. In order to guarantee these high field strengths at temperatures of up to 200°C, Samarium-Cobalt magnets (Sm_2Co_{17}) have been employed. Their Curie temperature is $T_C = 825°C$ and it is safe to operate them up to a threshold temperature of $T_O = 350°C$. Below T_O their loss in magnetization with increasing temperature is negligible and they always recover after cooling them back to room temperature. Operating temperatures beyond T_O irreversibly damage the magnetization of the material [151]. Finally, the ESFADOF transmission spectrum is quantified by two identical photodiodes (PD-S and PD-P), which monitor both polarizations of the ESFADOF exit polarizer, while scanning the wavelength of the probe laser.

2. **The 780 nm pump laser:** As ESFADOFs operate between two excited states, it is mandatory to populate the lower ESFADOF state. This is achieved by optical pumping on the $5S_{1/2} \rightarrow 5P_{3/2}$ Rb D_2 transition. For this purpose, the radiation of an external cavity diode laser (ECDL) [152] is tuned to the central wavelength of the Rb D_2 transition (780.2405 nm) and amplified up to 500 mW by a tapered amplifier [95–99, 153]. Prior to injecting the pump beam into the cell, additional optics shape its beam profile. The overlap of the probe beam with the pump beam is achieved by a dichroic mirror (DM). Sec. 4.3 addresses all relevant details of the measurement unit and the pump laser setup.
3. **The 543 nm probe laser:** In contrast to the pulsed Brillouin-lidar's light source, a tunable and spectrally narrow continuous wave laser source is advantageous for recording the ESFADOF transmission characteristics. For this purpose an Yb doped fiber amplifier seeded by an additional ECDL has been employed. Seeding by an ECDL ensures a small linewidth and tunability of the source [154]. The frequency scan of the probe laser is achieved by tuning the external cavity together with the injection current of the ECDL operating around 1086.60 nm. This infrared radiation is subsequently amplified by the Yb doped fiber amplifier [54, 59] and afterwards frequency converted by a nonlinear crystal via second harmonic generation [73, 155, 156]. The green probe laser radiation is injected into the ESFADOF device, superimposed to the pump beam and two photodiodes (PD-S and PD-P) record the transmitted intensities on the two complementary ESFADOF polarizations. The knowledge of the polarization separated intensities allows the computation of the ESFADOF transmission, while intrinsically taking care of all Fresnel-losses. A detailed discussion of the probe laser setup is subject of section 4.2.
4. **The frequency calibration unit:** The purpose of the frequency calibration unit is to map the experimental accessible data to an absolute frequency scale. This is done stepwise by two simultaneous measurements: (1) The nonlinear elongation of the 1086 nm ECDL piezos results in a nonlinear wavelength

change of the emitted radiation, while scanning the probe beam. With the help of additional frequency markers, this nonlinear frequency scan can be linearized. The frequency markers are delivered by recording the transmission spectrum of a solid, high finesse Fabry-Perot interferometer. Due to the interferometers periodicity, a frequency marker appears at each free spectral range. By applying a nonlinear fit to these markers, a linearization of the frequency scale is achieved. (2) As the frequency markers provide only a relative frequency scale, an additional absolute reference is mandatory in order to obtain an absolute frequency axis. For that purpose, a small part of the probe beam is used to record the absorption spectrum of the $5P_{3/2} \rightarrow 8D_{5/2}$ transition of a second Rb vapor cell simultaneously to the frequency markers and to the ESFADOF transmission. The second cell is also optically pumped on the $5S_{1/2} \rightarrow 5P_{3/2}$ Rb D_2 transition by an additional pump laser.

As this second cell is unperturbed by magnetic or electric fields, only Doppler-broadening and the hyperfine structure contribute to the spectrum. The contribution of the earth's magnetic field can be neglected, due to the weak coupling of this transition (cf. Sec. A). It is far smaller than all other measurement errors. By fitting a Voigt-profile to this absorption spectrum on the previously computed linear frequency scale an absolute frequency scale results. Hence, the origin of the frequency axis of all presented ESFADOF spectra, if not otherwise mentioned, refere to the center of the Rb $5P_{3/2} \rightarrow 8D_{5/2}$ transition wavelength (543.30 nm) [144].

Due to clarity reasons, the description of both components of this unit is divided: The generation of the frequency markers is part of the probe laser setup (cf. section 4.2), whereas the measurement of the absolute reference is incorporated into the measurement unit (cf. section 4.3). The data evaluation, which delivers an absolute frequency scale will be addressed in section 4.4.1 in more detail.

5. **The measurement electronics:** The employed measurement electronics amplify, condition and digitize all relevant signals and parameters during the measurements process, such that highly accurate transmission measurements become possible. Several photodiodes, trans-impedance amplifiers and A/D-converters have been employed. Special attention has been dedicated to the accuracy of the ESFADOF transmission measurements. The two recording photodiodes (PD-S and PD-P in Fig. 4.1) are identical and their built-in trans-impedance amplifiers operate with a laser trimmed resistance, so that their electrical response is identical up to 4 orders of magnitude [157]. The electrical signals are scaled to fit the maximum digitizing range of the employed A/D-card and each recorded channel is separately calibrated. This procedure allows to neglect electrical and digitizing noise compared to all other noise sources.
6. **The post-processing software:** As already mentioned above, the recorded raw data does not provide a linear and absolute frequency scale. Therefore extensive post-processing of the recorded data by several custom-developed programs is necessary. These programs transform the measured raw data into

absolute frequency calibrated ESFADOF transmission spectra. Afterwards, an averaging procedure eliminates temporal fluctuations of the probe lasers intensity and estimates the measurement error. The high complexity of this procedures demands for extensive computational resources, which required a sophisticated parallel processing of the involved substeps on a computer-grid. In particular, the nonlinearity of the frequency scan as well as the unavoidable frequency drift of the 543 nm probe laser on long time scales makes an absolute, linear frequency scale mandatory prior to averaging. A naive averaging procedure on the direct available time axis, without any linearization and compensations of the frequency drift would cause unwanted spectral broadening. A more detailed description of the post-processing procedure will be given in section 4.4.

4.1 Rb Vapor Cells

The implementation of the ESFADOF device has to comply with the restrictions imposed by the airborne compatibility. In addition, magnetic field strengths of up to 500 mT have to be provided in order to guarantee the spectral overlap of the ESFADOF transmission edges with the Brillouin-doublet. However, conventional solenoids as well as superconducting devices are not accessible for an airborne based system, though they potentially combine high flexibility with homogeneous fields. Nevertheless, their power consumption as well as the complexity of the systems are far from being tolerable on board an aircraft. Hence, the employment of permanent magnets offers the only approach to these high fields strengths within a practical framework. But, this couples the achievable magnetic field strengths to the geometry of the setup and thus to the geometry of the Rb vapor cells, which itself is restricted by the manufacturing process. This thesis explored two options of different cell designs; from here after denoted as *vapor cell I* and *vapor cell II*. Their geometry as well as their manufacturering process differ considerably. A schematic of how both designs have been employed in the experimental setup is depicted in Fig. 4.2:

Vapor cell I: This cell has been purchased from a commercial supplier [158]. It is a standard fused silica vapor cell, which has been filled with Rb of natural isotopic abundance and sealed by the manufacturer. The manufacturer restricted the minimum diameter to 25 mm, due to the employment of fused silica. This guarantees the high optical quality of its window panes. Placing permanent ring magnets in front of the entry window of the cell introduces an inhomogeneous magnetic field near the entry window of the vapor cell. The pump beam enters the vapor cell through the hollow core of the ring magnets and only a small volume near the entry window is responsible for the ESFADOF operation. Within this interaction volume the magnetic field strength is still high enough to ensure a sufficient separation of the Zeeman sublevels. The magnetic field strength of the magnets has been measured with the help of a calibrated Hall probe [159] along the symmetry axis at a distance of 2 mm

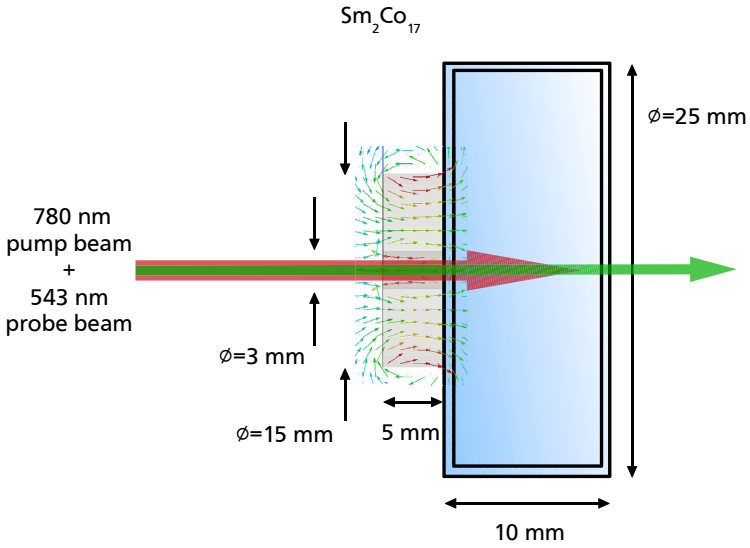

(a) Vapor cell I: Placing Sm_2Co_{17} permanent ring magnets in front of the cell introduces an inhomogeneous magnetic field near the entry window. Stacking 8 magnets together results in field strengths of up to 270 mT near the window pane and along the symmetry axis.

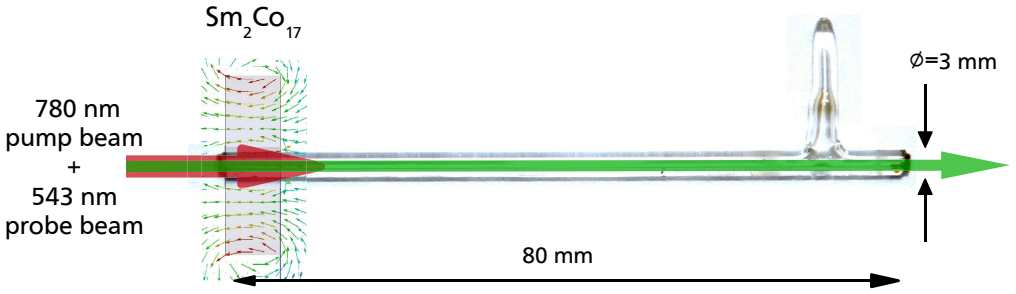

(b) Vapor cell II: Inserting vapor cell II into the hollow core of one ring magnet increases the magnetic field strength up to 530 mT along the symmetry axis.

Fig. 4.2: Schematic geometry of the implemented vapor cell designs.

from the surface, which corresponds to the window panes width. Stacking 8 ring magnets delivers a field strength of 270 mT. Stacking more magnets does not increase the field strength any further, as the distance to the cell increases as well. This measurement should be regarded rather as a rough estimation. Although a calibrated Hall-probe has been employed, the strong inhomogeneity of the magnetic field introduces large errors. However, it corresponds quite reasonably to the finite element calculations, made by the manufacturer of the magnets (cf. appendix C). Of course, stacking less magnets reduces the field strength. However, only the configuration, which delivers the highest possible field strength, has been investigated, as it ensures an almost complete spectral separation of the circularly polarized transitions. This circumstance allows for a qualitative comparison with the desired field strength of 500 mT.

Vapor cell II: Vapor cell II has been subsequently developed in–house. Its miniaturized design has been chosen in order to insert the cell inside the hollow core of the ring magnets (inner diameter of 3 mm). This increases the magnetic field strength up to 530 mT and shifts the ESFADOF transmission edges to the desired separation of $\pm$6.8–7.8 GHz around the central wavelength of the atomic transition. The field strength is mainly controlled by the inner diameter of the ring for a given material and magnetization. Increasing the outer diameter leads to a saturation and is limited by the manufacturing process.

However, a tradeoff between the increase in magnetic field strength and the geometry of vapor cell II results. This makes the manufacturing process very challenging, as it is not possible to apply conventional glass–blowing techniques. Due to the high softening temperature of fused silica ($\sim 1700^{\circ}$C), any attempt to melt the window panes on the small cell cladding destroys their optical quality and inhibits high quality spectroscopic measurements. In order to circumvent these problems a special glueing technique has been developed. It allows to seal the windows panes on the cell cylinder, while preserving their high optical quality. The employed epoxy (Epotek 353ND [160]) in combination with the developed technique proved good vacuum and temperature stability of up to 1.6×10^{-6} mbar and 200°C respectively. The leak rate of a test sample was not measurable, i.e. it lies below the leak detectors lower limit of approx. 5×10^{-8} mbar l/s. A more detailed description of the manufacturing proccess and a scanning electron microscope picture of the glued facet can be found in appendix B.

4.2 543 nm Probe Laser

The fiber amplifier and the frequency conversion unit consists of custom made components, which have been built according to state-of-the-art technologies. Hence, the following discussion covers only the necessary details as far as it is required for the understanding of the performed measurements. Further discussions can be found in the corresponding literature, e.g. Refs. [59, 62, 73, 161].

A schematic of the fiber amplifier setup together with the seed ECDL, beam diagnostics and the frequency conversion unit is depicted in Fig. 4.3. The master oscillator of the fiber amplifier is a custom-developed tripod ECDL. Its design employs the Littrow-configuration [94] in combination with three piezo mechanic transducers (PZT). This design, similar to the one reported by Führer *et al.* [162], allows an independent rotation of the grating (G) around all its axes. A schematic of this new design is presented in appendix D. This technique increases the accessible degrees of freedom and extends the mode–hop free tuning range. The ECDL's operating wavelength, 1086.60 nm, lies well within the amplification spectrum of the Yb fiber amplifier [59] and a mode–hop free tuning range of up to 90 GHz has been achieved. The radiation is delivered to the amplifier by a single mode patch fiber (PF). Prior to injecting the seed radiation into the Yb doped core of the fiber amplifier, two Faraday rotators (FR) and several beam splitter cubes (PBS) protect the ECDL from back propagating radiation and provide more

than 70 dB of isolation. An additional narrow band–pass filter (BP) suppresses spurious lasing between the laser diode and optics behind the fiber amplifier.

The fiber amplifier is operated in a single pass, forward pumping configuration and pumped by a fiber coupled pump diode (LIMO HLU32F400-976 [163]) at a wavelength of 976 nm using the cladding pump technique [55]. A dichroic mirror (DM) injects the pump radiation into the Yb doped double clad fiber. The Yb fiber has a length of 9.4 m, a core diameter of 10.1 µm and a D-shaped inner cladding. The D-shaped inner cladding enhances the pump absorption [164]. It has a diameter of 400 µm and a numeric aperture (NA) of 0.38. The 1000 ppm Yb^{3+} doped core has a very low NA of 0.07 and provides single-mode operation. Both fiber ends are connectorized in-house using standard high power SMA connectors with an 8° polish to avoid spurious lasing. An aperture (A) together with an additional highpass filter (ASE) cut the pump radiation and block amplified spontaneous emission from the output beam of the fiber amplifier. Subsequent to amplification, quarter– and half–waveplate retarders ($\lambda/4$, $\lambda/2$) adjust the polarization of the laser beam, which is aligned by a telescope (L1,L2) through the nonlinear crystal (KTP), where the frequency conversion takes place [73, 155, 156]. A nonlinear type II process within the $3\times3\times15$ mm^3 Potassium titanyl phosphate crystal (KTP crystal) is advantageous for the second harmonic generation [165]. KTP allows non critical phase matching at a temperature of 313.3°C, which offers a high output yield [166]. The second harmonic is separated by dielectric mirrors (HR-IR, HR-VIS) from the fundamental, which is used for additional beam diagnostics. Finally, the green probe laser beam is aligned with the ESFADOF experimental setup.

Behind the last dielectric mirror an additional photodiode (PD0) is placed, which monitors the green leak light. Its signal is used to control the pump intensity of the fiber amplifier. Thus, the intensity variation of the ECDL, which occurs due to the tuning, can be eliminated from the measurement. In order for this procedure to work, the fiber amplifier has to be seeded below the saturation limit. From the 1000 ppm Yb^{3+} doping of the fiber, the 2.35 mW of injected seed power extract up to 2.8 W of 1086.60 nm cw radiation from the 24 W launched pump power. This represents an amplification of 30.8 dB. After single pass frequency conversion, 3 mW of green laser light at 543.30 nm is available for experiments. In fact, for the ESFADOF transmission measurements 100 µW of green laser light are sufficient.

A wavelength meter (HighFinesse Ångstrom WS 7) and a low and a high finesse Fabry-Perot interferometer allow accurate frequency diagnostics. The wavelength meter monitors the frequency of the ECDL while adjusting the frequency range of the scan. During the ESFADOF measurements it is used for other purposes (see section 4.3 for details). The low finesse Fabry-Perot interferometer (LF-FPI) together with PD1 detects the position of potential mode–hops, whereas the high finesse Fabry-Perot interferometer (HF-FPI) and the photomultiplier tube (PMT) deliver frequency markers. Both signals are recorded permanently during all measurements and allow a reliable mode-hop detection as well as an accu-

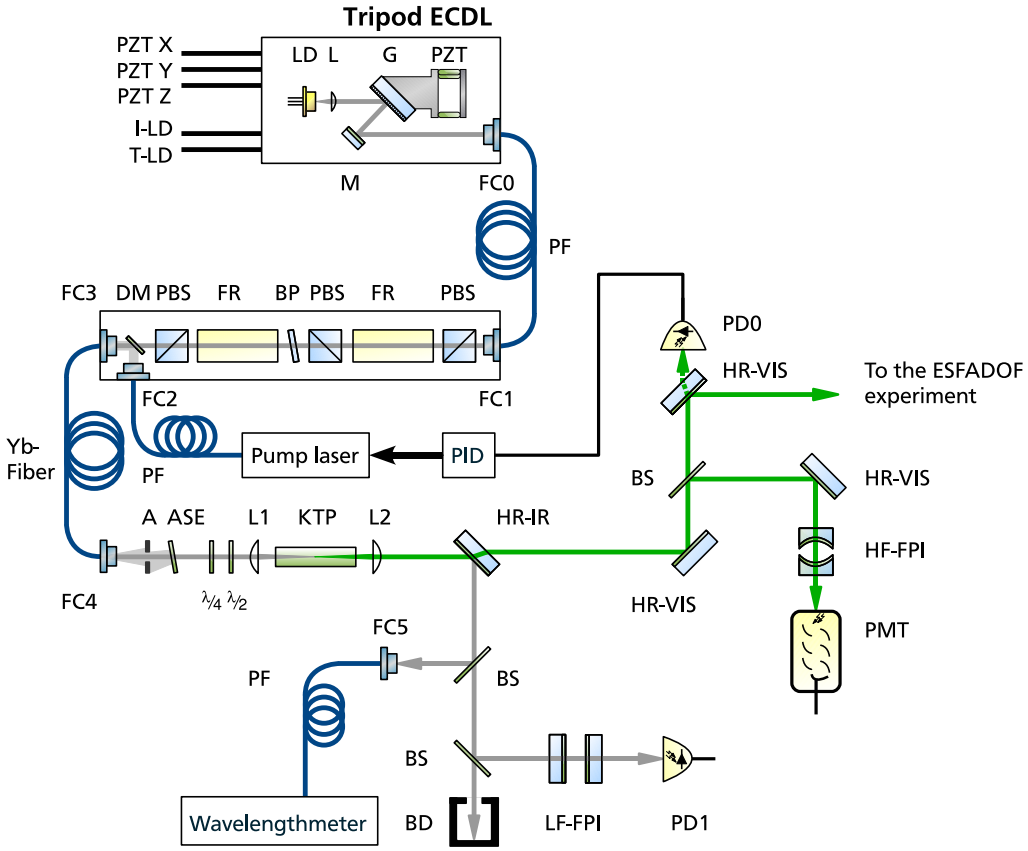

Fig. 4.3: Probe laser setup, together with several beam diagnostics (see text for details); with kind permission from Springer Science+Business Media [93]: Tripod external cavity diode laser (ECDL), piezo mechanic transducers (PZT), laser diode (LD), lenses (L,L1-2), grating (G), mirrors (M,HR-IR,HR-VIS), fiber couples (FC0-5), patch fibers (PF), polarizing beam splitter cubes (PBS), Faraday rotators (FR), band–pass filter (BP), dichroic mirror (DM), aperture (A), highpass filter (ASE), quarter and half waveplate retarders ($\lambda/4$,$\lambda/2$), nonlinear crystal (KTP), beam samplers (BS), beam dump (BD), low and high finesse Fabry-Perot interferometers (LF-FPI, HF-FPI), photodiodes (PD0-1), photo multiplier tube (PMT), closed–loop electronics (PID).

rate linearization of the frequency axis. In particular, the nonlinear elongation of the ECDL piezos result in a nonlinear wavelength change of the emitted radiation, while scanning the ECDL. By a nonlinear fit to the frequency markers, a linearization of the frequency scale can be achieved. The employed HF-FPI has a finesse of $>$300 and a free spectral range of FSR=1 GHz, which guarantees a relative frequency accuracy of at least 3.3 MHz. Sec. 4.4 elaborates this procedure towards an accurate and absolute frequency scale further.

4.3 Measurement Unit

The ESFADOF experimental setup is depicted in Fig. 4.4. It consists of the ESFADOF itself, marked by the broken line, a reference Rb vapor cell, which is used for frequency calibration purposes, and two pump lasers, which populate the lower ESFADOF state. The Rb vapor cells are mounted within custom made ovens equipped with heat pipes, which control the temperature and the number density of the Rb vapor. The 543 nm probe laser is provided by the frequency doubled Yb doped fiber amplifier, which was described in the previous section (cf. Fig. 4.3). By scanning the probe laser frequency, the photodiodes PD3–5 simultaneously record the transmission spectra of the ESFADOF device and the reference cell. A dielectric mirror (HR-IR) separates the green probe beam from the infrared leakage and sends it back into the cell.

The polarizer (P) and the analyzer (A) of Fig. 3.1 correspond to PBS-P and PBS-A, respectively. As discussed in Sec. 4.1, the magnetic field **B**, needed for FADOF operation, is provided by high temperature permanent ring magnets. Since the high magnetic field in the ESFADOF cell shifts the atomic levels considerably, it is advantageous to uncouple the pump processes of both cells employing two separate laser systems. This allows the independent selection of intensity, frequency and polarization for both pump beams. The reference cell is held constantly at a cell temperature of $T_{Ref} = 170^{\circ}$C and pumped by an ECDL providing 60 mW radiation around 780 nm. The operating wavelength has been 1 GHz red shifted from the center of the D2 transition by adjusting the operating temperature, the injection current and the piezo voltage of the ECDL. Thus, only the ^{85}Rb isotope has been excited (cf. appendix. A). Once appropriate values have been found, they are held constant by the employed electronics. An additional locking mechanism is not required, due to the negligible drift of the ECDL's emitted wavelength. The frequency jitter of the ECDL around its central operating frequency does not exceed 20 MHz during several hours.

The ESFADOF pump laser consists of an identical ECDL, whose emitted radiation is amplified by a tapered amplifier (TA) up to 500 mW. [96–99]. Two Faraday isolators (PBS,FR,PBS), placed in front of the ECDL and the tapered amplifier, provide isolation against unwanted back reflections. Photodiode PD2 is used to monitor the injected pump intensity. The effective beam diameters of the pump and the probe beam have been measured to not extend w_{Pump}=383(5) μm and w_{Probe}=233(5) μm over the whole ESFADOF setup (cf. Fig. 4.5) respectively. Pump and probe beam have been carefully overlapped and a wavelength meter

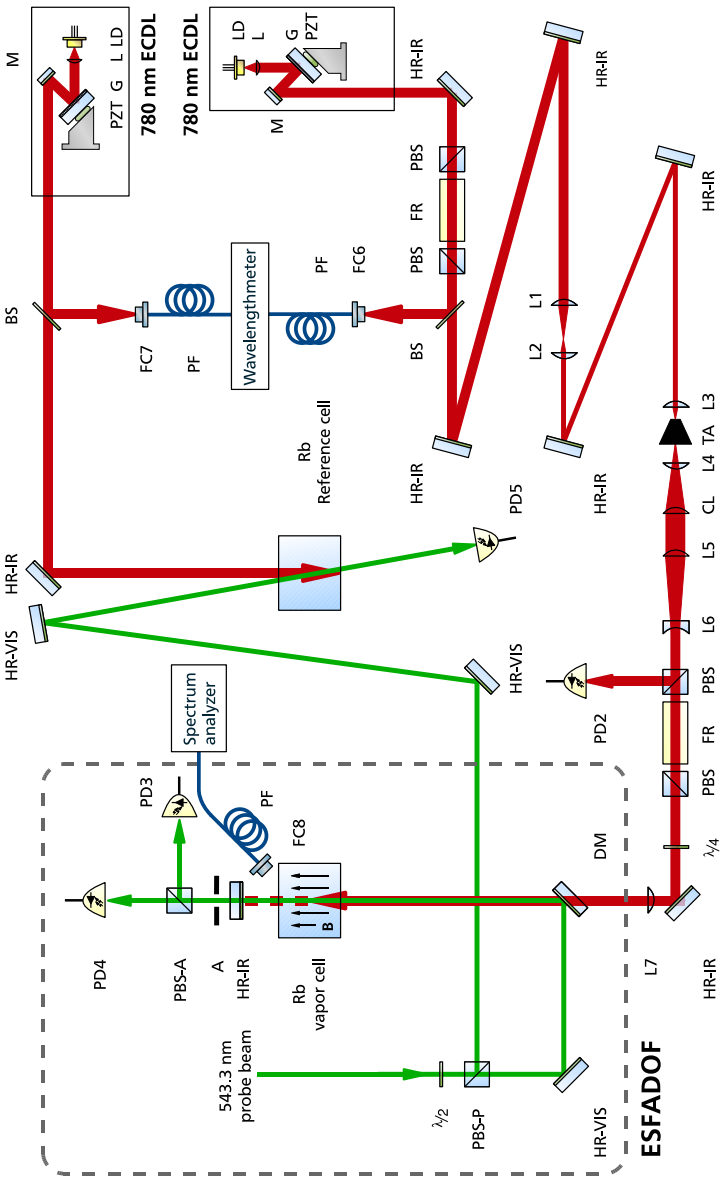

Fig. 4.4: Experimental setup of the ESFADOF experiment; with kind permission from Springer Science+Business Media [93]: Permanent ring magnets in front of the ESFADOF vapor cell provide a constant magnetic field (**B**). The additional reference cell allows an absolute calibration of the frequency scale. Two 780 nm ECDLs pump both vapor cells independently. The ESFADOF pump beam is amplified up to 500 mW by a tapered amplifier (TA) and shaped by appropriate optics (L4-L7; the cylindrical lens CL accounts for the TA slit profile). Two Faraday isolators (PBS, FR, PBS) uncouple the ESFADOF pump laser diode from back propagating radiation. A wavelength meter measures the emission wavelength of the pump lasers. The 543 nm probe laser radiation is provided by the frequency doubled Yb doped fiber amplifier setup depicted in Fig. 4.3.

monitors the pump laser wavelengths. In the following only the injected pump powers will be quoted. The corresponding pump intensities can be computed by relating these powers to the measured cross section of the pump laser.

In contrast to the pump ECDL of the reference cell, this one is connected through a custom *feed forward* electronic device to an additional frequency generator. The *feed forward* electronics allow for a mode–hop free frequency scan of the ECDL by establishing a linear dependency between the injection current and the piezo voltage, while simultaneously inducing a phase shift of π between both entities [94, 162]. In order to systematically investgate the influence of all accessible experimental parameters on the transmission spectrum of the ESFADOF device, two operational schemes of its pump ECDL have been employed:

1. **Fixed pump wavelength scheme:** Among all other experimental parameters the frequency detuning of the pump ECDL with respect to the $5S_{1/2} \rightarrow 5P_{3/2}$ transition center is a very important parameter. Hence it has to be held fixed when investigating the influence of all other parameters. The ECDL's temperature and injection current have been appropriately tuned in order to operate on the $5S_{1/2} \rightarrow 5P_{3/2}$ transition. In addition, a fine tuning of the operating wavelength within the ECDL's mode–hop free tuning range is achieved by adjusting the flat-top output voltage of the frequency generator. This defines via the *feed forward* device the ECDL's injection current and piezo voltage simultaneously. Again, this scheme benefits from the robust setup of the employed ECDL design, so that no additional locking mechanism is required.
2. **Scanning the pump wavelength scheme:** Complementary to scheme 1, all other experimental parameters are held fixed when scanning the wavelength of the ESFADOF pump laser. A mode–hop free tuning of the laser wavelength is achieved by changing the output voltage of the frequency generator to a sawtooth shape, which drives the ECDL injection current and the piezo voltage simultaneously through the same *feed forward* device [94]. The frequency scan of the pump ECDL is monitored permanently by feeding the output voltage of the frequency generator, U_{FG}, to the A/D-card of the measurement electronics, while simultaneously recording the output of the wavelength meter. A correlation between both entities is always possible as long as the turning points have been recorded. This task, together with the linearization of the frequency scale is carried out by the post-processing software (cf. Sec. 4.4).

4.4 Data Acquisition and Evaluation

The described setup allows for precise measurements of the transmission spectra of the ESFADOF device. A spectrum is achieved by simultaneously tuning the injection current and the piezo voltages of the tripod ECDL seeding the fiber amplifier by two identical computer controlled 16 bit D/A- and A/D-converters [167]. Each D/A- and A/D-converter offers two output channels and 64 input channels. Programmed by a custom developed LabVIEW interface they have been configured to work synchronously in order to control the experimental setup and record

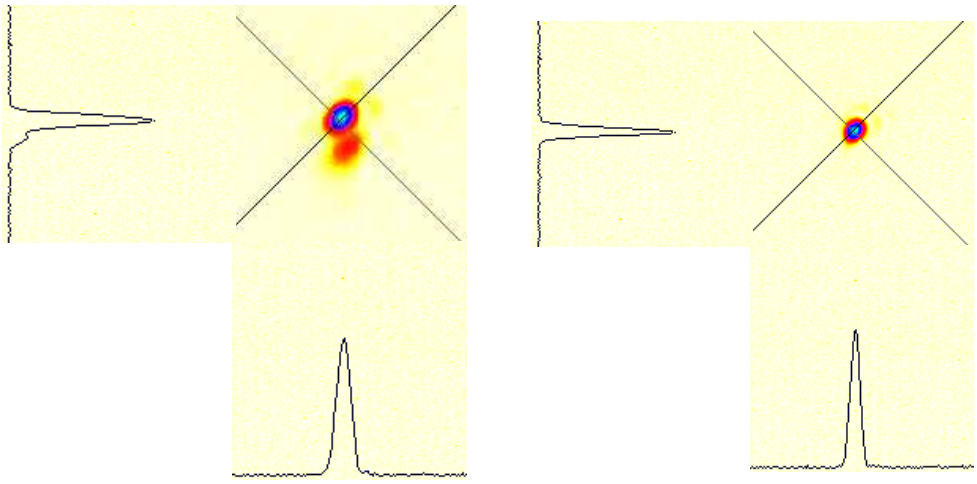

(a) Pump beam: w_{Pump}=383(5) µm. (b) Probe beam: w_{Probe}=233(5) µm.

Fig. 4.5: Beamprofiles of the pump and probe beams along the symmetry axis of the vapor cell. The quoted values correspond to the effective diameter.

all relevant data. Mode-hop free scanning is established using similar techniques to those described in Refs. [94, 162]. An additional *feed forward* electronic device is not required, as each signal can be controlled independently by the D/A-converter. Specifically, the following information is provided (cf. Fig. 4.3 and Fig. 4.4):

Output

PZT X: Modulation of the tripod ECDL's X piezo.

PZT Y: Modulation of the tripod ECDL's Y piezo.

PZT Z: Modulation of the tripod ECDL's Z piezo.

I-LD: Superimposed modulation to the tripod ECDL's injection current.

Input

PD1: The transmission signal of the low finesse etalon (LF-FPI) provides a very sensitive mode-hop indicator. Each mode-hop results in an discontinuous signal due to the accompanied phase shift of the low finesse transmission and enables the localization of the mode-hops. Although, mode-hop free scanning is established, the signal of PD1 is recorded permanently and delivers an unambiguous indicator. This enables to autonomously extract possible mode–hops from the measurement without any interaction during the post-processing.

PMT: The transmission signal of the high finesse etalon (HF-FPI) provides frequency markers at intervals of its FSR of 1 GHz providing the means to establish a linear frequency scale despite the nonlinear behavior of the piezo elongations (cf. Sec. 4.2).

PD2: The intensity of the ESFADOF pump laser.

PD3: The transmitted intensity of the ESFADOF, polarized perpendicularly to the entrance polarizer PBS-P.

PD4: The transmitted intensity of the ESFADOF, polarized parallel to the entrance polarizer PBS-P.

PD5: The transmission signal of the reference cell. In addition to the frequency markers, which provide only a relative frequency axis, this signal maps the data to an absolute scale. For that purpose, a Voigt profile on the underlying hyperfine structure of the $5P_{3/2} \rightarrow 8D_{5/2}$ transition is fitted to the data.

$U_{ESFADOF}$: Monitor output voltage of the ESFADOF temperature controller. The signal is proportional to the temperature of the ESFADOF vapor cell (not depicted).

U_{Ref}: Monitor output voltage of the reference cell temperature controller. The signal is proportional to the reference cell temperature (not depicted).

U_{FG}: Output voltage of the frequency generator, which drives the ESFADOF pump laser frequency (not depicted).

All signals are amplified if necessary and uncoupled from the D/A- and A/D-converters by custom made electronics. Each A/D-converter allows a maximum sample rate of R_{DAQ}=100k samples/s while multiplexing the channels [167]. The frequency span of the probe laser has been tuned in order to cover 30 GHz, such that the ESFADOF transmission spectrum can be fully resolved with high spectral accuracy by applying a saw-tooth signal to the tripod ECDL's injection current and driving piezos. A record consists of 40 000 data samples per channel accumulated within 2.5 seconds. The applied saw-tooth signal shape offers a rising ramp within 36 000 data samples, which potentially guarantees sub-MHz sampling of the ESFADOF transmission along a frequency span of 30 GHz. However, the achieved spectral resolution is determined by the linewidth of the probe laser, which is measured by the spectral width of the etalon-markers (cf. Sec. 4.4.1).

As mentioned above, the closed-loop control of the fiber amplifier intensity locks the probe laser intensity to a certain value, so that the absolute transmission of the ESFADOF can be computed from the signals of PD3 and PD4. This allows to account directly for all Fresnel losses and for the different transmissions and reflections of the employed polarizing beam splitter cubes. Sec. 4.4.3 addresses this subject in more detail. However, the locking-technique is limited to the dynamics of the whole signal chain, which comprises in particular the pump laser of the fiber amplifier and the fiber amplifier itself (cf. Fig. 4.3). The smallest bandwidth within this chain is the pump laser of the fiber amplifier. Its driver electronics offer a modulation bandwith of $\Gamma_{\text{FA-Pump}} = 5$ kHz only and defines the achievable accuracy [163]. This can be understood as an additional lowpass filter inside the locking chain, which considerably restricts the locking mechanism: Thus, responses beyond the intrinsic modulation bandwidth are not possible and steep intensity fluctuations of the probe laser result in a damped response, but are not fully surpressed. This is of particular interest, as fiber amplifiers are well

known for their intensity and polarization fluctuations [168], which require sophisticated setups in order to guarantee an intrinsic compensation [169]. In the present case any fluctuation of the fiber amplifier's output polarization influences also the intensity of the second harmonic, which adds another noise source to the probe laser intensity.

Nevertheless, a transmission accuracy of approx. 3% has been achieved when recording a single spectrum by applying the locking technique (cf. Fig. 4.8a). Considerably higher accuracies are possible. This requires a more sophisticated averaging procedure along the calibrated frequency axis. Sec. 4.4.2 addresses this technique and Sec. 4.4.3 discusses the achieved accuracies. Briefly speaking, the measurement procedure can be summarized for both operation schemes of the ESFADOF pump ECDL as follows (cf. also Sec. 4.3):

1. **Fixed pump wavelength scheme:** The influence of all other experimental parameters has been recorded by changing the parameter values individually and discretely. For a fixed parameter combination a measurement set of 200 individual data sets has been recorded. Afterwards all individual data sets have been frequency calibrated by the post-processing software prior to averaging. In contrast to the pump ECDL, the tripod ECDL, which defines the wavelength of the probe beam, shows a much larger sensitivity to thermal changes of its surroundings. Hence, it is mandatory to perform the averaging procedure along an absolute frequency scale in order to account for long–term frequency drifts of the probe laser. Drifts of several hundred MHz within a few hours accompanied with mode–hops around the turning points of the saw-tooth signal have been observed in the worst case. These drifts are driven thermally. However, averaging on an absolute frequency scale discards any influence of possible frequency drifts and increases the accuracy of the ESFADOF transmission spectra by at least one order of magnitude. The transmission accuracy after averaging is governed by electrical and intrinsic noise. Averaging more than 200 data sets does not increase the accuracy any further.
2. **Scanning the pump wavelength scheme:** As described above, this scheme holds all other experimental parameters constant, while continuously changing the wavelength of the ESFADOF pump laser. For that purpose a saw-tooth signal has been applied to the scanning piezo of the ECDL, while accordingly modulating its injection current. The period of the saw-tooth signal is set to 10^{-4} Hz, such that the rising ramp of the saw-tooth signal induces a frequency change of about 15 GHz within 8750 s. In other words, these values correspond to a frequency change of 1.7 MHz/s or 4.3 MHz per ESFADOF spectrum (one spectrum takes 2.5 s), which is fairly negligible compared to the maximum encountered frequency jitter of 20 MHz of the ESFADOF pump laser. Thus, 3 500 individual spectra have been accumulated within 8750 s. They reflect the ESFADOF transmission change, while scanning the frequency of the pump laser. In addition, the driving voltage of the frequency generator U_{FG} as well as the current pump laser wavelength are monitored permanently during the measurement process by the A/D-card and the controlling computer respectively. This enables the post-processing software to correlate the

emission wavelength of the ESFADOF pump laser (measured by the wavelength meter) with U_{FG} and hence to assign a measured emission wavelength to each individual data set. The long scanning periode has been chosen in order to allow for an additional averaging procedure, which, similar to scheme 1, increases, the accuracy of the ESFADOF spectra. However, due to the continuous frequency change, a more sophisticated post-processing is required. First of all, each individual data set has to be equipped with absolute frequency scales. This is achieved by the same procedure as it has been the case for scheme 1. The subsequent averaging procedure employs the same techniques in averaging the spectra on the absolute frequency scale, but in contrast to scheme 1, establishes a running averages scheme along the slow frequency change of the pump laser. For that purpose, 58 subsets have been extracted from the entire measurement set. Each subset consists of 120 individual data sets. They cover a frequency span of approx. 250 MHz and overlap with the neighboring sub sets by approx. 125 MHz. Each subset is individually averaged and the corresponding mean pump frequency is assigned to the averaged spectra. This procedure corresponds to a running averages scheme evaluated only on fixed positions along the pump frequency scale.

4.4.1 Assigning an Absolute Frequency Scale

Fig. 4.6 shows a schematic flow chart of the frequency calibration process. The following substeps have been implemented as LabVIEW programs:

1. **Mode–hop detection:** As mentioned above, the thermal drift of the probe laser electronics causes a frequency drift of the tripod ECDL and eventually results in mode–hops near the turning points of the scan ramp. Discontinuities in the transmission spectrum of the low-finesse etalon, measured by PD1, reflect the position of potential mode–hops and as long as these occur near the turning points of the scan ramp it is possible to extract them from the data set; otherwise the data set has to be discarded from the measurement set. The first derivative of the PD1 signal allows to detect potential mode–hops and subsequently extract their positions autonomously by the post-processing software. A region of interest (ROI) is defined as 3 times the full width half maximum (FWHM) of the absorption signal of the reference cell, measured by PD5. Whenever mode–hops lie within this ROI or a ROI can not be defined the whole data set has to be discarded; otherwise a mode–hop free subset from the data set is extracted and processed further.

2. **Etalon fit:** The time dependent transmission of the high finesse etalon, PMT(t), can be represented by

$$\mathrm{PMT(t)} = \mathrm{a_0} + \frac{\mathrm{a_1 P_{Amp}(t)}}{1 + \frac{4\mathrm{R}}{(1-\mathrm{R})^2}\sin^2\left(\pi\frac{\nu(\mathrm{t})}{\mathrm{FSR}}\right)}, \tag{4.1}$$

where FSR=1 GHz represents the free spectral range of the high finesse etalon, a_0 a constant baseline, R the mirror reflectivity and a_1 the maximum amplitude of the transmission peaks. By setting $P_{Amp}(t) = P^0_{Amp} + P^1_{Amp}\,t$, a linear

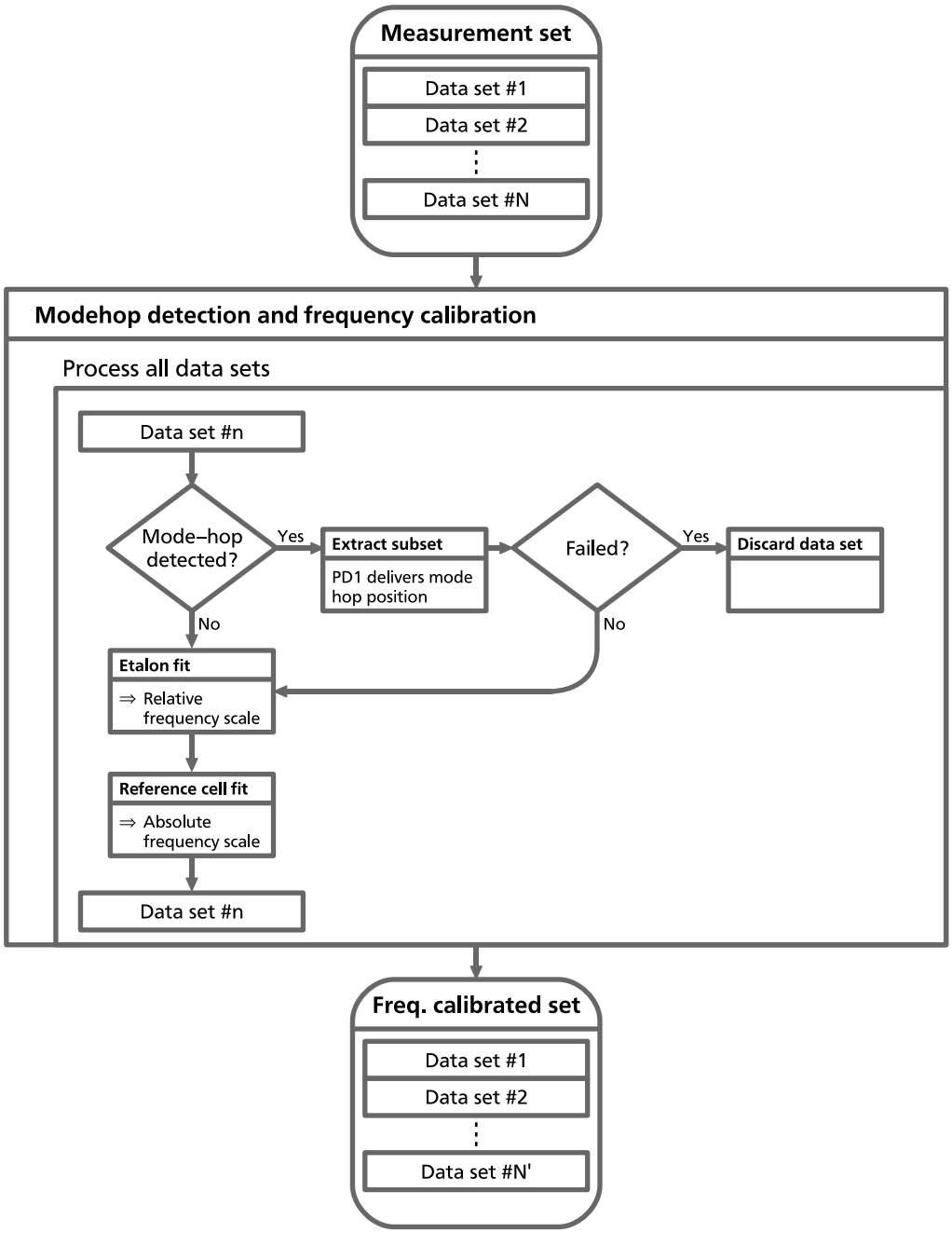

Fig. 4.6: Schematic flowchart of the mode–hop extraction and frequency scale calibration: An absolute frequency scale is attached to each data set of an entire measurement set. The region of interest (ROI) is defined as 3 times the full width half maximum (FWHM) of the reference cell spectrum along the time axis. A data set is discarded, whenever a mode–hop lies within the ROI; otherwise a mode–hop free subset is extracted and processed further. This procedure takes approx. 2.5 min. for each individual data set on a standard personal computer.

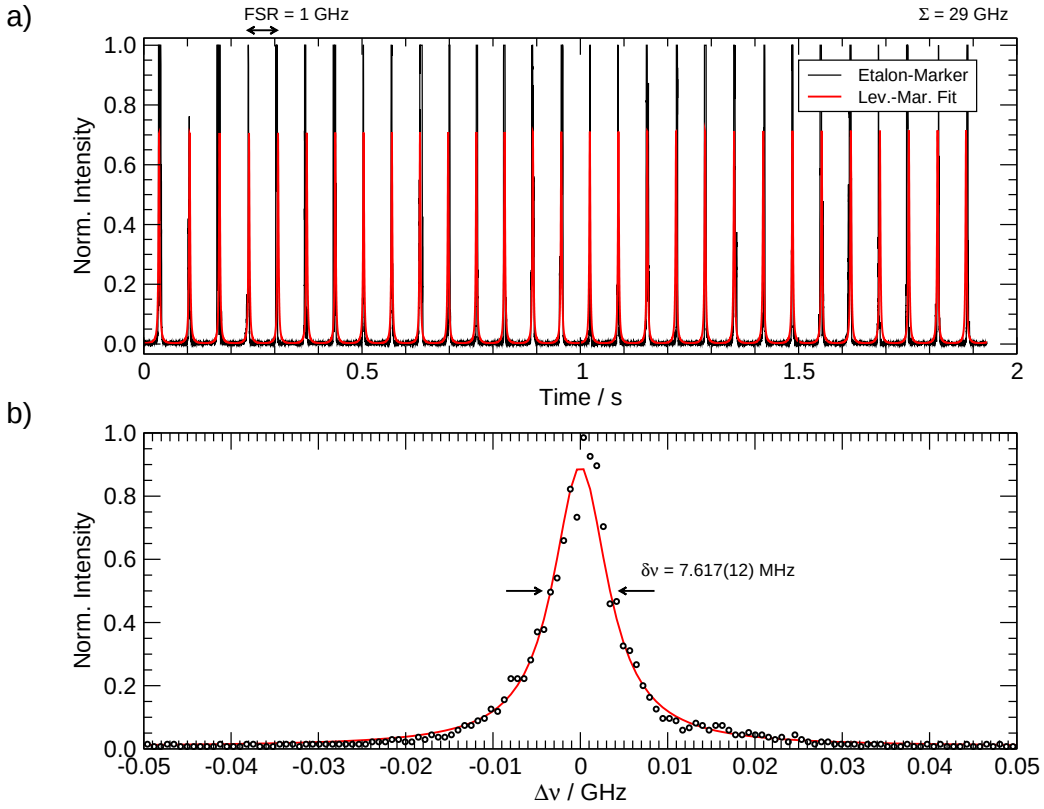

Fig. 4.7: a) By fitting Eq. 4.1 to the time dependent PMT signal a linear frequency scale is obtained: The presented data span a frequency range of 29 GHz. The peak distances change, due to the nonlinear piezo elongation. The agreement between fit and data is excellent. As the second peak shows, a large number of samples is required in order to fully resolve the interference fringes. Any undersampling leads to information loss. b) Spectral width of the probe laser: The data have been measured in keeping the frequency of the probe laser constant, while scanning the mirror spacing of the high finesse Fabry-Perot interferometer by a piezo electric transducer. Although only a close-up of one peak is depicted several others have been measured within one scan, such that Eq. 4.1 and the fitting procedure apply as well.

intensity change is incorporated into the model. This feature has been implemented for compatibility reasons. The fact that a mode–hop free scanning of the ECDLs wavelength requires a linear modulation of its injection current, leads to a corresponding linear modulation of the laser intensity, which is also reflected by the transmission of the interferometer. However, as the intensity of the probe laser has been locked, this feature becomes obsolete for the present case. $\nu(\mathrm{t})$ is the relative frequency change of the probe laser and represents the linear frequency axis of the measurement. A polynomial expansion of the frequency change $\nu(\mathrm{t})$ with respect to the time variable accounts for the nonlinear piezo elongations:

$$\nu(\mathrm{t}) = \sum_{\mathrm{i}=0}^{\mathrm{N}_\nu} \mathrm{p_i t^i} = \mathrm{n(t)\,FSR}. \tag{4.2}$$

The right–hand side relates this expression to the free spectral range (FSR) of the interferometer. Truncating the polynomial after the 3^{rd} order ($\mathrm{N}_\nu = 3$) is accurate enough for a tuning range of approx. 30 GHz. Longer elongations might require higher polynomial orders. By employing a Levenberg-Marquardt algorithm [137], Eq. 4.1 is fitted to the time dependent PMT signal and the frequency scale, $\nu(\mathrm{t})$, is extracted from the etalon markers. The fitting procedure can be optimized by excluding the baseline. This is achieved by extracting and proceeding only data samples within a region of interest around each individual interference fringe of the PMT signal. However, the iterative Levenberg-Marquardt algorithm requires appropriate start parameters in order to converge to a satisfying result within reasonable time. This is of particular importance in order to circumvent the periodic δ-function–like behavior of Eq. 4.1, which leads to nonscientific solutions, when choosing the wrong start parameters. Appropriate start parameters are estimated by an additional program prior to fitting. This program extracts the peak amplitudes, $\mathrm{A_k}$, and locations, $\mathrm{t_k}$, from the PMT(t) signal. These pairs allow to fit $\mathrm{P_{Amp}(t)}$ to the amplitude information, which extracts $\mathrm{P^0_{Amp}}$ and $\mathrm{P^1_{Amp}}$ from the data. In addition Eq. 4.2 is fitted to the peak locations. This already results in a very good estimation of its polynomial coefficients:

$$\sum_{\mathrm{i}=0}^{\mathrm{N}_\nu} \mathrm{p_i t_k^i} = \mathrm{k\,FSR}. \tag{4.3}$$

The baseline, $\mathrm{a_0}$, as well as the peak amplitude $\mathrm{a_1}$ are also estimated from the data. The start parameter of the reflectivity, R, is set to 99.99%, as the Levenberg-Marquardt algorithm always changes this term to more reasonable values. Subsequently to this estimation, the following fit parameters are passed to the Levenberg-Marquardt algorithm: $\mathrm{a_0}$, $\mathrm{a_1}$, R and $\mathrm{p_i}$. Fig. 4.7a compares the result of a successful fit, computed from Eq. 4.1, with some sample data. After each fit a linear frequency scale is computed from Eq. 4.2 and attached to the data set. The fit rapidly converges due to the appropriate parameter estimation and is therefore superior to the former employed evolutionary algorithm [21]. However, care has to be taken in order to resolve the etalon

fringes adequately. An undersampling of the peak structure leads to beating effects between the periodicity of the interferometer and the sampling rate of the A/D-converter and eventually to the loss of interference fringes. Hence, the data acquisition requires a reasonable high resolution along the time axis in order to resolve these fringes.

In order to estimate the minimum required resolution it is useful to evaluate the spectral width of the probe laser. The emission wavelength of the probe laser has been held constant for this purpose, while simultaneously scanning the mirror spacing of the high finesse Fabry-Perot interferometer and recording the PMT signal. By covering several free spectral ranges of the interferometer Eq. 4.1 can be applied too and the same nonlinear fit procedure extracts via

$$\frac{\mathrm{FSR}}{\delta\nu} = \frac{\pi\sqrt{\mathrm{R}}}{\text{1-R}} \tag{4.4}$$

a spectral width of $\delta\nu = 7.617(12)$ MHz from the data. Fig. 4.7b shows a close-up of an interference fringe obtained by this procedure. As a rule of thumb, the parameter estimation procedure requires at least 9 data points per interference fringe in order to deliver reliable results. Hence, an overall spectral width of 30 GHz requires at least 36 000 data samples in order to resolve the quoted spectral width of the probe laser, which explains the above introduced number of data samples. In addition, the above quoted value defines the accuracy of the relative frequency scale.

3. Reference cell fit: An absolute frequency scale is obtained by fitting a Voigt-profile to the absorption spectrum of the reference cell. Again, a reduction of the available data samples saves computational time and makes the procedure more efficient, without affecting the achievable accuracy. For that purpose, it is useful to define a region of interest (ROI) around the absorption dip of the reference cell spectrum. This ROI covers a span of 3 times the full width half maximum (FWHM) of the dip along the time axis and is fully sufficient for an accurate fit.

The relative frequency scale is transformed into an absolute scale by including an additional frequency shift, $\Delta\nu_{\mathrm{Ref}}$, to the Voigt-profile. According to Sec. 3.5, the following fit parameters have been included: The vapor cell temperature $\mathrm{T_{Cell}}$ and the mentioned frequency shift $\Delta\nu_{\mathrm{Ref}}$. The fit algorithm omits the direct simulation of the pumping process, as it does not affect the exact location of the transmission center. It is rather more convenient to extract the minimum transmission amplitude from the data and to equally distribute the population of the $5\mathrm{P}_{3/2}$ state on all its sublevels. This procedure is fairly reasonable due to the broad absorption spectrum of the $5\mathrm{S}_{1/2} \rightarrow 5\mathrm{P}_{3/2}$ pump transition at the employed high vapor temperature of $\mathrm{T_{Ref}}$=170°C, in combination with the frequency redistribution of the radiation trapping process [139]. In addition, the probe laser beam probes only a small volume near the entry window of the pump beam (cf. Fig. 4.4), where these assumptions are valid. This procedure keeps the computational efforts to a reasonable amount, in particular as it is mandatory to account for the underlying hyperfine-structure of

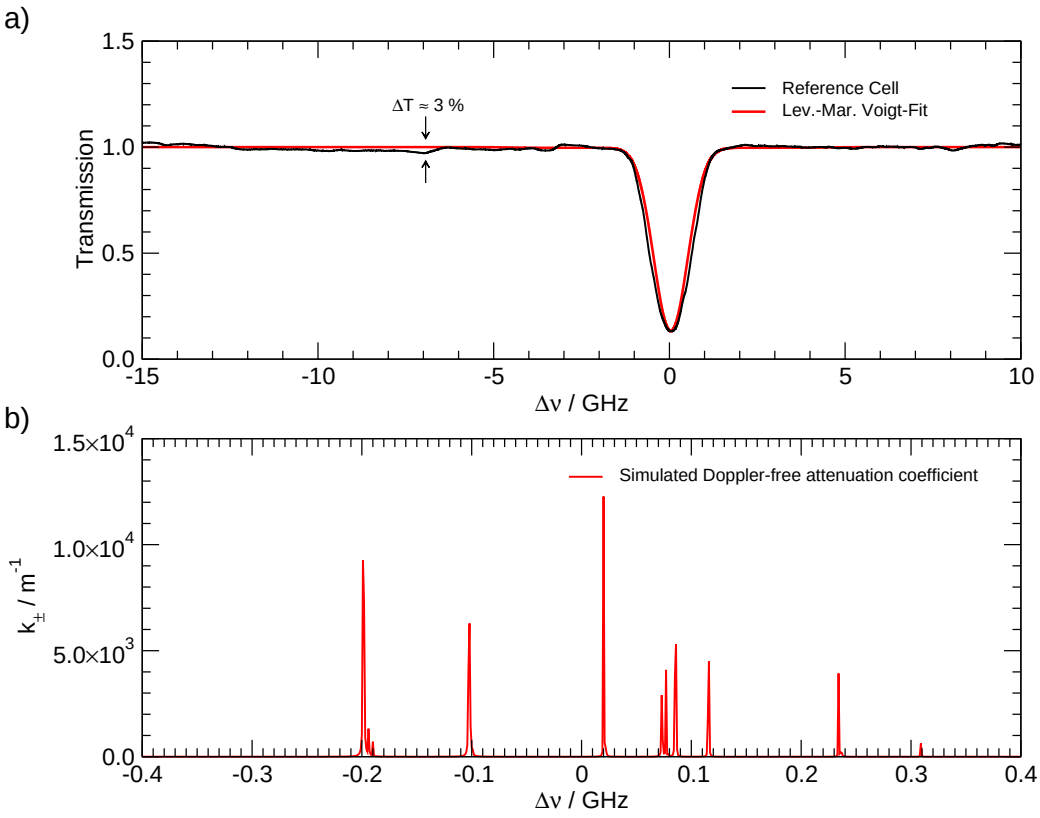

Fig. 4.8: a) Transmission spectrum of the reference cell: By fitting a Voigt-profile to the data, an absolute frequency scale is obtained. A value of $\Delta\nu_{\mathrm{Ref}}$=18.87(8) GHz has been fitted to the data in this particular case. The zero marks the center of the $5P_{3/2} \rightarrow 8D_{5/2}$ transition. The mentioned limitations on the achievable transmission accuracies of approx. 3%, when regarding only one single scan, are indicated in the plot. b) Simulated Doppler-free attenuation coefficient of the $5P_{3/2} \rightarrow 8D_{5/2}$ transition. The hyperfine-structure of this transition is clearly visible. It broadens the transmission spectrum by approx. 400 MHz and induces a slight asymmetry. This plot has been calculated by employing the framework of chapter 3. An equal distributed population of the $5P_{3/2}$ states at a cell temperature of $T_{\mathrm{Ref}} = 170°C$ has been assumed. Due to the frequency redistribution of the radiation trapping process, this assumption is reasonable [139].

the $5P_{3/2} \rightarrow 8D_{5/2}$ transition. As Fig. 4.8b suggests, the hyperfine structure broadens the transmission spectrum by approx. 400 MHz and introduces a small asymmetry to the absorption spectrum. Omitting these features introduces a systematic error to the absolute frequency scale. An overall accuracy of the absolute frequency scale of 60 MHz can be extracted from the data.

Particular care has been taken in order to keep the computational effort as small as possible. However, the described mode–hop extraction and frequency calibration procedure requires approx. 2.5 minutes of total computational time for each individual data set on a standard personal computer (4 GHz AMD processor). For a full measurement set, which comprises 200 individual spectra, the computational effort sums up to approx. 500 minutes. Thus, a systematic investigation of the influence of several experimental parameters results in several thousand individual data sets, which all have to be equipped with individual absolute frequency scales. This huge amount of data requires an extensive parallel post-processing in order to keep computational times to reasonable values. For that purpose a parallel computing scheme, which dispersed all spectra on 16 individual personal computers, has been implemented. This allowed to process the acquired data within two months of continuous operation.

4.4.2 Averaging Procedure

As it has been already discussed and as Fig. 4.8a indicates, the achievable maximum transmission accuracy of one single scan is limited to approx. 3% due to intensity fluctuations of the probe laser. Considerably higher accuracies can be obtained, by averaging several identical spectra on a calibrated frequency scale. An additional program performs this averaging procedure (cf. Fig. 4.9). It can be separated into the following sub-steps:

1. **Quality control and data reduction:** The frequency calibration procedure takes extensive care in order to deliver a good parameter estimation, such that the Levenberg-Marquardt algorithm rapidly converges and produces accurate results. However, errors can not be fully excluded and as the averaging procedure relies on an accurate frequency scale, it is mandatory to perform a quality control prior to averaging. For this purpose, the theoretical time dependent PMT signal is computed by inserting the result of the fit procedure into Eq. 4.1. This allows to extract the number of interference fringes from this simulated PMT signal and to compare it with the number extracted by the same procedure from the data set. Any discrepancies between both values lead to the dismission of the data set. In addition, the fit procedure might deliver the right number of interference fringes, but at the same time overestimate their spectral width by several factors. Such a result potentially leads to wrong positions of the interference fringes along the frequency scale, which is literally smeared out. Hence, each data set, whose spectral width extends the mean spectral width by at least a factor of two is discarded from the averaging procedure. All other data sets pass and define a common frequency scale. A

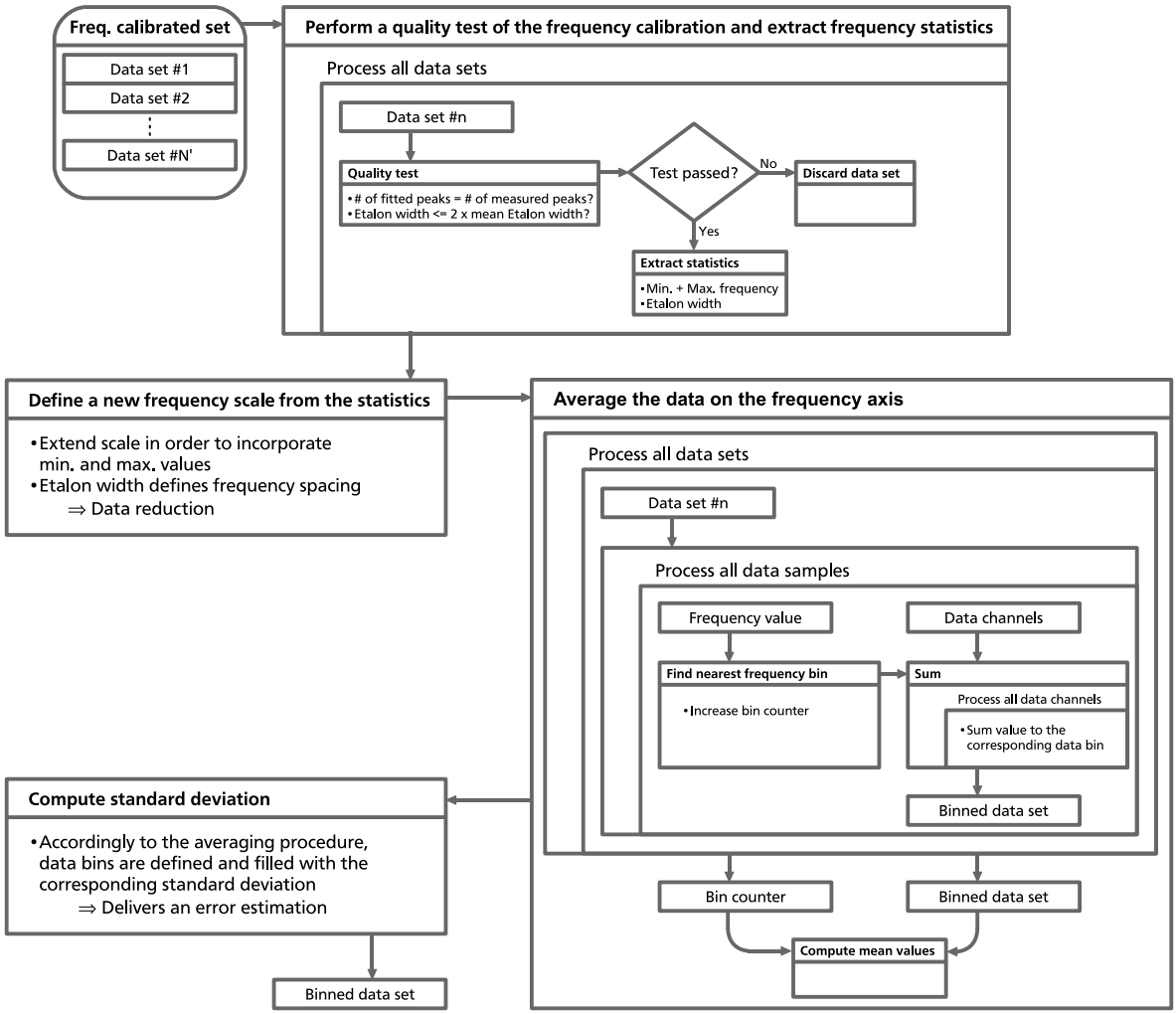

Fig. 4.9: Schematic flowchart of the averaging procedure: A quality control procedure selects the data sets and extracts statistical information, which allow the definition of an auxiliary frequency scale, upon which the averaging procedure acts. The mean value for each data channel and for each frequency value of this scale is computed from the entire frequency calibrated measurement set. A similar procedure also allows the computation of the frequency separated standard deviation of each channel, which allows to accurately estimate the ESFADOF transmission error.

data reduction without any information loss can be achieved in reducing the frequency spacing of this scale whith respect to the etalon width (cf. Eq. 4.4). In view of the obtained result, a frequency spacing of $\delta\nu/2$ is fairly reasonable and accounts for the minimum sample rate, which guarantees the best possible accuracy according to the Nyquist-Shannon theorem [170]. The adjusted frequency spacing reduces the data samples by a factor of 4 and allows to spectrally overlap two consecutive frequency bins. Based on this reduced frequency scale all, other data channels are mapped to similar bins upon which the averaging procedure operates.

2. **Averaging procedure:** The initialization takes the discussed reduced frequency scale and accordingly defines a binned data set, which comprises channels of the same length. They store the result during the averaging procedure. It can be separated into three loops: (1) The first loop processes all frequency calibrated data sets and passes the data to the inner loops of the procedure. (2) The second loop processes all data samples of the current frequency scale and maps the current value to the nearest frequency bin along the common frequency scale and increments the corresponding value of the bin counter array. (3) The third loop consecutively processes all data channels. It adds the data value, which corresponds to the current frequency, to the corresponding data bin, which is defined by the position of the current frequency bin. After processing all data sets, an average value within the binned data set is computed. For this purpose the data channels are processed separately. Each entry of each data channel is divided by its corresponding bin counter value, such that a frequency separated average over all data sets is obtained.
3. **Standard deviation:** A similar procedure extracts a frequency separated standard deviation. This allows to estimate the measurement error after averaging. This result is attached to the binned data set, which is saved separately.

4.4.3 ESFADOF Transmissions

The averaged intensity signals obtained of both output polarizations so far have to be processed further in order to achieve absolute transmissions. By taking advantage of the fact, that the employed setup allows to measure transmission spectra for both output polarizations beyond the influence of the ESFADOF device, it is possible to define the 100%-transmission level individually for each spectrum. This eliminates all additional influences intrinsically, which do not emerge from the Faraday-effect, like etaloning and Fresnel losses.

Let $\xi_{\mathrm{S}}(\Delta\nu)$ and $\xi_{\mathrm{P}}(\Delta\nu)$ denote the averaged signal amplitudes of PD3 (S-polarized ESFADOF spectra) and PD4 (P-polarized ESFADOF spectra) respectively, then the following factorization applies:

$$\xi_{\mathrm{S}}(\Delta\nu) = \kappa(\Delta\nu)\,\mathrm{T}_{\mathrm{S}}(\Delta\nu), \tag{4.5}$$

$$\xi_{\mathrm{P}}(\Delta\nu) = \kappa(\Delta\nu)\,\mathrm{T}_{\mathrm{P}}(\Delta\nu) \text{ and} \tag{4.6}$$

$$\kappa(\Delta\nu) = \kappa_{\mathrm{S}}(\Delta\nu) + \kappa_{\mathrm{P}}(\Delta\nu). \tag{4.7}$$

$T_S(\Delta\nu)$ and $T_P(\Delta\nu)$ represent the normalized S- and P-polarized transmission spectra of the ESFADOF device. The P-polarization is parallel to the entry polarization of the probe laser, whereas the S-polarization is perpendicular. $\kappa(\Delta\nu)$ is a frequency dependent normalization factor, which simultaneously accounts for the injected probe laser intensity and for frequency dependent etaloning, which emerges from interference effects between the facets of the vapor cell's window panes. Fig. 4.10 depicts a raw data sample and illustrates the following sub-steps, which finally lead to the deduction of the normalized ESFADOF transmission spectra. The resulting $T_S(\Delta\nu)$ and $T_P(\Delta\nu)$ will be presented in Fig. 4.11.

1. **Extraction of data outside the ESFADOF range:** Due to the fact, that the atomic $5P_{3/2} \rightarrow 8D_{5/2}$ transition scatters a considerable amount of photons off the probe laser beam, it is mandatory to define the 100%-transmission level from subsets of the transmission spectra, which are uninfluenced by the ESFADOF device. For that purpose, the subset, which contains the ESFADOF influence, has to be excluded from the normalization process. The subset extraction estimates the full width half maximum (FWHM) of the entire ESFADOF spectrum and increases this value by a factor of 3 in order to incorporate the whole ESFADOF spectrum. The resulting subsets $\xi^n_S(\Delta\nu)$ and $\xi^n_P(\Delta\nu)$ are indicated by the gray background in Fig. 4.10.
2. **Definition of 100% transmission:** The commercially purchased vapor cell I does not posses an antireflexion coating and shows unavoidable interference effects (etaloning), due to its parallel window panes. It is the most disturbing effect of the current setup and has to be taken into account in order to correctly define the 100% transmission level. These interference effects imprint periodic intensity modulations on the probe laser beam, while scanning its wavelength. In contrast, the tilted and tapered window panes of vapor cell II reduce this effect considerably. An estimation of the periodicity of these modulations can be obtained by inserting the width, d=1.3 mm, and the index of refraction, n=1.46 for 543 nm light [78], of the involved fused silica window panes into the relation of the free spectral range: FSR=$\frac{c}{2nd}$. This results in FSR=79 GHz, which considerably exceeds the scan-width of approx. 30 GHz. Therefore, it is sufficient to approximate this modulation by a polynomial expansion of second order:

$$\kappa_S(\Delta\nu) = \sum_{i=0}^{2} \kappa_i^S \, \Delta\nu^i \text{ and} \tag{4.8}$$

$$\kappa_P(\Delta\nu) = \sum_{i=0}^{2} \kappa_i^P \, \Delta\nu^i. \tag{4.9}$$

The expansion coefficients are obtained by a fit of Eqs. 4.8 and 4.9 to the uninfluenced subsets $\xi^n_S(\Delta\nu)$ and $\xi^n_P(\Delta\nu)$ respectively. The result allows an interpolation of $\kappa(\Delta\nu)$ within the subset, which contains the ESFADOF influence. This is indicated by the broken lines in Fig. 4.10. The non–vanishing $\kappa_S(\Delta\nu)$ reflects geometrical limitations of the setup ajustement. As it is impossible to fully parallelize both polarizing beam splitter cubes (PBS-P and

PBS-A in Fig. 4.4), a small angle, $\delta\phi$, between both polarization persists and leads to $\kappa_S(\Delta\nu) \neq 0$.

3. Normalization of the ESFADOF spectra: A normalization results by setting

$$\frac{\xi_S^n(\Delta\nu)}{\kappa(\Delta\nu)} + \frac{\xi_P^n(\Delta\nu)}{\kappa(\Delta\nu)} = T_S^n(\Delta\nu) + T_P^n(\Delta\nu) = 1 \tag{4.10}$$

and subsequent interpolation into the subset, which contains the ESFADOF influence:

$$T_S(\Delta\nu) = \frac{\xi_S(\Delta\nu)}{\kappa(\Delta\nu)} \text{ and}$$
$$T_P(\Delta\nu) = \frac{\xi_P(\Delta\nu)}{\kappa(\Delta\nu)}. \tag{4.11}$$

By applying this procedure Fig. 4.11 results. It shows the normalized ESFADOF transmissions, which correspond to the data of Fig. 4.10. This normalization procedure has been applied to all evaluated data sets. Subsequently, these sets have been bundled and examined by an additionally developed LabVIEW and Mathematica software package. This software extracts all relevant features, like peak positions, their transmission, the full width half maximum, the transmission at $\pm$7–8 GHz and many other parameters. The results of several measurements will be discussed in detail in chapter 5.

4.4.4 Estimation of the ESFADOF Transmission Errors

The subsequent computation of the standard deviation after averaging the measurement spectra allows an accurate error estimation of the ESFADOF transmissions. The lower part of Fig. 4.10 shows the corresponding standard deviations, which result after averaging the raw data. As the described normalization procedure applies to the standard deviation as well, these signals can be normalized accordingly, as depicted in the lower part of Fig. 4.11.

Let $\Delta\xi_S$ and $\Delta\xi_P$ denote the standard deviation of the averaged raw signals (cf. lower part of Fig. 4.10). Then, by applying the discussed normalization procedure, an error estimation of the normalized transmissions results:

$$\Delta\tilde{T}_{S,P} = \frac{\Delta\xi_{S,P}}{\kappa} \tag{4.12}$$

However, a thorough error estimation of the absolute transmission needs some further consideration. The normalization function κ is extracted from the measurements and contributes to the total measurement error:

$$\Delta T_{S,P} = \sqrt{\left|\partial_{\xi_{S,P}} T_{S,P}\, \Delta\xi_{S,P}\right|^2 + \left|\partial_\kappa T_{S,P}\, \Delta\kappa\right|^2} \text{ or}$$
$$= \sqrt{\left|\frac{1}{\kappa}\, \Delta\xi_{S,P}\right|^2 + \left|-\frac{\xi_{S,P}}{\kappa^2}\, \Delta\kappa\right|^2}. \tag{4.13}$$

Inserting Eqs. 4.11 and 4.12 into Eq. 4.13 results in

$$\Delta T_{S,P} = \sqrt{\left|\Delta\tilde{T}_{S,P}\right|^2 + \left|T_{S,P}\,\frac{\Delta\kappa}{\kappa}\right|^2}, \tag{4.14}$$

which allows an estimation of the maximum observed transmission error:

1. P-Polarized spectra: The fact, that $T_P \leq 1$ and $\frac{\Delta\kappa}{\kappa} \leq \Delta\tilde{T}_P$ results in the following upper limit for the error of the absolute P-polarized transmission:

$$\begin{aligned}\Delta T_P &\leq \sqrt{\left|\Delta\tilde{T}_P\right|^2 + \left|\Delta\tilde{T}_P\right|^2} \\ &\leq \sqrt{2}\,\max(\Delta\tilde{T}_P).\end{aligned} \tag{4.15}$$

2. S-Polarized spectra: As $T_S \ll 1$, it is more accurate to insert the maximum achieved transmission, $\max(T_S)$, while keeping $\frac{\Delta\kappa}{\kappa} \leq \Delta\tilde{T}_P$. Thus, the following upper limit for the error of the absolute S-polarized transmission results:

$$\Delta T_S \leq \sqrt{\left|\Delta\tilde{T}_S\right|^2 + \left|\max(T_S)\,\max(\Delta\tilde{T}_P)\right|^2}. \tag{4.16}$$

Fig. 4.11 shows typical values for $\Delta\tilde{T}_P$ and $\Delta\tilde{T}_S$. By inserting $\max(\Delta\tilde{T}_P) = 1.0 \times 10^{-3}$ and $\max(\Delta\tilde{T}_S) = 1.6 \times 10^{-4}$ into Eqs. 4.15 and 4.16, the following upper error estimations result:

$$\Delta T_P \leq 1.4 \times 10^{-3} \text{ and} \tag{4.17}$$

$$\Delta T_S \leq 2.3 \times 10^{-4}. \tag{4.18}$$

Within this thesis, all quoted transmission errors have been obtained by this procedure.

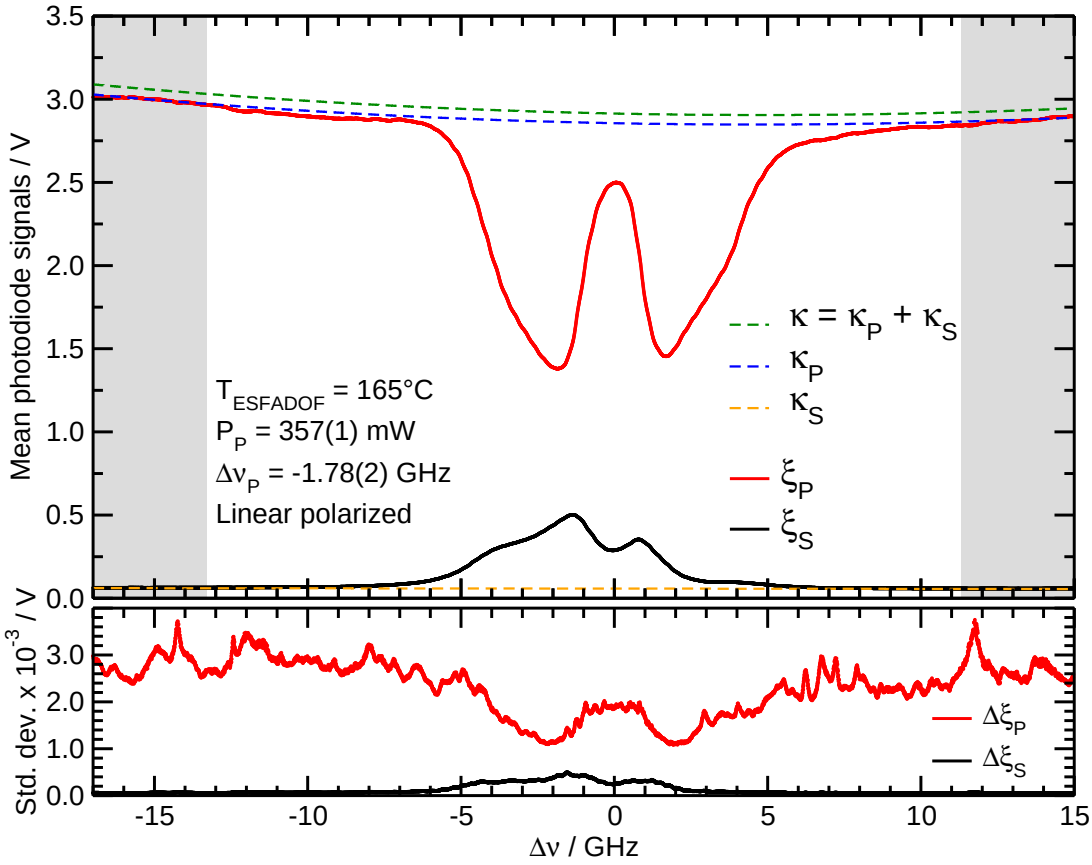

Fig. 4.10: Raw intensity signal of a measurement after averaging: The cell temperature was $T_{ESFADOF} = 165°C$, the linear polarized pump beam has been detuned by $\Delta\nu_p = -1.78(2)$ GHz and a pump power of $P_P = 357(1)$ mW has been injected into the cell. ξ_S and ξ_P denote the averaged signal amplitudes of PD3 and PD4 respectively. The gray background indicates the subsets, which are used for normalization purposes. A normalization is achieved by computing the sum of both output polarizations within these subsets, while taking additional etaloning effects into consideration. Inbetween these subsets an interpolation of the normalization functions is required. This is indicated by the broken lines. The lower part of the plot shows the corresponding standard deviation, which results from the averaging procedure.

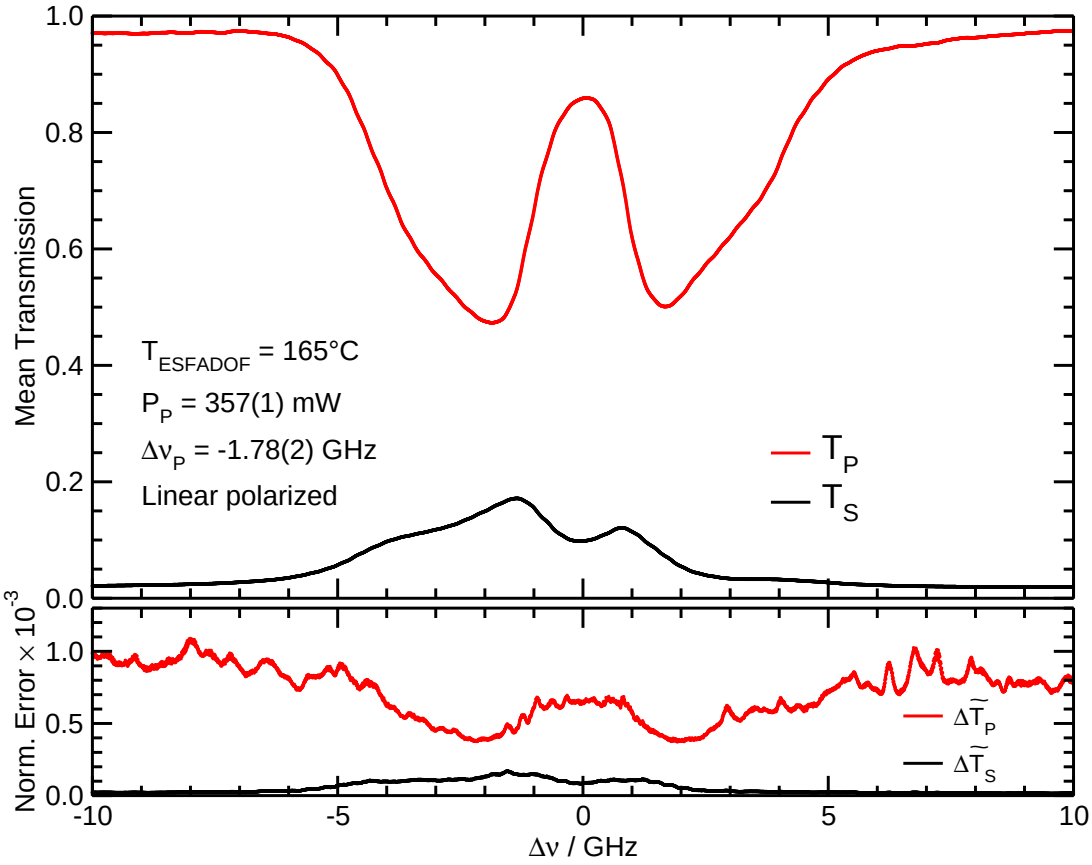

Fig. 4.11: Normalized ESFADOF spectra: The described normalization procedure transforms the raw data of Fig. 4.10 into these normalized ESFADOF spectra. A maximum transmission of 17.14(2)% has been obtained from the quoted parameter combination. Please note also the implications of the normalization procedure on the standard deviation.

5

Discussion of the Experimental Results

The experimental setup, which was the focus of the previous chapter, allows accurate measurements of the ESFADOF transmission characteristics. The influence of several important control parameters on the ESFADOF transmission characteristics has been systematically investigated by employing the measurement principle of Sec. 4.4 together with the described extensive data post-processing. The results of this study will be the contents of Sec. 5.2. They have been obtained by employing vapor cell I and demonstrate Rubidium ESFADOF operation and its operational limits. Section 5.3 focuses on these limits. In addition, Sec. 5.4 examines the results obtained with vapor cell II, which allows the employment of higher magnetic fields. As proof of concept, these measurements demonstrate the general feasibility of the ESFADOF edge-filter as Brillouin-lidar detector system.

In order to facilitate the upcoming discussion of this chapter, it is useful to have a closer look on the general influence of the investigated control parameters.

5.1 Overview of the Experimental Parameters

There are a number of external parameters influencing the ESFADOFs spectral characteristics: (1) The vapor cell temperature and the corresponding vapor density, (2) the magnetic field strength, (3) the length of the interaction volume and (4) the pump laser geometry, which comprises the intensity of the pump laser, its polarization and detuning from the D2 absorption center.

Of particular interest is the magnetic field strength. A magnetic field strength of the order of 500 mT is required to achieve the spectral overlap of the ESFADOF transmission edges with the Brillouin-doublet. However, the discussion of Sec. 4.1 shows the strong influence of the vapor cell geometry on the magnetic field strength, when employing permanent magnets, such that not every conceivable configuration is possible. By extension, the unavoidable inhomogeneous magnetic fields as well as the employed pump geometry restrict the length of the interaction volume and thus the achievable ESFADOF transmission. Hence, as Fig. 5.1 suggests, any optimization of the ESFADOF spectral characteristics has to take the interplay of all parameters into consideration.

In order to facilitate the discussion of the measured ESFADOF spectra, it is usefull to gain more insight on this interplay. The following subsections are

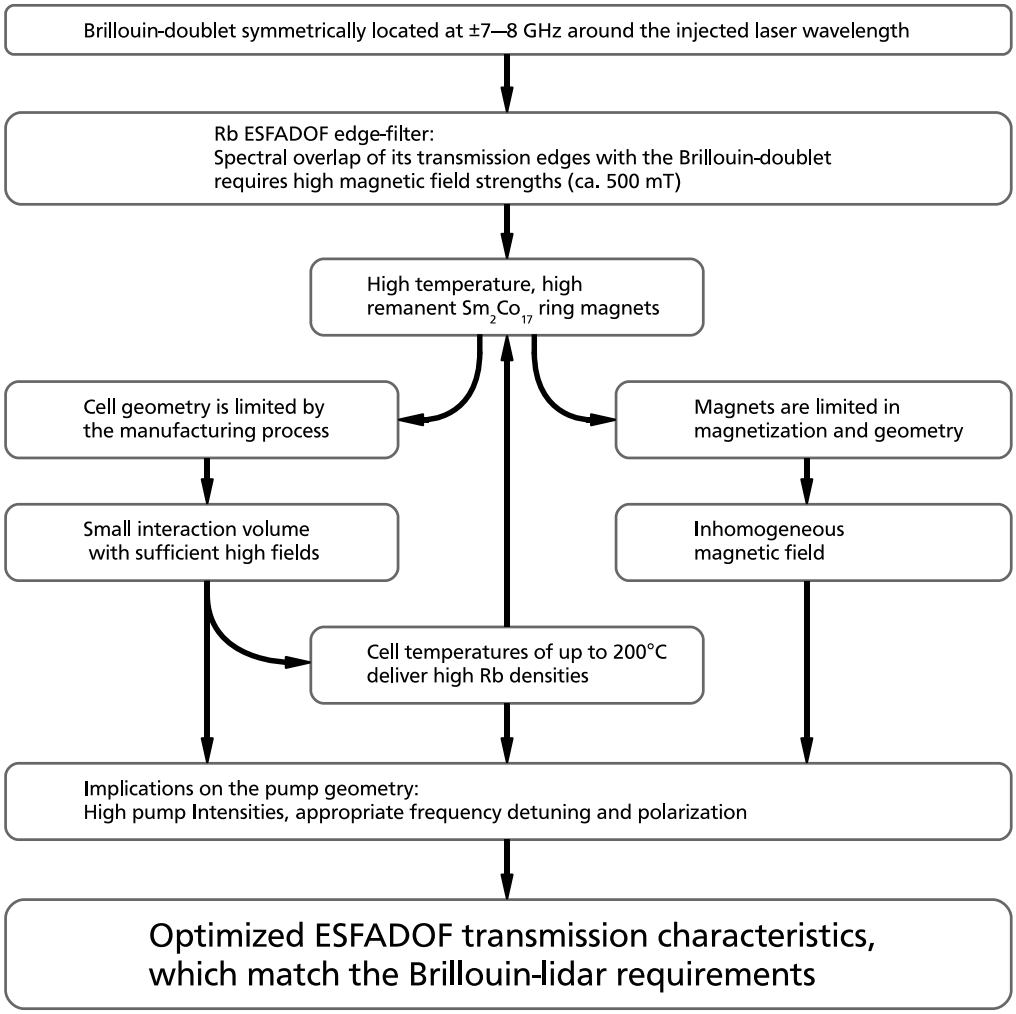

Fig. 5.1: Schematic of the experimental implications towards an optimized transmission: The ESFADOF design as well as the experimental parameters have to be adapted in order to suit the Brillouin-lidar requirements. The specific realizations as well as the exact choice of all external parameters have to comply with severe restrictions due to the manufacturing process and the airborne compatibility. The arrows indicate direct influence.

therefore intended to give an overall overview of the implications of the vapor cell temperature and the pump geometry on the ESFADOF device.

5.1.1 Vapor Cell Temperature

Generally speaking, ESFADOF spectra depend on several different terms which themselves are influenced by the temperature of the vapor (cf. also Secs. 3.5 and 3.6):

1. **The Rb vapor density:** The density of the Rb vapor increases exponentially with the temperature [78]. The corresponding dependency as well as a plot of the temperature dependent Rb density can be found in appendix A and Fig. A.1. Generally speaking, increasing the Rb vapor density mainly increases the opacity of the vapor.

   Due to the fact, that the accessible vapor volume is limited by the measurement geometry (cf. Fig. 4.1), increasing the vapor density results in more atoms, which interact with the high magnetic fields close to the permanent ring magnets at the cell entrance. This increases the dispersion and leads to significantly higher transmissions of the ESFADOF spectra.

   Moreover, radiation trapping processes profit from high vapor densities as well (cf. Sec. 3.6.3). Increasing the opacity of the vapor simultaneously increases the amount of trapped radiation [138, 139]. Generally speaking, increasing the vapor density increases the trapping volume around the pump laser beam, up to a certain threshold density. When increasing the vapor density further the contrary effect appears and the trapping volume shrinks. In order to shed light on this effect, Scholz *et al.* performed measurements concerning the influence of the vapor density on the spatial extent of the trapping region [171]. They investigated the radial extent of the trapping volume in optically pumped and pressure broadenend Sodium vapor. Their experiments prove that beyond a certain density threshold the trapped radiation remains confined to a smaller volume compared to lower vapor densities. They quote temperature thresholds of 220°C and 240°C for their experimental conditions, which comprise also additional Argon partial pressures of 20 hPa and 200 hPa respectively. In addition, Scholz *et al.* solved the radiation trapping problem numerically and reproduced the measurements with good agreement. The authors showed that the confinement of the radiation increases also with increased Argon partial pressure, i.e. with an increased spectral overlap of the pump laser with the atomic transition. However, their results can not be transformed to Rb vapor quantitatively, as they investigated pressure broadened Sodium vapor. More evidence on that topic delivers the radial profile of the pumped region. A reasonable indicator for the diameter of the trapping region is the energy pooling fluorescence. In particular, the $6P_{3/2} \rightarrow 5S_{1/2}$ and $6P_{1/2} \rightarrow 5S_{1/2}$ transition fluorescence (420 nm and 421 nm respectively) allow an excellent spectral discrimination from the pump laser. By imaging this fluorescence on a screen, it is possible to gain a rough estimation of the trapping diameter. Figure 5.2 shows the corresponding measurements for different cell temperatures. The

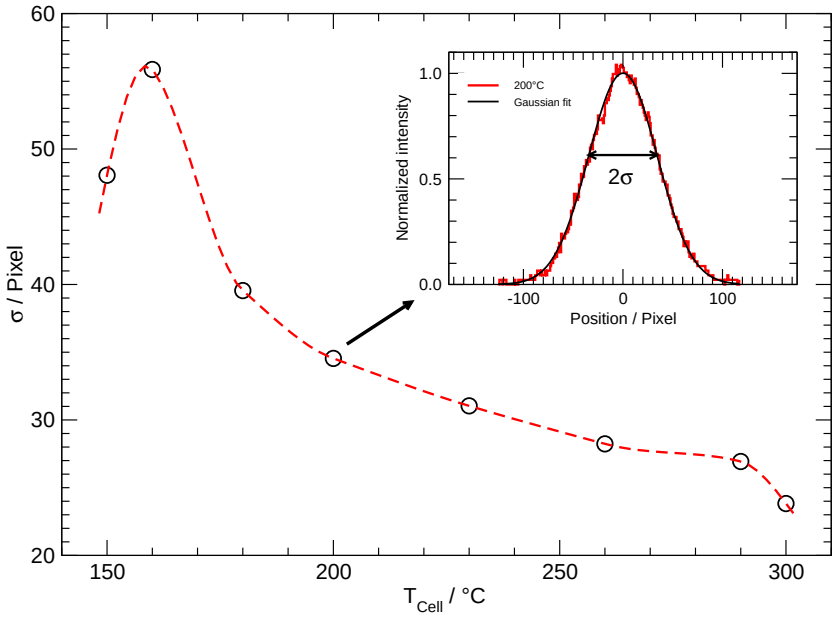

Fig. 5.2: Temperature dependence of the trapping volume: The confinement of the trapped radiation upon the increase of the number density is clearly visible for temperatures >160°C. The inset shows a cross section through one corresponding radial profile and a Gaussian fit to the data. The dashed line is a cubic spline fit and underlines the confinement. Please note that the presented measurement estimates the radial profile by imaging the energy-pooling fluorescence of the vapor cell. The surrounding oven did not allow a perpendicular access, so that the fitted profile widths σ can only be compared relative to each other.

circles mark the measured full width half maximum of an arbitrary cross section through the imaged fluorescence and the dashed line a cubic spline fit through these points. The shrinking of the trapping volume, when increasing the cell temperatures beyond 160°C, is clearly apparent. The employed technique gives only a rough estimate of the absolute diameter, however the values can be compared relatively, which proves that the confinement of the trapped radiation has to be taken into account for temperatures beyond 160°C.

For the sake of completeness, it has to be mentioned that for pump intensities, which exceed the saturation intensity of the vapor by orders of magnitude, nonlinear radiation trapping effects appear. Stacewicz *et al.* and Scholz *et al.* performed extensive measurements on this topic [172–174]. By exciting sodium vapor with laser pulses of several kW/cm^2 in intensity, they have been able to demonstrate the saturation of the vapor far beyond the pumped volume. The fact that subnatural decays, i.e. decays faster than the natural lifetime of the excited atoms, result from the nonlinearity of these high pumped vapors, is striking. However, the available intensities of the employed cw pump laser do not reach values to observe this effect.

2. **The energy pooling quenching rate:** The energy pooling quenching rate depends on the mean velocity of the Rb atoms, $v_{RMS} = \sqrt{\frac{3k_B T}{m_{Rb}}}$, which itself has a square root dependency on the local vapor temperature. However, the small cross section of this process, $\sigma^{EP}_{5P_{3/2} \leftrightarrow 5D} = 3 \times 10^{-14}$ cm^2 [140], will only extract a minor amount of Rb atoms from the $5P_{3/2}$ state (cf. Sec. 3.6.2).
3. **The Doppler width:** The Doppler width, $\nu_D = 2\nu\sqrt{\frac{2\ \ln 2\ k_B T}{mc^2}}$, is also proportional to the square root of the local vapor temperature and affects the width of the ESFADOF spectra directly. However, the exponential increase of the Rb vapor density covers this effect as long as the vapor remains saturated.

5.1.2 Pump Geometry

Besides the vapor cell temperature, the choice of the implemented pump geometry has the strongest effect on the ESFADOF transmission spectrum and offers some distinct control parameters, such as the pump laser intensity, its detuning from the D2 line center, its spectral width and its polarization. These parameters allow to tailor the ESFADOF spectra within certain limits as they directly influence the population of the lower ESFADOF state:

1. **The pump intensity:** The amount of excited state atoms is directly influenced by the pump intensity. Saturating the vapor is advantageous in order to obtain the maximum ESFADOF transmission. In addition, as the energy-pooling quenching rate is proportional to the square of the excited state population (cf. Sec. 3.6.2), increasing the $5P_{3/2}$ population also increases the losses. However, this loss channel saturates also with the saturation of the vapor.

   A quite more advantageous effect when increasing the pump intensity emerges from the imprisonment of the pump radiation within the vapor cell (cf. Sec. 3.6.3). Trapped photons can undergo a high number of absorption and reemission cycles within the highly opaque vapor before they eventually reach the initially pumped region again or escape from the vapor cell [139]. Meanwhile they experience a significant change in frequency and polarization [138, 139, 175]. These photons can be absorbed again by atoms within the initially pumped region and hence populate excited states, whose spectral overlap with the initial pump laser almost vanishes. This effect is of particular importance, as the confinement of the trapped radiation reinjects a significant amount of the trapped radiation back into the interaction volume. Hence, this effect can be regarded as an advantage and Sec. 5.2.2 further elaborates on this discussion.
2. **The detuning of the pump laser:** The spectral overlap between the pump laser and the $5S_{1/2} \rightarrow 5P_{3/2}$ pump transition influences the amount of absorbed radiation. Due to the spectrally narrow laser source, this additional degree of freedom potentially offers the possibility to tailor the ESFADOF spectral characteristics to some extent. However, it can not be uncoupled from radiation trapping effects and the inhomogeneous magnetic fields. Its influence will be examined in Sec. 5.2.3.

3. **The polarization of the pump laser:** For the Brillouin-lidar detector, symmetric ESFADOF transmission spectra are advantageous. Hence, an extensive polarization of the Rb vapor has to be avoided, as it suppresses complementary transitions. In view of the high inhomogeneity of the employed magnetic fields a linear polarization perpendicular to the quantization axis appears to be advantageous, as it potentially supplies σ^+ and σ^- transitions. In addition, the optical pumping process benefits from the frequency and polarization redistribution of the trapped radiation within the saturated vapor. In fact, the best results have been obtained by injecting a linear polarized pump beam into the ESFADOF vapor cell, which is why the following discussion will be restricted to a linear polarization of the pump beam.
4. **The spectral width of the pump laser:** At this point, the spectral width of the pump laser needs some distinct consideration. For the sake of completeness, it has been included as an accessible parameter, though it is not exploited in the present experimental setup. The spectral width of the pump laser is imposed by the ECDL master oscillator, which seeds the tapered amplifier. Typical values of the spectral width are of the order of a few MHz, which means that the pump laser reaches only distinct velocity groups within the Zeeman- and Doppler-broadened absorption profile. This is of particular importance, as the large hyperfine-structure of the Rb $5S_{1/2} \rightarrow 5P_{3/2}$ transition in combination with the high magnetic fields lead to a considerable spreading of the Rb $5S_{1/2} \rightarrow 5P_{3/2}$ absorption spectrum. Increasing the spectral width of the pump laser to the extent that it almost perfectly matches the spectral absorption profile of the Zeeman and Doppler broadened Rb vapor, would certainly improve the energy deposition into the vapor. In addition, the frequency redistribution due to the radiation trapping process would become less important and, as an appreciated side effect, it would become easier to simultaneously pump σ^+ and σ^- transitions when applying strong magnetic fields. Hence symmetric ESFADOF transmission spectra can be expected, when mapping the spectral width of the pump laser with the spectral width of the involved pump transitions. A significant increase in absolute transmission can also be expected.

   Recently, Gourevitch *et al.* published the development of a high power volume Bragg laser diode (VOBLA), which operates around 780 nm and offers a spectral width of 7 GHz and up to 2 W of laser power [176]. In view of the above discussion, this development is a very promising tool, as it would allow an optimized spectral overlap between the pump laser and the Doppler- and Zeeman- broadened absorbtion profile. The Brillouin-lidar requirement of approx. 500 mT result in a spectral width of the Rb $5S_{1/2} \rightarrow 5P_{3/2}$ transition, which easily exceeds 7 GHz.

5.2 Vapor Cell I: 270 mT

Detailed investigations were carried out: (1) on the influence on the vapor cell temperature, which is connected to the Rb vapor density, (2) on the influence of the pump intensity and (3) on the influence of the frequency detuning of the pump laser.

Several graphical representations of the same data will be presented: The 3D representation is intended to give a general overview of the influence on the investigated control parameter. It shows both ESFADOF exit polarizations, where the P-polarization refers to the parallel polarization with respect to the ESFADOF entry polarizer and the S-polarization to the perpendicular one, refered to as the ESFADOF transmission spectrum. The black broken lines perpendicular to the control parameter axis indicate the performed measurements. The plot linearly interpolates between these discrete measurements and the white broken line indicates zero frequency detuning of the probe laser. As extensively discussed in the last chapter, the frequency change of the probe laser was carried out continuously, whereas the control parameter was changed discretely, such that each ESFADOF-spectrum of the 3D compilation corresponds to one individal 2D spectrum (cf. Fig. 4.11). In addition, the 2D representation of the S-polarized ESFADOF transmission spectra will allow a more detailed comparison.

5.2.1 Influence of the Vapor Cell Temperature

It is evident that in consideration of the current experimental setup, high temperatures in combination with low pump intensities lead to minor dispersions only, and therefore can not induce high ESFADOF transmissions. On the other hand, saturating low vapor densities has the same effect. Hence, significant ESFADOF transmissions can only be expected when saturating high vapor densities.

Figure 5.3 offers a 3D depiction of several ESFADOF spectra recorded at different cell temperatures. A constant pump power of 500 mW was applied. The linearly polarized pump radiation has been placed on the center of the Rb D2 transition. A more detailed overview is given by the 2D representation of the same data in Fig. 5.4.

The following behavior can be observed: (1) Increasing the cell temperature increases the number density of the atomic gas and therefore the ESFADOF transmission. (2) A maximum transmission of 16.98(1)% has been achieved. (3) A concentration of the lower ESFADOF state population in favor of the red shifted peak can be observed. It indicates that σ^+-transitions contribute more to the spectral characteristics than the σ^--transitions. This leads to the conclusion, that in spite of the zero frequency detuning and the linear polarization of the pump beam a certain amount of the Rb vapor along the pump beam axis remains polarized. (4) The asymmetry of the peaks persist with increasing temperature. (5) Their full width half maximum (FWHM), which is depicted in the inset of Fig. 5.4, remains approximately constant up to a temperature of 163°C. (6) Beyond this temperature the FWHM rises as the transmission peaks become more structured.

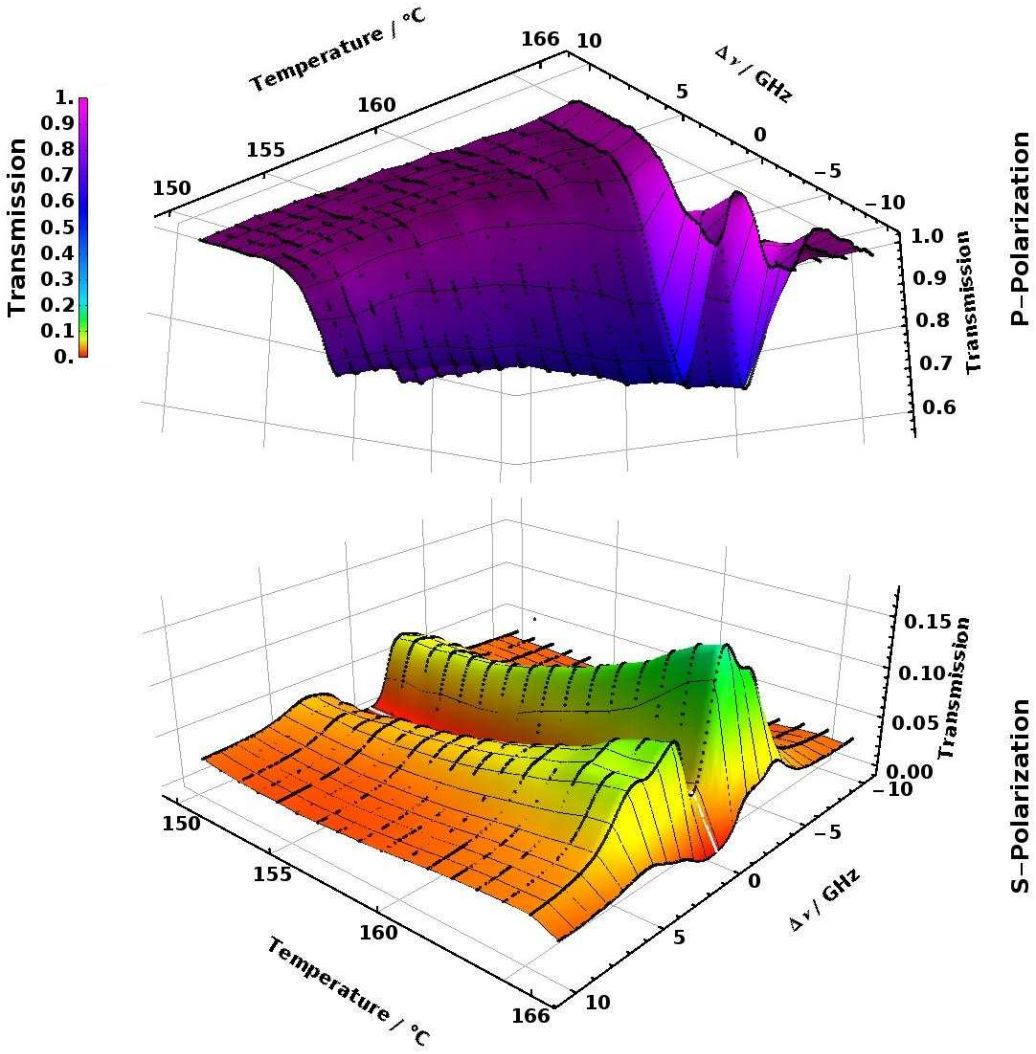

Fig. 5.3: 3D representation of both ESFADOF transmission spectra as a function of cell temperature: The upper graph shows the transmission spectra of the P-polarization and the lower graph compiles the ones of the S-polarization. The black dotted lines mark the measured data and the white dashed line zero frequency detuning of the probe beam (zero corresponds to 543.30 nm). For the clarity of the presentation, the data has been linearly interpolated along the power axis and the frequency axis has been reversed. A magnetic field strength of B_z =270 mT is applied. The linearly polarized pump laser injects P_{Pump} =500 mW of radiation into the vapor and its wavelength is placed at the center of the D2 transition. A clear dependency of the ESFADOF transmission on the rising temperature can be observed. Striking is the existence of an upper temperature threshold at 165°C, which limits the achievable maximum transmission. Beyond this temperature the maximum ESFADOF transmission reduces to 5%.

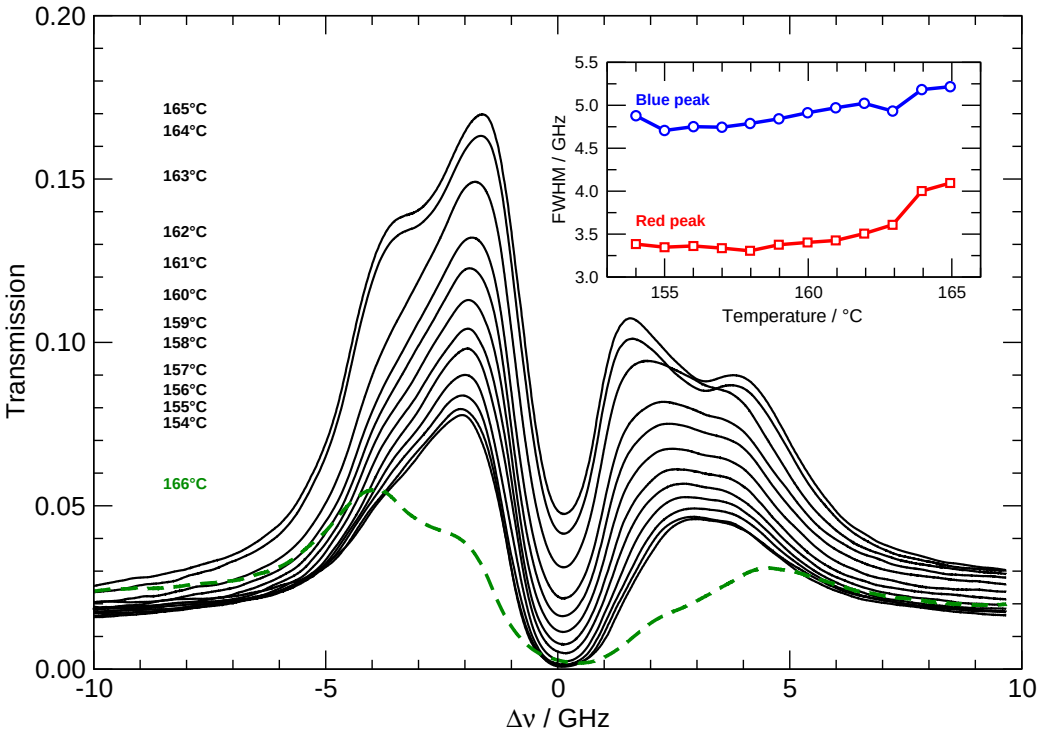

Fig. 5.4: 2D graphical representation of the temperature dependence of the S-polarization: The experimental parameters are the same as in Fig. 5.3 and the corresponding cell temperatures are annotated. This view allows a closer look on the frequency characteristics. The inset shows the corresponding full width half maximum values for the red and blue shifted peaks. For the clarity of the representation, only spectra beyond a cell temperature of $T_{ESFADOF} = 154°C$ are included. The spectra from 150°C to 154°C do not change significantly in absolute transmission or in spectral shape. A concentration of the lower ESFADOF state population in favor of the red shifted peak can be observed. It indicates that ΔM=+1 transitions contribute stronger to the spectral characteristics than the ones for $\Delta M = -1$. This indicates, in spite of the zero frequency detuning and the linear polarization of the pump beam, a certain amount of atomic polarization. The dashed curve corresponds to the ESFADOF transmission breakdown. The considerable change in spectral shape is striking. A more detailed discussion of the underlying physics follows in Sec. 5.3.

A clear double hump profile appears for both peaks. (7) Beyond a cell temperature of 165°C, the transmission of the ESFADOF spectra collapses suddenly and remains constant at a transmission of 5% with increasing temperature. Striking is the pronounced change in spectral shape, as the maximum transmission of the red and blue shifted peaks move towards the outside of the spectrum. This can be interpreted as a significant depopulation of the former highly occupied levels.

The redistribution of the $5P_{3/2}$ population between cell temperatures of 163°C and 166°C can be correlated to the spatial confinement of the trapped radiation (cf. Sec. 5.1.1). Fig. 5.2 shows that this confinement begins to dominate above cell temperatures of 160°C. The radiation undergoes several absorption and reemission processes, which are all accompanied with frequency redistribution of the trapped photons [138, 139]. Hence, indirectly pumped sublevels are excited by this trapped radiation and cause the described spectral broadening of the ESFADOF spectrum [177, 178].

The transmission breakdown is caused by the onset of a laser-induced plasma inside the vapor cell. The plasma ionizes the majority of the Rb vapor and considerably depletes the population of the lower ESFADOF state, which explains the breakdown. A more detailed discussion of the underlying physics will be given in Sec. 5.3.

5.2.2 Influence of the Pump Intensity

The influence of the pump intensity has been measured by increasing the injected power of the pump laser, while keeping the beam cross section constant. The corresponding results are compiled in Fig. 5.5, which shows again a 3D overview of the measured data. More details can be extracted from Fig. 5.6, which shows a 2D representation. The $P_{Pump} = 402.4(5)$ mW of maximum injected pump power corresponds to a pump intensity of $I_{Pump} = 418.2(5)$ W/cm^2, when relating the laser power to the beam diameter of 383 μm.

The temperature of the vapor cell was 165°C and the linear polarized pump beam has been detuned by $\Delta\nu_P = -1.78(2)$ GHz from the center of the D2 pump transition. As expected a strong correlation with the injected pump power appears: The ESFADOF transmission rapidly rises with increasing pump power. It saturates along with the population of the pumped $5P_{3/2}$ level. A maximum transmission of 17.14(1)% has been reached, when injecting a pump power of 358.6(5) mW. At a pump power of 387.8(5) mW the transmission collapses. When increasing the pump power further, the ESFADOF spectra show an almost constant spectrum with a maximum transmission of 4%.

In contrast to the measurements of the last section, which required 500 mW of pump power to induce the plasma, this configuration needs only 387.8 mW of laser power for the same cell temperature. This can be attributed to the frequency detuning of the pump laser, which lead to an increased spectral overlap between

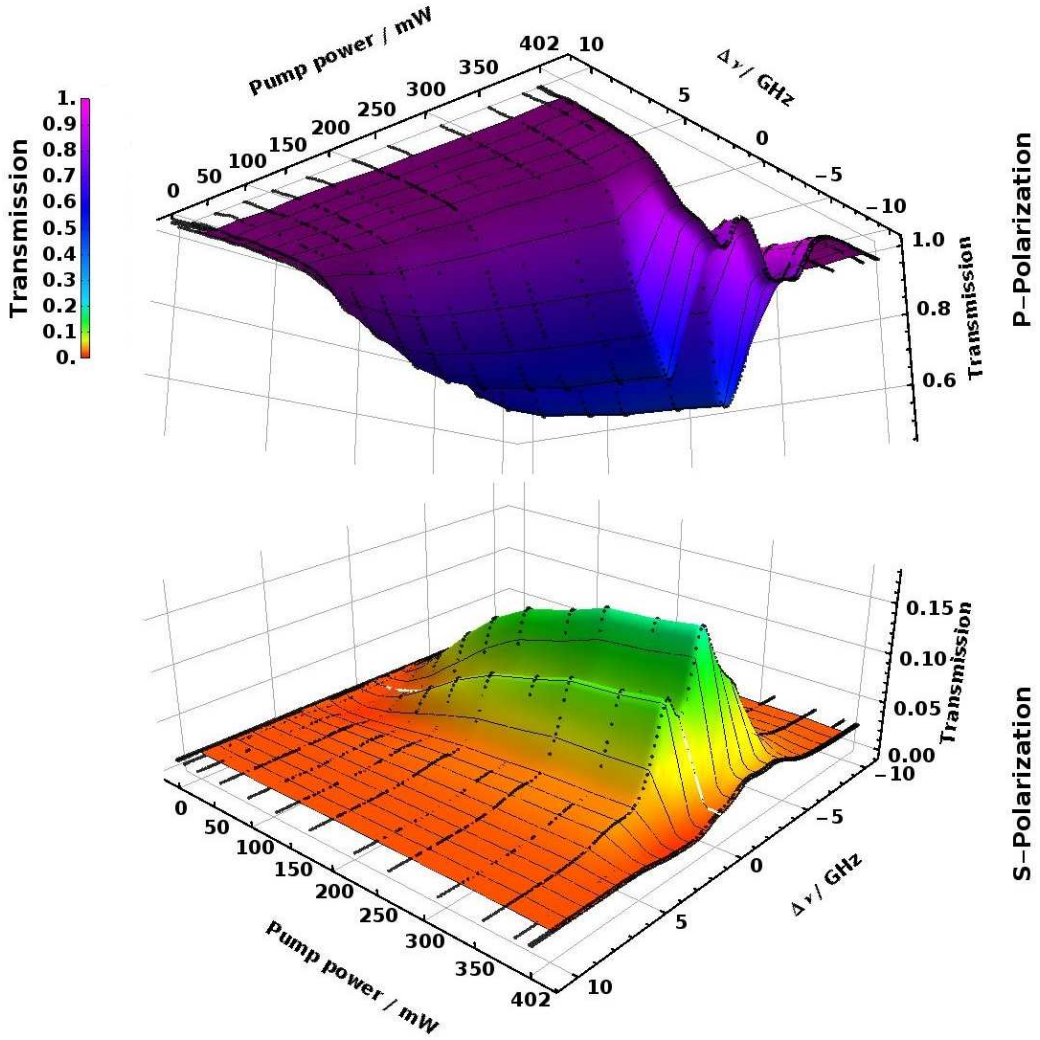

Fig. 5.5: 3D representation of the recorded ESFADOF spectra with increasing pump power: The temperature of the vapor cell was 165°C; a magnetic field strength of B_Z =270 mT has been applied and the linear polarized pump beam has been detuned by $\Delta\nu_P = -1.78(2)$ GHz from the center of the D2 pump transition. As expected, a strong correlation of the maximum transmission with the injected pump power appears. The ESFADOF maximum transmission rises with increasing pump power up to a maximum value of 17.14(1)%. At a pump power of $P_{Pump} = 387.8(5)$ mW the ESFADOF spectra collapses to a few percent of transmission. More details can be extracted from Fig. 5.6.

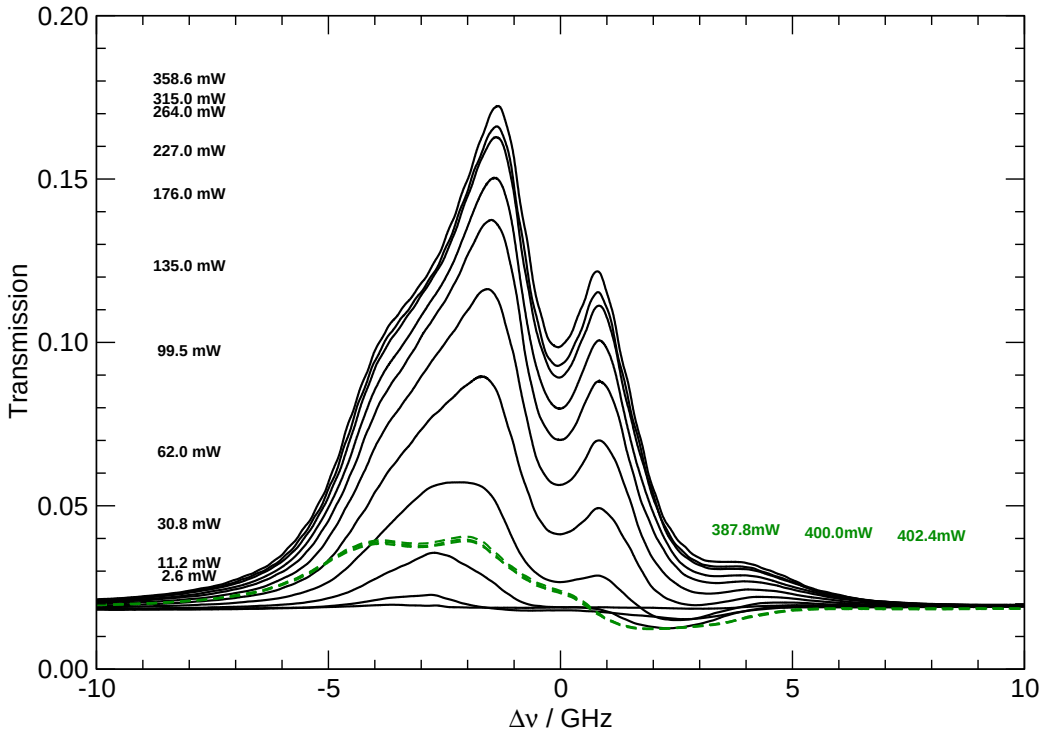

Fig. 5.6: 2D graphical representation of the S-polarization of Fig. 5.5: The experimental parameters are the same as in Fig. 5.5 and the corresponding pump powers are annotated. The dashed curves have been recorded after the transmission breakdown. Their spectral shapes as well as the maxmum transmission insignificantly change, when increasing the pump power further.

the pump laser and the absorption spectrum of the D2 transition. In addition, the frequency detuning significantly changes the spectral shape in favor of the red shifted peak, but only has a little influence on the maximum transmission. In comparison to the last section, it increases only slightly from 16.98(1)% to 17.14(1)%, which clearly indicates the saturation of the vapor. In addition, the resulting redistribution of the $5P_{3/2}$ population leads to a stronger polarization of the Rb atoms, which is reflected by the pronounced red shifted peak. The next section will discuss the influence on the frequency detuning of the pump laser in more detail.

5.2.3 Influence of the Pump Frequency Detuning

The last section already showed an influence of the frequency detuning from the $5S_{1/2} \rightarrow 5P_{3/2}$ transition center. By slightly red shifting the pump laser, an improved spectral overlap between the pump laser and the absorption spectrum of the D2 transition is achieved. This effect is based on the pronounced hyperfine structure of the $5S_{1/2} \rightarrow 5P_{3/2}$ transition of both Rb isotopes (^{85}Rb and ^{87}Rb), which splits the transition lines. In combination with the applied inhomogeneous strong magnetic fields a considerably broadened D2 absorption spectrum results. The spectral overlap between the broadenend D2 absorption line and the pump beam

introduces another control parameter, which facilitates the symmetrization of the transmission spectrum. This can be understood as a coupled process including the directly acting pump laser, the population redistribution by the radiation trapping process, polarization disturbing collisions and depopulation due to quenching processes. As the following results show, these effects can be balanced out by an appropriate choice of the frequency detuning of the pump ECDL in order to obtain symmetric ESFADOF transmission edges. As explained in chapter 2 symmetric transmission edges are advantageous for the Brillouin-lidar edge-filter receiver, as they intrinsically compensate small frequency fluctuations of the Brillouin-lidars transmitter laser.

Fig. 5.7 shows a 3D compilation of several recorded ESFADOF spectra depending on the wavelength of the pump ECDL and Fig. 5.8 shows the corresponding contour plot representation. The frequency detuning ν_P from the Rb D2 transition center has been chosen to cover a span of 15 GHz starting at -14 GHz. Evaluating the data reveals the following insight:

1. While scanning the wavelength of the pump ECDL, a strong correlation of the ESFADOF transmission characteristics with the spectral overlap between the pump laser and the broadened Rb D2 absorption line can be observed.
2. It is possible to maximize the ESFADOF transmission by optimizing the spectral overlap. A maximum transmission of 16.11(1)% can be observed for a pump detuning of $\Delta\nu_P = -1.62(2)$ GHz.
3. Fig. 5.9 summarizes the peak transmissions for the red and blue shifted ESFADOF peaks respectively. The blue shifted peak continuously shows less transmission than the red shifted one.
4. For pump detunings of $\Delta\nu_P = 0.58(2)$ GHz and $\Delta\nu_P = 0.98(2)$ GHz, symmetric inner edges of the ESFADOF transmission can be observed. The corresponding transmission spectra are shown as inset in Fig. 5.9. Please note that the symmetry axis is located 0.15(1) GHz red shifted from the ESFADOF transition center.

The discussed measurements show in particular that it is possible to symmetrize the ESFADOF transmission spectrum by choosing an appropriate frequency detuning of the pump laser. Although these spectra do not cover the Brillouin-doublet, they represent an important proof of concept:

Let $S_B(\Delta\nu, \nu_B, \delta\nu_B)$ denote the normalized spectral profile of the Brillouin-doublet with respect to its peak intensity

$$\begin{aligned} S_B(\Delta\nu, \nu_B, \delta\nu_B) &= L_B(\Delta\nu - \nu_B, \delta\nu_B) + L_B(\Delta\nu + \nu_B, \delta\nu_B) \\ &= \frac{(\delta\nu_B/2)^2}{(\Delta\nu - \nu_B)^2 + \left(\frac{\delta\nu_B}{2}\right)^2} + \frac{(\delta\nu_B/2)^2}{(\Delta\nu + \nu_B)^2 + \left(\frac{\delta\nu_B}{2}\right)^2}, \end{aligned} \tag{5.1}$$

where $\Delta\nu$ represents the frequency shift from the injected Brillouin-lidar laser wavelength, ν_B denotes the temperature dependent Brillouin-shift and $\delta\nu_B$ the

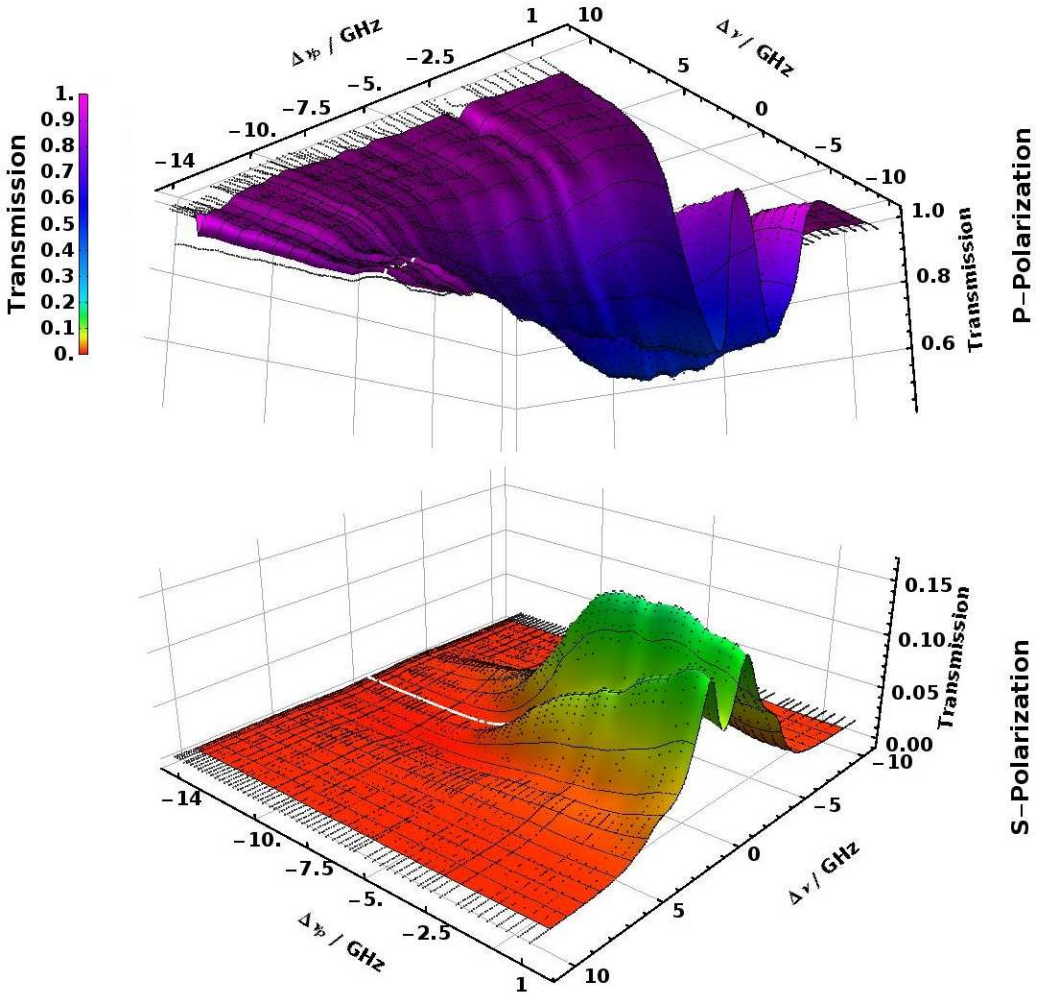

Fig. 5.7: 3D plot representation of the ESFADOF transmission spectra as a function of the frequency detuning of the pump laser: The cell temperature was $T_{ESFADOF} = 165°C$, a magnetic field strength of $B_z = 270$ mT has been applied and $P_{Pump} = 400$ mW of linear polarized laser power has been injected into the vapor cell. The pump ECDL has been frequency tuned and $\Delta\nu_P$ represents its frequency shift from the D2 transition center. While scanning the wavelength of the pump ECDL, a strong correlation of the ESFADOF transmission characteristics with the spectral overlap between the pump laser and the broadened Rb D2 absorption line can be observed. A maximum transmission of 16.11(1)% has been achieved for a pump detuning of $\Delta\nu_P = -1.62(2)$ GHz. Fig. 5.8 shows a contour plot representation of the same data and Fig. 5.9 summarizes the peak transmissions.

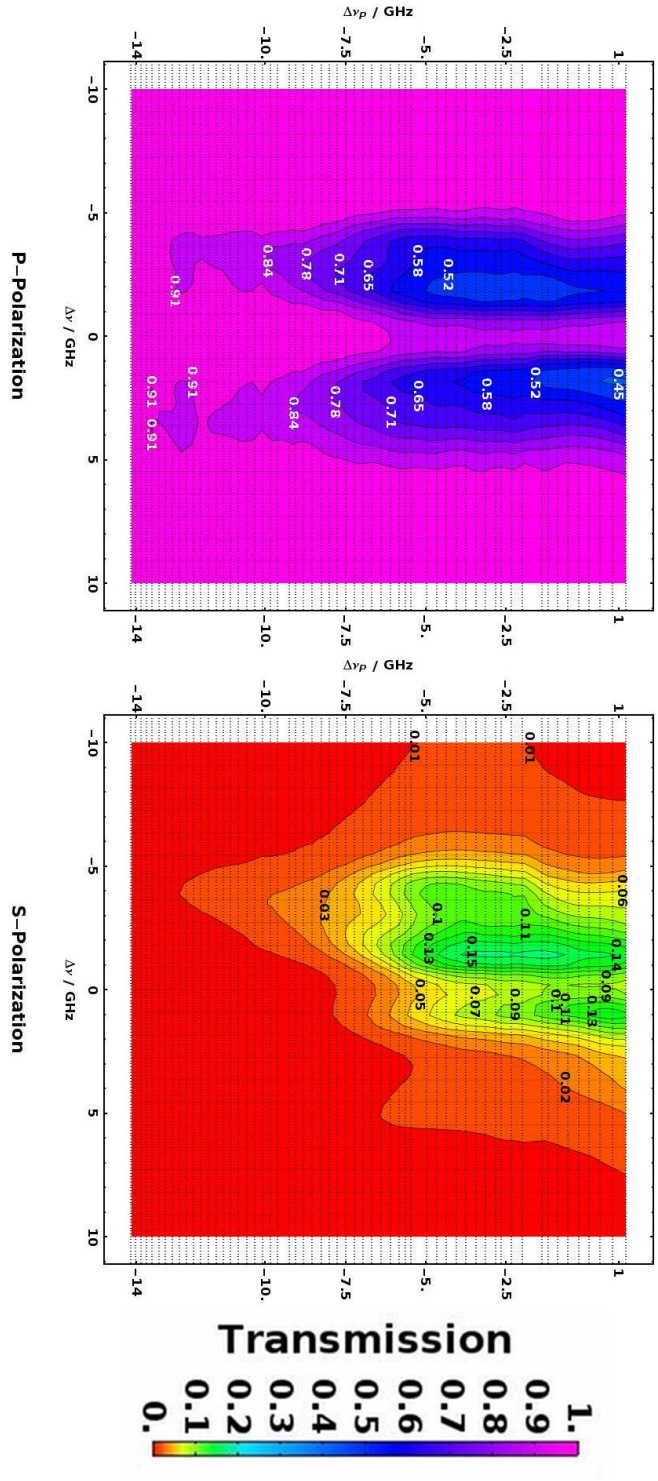

Fig. 5.8: Contour plot representation of the ESFADOF transmission spectra as a function of the frequency detuning of the pump laser: The plot shows the same data as the 3D representation in Fig. 5.7.

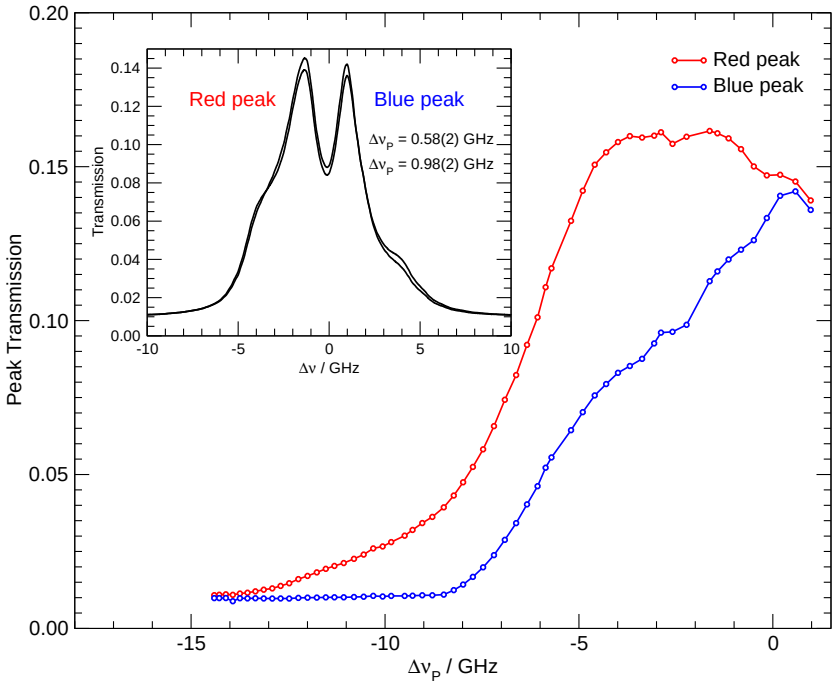

Fig. 5.9: Peak transmissions of the red and blue shifted ESFADOF peaks as a function of frequency detuning of the pump laser: The increase in maximum transmission as well as the pronounced asymmetry of the ESFADOF transmission spectrum is clearly apparent (cf. Fig. 5.7). The inset shows the ESFADOF transmission spectra for a frequency detuning of $\Delta\nu_P = 0.58(2)$ GHz and $\Delta\nu_P = 0.98(2)$ GHz respectively, which both show a pronounced symmetry of the inner transmission edges. The symmetry axis is located 0.15(1) GHz red shifted from the ESFADOF transition center. Figs. 5.10 and 5.11 investigate the symmetry further.

spectral width of the Brillouin-scattering $L_B(\Delta\nu - \nu_B, \delta\nu_B)$. The spectral profile of the Brillouin-doublet after passing the ESFADOF device, with respect to the center of the $5P_{3/2} \rightarrow 8D_{5/2}$ transition, is the simple multiplication of $S_B(\Delta\nu - \Delta\nu_S, \nu_B, \delta\nu_B)$ with the ESFADOF transmission spectrum $T_S(\Delta\nu)$:

$$T'_B(\Delta\nu) = T(\Delta\nu) \times S_B(\Delta\nu - \Delta\nu_S, \nu_B, \delta\nu_B), \tag{5.2}$$

where $\Delta\nu_S \neq 0$ shifts the injected laser frequency from the center of the $5P_{3/2} \rightarrow 8D_{5/2}$ transition. A photodetector, which captures the signal after passing the ESFADOF device, will integrate it spectrally, hence

$$T_B(\nu_B, \delta\nu_B) = C \int T(\Delta\nu') \times S_B(\Delta\nu' - \Delta\nu_S, \nu_B, \delta\nu_B)\, d\Delta\nu'. \tag{5.3}$$

By setting $C = \frac{2}{\pi\nu_B}$ a normalization with respect to the integrated intensity of the Brillouin-doublet results. Inserting Eq. 5.1 into Eq. 5.3 yields

$$= C \int T(\Delta\nu') \times L_B\left(\Delta\nu' - (\Delta\nu_S + \nu_B), \delta\nu_B\right) d\Delta\nu' + \tag{5.4}$$

$$C \int T(\Delta\nu') \times L_B\left(\Delta\nu' - (\Delta\nu_S - \nu_B), \delta\nu_B\right) d\Delta\nu', \tag{5.5}$$

which can be interpreted as a convolution between the ESFADOF transmission spectrum T and the Lorentz-profile of the Brillouin-peaks L_B:

$$T_B(\nu_B, \delta\nu_B) = C\left(\widetilde{T}_B(\Delta\nu_S + \nu_B, \delta\nu_B) + \widetilde{T}_B(\Delta\nu_S - \nu_B, \delta\nu_B)\right) \text{ and} \quad (5.6)$$

$$\widetilde{T}_B(\Delta\nu, \delta\nu_B) = \int T(\Delta\nu') \times L_B\left(\Delta\nu' - \Delta\nu, \delta\nu_B\right) d\Delta\nu' = (T * L_B)(\Delta\nu) \quad (5.7)$$

Eqs. 5.6 and 5.7 are important results. They show, that the photodetector captures a signal $T_B(\nu_B, \delta\nu_B)$, which is proportional to the convolution of the ESFADOF transmission spectrum $T(\Delta\nu)$ with the Lorentz-profile $\widetilde{T}_B(\Delta\nu, \delta\nu_B)$, evaluated at the Brillouin-shift ν_B, for a given spectral width $\delta\nu_B$. Hence, this relationship can be exploited to analyze the signal change ΔT caused by a sufficiently small frequency jitter $\delta\nu$, superimposed on the central frequency $\nu_T = \nu_0 + \Delta\nu_S$ of the Brillouin-transmitter: $\Delta\nu_S \rightarrow \Delta\nu_S + \delta\nu$. For that purpose it is sufficient to linearize $\widetilde{T}_B$ around $\Delta\nu'$, which yields the following:

$$\Delta T_B(\nu_B, \delta\nu_B) = C\left(\Delta\widetilde{T}(\Delta\nu_S + \nu_B) + \Delta\widetilde{T}(\Delta\nu_S - \nu_B)\right) \text{ with} \quad (5.8)$$
$$\Delta\widetilde{T}(\Delta\nu') = \partial_{\Delta\nu}\widetilde{T}(\Delta\nu)|_{\Delta\nu=\Delta\nu'} \times \delta\nu.$$

Figs. 5.10 and 5.11 evaluate $\widetilde{T}_B$ for both discussed symmetric ESFADOF transmission spectra (cf. Fig. 5.9) and a mean spectral width of the Brillouin-backscatter of $\overline{\delta\nu_B} = 500$ MHz [40]. By investigating the first derivative $\partial_{\Delta\nu}\widetilde{T}(\Delta\nu)$ and its symmetric inversion the following conclusions result:

1. The absolute value of the first derivative $\left|\partial_{\Delta\nu}\widetilde{T}(\Delta\nu)\right|$ shows a maximum value of 7.5×10^{-5} MHz^{-1} and 7.0×10^{-5} MHz^{-1} for a pump detuning of $\Delta\nu_P = 0.58(2)$ GHz and $\Delta\nu_P = 0.98(2)$ GHz respectively. By dividing the achieved absolute accuracy of the ESFADOF transmission measurement of 2.5×10^{-4} by these values a tolerable frequency jitter of 3.3 MHz and 3.6 MHz results. This result is not surprising, as the probe laser line width has been measured to not exceed 7 MHz (cf. Sec. 4.4.1).
2. The symmetric inversion of the first derivative $\partial_{\Delta\nu}\widetilde{T}(-(\Delta\nu - 2\Delta\nu_S))$, with respect to the symmetry point $\Delta\nu_S$, located 150 MHz red shifted from the transition center, shows a high congruence with the first derivative $\partial_{\Delta\nu}\widetilde{T}(\Delta\nu)$ between -1.3 GHz and 0.9 GHz.
3. The mentioned congruence between the first derivative and its symmetric inversion indicates already a significant increase in measurement accuracy, whenever the symmetry of the ESFADOF transmission edges can be exploited. By evaluating Eq. 5.8 it is possible to estimate the influence of the frequency jitter of the Brillouin-lidar transmitter to

$$\begin{aligned}\Delta T_B(\nu_B, \delta\nu_B) &= C\left(\Delta\widetilde{T}(\Delta\nu_S + \nu_B) + \Delta\widetilde{T}(\Delta\nu_S - \nu_B)\right) \quad (5.9)\\ &= C\Big(\partial_{\Delta\nu}\widetilde{T}(\Delta\nu)|_{\Delta\nu=\Delta\nu_S+\nu_B} - \\ &\qquad \partial_{\Delta\nu}\widetilde{T}(-(\Delta\nu - 2\Delta\nu_S))|_{\Delta\nu=\Delta\nu_S+\nu_B}\Big) \times \delta\nu.\end{aligned}$$

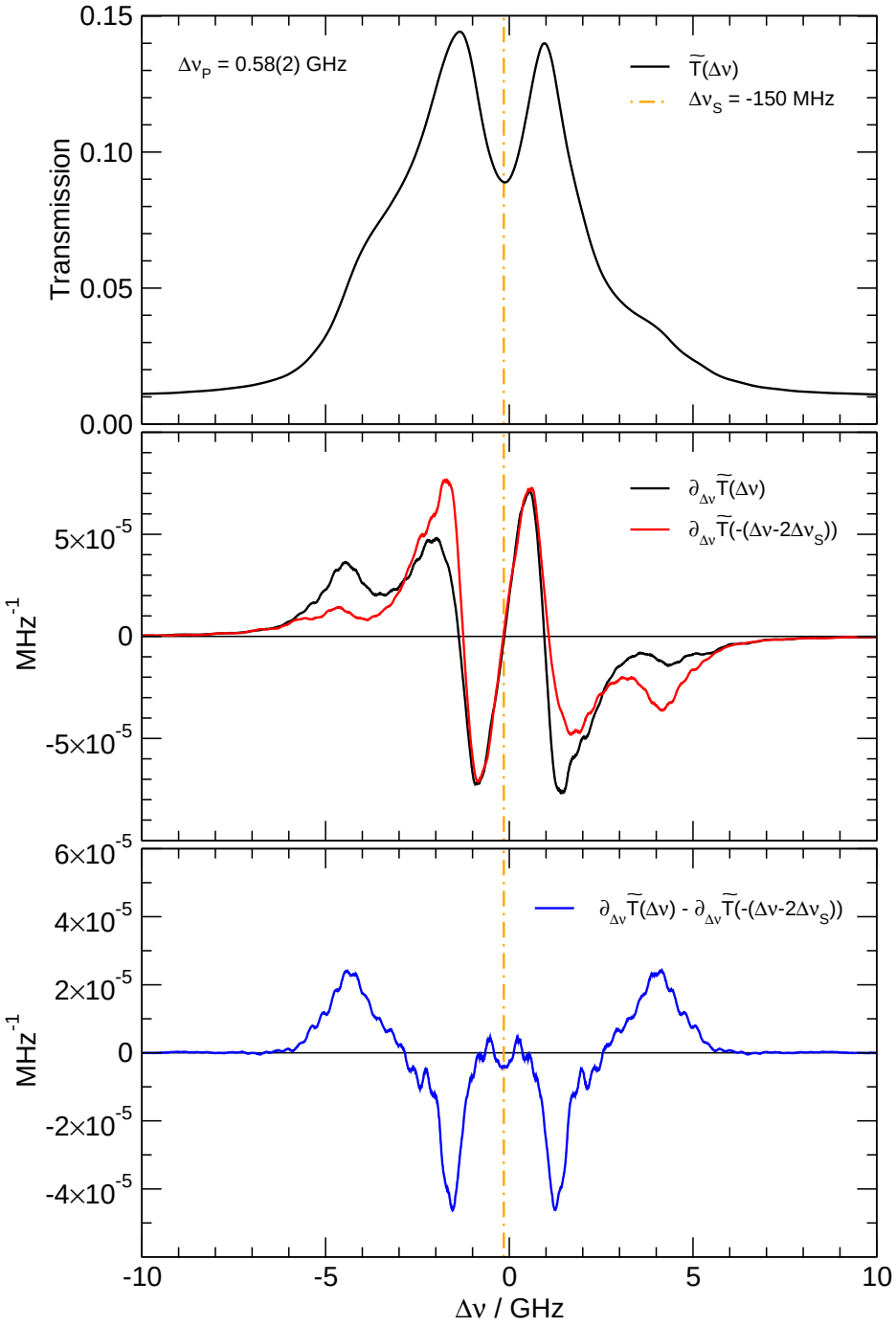

Fig. 5.10: Evaluation of the edge symmetry for a pump detuning of $\Delta\nu_P = 0.58(2)$ GHz: The ESFADOF spectrum and all other parameters correspond to the ones of Fig. 5.9. The plots show the ESFADOF transmission spectra, their derivative and the symmetric inversion of the derivative. The high degree of congruence between -1.3 GHz and 0.9 GHz of the ESFADOF spectra derivative and its symmetric inversion are advantageous in increasing the accuracy of the Brillouin-lidar edge-filter. The last row shows the difference between the derivative of the ESFADOF transmission and its symmetric inversion and quantifies the mentioned congruence. This proves a very effective compensation of small frequency fluctuations of the Brillouin-lidar transmitter.

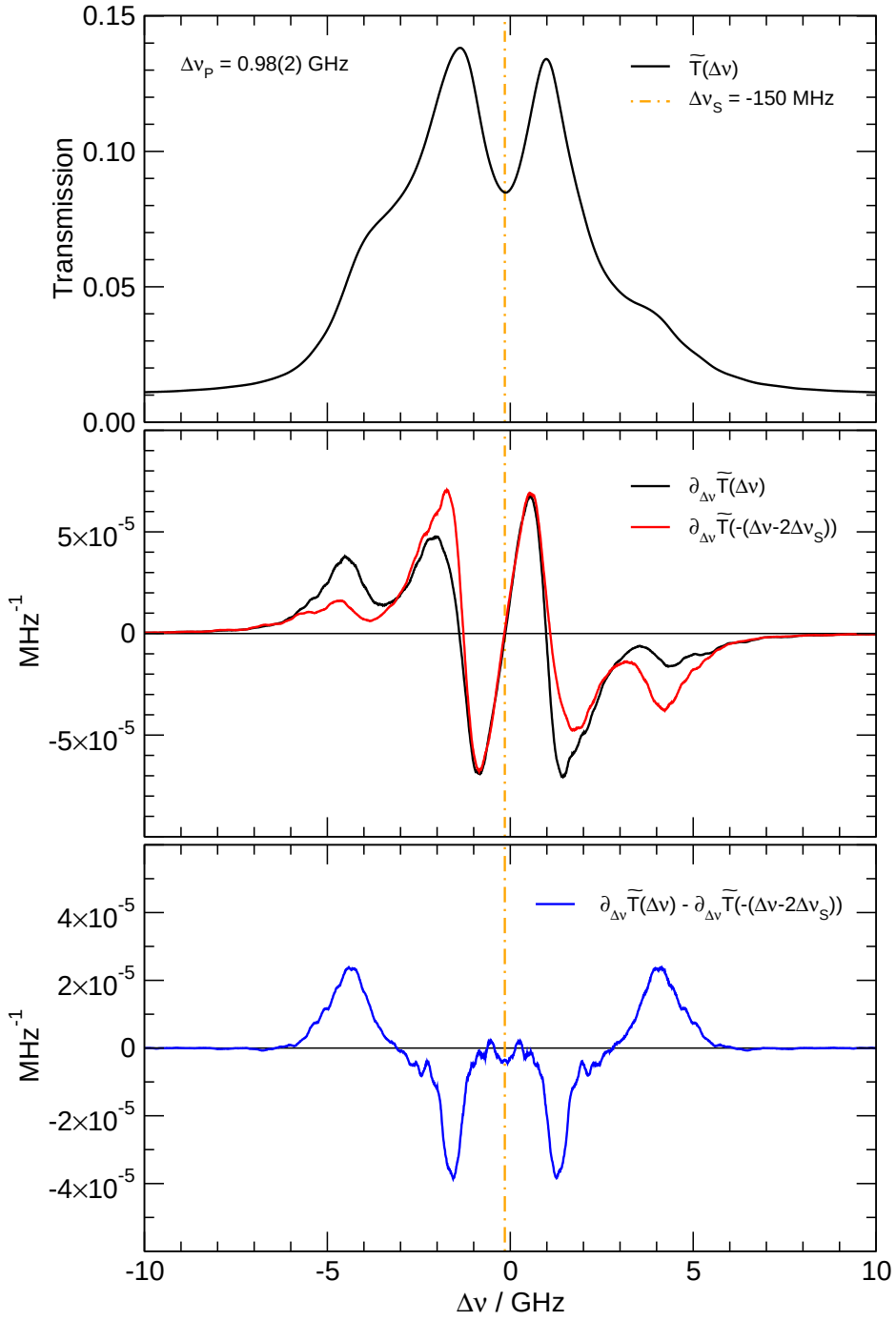

Fig. 5.11: Evaluation of the edge symmetry for a pump detuning of $\Delta\nu_P = 0.98(2)$ GHz: The ESFADOF spectrum and all other parameters correspond to the ones of Fig. 5.9. Compard to fig. 5.10 the symmetry is even more pronounced.

The last row of Figs. 5.10 and 5.11 evaluate the symmetry quantitatively by plotting the difference between the first derivative and its symmetric inversion

$$\Theta_S(\Delta\nu,\Delta\nu_S) = \partial_{\Delta\nu}T(\Delta\nu) - \partial_{\Delta\nu}T(-(\Delta\nu - 2\Delta\nu_S)). \qquad (5.10)$$

By minimizing $\int|\Theta_S(\Delta\nu,\Delta\nu_S)|\,d\Delta\nu$ with respect to $\Delta\nu_S$, the symmetry point $\Delta\nu_S = -150$ MHz results. The plot shows, that even in the worst-case scenario only fluctuation of 4.6×10^{-5} MHz^{-1} and 3.8×10^{-5} MHz^{-1} arise for pump detunings of $\Delta\nu_P = 0.58(2)$ GHz and $\Delta\nu_P = 0.98(2)$ GHz respectively. These values are already a factor of 1.75 better than employing only one single edge. However, evaluating the same entity between -1.3 GHz and 0.9 GHz, where the highest degree of symmetry has been achieved, reveals maximum transmission fluctuations of only 6×10^{-6} MHz^{-1} and 4×10^{-6} MHz^{-1} for the same pump detunings. Hence, a significant increase in signal accuracy results intrinsically from the symmetric transmission edges. Precisely speaking, the signal accuracy increases by a factor of at least 12.5 and 17.5 for the same pump detunings. Conversely, when considering the achieved transmission accuracy of 2.5×10^{-4}, these values translate to a tolerable laser frequency jitter of 42 MHz and 63 MHz without degrading the current accuracy limitations.

The demonstrated symmetry of the ESFADOF transmission spectra and the accompanied increase in signal accuracy, when exploiting the symmetry of the Brillouin-doublet is an important result. The above discussion proves, that laser frequency fluctuations can be neglected as long as they do not extend the values of tolerable laser frequency jitter. This result is very comfortable, as no sophisticated laser stabilization is necessary to guarantee the achieved transmission accuracy of 2.5×10^{-4}. Current available distributed feedback laser diodes provide sub-MHz linewidths when temperature and injection current stabilized without any other external locking mechanism [179]. However, the current design specifications of the Brillouin-lidar demand for 10 ns, Fourier-limited pulses in order to guarantee a spatial resolution of 1 m within the water column. Due to the Fourier-limit the frequency bandwidth of the laser pulses is at least 44 MHz [16, 54], which lies well within the discussed accuracy.

5.3 ESFADOF Operational Limits

The last section discussed the influence of the accessible control parameters in order to optimize the ESFADOF transmission spectrum. As expected, the pump geometry has an enormous influence on the population of the lower ESFADOF state and thus on the ESFADOF transmission spectrum. Within certain limits, which depend on the vapor cell temperature, the injected pump intensity and the spectral overlap between the pump laser and the $5S_{1/2} \rightarrow 5P_{3/2}$ pump transition, stable ESFADOF operation with considerable transmissions of up to 17% has been demonstrated. As it has been shown, exceeding these limits results in a collapse of the ESFADOF spectra. Beyond the mentioned limits a laser-induced plasma is maintained by the pump laser and the plasma considerably consumes

the $5P_{3/2}$ population, which explains the transmission breakdown.

The possibility of inducing a plasma in alkali-metal vapors is particularly remarkable, as it demands only relatively low laser intensities of the order of a few hundred W/cm^2, a fact, which has been noted and elaborated already by Measures in 1969. His proposed theoretical description of the laser-induced plasma in alkali-metal vapors [180] is the basis of current theoretical predictions [181, 182]. Lucatorto and McIlrath demonstrated in 1976 the formation of a laser-induced plasma in Sodium vapor [183, 184]. They have been unaware of the work of Measures. However, Measures subsequently published in 1977 a theoretical description of the observations of Lucatorto and McIlrath [185]. In addition, Chéret, Barbier and their co–workers investigated the laser-induced ionization of Rb vapors systematically [140, 186–188]. Besides these first investigations a large amount of authors contributed to the understanding of the physics behind laser-induced plasma in alkali-metal vapors throughout the decades. It would certainly exceed the purpose of this thesis to reference every single contribution. However, to the best knowledge of the author, the review articles of Bahns *et al.* [189] and Stwalley and Bahns [190] offer the best overview on this topic and a very extensive bibliography. In addition, A. C. Tam extensively reported on plasma formation in alkali metal vapors in 1982 [191] and Papas *et al.* published some recent results [192].

However, this highly nonlinear coupled system is still an interesting research field and the development of ultra cold atomic gases also made the physics of ultra cold neutral plasma visible. This is a new research field along the frontiers among plasma, atomic and solid state physics [193].

The main purpose of the following discussion is an overall understanding of the ESFADOF operational limits, which are dominated by the laser-induced plasma. Sec. 5.3.1 presents that the ESFADOF transmission breakdown is accompanied by a pronounced hysteresis; Sec. 5.3.1 will explain the physical processes which maintain the plasma and Sec. 5.3.3 ends with an overview of the ESFADOF operation along the plasma maintenance threshold. By operating the ESFADOF device below this threshold it was possible to measure the highest so far realized ESFADOF transmissions on the Rubidium $5P_{3/2} \rightarrow 8D_{5/2}$ resonance. They represent a milestone towards a practicable realization of the Brillouin-lidar detector. Furthermore, Sec. 5.3.3 will also discuss the observed functional behavior, which separates the ESFADOF operation from the laser-induced plasma phase.

5.3.1 ESFADOF Hysteresis

The induction of the plasma phase is accompanied with a hysteretic behavior. Figs 5.12– 5.15 show a compilation of several ESFADOF spectra, which demonstrate the hysteresis. The spectra have been recorded while adiabatically increasing and afterwards decreasing the pump power, meaning that the pump power changes on time scales, which are orders of magnitude slower than the inner pro-

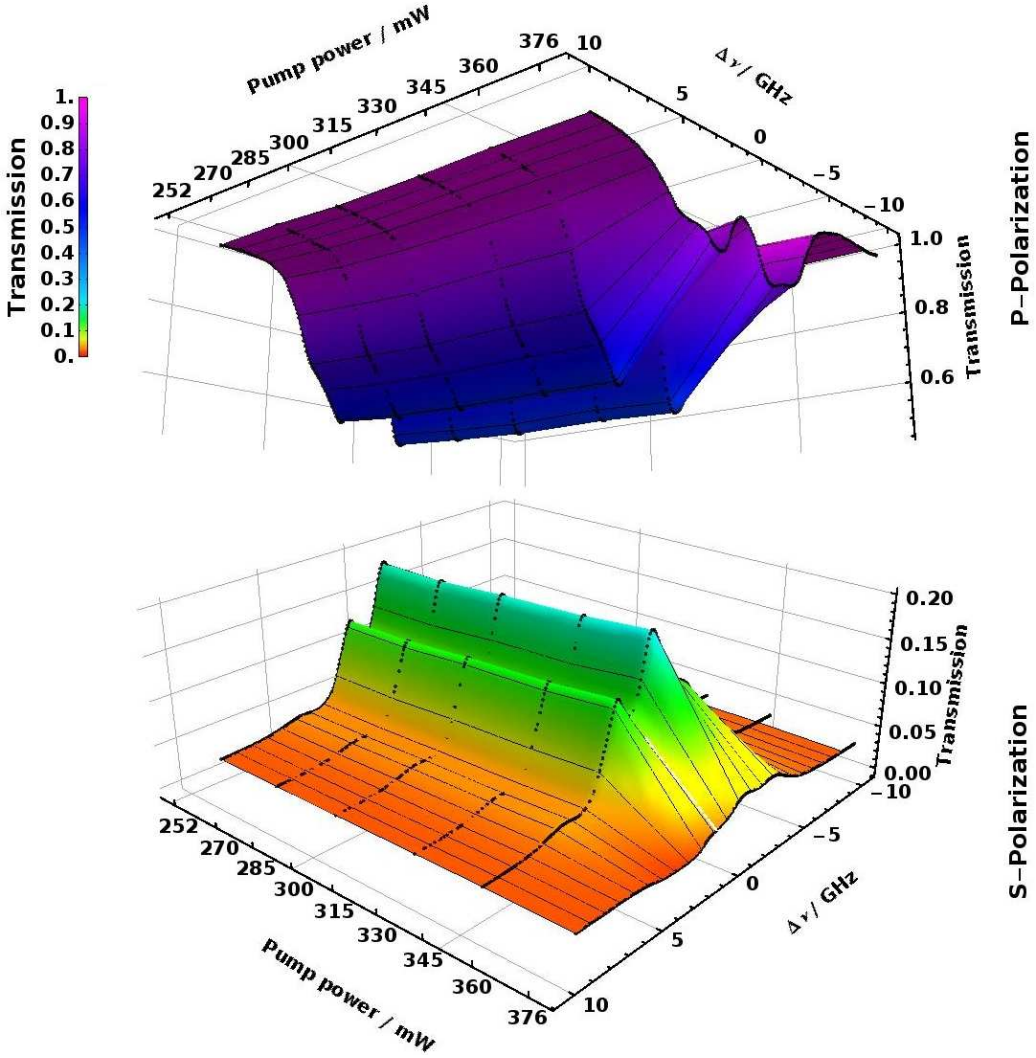

Fig. 5.12: 3D representation of the recorded ESFADOF transmission hysteresis, when increasing the pump power: The upper part of the figures represent the P-polarization of the ESFADOF output PBS and the lower part its S-polarization. The cell temperature was $T_{ESFADOF} = 165.5°C$ and a magnetic field strength of $B_z = 270$ mT has been applied to vapor cell I. The pump power P_{Pump} has been changed adiabatically, while keeping the linear polarized pump beam $\Delta\nu_P = -1.76(3)$ GHz detuned from the $5S_{1/2} \rightarrow 5P_{3/2}$ transition center. The ESFADOF transmission spectra collapse at $P_{Pump} = 376(1)$ mW after adiabatically increasing the pump power and the maximum ESFADOF transmission drops from 19.71(1)% at $P_{Pump} = 349$ mW to 4.77(1)%. A 2D plot representation of the S-polarization can be found in Fig. 5.14.

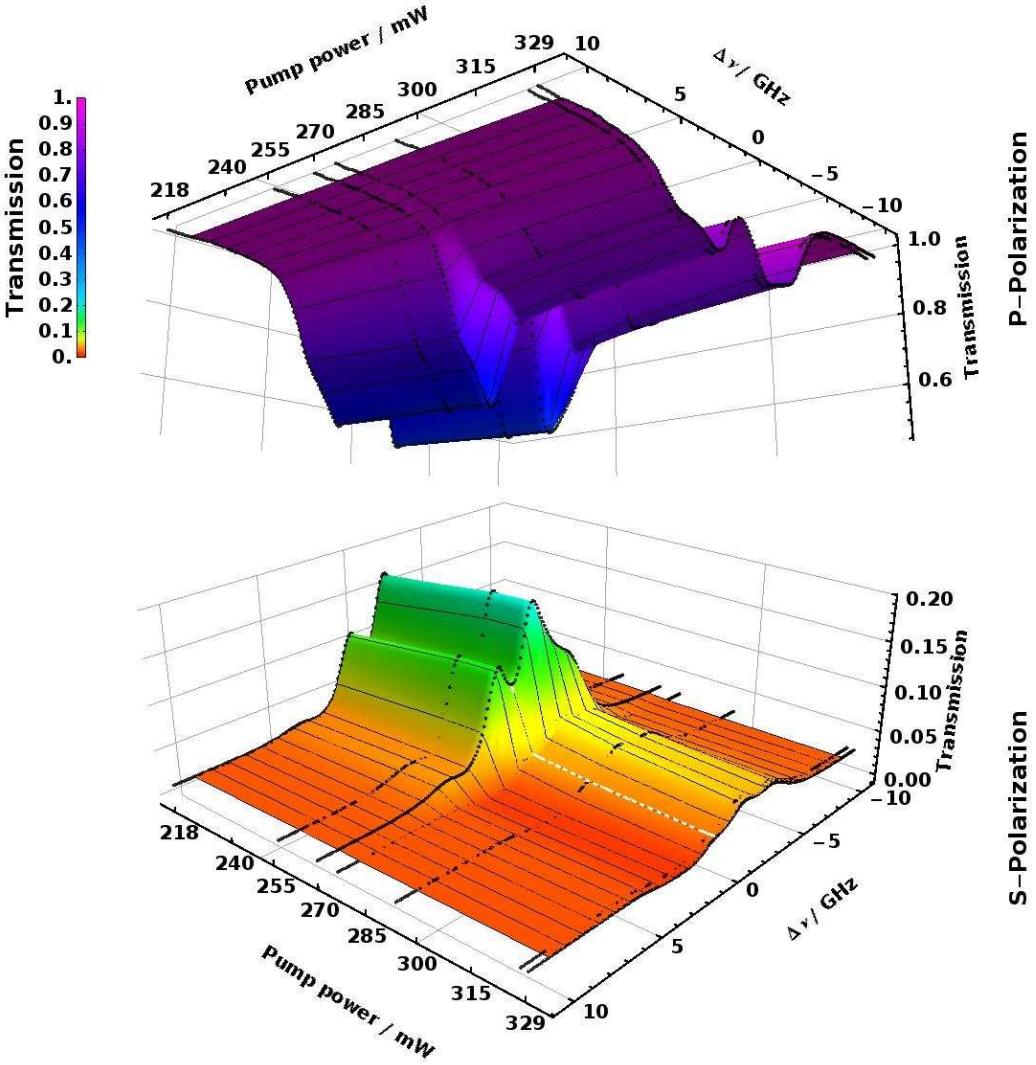

Fig. 5.13: 3D representation of the recorded ESFADOF transmission hysteresis, when decreasing the pump power: All other parameters correspond to Fig. 5.12 and only the direction of the pump power change has been reversed. The ESFADOF transmission spectra recover at 270 mW while adiabatically decreasing the pump power P_{Pump} and the maximum ESFADOF transmission rises from 6.72(1)% at $P_{Pump} = 278$ mW to 19.11(1)% respectively. Striking is the hysteretic behavior once the laser-induced plasma sets in. Compared to Fig. 5.12, where the pump power has been increased, the system shows, depending on the pump history, between $P_{Pump} = 270$ mW and $P_{Pump} = 376$ mW two stable states. A 2D representation of the S-polarization can be found in Fig. 5.15.

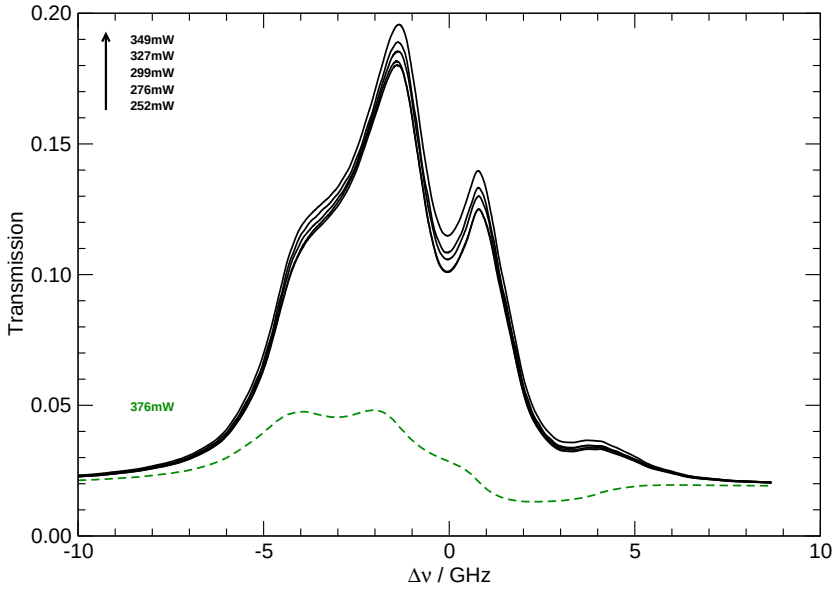

Fig. 5.14: 2D representation of the recorded ESFADOF transmission hysteresis, when increasing the pump power: The plot shows the same data as Fig. 5.12 and the arrow indicates the direction of power change.

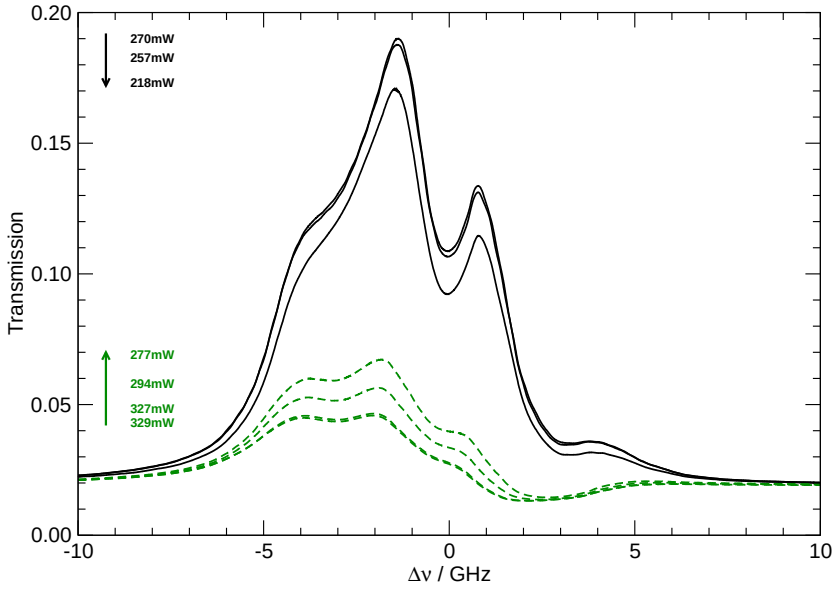

Fig. 5.15: 2D representation of the recorded ESFADOF transmission hysteresis, when decreasing the pump power: The plot shows the same data as Fig. 5.13 and the arrows indicate the direction of power change.

cesses of the atomic vapor. This allows for a full equilibration of the system before further changes occur. Striking is the fact, that the history of the injected pump intensity influences the ESFADOF transmission once the plasma phase has been induced. Furthermore, inspecting the data reveals the following details:

1. The ESFADOF transmission spectra undergo sudden changes, which depend on the systems history. Between $P_{Pump} = 270(1)$ mW and $P_{Pump} = 376(1)$ mW two stable states exist.
2. It is possible to cycle through the hysteresis loop repeatedly, by tuning the pump power.
3. The ESFADOF transmission spectrum collapses at 376(1) mW, when adiabatically increasing the pump power P_{Pump}. The maximum ESFADOF transmission changes from 19.71(1)% at $P_{Pump} = 349(1)$ mW to 4.77(1)%.
4. The ESFADOF transmission spectra recover at 270(1) mW, when adiabatically decreasing the pump power P_{Pump}. The maximum ESFADOF transmission rises from 6.72(1)% at $P_{Pump} = 277(1)$ mW to 19.11(1)%.
5. When increasing the pump power (cf. Fig. 5.12 and Fig. 5.14), the maximum ESFADOF transmission slightly increases between $P_{Pump} = 270$ mW and $P_{Pump} = 349(1)$ mW by 2.11(1)%, revealing a positive slope of 0.02%/mW. Due to the highly saturated medium, increasing the pump intensity induces only small changes on the lower ESFADOF state population.
6. When decreasing the pump power (cf. Fig. 5.13 and Fig. 5.15), the maximum ESFADOF transmission slightly increases between $P_{Pump} = 329(1)$ mW and $P_{Pump} = 277(1)$ mW by 2.8(1)%, revealing a negative slope of -0.04%/mW. Hence, increasing the pump power on this branch of the hysteresis has the opposite effect. Once the system is in the plasma state the consumption of the lower ESFADOF state population dominates and increases with increasing pump intensity.
7. In addition, the 2D representation of the data (cf. Fig. 5.14 and Fig. 5.15) reveal significant changes of the spectral shape, which indicates the loss of the former degree of atomic polarization, which has been imposed by the pump laser and the trapped radiation.

In addition, the hysteresis of the ESFADOF device is also reflected by the absorbed pump intensity. Specifically, tilting the feedback mirror (HR-IR behind the vapor cell in Fig. 4.4) by 45° allows the measurement of the transmitted pump power by an additional power meter. Figure 5.16 shows a compilation of measured Rb vapor cell transmissions of the pump beam for two different temperatures, $T_{ESFADOF} = 165°C$ and $T_{ESFADOF} = 173°C$. The arrows in the plot indicate the direction of the adiabatic pump power change.

When considering only the case where the cell temperature was $T_{ESFADOF} = 165°C$, the plot can be decomposed into 3 different regimes: (1) For pump powers of up to approx. 160 mW the transmission shows a linear behavior, (2) between 160 mW and 240 mW a kink in the transmission appears, whereas (3) the transmission saturates to approx. 28%. In contrast to Figs. 5.12 and 5.13, the

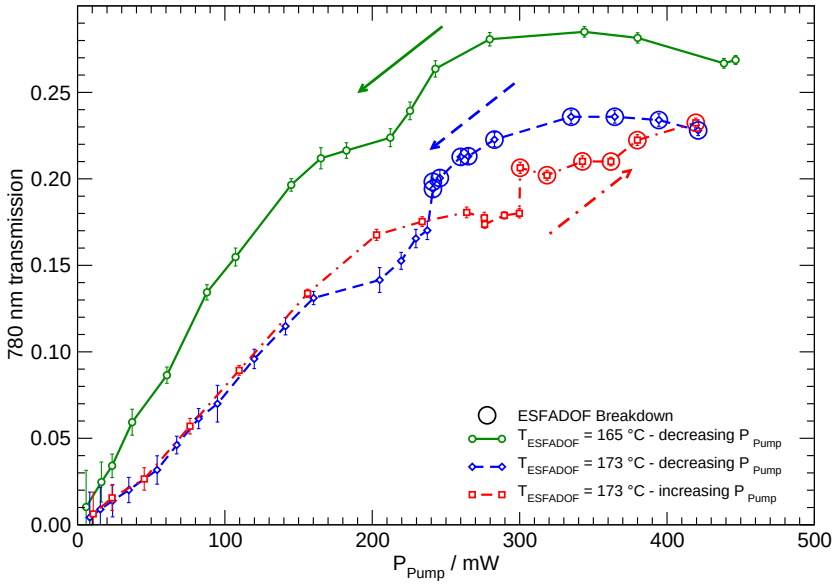

Fig. 5.16: Transmission of the 780 nm pump beam through the Rb vapor cell I for two different cell temperatures: The magnetic field strength was $B_z = 270$ mT and a parallel polarized pump beam with a detuning of $\Delta\nu_P = -1.76(3)$ GHz has been injected into the cell while adiabatically changing the pump power P_{Pump}. The arrows indicate the direction of power change. At low pump powers a linear behavior of the transmission can be observed, whereas the transmission shows pronounced kinks and saturates at high pump powers. The $T_{ESFADOF} = 173°C$ case reveals two different hystereses. The first one, around a pump power of 200 mW, indicates feedback driven optical bistability [194] and the second one, marked by the circled data points, has its origins in the onset of a laser-induced plasma inside the Rb vapor.

formation of a laser induced plasma could not be observed any more. This can be attributed to the lack of reinjected pump laser power by the tilted feedback mirror. However, the situation changes dramatically when increasing the temperature of the vapor cell to $T_{ESFADOF} = 173°C$, which results also in a Rb vapor density increase. Although the feedback mirror remained tilted a plasma has been induced inside the vapor cell. The circled data points in Fig. 5.16 mark the observed laser induced plasma. Striking is the fact that the data reveals two different hystereses. The downward directed branch corresponds to a pump power decrease (blue dashed curve in Fig. 5.16) and the upward directed one to a pump power increase (red dot dashed curve in fig, 5.16). Both curves follow the same path up to a pump power of $P_{Pump} = 160$ mW and differ significantly beyond this value. In contrast to the colder cell, a first kink appears at approx. $P_{Pump} = 45$ mW and, despite the coarse resolution, indicates a first nonlinear behavior. For higher pump powers the following observations result:

1. The red upward directed curve shows a higher transmission than the blue downward directed curve between $P_{Pump} = 160$ mW and $P_{Pump} = 240$ mW.

The latter exhibits a clear kink between these limits. Noticeable is the fact that within the errors of the measurement the turning points of this kink correspond to the one already observed for $T_{ESFADOF} = 165°C$. Unfortunately the upward directed case for $T_{ESFADOF} = 165°C$ has not been measured. Due to the lack of optical feedback by the tilted mirror, optical bistability has not been expected [194, 195]. However, the measurements with $T_{ESFADOF} = 173°C$ indicate optical bistability for this pump power range. This hysteresis resembles the one reported by Ackemann *et al.* [194]. Although direct feedback was not present, it is reasonable to assume that the strong nonlinear coupling of the pumped Rb atoms with the trapped radiation together with the Fresnel reflections of the window panes is responsible for the encountered optical bistability. This assumption is corroborated by several other publications [177, 178, 196, 197]. However, Ackemann *et al.* emphasized, that the encountered resonatorless optical bistability emerges from transversal magnetic fields, which allow for light induced level crossings [194]. Thus, the recorded optical bistability has its origins in those parts of the vapor cell, where transverse magnetic fields dominate, i.e. apart from the pump beam injection, where the permanent ring magnets reside. On the other hand, the ESFADOF spectral characteristics emerge from the longitudinal magnetic field components, which dominate the first part of the Rb vapor cell (cf. fig. 4.2(a)). Further investigations of this topic have been omitted as they do not contribute directly to the main purpose of this thesis.

2. Increasing the pump power further leads to a saturation of the red upward directed curve and at a pump power of $P_{Pump} = 300$ mW a sudden change in transmission occurs. At this value the cell transmission increases stepwise by 2.6(3)% after slightly increasing the pump power. Any further pump power increment leads only to small changes in transmission. After reaching $P_{Pump} = 420$ mW the pump power has been decreased subsequently and the blue downward directed curve results. Compared to the red upward directed one, this curve shows an overall higher transmission up to $P_{Pump} = 240$ mW. Decreasing the pump power further again results in a stepwise change of transmission, which decreases approximately by the same amount, i.e. by 2.4(4)%. At this point both curves intersect. Again, together with the stepwise changes in pump power transmission, which lies 60 mW apart, the laser-induced plasma suddenly sets in or ceases, when increasing or decreasing the pump power respectively. The circled data points in Fig. 5.16 mark the observation of the laser-induced plasma by the emitted fluorescence spectrum. A detailed discussion of the emitted fluorescence will be given in Sec. 5.3.2.

In conlusion, both hysteresis are particularly remarkable: The first develops due to the feedback action of the trapped radiation inside the high opaque Rb vapor in combination with the presence of transverse magnetic fields [194, 195]. The second hysteresis dramatically affects the population of the pumped level and hence the ESFADOF transmission. But, in contrast to the first discussed above, the second does not emerge from external feedback. It is rather an intrinsic property of the laser-induced plasma inside the hot high density vapor. Sec. 5.3.3 will elab-

orate this further by taking the different reaction chains, which give rise to and maintain the laser induced plasma, into consideration.

5.3.2 Laser-Induced Plasma

This section is intended to elaborate the physics behind the laser-induced plasma as the main limiting factor of the ESFADOF operation in alkali-metal vapors. The fluorescence spectrum, which emanates from the vapor cell, confirms the plasma formation and a comparison with the literature allows to pinpoint the involved reaction chains.

Fig. 5.17a shows a fluorescence spectrum recorded after the collapse of the ESFADOF spectra and Fig. 5.17b shows a spectrum after decreasing the pump power, i.e. when the ESFADOF spectra has recovered. They have been recorded far away from the pumped volume on the opposite side of the vapor cell. The fluorescence has been captured by an optical fiber and examined by an optical spectrum analyzer (AvaSpec-1024-2, cf. Fig. 4.4). Examining the fluorescence of the Rb vapor reveals the following general behavior:

1. Below the ESFADOF breakdown threshold, the fluorescence of the direct pumped transition as well as energy-pooling processes (cf. Sec. 3.6.2) dominate the spectrum and the fluorescence emerging from the energy-pooling process can only be observed within the pumped volume. This fluorescence results from collisions of two excited Rb atoms, which transfer one atom to the ground state and the second atom to an even higher level [140], from where the atom decays spontaneously. Thus, the fluorescence from these levels is an indicator of energy-pooling. A possible energy defect is provided by the kinetic energy of the collision partners. As the energy-pooling processes consume the population of the lower ESFADOF state, a reduction in ESFADOF transmission is the direct consequence.
2. The fluorescence spectrum of the Rb vapor gains significantly in complexity and extends over the whole vapor cell, when the plasma formation threshold has been exceeded. Thus, an important amount of Rb atoms far away from the pumped volume are excited to high lying states.
3. Reducing the pump power or the spectral overlap between the pump laser and the D2 absorption line by detuning the pump laser wavelength, recovers the ESFADOF spectra and limits the energy-pooling processes again to the pumped volume.

Tab. 5.1 summarizes the observed Rb transition lines. Striking is the fact that every Rb spectral line within the sensitivity range of the employed spectrometer can be observed above the plasma threshold and that high lying Rydberg-states as high as the $11s_{1/2}$ state (line 7) located at 3.957502 eV, just 0.2195 eV below the Rb ionization limit of $E_{Ion}^{Rb} = 4.1771$ eV [199], have been excited [144]. However, when allowing only energy-pooling processes such highly excited states, as the $11S_{1/2}$ level, can not be populated. A comparison of the measured fluorescence spectra to those measured by Saha *et al.* , who give a detailed characterization of

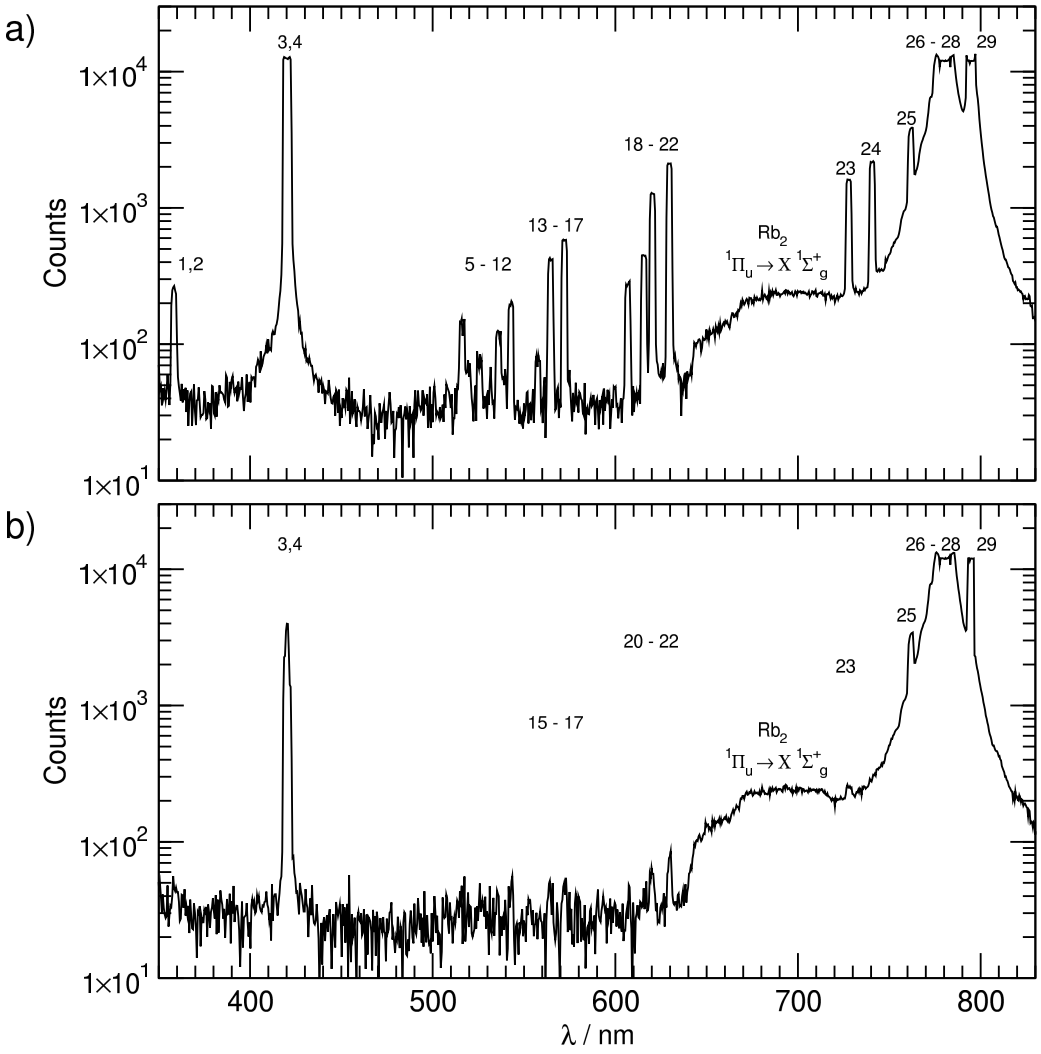

Fig. 5.17: Fluorescence spectra of the Rb vapor cell, recorded far apart from the pumped volume and at a cell temperature of $T_{\mathrm{ESFADOF}} = 173\ ^{\circ}\mathrm{C}$; with kind permission from Springer Science+Business Media [93]: The numbers correspond to the transition lines listed in Tab. 5.1. As the spectrometer's resolution is 1 nm, not every single transition is fully resolved. The $^1\Pi_\mathrm{u} \rightarrow X\,^1\Sigma_\mathrm{g}^+$ transition of the Rb dimer between 650–710 nm is clearly visible in both spectra [198]: a) Spectrum recorded after exceeding the laser-induced-plasma threshold. The pump power was $\mathrm{P_{Pump}} = 500$ mW and the maximum ESFADOF transmission collapses to 6.62(1)%. The 780 nm pump wavelength dominates the right part and buries some unresolved spectral lines. The captured intensity of the lines 3,4 and 29,30 saturate the spectrometer CCD. b) By decreasing the pump power to $\mathrm{P_{Pump}} = 253$ mW the ESFADOF spectra recover to a maximum transmission of 14.6% and the fluorescence spectra lose complexity. Only the dominant contributions from the energy-pooling process remain visible, while the spatial distribution reduces to the pumped volume. Here, only the lines 29 and 30 saturate the spectrometer CCD. The lines 3 and 4 are now clearly visible.

Table 5.1: Summary of the observed transition lines: The line numbers correspond to the one used in Fig. 5.17 and the recorded spectra have been compared with Kurucz atomic line database [144]. Values are taken from the Kurucz atomic line database. As electron capture by the Rb^+-ions into high lying Rydberg-states drive the excitation of these high levels, it is reasonable that all energetically close levels are excited [200, 201]. The pump transition is bold.

Line number	λ_{Vac} / nm	Transition	Line number	λ_{Vac} / nm	Transition
1	358.8070	$7P_{3/2} \rightarrow 5S_{1/2}$	16	572.5695	$7D_{5/2} \rightarrow 5P_{3/2}$
2	359.2593	$7P_{1/2} \rightarrow 5S_{1/2}$	17	572.6190	$7D_{3/2} \rightarrow 5P_{3/2}$
3	420.2972	$6P_{3/2} \rightarrow 5S_{1/2}$	18	607.2427	$8S_{1/2} \rightarrow 5P_{1/2}$
4	421.6706	$6P_{1/2} \rightarrow 5S_{1/2}$	19	616.1324	$8S_{1/2} \rightarrow 5P_{3/2}$
5	516.6504	$4D_{3/2} \rightarrow 5S_{1/2}$	20	620.8022	$6D_{3/2} \rightarrow 5P_{1/2}$
6	516.6621	$4D_{5/2} \rightarrow 5S_{1/2}$	21	630.0066	$6D_{5/2} \rightarrow 5P_{3/2}$
7	517.1088	$11S_{1/2} \rightarrow 5P_{1/2}$	22	630.0963	$6D_{3/2} \rightarrow 5P_{3/2}$
8	532.3850	$10S_{1/2} \rightarrow 5P_{1/2}$	23	728.1995	$7S_{1/2} \rightarrow 5P_{1/2}$
9	536.4084	$8D_{3/2} \rightarrow 5P_{1/2}$	24	741.0207	$7S_{1/2} \rightarrow 5P_{3/2}$
10	539.2057	$10S_{1/2} \rightarrow 5P_{3/2}$	25	762.1021	$5D_{3/2} \rightarrow 5P_{1/2}$
11	543.3035	$8D_{5/2} \rightarrow 5P_{3/2}$	26	775.9782	$5D_{5/2} \rightarrow 5P_{3/2}$
12	543.3333	$8D_{3/2} \rightarrow 5P_{3/2}$	27	776.1564	$5D_{3/2} \rightarrow 5P_{3/2}$
13	558.0326	$9S_{1/2} \rightarrow 5P_{1/2}$	**28**	**780.2405**	$\mathbf{5P_{3/2} \rightarrow 5S_{1/2}}$
14	564.9329	$7D_{3/2} \rightarrow 5P_{1/2}$	29	794.9783	$5P_{1/2} \rightarrow 5S_{1/2}$
15	565.5309	$9S_{1/2} \rightarrow 5P_{3/2}$			

the violet emission from heavily optically pumped Rb vapors [200], and by Ban *et al.* , who investigated the Rb_2 diffuse band emission [201], sheds more light on the above observations. The measured fluorescence spectra of Fig. 5.17 agree in detail with the ones published by the cited authors and suggest the induction of a plasma inside the vapor cell. In addition, the sudden spatially extended phase change of the Rb vapor can not be explained by energy-pooling processes, though they are responsible for the induction of the reaction chains, which maintain the laser-induced plasma [190]. A more detailed discussion of the underlying physical processes sheds more light on these observations.

In fact, the energy pooling process, which is driven by the optical pumping on the $5S_{1/2} \rightarrow 5P_{3/2}$ transition, is the key-process for the formation of the laser-induced plasma, as it moderately populates some excited atomic levels, from which ionization processes occur [190]. Specifically, the Rb(6P), Rb(5D) and Rb(7S) levels are energetically close to the Rb(5P) + Rb(5P) molecular asymptotes. By taking optical pumping into consideration ($h\nu_P$ represents the energy of the 780 nm pump photon) these levels are populated by the following reaction chains [140, 201, 202]:

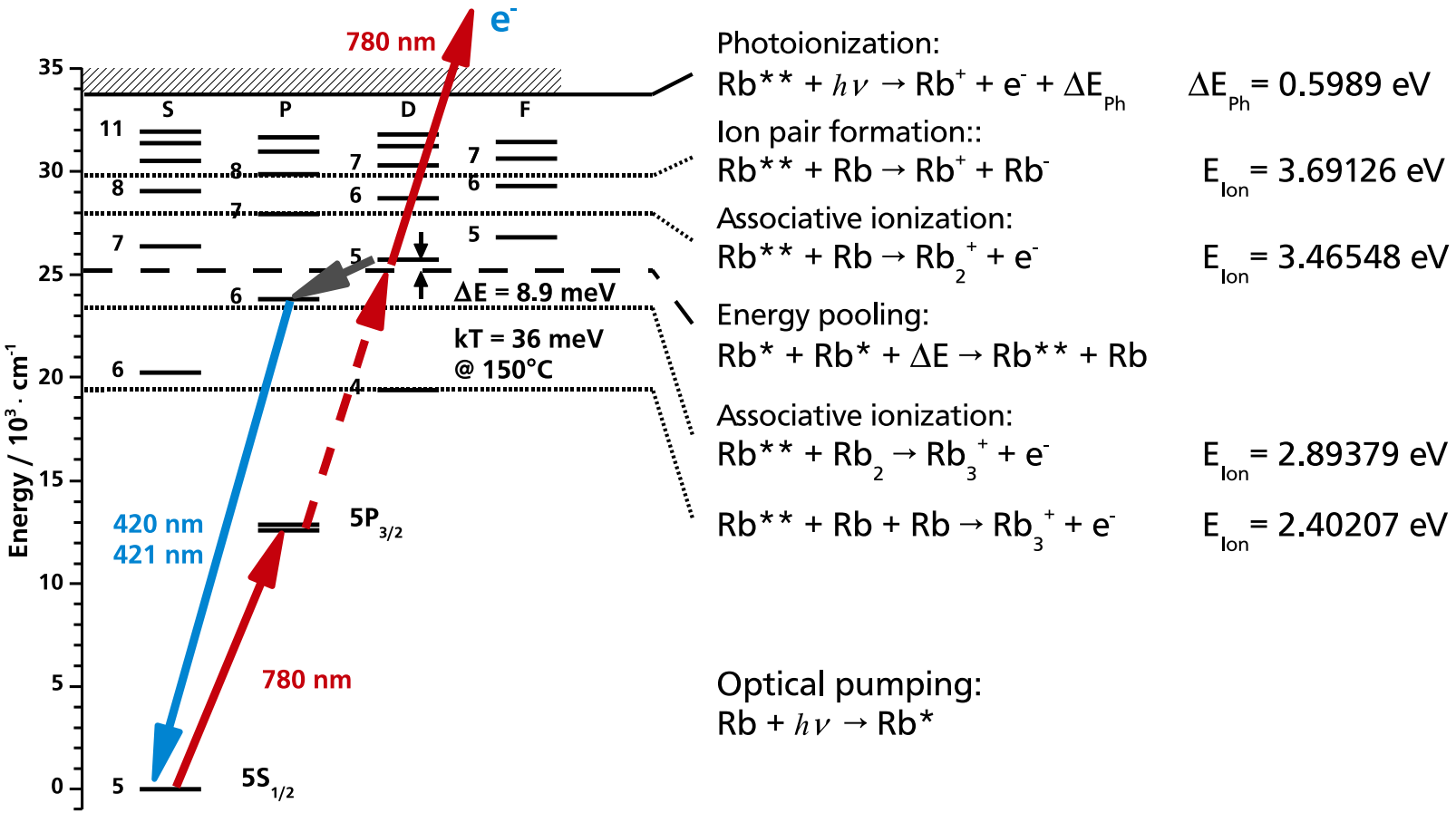

Fig. 5.18: Rubidium Grotian energy level diagram together with some ionization potentials: Photonic transitions are indicated by solid arrows and the main energy pooling pathway, reaction 5.13, is indicated by the broken arrow. The solid line marks the ionization potential of one single Rb atom and the dashed line marks the energy sum of the quoted energy-pooling process. Dotted lines mark the corresponding threshold energies E_{Ion} for the listed ionization processes. The photoionization process result in an energy excess of $\Delta E_{Ph} = 0.5989$ eV, which is transferred to the electron. Reactions and energetics accord with Refs. [186, 190, 201].

- Energy pooling:

$$\mathrm{Rb}(5S_{1/2}) + h\nu_P \rightarrow \mathrm{Rb}^{*}(5P_{3/2}) \tag{5.11}$$

$$\mathrm{Rb}^{*}(5P_{3/2}) + \mathrm{Rb}^{*}(5P_{3/2}) + \Delta E \rightarrow \mathrm{Rb}^{**}(6P_{1/2,3/2}) + \mathrm{Rb}(5S_{1/2}),\quad \Delta E = \text{-}0.2118\ \mathrm{eV} \tag{5.12}$$

$$\mathrm{Rb}^{*}(5P_{3/2}) + \mathrm{Rb}^{*}(5P_{3/2}) + \Delta E \rightarrow \mathrm{Rb}^{**}(5D_{3/2,5/2}) + \mathrm{Rb}(5S_{1/2}),\quad \Delta E = 0.0283\ \mathrm{eV} \tag{5.13}$$

$$\mathrm{Rb}^{*}(5P_{3/2}) + \mathrm{Rb}^{*}(5P_{3/2}) + \Delta E \rightarrow \mathrm{Rb}^{**}(6S_{1/2}) + \mathrm{Rb}(5S_{1/2}),\quad \Delta E = 0.1034\ \mathrm{eV} \tag{5.14}$$

Negative values for ΔE represent an energy excess, whereas positive values stand for energy defects. The energy gap is compensated by the thermal bath, as the mean kinetic energy of the Rb atoms, $\frac{3}{2}$kT, lies between 55–61 meV for the vapor temperatures of interest, $T_{ESFADOF} = 150 - 200°C$. Ban *et al.* investigated the emitted spectral intensity for different pump intensities [201]. They found, that in particular the blue fluorescence line 4 (420.2 nm, cf. Fig. 5.17 and Tab. 5.1) exhibits a quadratic dependency on the injected pump intensity. From that observation they conclude that the energy-pooling process is the dominant population mechanism of the Rb($6P_{3/2}$) state (marked by a broken arrow in Fig. 5.18). Additionally, their quoted laser induced fluorescence spectrum (Fig. 3 in Ref. [201]) does not show the same pronounced spectral lines emerging from high lying excited states. Thus, they operate below the plasma formation threshold. Their far detuned pump laser, which operates at 782 nm and the presence of additional buffer gas (52 Torr of Argon) corroborate this observation. Hence, they exclude three photon ionization and subsequent recombination as the effective population mechanism for the Rb($6P_{3/2}$) level. This observation agrees well with Fig. 5.17b, which has been recorded below the plasma formation threshold. There, a pronounced peak at 420 nm confirms the population of the Rb(6P) levels by the energy-pooling process. The absence of the majority of all other transition lines, which mainly emerge from high lying Rydberg-states, discard ionization processes and subsequent recombination into Rydberg-states.

The case changes dramatically as soon as the ESFADOF spectra collapse (cf. Fig. 5.17a). A large amount of transition lines appear. They emerge from high lying Rydberg-states. In particular line 7 starts from the $11S_{1/2}$ state, which lies only 0.2195 eV below the Rb ionization limit. As the above discussion showed, these high lying states can not be populated by the energy-pooling process. Thus, only ionization processes and subsequent recombination into Rydberg-states is able to explain the fluorescence spectrum of Fig. 5.17a. In addition, the entire vapor cell volume shows similar emission spectra, as soon as the breakdown of the ESFADOF spectra occurs. In conclusion, a plasma is induced and maintained by the pump laser, once the mentioned thresholds have been exceeded [189, 190]. These observations agree well with the observations of Saha *et al.*, which characterized the violet emission from heavily optically pumped Rb vapor [200].

By comparing the Rb energy level diagram (cf. Fig. 5.18) with the potentials for several ionization pathways it is possible to pinpoint the following reaction chains, which lead to the ionization of the Rb vapor [186, 187, 190, 201]:

- Penning ionization, e.g.:

$$\begin{aligned} Rb^{**}(6D_{3/2}) + Rb^{*}(5P_{3/2}) &\rightarrow Rb^{+} + Rb(5S_{1/2}) + e^{-} \\ Rb^{**}(6D_{5/2}) + Rb^{*}(5P_{3/2}) &\rightarrow Rb^{+} + Rb(5S_{1/2}) + e^{-} \\ Rb^{**}(8S_{1/2}) + Rb^{*}(5P_{3/2}) &\rightarrow Rb^{+} + Rb(5S_{1/2}) + e^{-} \\ Rb^{**}(7D_{5/2}) + Rb^{*}(5P_{3/2}) &\rightarrow Rb^{+} + Rb(5S_{1/2}) + e^{-} \end{aligned} \tag{5.15}$$

- Ion-pair formation:

$$Rb^{**}(8P_{1/2}) + Rb \rightarrow Rb^{+} + Rb^{-}\ ,\ E_{Ion} = 3.69126\ \text{eV} \tag{5.16}$$

- Two-body associative ionization to the Rb dimer ion:

$$Rb^{**}(6D_{3/2}) + Rb \rightarrow {Rb_2}^{+} + e^{-}\ ,\ E_{Ion} = 3.46548\ \text{eV} \tag{5.17}$$

- Two-body associative ionization to the Rb trimer ion:

$$Rb^{**}(6P_{1/2}) + Rb_2 \rightarrow {Rb_3}^{+} + e^{-}\ ,\ E_{Ion} = 2.89379\ \text{eV} \tag{5.18}$$

- Three-body associative ionization to the Rb trimer ion:

$$Rb^{**}(6S_{1/2}) + Rb + Rb \rightarrow {Rb_3}^{+} + e^{-}\ ,\ E_{Ion} = 2.40207\ \text{eV}. \tag{5.19}$$

The amount of excitation, E_{Ion}, needed to produce these types of ionization lies well within the energetics of the recorded fluorescence (cf. Fig. 5.18). However, when allowing only energy pooling processes, reactions 5.18 and 5.19 are the only possible ionization pathways which themselves produce free electrons, though reaction 5.19 is less probable as it involves three-body collisions. Remarkable is the fact, that the dissociative recombination of the Rb trimer ion results in neutral Rb atoms in the ground state [201]. Hence, photoionization of the excited Rb atoms is mandatory for producing Rb^{+}-ions [186]:

- Photoionization:

$$\begin{aligned} Rb^{**}(5D_{3/2}) + h\nu_P &\rightarrow Rb^{+} + e^{-} + \Delta E_{Ph}\ ,\ \Delta E_{Ph} = 0.5986\ \text{eV} \\ Rb^{**}(5D_{5/2}) + h\nu_P &\rightarrow Rb^{+} + e^{-} + \Delta E_{Ph}\ ,\ \Delta E_{Ph} = 0.5990\ \text{eV} \end{aligned} \tag{5.20}$$

$$\begin{aligned} Rb^{**}(6P_{1/2}) + h\nu_P &\rightarrow Rb^{+} + e^{-} + \Delta E_{Ph}\ ,\ \Delta E_{Ph} = 0.3525\ \text{eV} \\ Rb^{**}(6P_{3/2}) + h\nu_P &\rightarrow Rb^{+} + e^{-} + \Delta E_{Ph}\ ,\ \Delta E_{Ph} = 0.3621\ \text{eV} \end{aligned} \tag{5.21}$$

ΔE_{Ph} represents the energy excess of this process. When taking the conservation of momentum in combination with the vanishing ratio between the involved masses ($m_e/m_{Rb} \ll 1$) into consideration, this energy excess is transferred mainly to the released free electron: $\frac{1}{2} m_e v_e^2 = \Delta E/(1+\frac{m_e}{m_{Rb}})$. The cross-section of these

processes are $\sigma_{\text{PI-5D}} = 16 \times 10^{-18}$ cm^2 and $\sigma_{\text{PI-5D}} = 15 \times 10^{-18}$ cm^2 for the 5D and 6P states respectively [186]. These values are 4 orders of magnitude lower than the energy-pooling cross-section $\sigma^{\text{EP}}_{5\text{P}_{3/2}\leftrightarrow 5\text{D}} = 3 \times 10^{-14}$cm^2 [140] and 9 orders of magnitude lower than the Doppler-width integrated D2 absorption cross section ($\sigma_{\text{D}}^{\text{D2}} = 6 \times 10^{-9}$cm^2). However, once Rb^+ ions and free electrons are available, they can produce other ions by subsequent processes. In particular, when examining the later discussed recombination reaction of Rb^+ ions (reaction 5.30), it can be seen, that they always result in neutral, highly excited Rb atoms. In addition, these highly excited levels are susceptible for Honbeck-Molnar ionization [187, 188]:

- Honbeck-Molnar ionization: nl$\geq$5D

$$\text{Rb}^{**}(\text{nl}) + \text{Rb}(5\text{S}_{1/2}) \rightarrow \text{Rb}_2^+ + \text{e}^- \tag{5.22}$$

In addition to the creation, transfer and decay processes have to be considered as well. They play a significant role in the maintenance of the plasma phase. Generally speaking, each creation process has its reversed representation by simple time reversal, e.g. energy transfer collisions can also produce two moderately excited atoms from only one highly excited one:

- Energy transfer collisions:

$$\text{Rb}^{**} + \text{Rb} \rightarrow \text{Rb}^{*} + \text{Rb}^{*} \tag{5.23}$$

This is the inversion of the energy pooling process (cf. reactions 5.12–5.14). Processes involving electrons have to be considered as well. Of particular interest are superelastic collisions:

- Superelastic collisions:

$$\text{Rb}^{*} + \text{e}^- \rightarrow \text{Rb} + (\text{e}^-)^{*} \tag{5.24}$$

$(\text{e}^-)^{*}$ indicates a translationally hot electron that can provide the energy for various processes, as

- Collisional excitation (inverse of reaction 5.24):

$$\text{Rb} + (\text{e}^-)^{*} \rightarrow \text{Rb}^{*} + \text{e}^- \tag{5.25}$$

- Collisional ionization of excited Rb atoms by hot electrons:

$$\text{Rb}^{*} + (\text{e}^-)^{*} \rightarrow \text{Rb}^{+} + 2\text{e}^- \tag{5.26}$$

The same argument, which applied for the photoionization, has to be considered again when regarding the conservation of momenta of superelastic collisions. This circumstance provides the electrons with the majority of the excitation energy and considerably heats the electron temperature of the plasma to thousands of Kelvin,

though the ions still reflect the temperature of the surrounding bath [180]. In particular, these hot electrons are able to excite or to ionize atoms not directly affected by the pump beam [185]. In combination with the ionic transfer processes (see below) a considerable amount of excitation leaves the direct pumped volume and explains the observed fast ionization of the whole vapor cell.

When considering the produced atomic and molecular ions, alkali-metals tend to convert atomic ions into molecular ones, as these processes are significantly exoergic (cf. reactions 5.17– 5.19 and Fig. 5.18) [190]:

- Ionization transfer: $E_{Ion}(Rb) > E_{Ion}(Rb_2) > E_{Ion}(Rb_3)$

$$Rb^+ + Rb_2 \rightarrow Rb_2^+ + Rb(5S_{1/2}) \tag{5.27}$$
$$Rb_2^+ + Rb_2 \rightarrow Rb_3^+ + Rb(5S_{1/2}) \tag{5.28}$$

However, further conversion to Rb_n^+ $(n > 3)$ does not occur because $E_{Ion}(Rb_4) > E_{Ion}(Rb_3)$ [190]. In conclusion, the laser induced plasma consists of a mixture of Rb^+, Rb_2^+ and Rb_3^+, with Rb_3^+ dominating at high temperatures in the thermal equilibrium. Stwalley and Bahns quote a relationship of 99:1 between the ionized Rb trimer (Rb_3^+) and the sum of the Rb monoatomic and dimer ions (Rb^+, Rb_2^+) [190]. However, the fluorescence spectrum, which emerges from the laser-induced plasma (cf. Fig. 5.17a), proves the existence of highly excited monoatomic Rubidium. These Rydberg-states result from the different recombination processes, as radiative recombination by the Rb^+-ion and three-body recombination ($h\nu$ represents the different energies of the decay photons) [190]:

- Radiative recombination:

$$Rb^+ + e^- \rightarrow Rb^{**} \rightarrow Rb^* + h\nu \rightarrow Rb + h\nu + h\nu \tag{5.29}$$

- Three-body recombination:

$$Rb^+ + e^- + \left\{ \begin{matrix} Rb \\ e^- \end{matrix} \right\} \rightarrow Rb^{**} + \left\{ \begin{matrix} Rb \\ e^- \end{matrix} \right\} \tag{5.30}$$

Reaction 5.29 is highly restricted due to the conservation of linear and angular momentum, whereas the three-body recombination is not. For the molecular ions dissociative recombination dominates and again many different states can be produced:

- Dissociative recombination:

$$Rb_2^+ + e^- \rightarrow \left\{ \begin{matrix} Rb^* + Rb \\ Rb^* + Rb^* \end{matrix} \right\} \tag{5.31}$$
$$Rb_3^+ + e^- \rightarrow \left\{ \begin{matrix} Rb_2^* + Rb \\ Rb_2 + Rb^* \end{matrix} \right\} \tag{5.32}$$

More precisely, Ban *et al.* conclude from their observations that the recombination of the Rubidium trimer ion produces Rb ground state atoms, where an energy excess of $\Delta E^{e^-}_{Rb_3^+} = 0.417715$ eV is released to the thermal energy of the vapor. They showed that the following ionization and subsequent recombination chain contributes to the population of the $Rb_2(2^3\Pi_g)$ state [201]:

- Two-body associative ionization to the Rb trimer ion (cf. reaction 5.18):

$$Rb^{**}(6P_{1/2}) + Rb_2(X^1\Sigma_g^+) \rightarrow {Rb_3}^+ + e^- \tag{5.33}$$

- Subsequent dissociative recombination (cf. reaction 5.32):

$$ {Rb_3}^+ + e^- \rightarrow Rb_2(2^3\Pi_g) + Rb(5S_{1/2}) + \Delta E^{e^-}_{Rb_3^+} \tag{5.34}$$

$$ Rb_2(2^3\Pi_g) \rightarrow Rb_2(1^3\Sigma_u^+) + h\nu \tag{5.35}$$

$$ Rb_2(1^3\Sigma_u^+) \rightarrow Rb(5S_{1/2}) + Rb(5S_{1/2}) \tag{5.36}$$

The excited $Rb_2(2^3\Pi_g)$ molecules relax to the $Rb_2(1^3\Sigma_u^+)$ state and the emitted photons, $h\nu$, form a diffuse band between 602 nm and 609 nm. The fact that the molecular asymptotes of the $Rb_2(1^3\Sigma_u^+)$ state result in the dissociation of the Rb dimer to $Rb(5S_{1/2})$ ground state atoms (reaction 5.36) is remarkable.

However, the fact, that this diffuse band could not be observed in Fig. 5.17 needs some further consideration. From the measurements of Ban *et al.* (Fig. 3 in Ref. [201]) it is possible to estimate the ratio between the peak emission of the mentioned diffuse band and the one of the Rb dimer $^1\Pi_u \rightarrow X^1\Sigma_g^+$ transition to 6:100. Relating this ratio to the peak emission of approx. 245 counts for the same Rb dimer $^1\Pi_u \rightarrow X^1\Sigma_g^+$ transition in Fig. 5.17 results in a peak emission of 15 counts, which emerges from the emitted photons of reaction 5.35. This value is completely covered by the noise baseline, which contributes permanently with 35 counts, though the spectra in Fig. 5.17 have been corrected for dark counts. This explains why it was not possible to observe the diffuse band directly. However, to the best knowledge of the author, there is no reason why the dissociative recombination of the ionized Rb trimer should not occur.

The fact, that Fig. 5.16 showed only modest changes of the transmitted pump power when entering or leaving the plasma phase ($\sim$2.5%) is Striking. Thus, the relative amount of photons extracted from the pump beam by the plasma changes little. Increasing the pump power further increases the transparency of the plasma almost linearly, leading to the conclusion, that less pump power is needed to maintain the plasma phase. Although the available pump power was limited, the absorbed pump power by the plasma might saturate nonetheless. However, this is in particular remarkable, as the measured ESFADOF spectra prove the collapse of the $5P_{3/2}$ population as soon as the plasma sets in. In addition, the above discussion (cf. Secs. 5.2 and 5.3.1 and in particular figures 5.12– 5.15) demonstrate that the pump laser does not significantly affect the $5P_{3/2}$ population any more, as long as the plasma phase persist. In addition, Fig. 5.16 indicates that the amount of extracted photons remains essentially the same during the plasma phase. Due

to the relatively low photoionization cross sections of $\sigma_{\text{PI-5D}} = 16 \times 10^{-18}$ cm^2 and $\sigma_{\text{PI-6D}} = 15 \times 10^{-18}$ cm^2 (photoionization emerging from other levels show significantly lower cross sections [186]), photoinization processes can not be responsible for the observed high absorption of the pump laser. Thus, only a comparable strong coupling as the direct absorption of the pump laser photons by the $5S_{1/2} \rightarrow 5P_{3/2}$ transition, $\sigma_{\text{D}}^{\text{D2}} = 6 \times 10^{-9}$cm^2 (integrated over the Doppler-width), is capable to maintain the measured high degree of absorption during the plasma phase. In addition, despite their reduced transmission the ESFADOF spectra, recorded during the plasma phase, do not show any significant spectral broadening. Thus, any extreme temperature rise of the Rb vapor can be excluded. This causes on the one hand a significant increase of the vapor density and thus leads to a higher amount of non–ionized Rb atoms, but on the other hand induces a corresponding significant Doppler-broadening of the absorption line, which has not been observed. In conclusion, the temperature of the Rb vapor remains bound to the surrounding bath, even more as the temperature is externally controlled. In view of these facts, it is quite striking that the plasma phase persists in extracting nearly the same amount of photons from the pump beam. In other words: due to the fact that the plasma phase keeps a significant amount of the Rb vapor ionized [190] or bound to other states (cf. Fig. 5.17a), the resulting density reduction of the neutral ground state atoms has to be compensated by other processes in order to maintain the high absorption of the pump beam, while keeping the vapor density constant.

In order to gain more insight of the physical process, which finally explains this observation, it is useful to recall the rate equations (cf. Sec. 3.6), which describe the Rb $N_{5S_{1/2}}(\mathbf{r})$ ground state population and the $N_{5P_{3/2}}(\mathbf{r})$ excited state population of the nonionized phase. However, considering only the fine structure is sufficient at this point:

$$\begin{aligned}
\tfrac{\mathrm{d}}{\mathrm{dt}} N_{5S_{1/2}}(\mathbf{r}) \;=\; & \underbrace{\sum_{\mathrm{nl}>5S} A_{\mathrm{nl}\rightarrow 5S_{1/2}} N_{\mathrm{nl}}(\mathbf{r})}_{\text{Spont. decay}} \\
& \underbrace{- \int \mathrm{d}\nu \frac{I_{\text{Pump}}(\nu,\mathbf{r})}{h\nu_{\text{P}}} \sigma_{5S_{1/2}\leftrightarrow 5P_{3/2}}(\nu) \left[N_{5S_{1/2}}(\mathbf{r}) - \frac{g_{5P_{3/2}}}{g_{5S_{1/2}}} N_{5P_{3/2}}(\mathbf{r}) \right]}_{\text{Absorption and stim. emission}} \\
& \underbrace{+ \sum_{\text{n'l'} \in \{6P,\,5D\}} v_{\text{RMS}} \sigma^{\text{EP}}_{5P_{3/2}\rightarrow \text{n'l'}} \left[N^2_{5P_{3/2}}(\mathbf{r}) - \frac{g_{5P_{3/2}}}{g_{\text{n'l'}}} e^{\frac{\Delta E_{\text{EP}}}{k_B T}} N_{\text{n'l'}}(\mathbf{r}) N_{5S_{1/2}}(\mathbf{r}) \right]}_{\text{Energy–pooling + energy transfer}} \\
& \underbrace{- A_{5P_{3/2}} \int_{\text{V}} \mathrm{d}\mathbf{r}' N_{5P_{3/2}}(\mathbf{r}') G(\mathbf{r},\mathbf{r}'),}_{\text{Radiation trapping}}
\end{aligned} \tag{5.37}$$

$$\begin{aligned}\frac{\mathrm{d}}{\mathrm{dt}}\mathrm{N}_{5\mathrm{P}_{3/2}}(\mathbf{r}) \;=\; & \underbrace{-\mathrm{A}_{5\mathrm{P}_{3/2}\to 5\mathrm{S}_{1/2}}\mathrm{N}_{5\mathrm{P}_{3/2}}(\mathbf{r})+\sum_{\mathrm{nl}>5\mathrm{P}}\mathrm{A}_{\mathrm{nl}\to 5\mathrm{P}_{3/2}}\mathrm{N}_{\mathrm{nl}}(\mathbf{r})}_{\text{Spont. decay}} \\ & \underbrace{+\int \mathrm{d}\nu\,\frac{\mathrm{I}_{\mathrm{Pump}}(\nu,\mathbf{r})}{\mathrm{h}\nu_{\mathrm{P}}}\sigma_{5\mathrm{S}_{1/2}\leftrightarrow 5\mathrm{P}_{3/2}}(\nu)\left[\mathrm{N}_{5\mathrm{S}_{1/2}}(\mathbf{r})-\frac{\mathrm{g}_{5\mathrm{P}_{3/2}}}{\mathrm{g}_{5\mathrm{S}_{1/2}}}\mathrm{N}_{5\mathrm{P}_{3/2}}(\mathbf{r})\right]}_{\text{Absorption and stim. emission}} \\ & \underbrace{-\sum_{\mathrm{n'l'}\,\in\{6\mathrm{P},\,5\mathrm{D}\}}2\mathrm{v}_{\mathrm{RMS}}\sigma^{\mathrm{EP}}_{5\mathrm{P}_{3/2}\to \mathrm{n'l'}}\left[\mathrm{N}^2_{5\mathrm{P}_{3/2}}(\mathbf{r})-\frac{\mathrm{g}_{5\mathrm{P}_{3/2}}}{\mathrm{g}_{\mathrm{n'l'}}}\mathrm{e}^{\frac{\Delta \mathrm{E}_{\mathrm{EP}}}{\mathrm{k_B T}}}\mathrm{N}_{\mathrm{n'l'}}(\mathbf{r})\mathrm{N}_{5\mathrm{S}_{1/2}}(\mathbf{r})\right]}_{\text{Energy–pooling + energy transfer}} \\ & \underbrace{+\mathrm{A}_{5\mathrm{P}_{3/2}}\int_{\mathrm{V}}\mathrm{d}\mathbf{r}'\mathrm{N}_{5\mathrm{P}_{3/2}}(\mathbf{r}')G(\mathbf{r},\mathbf{r}')}_{\text{Radiation trapping}}\,. \end{aligned} \tag{5.38}$$

The $\mathrm{g_{nl}}$-terms stand for the degeneracies of the involved states, $\mathrm{v_{RMS}}$ for the root-mean-square velocity of the atoms and $\Delta\mathrm{E_{EP}}$ denotes the energy pooling transition energy gap. Of course, all temporal derivatives vanish in the steady state and together with the corresponding equations, which describe the population transfer to and from all other involved states, a steady state distribution results. The trapped radiation, described by the trapping operator $\mathrm{A}_{5\mathrm{P}_{3/2}}\int_V \mathrm{d}\mathbf{r}'\,G(\mathbf{r},\mathbf{r}')$, mainly affects the indirectly pumped sub-levels through its frequency redistribution [138, 139]. The involved laser intensity saturates the vapor, but does not reach the nonlinear radiation trapping regime [172–174]. Hence, the contribution of the radiation trapping can be neglected for the following discussion. Along the pump beam the Rb atoms cycle permanently between the $5\mathrm{S}_{1/2}$ ground state and the $5\mathrm{P}_{3/2}$ pumped level due to the saturation of the vapor. However, spontaneous decay as well as the energy pooling process, permanently extract energy from the pump beam. As a first approximation, the energy pooling process can be neglected; it contributes only little compared to the natural decay (cf. Sec. 3.6.2). Then, the photon scattering rate of the atomic vapor from the laser field can be compared to the one of a pure two level system [74]:

$$\Gamma^{\gamma,\gamma'}_{\mathrm{Ph}}=\frac{\mathrm{s}^{\gamma,\gamma'}_0\Gamma_{\gamma,\gamma'}/2}{1+\mathrm{s}^{\gamma,\gamma'}_0+(2\delta/\Gamma_{\gamma,\gamma'})^2}. \tag{5.39}$$

$\Gamma_{\gamma,\gamma'}$ represents the natural linewidth of the involved $\gamma\to\gamma'$ transition, $\mathrm{s}^{\gamma,\gamma'}_0$ the saturation parameter $\mathrm{s}^{\gamma,\gamma'}_0=\mathrm{I_{Pump}}/\mathrm{I}^{\gamma,\gamma'}_{\mathrm{S}}$ and $\delta=\nu-\nu_{\gamma,\gamma'}$ the detuning from the line center. Due to the hard pumping close to the Rb D2 absorption line ($\delta\approx 0$, $\mathrm{s}^{5\mathrm{S}_{1/2},5\mathrm{P}_{3/2}}_0\gg 1$ for $\mathrm{I}^{5\mathrm{S}_{1/2},5\mathrm{P}_{3/2}}_{\mathrm{S}}=3.17$ mW/cm^2 and $\mathrm{I_{Pump}}>100$ W/cm^2), the photon scattering rate $\Gamma^{\gamma,\gamma'}_{\mathrm{Ph}}$ converges to $\Gamma_{\gamma,\gamma'}/2$. Although $\Gamma^{\gamma,\gamma'}_{\mathrm{Ph}}$ is independent of the vapor density, the beam attenuation is not. When allowing for the entire Zeeman-splitted hyperfine structure to participate, while according for the inhomogeneous magnetic field, the scattered intensity from the laser beam traveling along the $\mathbf{e}_z$–axis becomes

$$\frac{\mathrm{d}}{\mathrm{dz}}\mathrm{I}_{\mathrm{Pump}}(\mathbf{r},\nu) = \mathrm{h}\nu_{\mathrm{P}} \sum_{\gamma\rightarrow\gamma'} \Gamma_{\mathrm{Ph}}^{\gamma,\gamma'}(\mathbf{r},\nu) \left[\mathrm{N}_{\gamma'}(\mathbf{r}) - \mathrm{N}_{\gamma}(\mathbf{r})\right], \tag{5.40}$$

which translates in the hard pumping regime ($\mathrm{s}_0^{\gamma,\gamma'} \gg 1$) to

$$\frac{\mathrm{d}}{\mathrm{dz}}\mathrm{I}_{\mathrm{Pump}} \approx \frac{\mathrm{I}_{\mathrm{s}}}{2\,\mathrm{h}\nu_{\mathrm{P}}}\sigma_{5\mathrm{S}_{1/2}\leftrightarrow 5\mathrm{P}_{3/2}} \left[\mathrm{N}_{5\mathrm{P}_{3/2}} - \mathrm{N}_{5\mathrm{S}_{1/2}}\right]. \tag{5.41}$$

In conclusion, as the strong pump laser equilibrates the populations of the $5\mathrm{S}_{1/2} \rightarrow 5\mathrm{P}_{3/2}$ pump transition, Eqs. 5.40 and 5.41 demand for an increase of the transmitted pump intensity when significantly reducing the density of the involved states. In particular, the considerably decreased ESFADOF transmission proves the substantial decrease of the $5\mathrm{P}_{3/2}$ population. This stands in direct contrast to the measured pump transmission during the plasma phase (circled data points in Fig. 5.16). As both observations have to be satisfied, Eq. 5.40 has to be extended in order to extract the same photon number from the pump beam. Superelastic collisions (cf. reaction 5.24) among free electrons and excited atoms are reasonable candidates. The cross section of this process is linked via the Coulomb interaction to the one of the photon transition [180, 181, 203]. It has been described that the production of free electrons by several possible reactions occurs permanently. Even below the plasma threshold, a non vanishing amount of free electrons exists. However, as the above discussed measurements prove, a certain intensity threshold has to be reached in order to ignite the plasma. This can be understood as a balance between the production of free electrons and their annihilation by reverse processes. In addition, the pool of free electrons couples to the pump laser via superelastic collisions, which de-excite the $5\mathrm{P}_{3/2}$ state. Hence a considerable amount of pump photons is extracted and dispersed over the vapor cell without being fed back via stimulated emission to the pump beam [185].

Moreover, the encountered hysteresis suggest the bistable behavior of this process. This can be understood, when taking the potential curves of the produced Rb molecules into consideration [190]. Although the ionization potential of the various processes (cf. Fig. 5.18) has to be provided, the ionized Rb atoms or molecules release their binding energy to the plasma, e.g. through ionization transfer processes (compare reactions 5.27–5.28 with 5.16–5.19), which explains the observation that the majority of the plasma consists of ionized Rb trimers. More precisely, once a considerable pool of excited neutral atoms, monoatomic ions, ionized clusters and free electrons has been created, transfer processes such as energy transfer collisions, ionization transfer, superelastic collisions, collisional excitation and ionization dominate and couple the whole atomic vapor to the pump beam. Then, the plasma phase subsists as long as the injected laser power is able to compensate for the losses. Loss channels include the escape of radiation from the vapor and dissipation by the hot electron gas. In other words, the increased pump power, which ignites the plasma, can be understood as the necessity to pass over the plasma's collective potential barrier. Afterwards, only the losses need to be compensated, and the plasma phase persist even for lower pump intensities,

which explains the hysteresis. This interpretation is corroborated by the theoretical description of Measures [180]. The strong coupling between the pump laser and the laser induced plasma introduces in his coupled rate equation model a source of pseudo-ground state atoms, which posses a considerably reduced ionization energy [185].

5.3.3 Operation along the Plasma Maintenance Threshold

Due to the fact, that the ESFADOF operation is limited by the laser-induced plasma phase of the Rb vapor, it is of particular interest to examine, whether the encountered ESFADOF operational limits can be extended when operating along the plasma maintenance threshold. For that purpose, any increase of the vapor density demands a simultaneously decrease of the pump intensity, in order to guarantee reliable ESFADOF operation and exclude any plasma formation.

It is useful to summarize some obtained results: Section 5.2.2 showed, that 387.8(5) mW of injected pump power is enough to induce a plasma inside the Rb vapor cell. The cell temperature was 165°C and the linear polarized pump beam has been detuned by $\Delta\nu_{\mathrm{P}} = -1.78(2)$ GHz from the center of the D2 pump transition. In addition, Sec. 5.3.1 showed that the induction of the plasma is accompanied by a very distinct hysteresis. Although higher pump intensities are necessary to induce the plasma, far lower ones are enough to maintain it. Reducing the pump intensity below a certain pump threshold results in the recovery of the ESFADOF spectra and the plasma cease to exist. Furthermore, due to the saturation of the $5P_{3/2}$ pump level, Fig. 5.14 and Fig. 5.15 showed that the ESFADOF transmissions do not significantly suffer in magnitude between the recovery point of the ESFADOF spectra and the plasma induction. Hence, these observations allow for a further increase of the vapor cell temperature: As long as the injected pump intensity is limited to this recovery threshold, stable ESFADOF operation can be guaranteed.

Figures 5.19–5.20 show ESFADOF spectra beyond a cell temperature of 165°C. The annotated pump intensities, which are located just at the recovery point of the ESFADOF spectra, i.e. when the plasma suddenly ceases to exist, have been obtained by injecting first of all the maximum available pump power, which always induced a plasma, and afterwards decreasing the pump power. The first data set has been extracted from Fig. 5.13.

An examination of these figures reveals the following:

1. When operating slightly below the plasma maintenance threshold, i.e. when the ESFADOF spectra recover, a maximum absolute ESFADOF transmission exists. Precisely speaking, a cell temperature of 179°C and an injected pump power of 147(2) mW delivers a maximum ESFADOF transmission of 25.01(1)%. This value is the highest so far experimentally demonstrated ESFADOF transmission obtained on the green $5P_{3/2} \rightarrow 8D_{5/2}$ transition. This can be attributed to the increased vapor density.

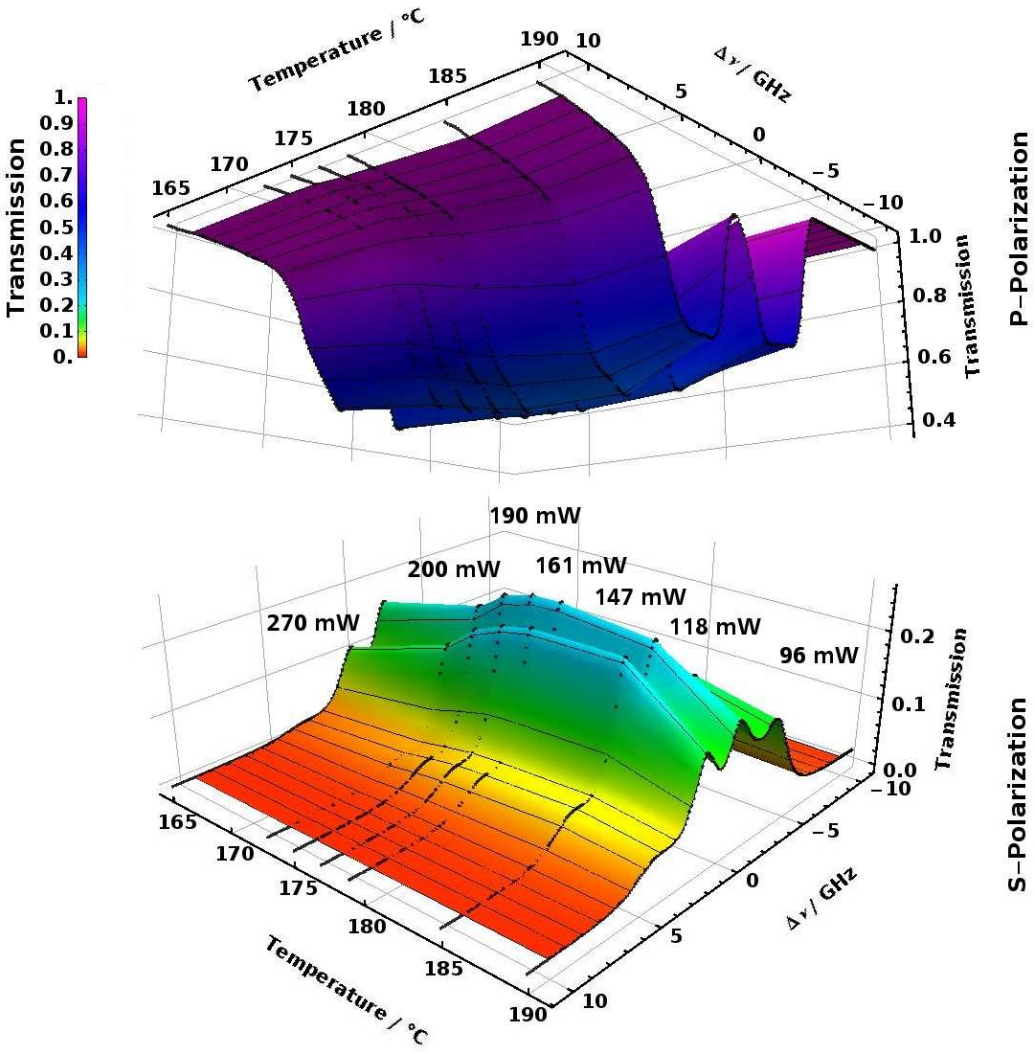

Fig. 5.19: 3D representation of the ESFADOF transmission spectra as a function of cell temperature just below the plasma formation pump threshold: The corresponding pump powers are annotated to the black dotted lines, which mark the measured ESFADOF spectra. All other parameters are the same as in Fig. 5.5. The maintenance of the laser-induced plasma can be inhibited by reducing the pump power after increasing the cell temperature. The annotated values mark the recovery point of the ESFADOF spectra. Compared to Fig. 5.5, this procedure increases the maximum achievable ESFADOF transmission up to a maximum value of 25.01(1)% for a cell temperature of 179°C and an injected pump power of 147 mW. Increasing the temperature further, while simultaneously decreasing the injected pump power, reduces the maximum ESFADOF transmission.

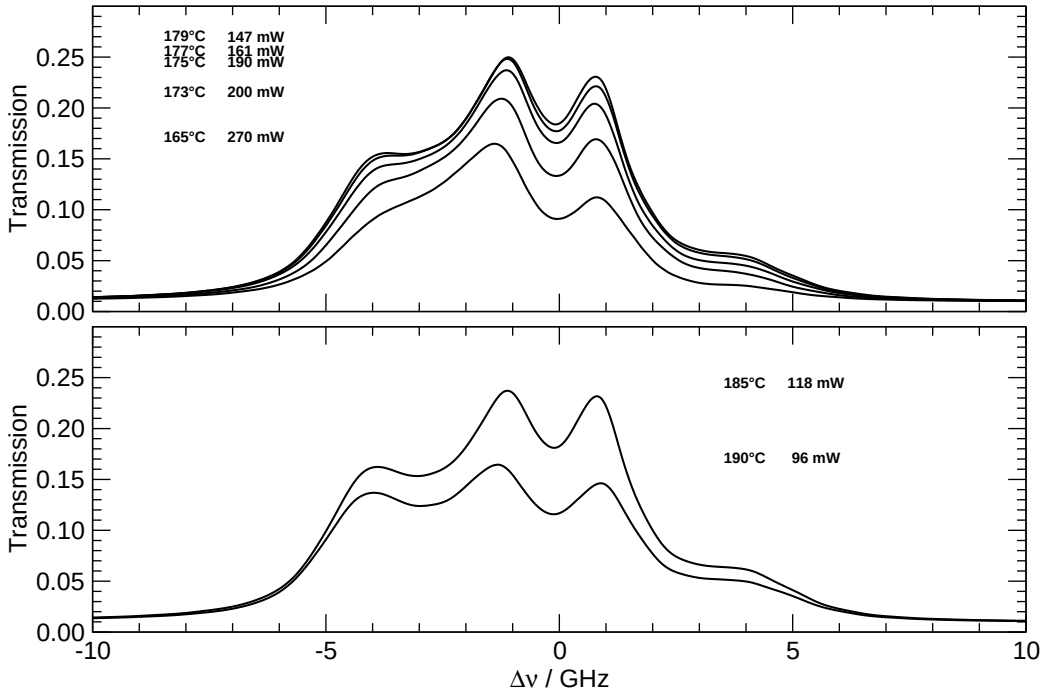

Fig. 5.20: 2D graphical representation of the temperature dependence of the S-polarization: The experimental parameters are the same as in Fig. 5.5 and the corresponding cell temperatures and pump powers are annotated. The plot is splitted for clarity. The ESFADOF spectra increase when increasing the cell temperature. A maximum transmission of 25.01(1)% has been achieved.

2. Increasing the cell temperature further decreases the ESFADOF transmission spectrum. This effect can be attributed to the limited amount of injected pump power, which is required to inhibit the plasma induction. In combination with the increased quenching rates at higher temperatures a decreased $5P_{3/2}$ population results.
3. When comparing Fig. 5.20 with Fig. 5.6 an overall increase of the ESFADOF transmission can be observed. This holds even for low pump powers. Specifically, the spectrum recorded at a cell temperature of 190°C with a pump power of 96.3(5) mW reveals a maximum transmission of 16.44(1)%, where the spectrum recorded at 165°C with a pump power of 99.5(5) mW offers only a maximum transmission of 8.95(1)%. This effect can also be attributed to the significantly increased number density within the interaction volume.
4. The spectra gain in structure when increasing the cell temperature. In particular the blue shifted peak is affected. This again is a consequence of the increased confinement of the trapped radiation and its frequency redistribution, which disperses the injected pump photons over a wide range of the $5P_{3/2}$ sublevels.

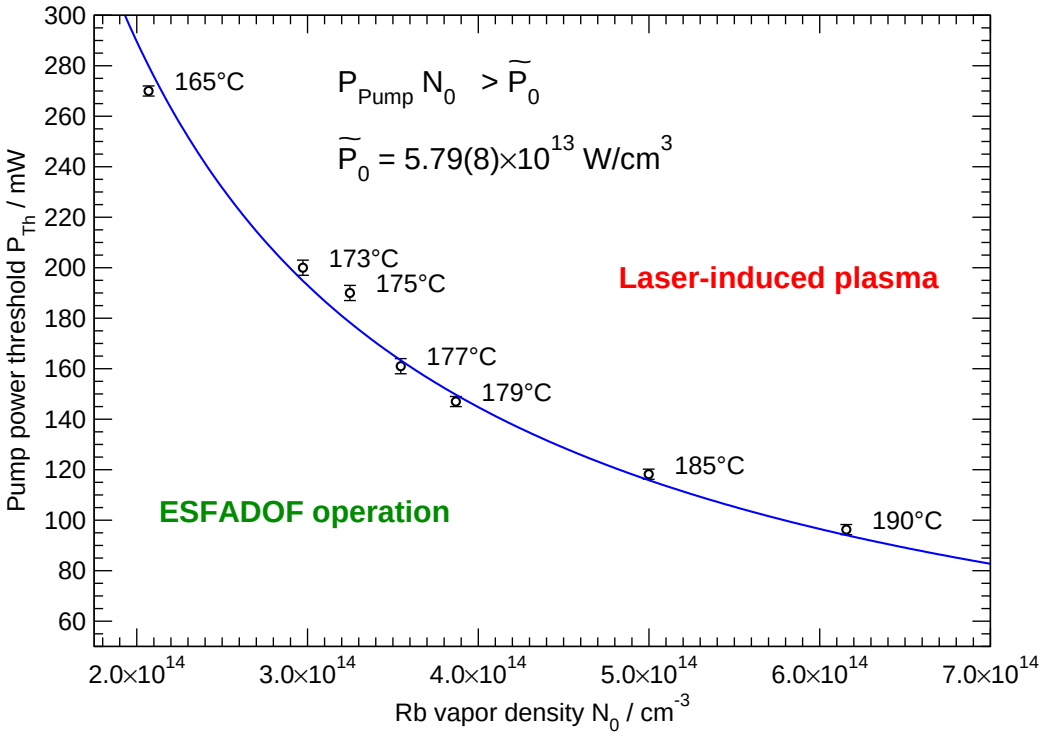

Fig. 5.21: The plasma maintenance threshold: Striking is the clear correlation between the Rb vapor density and the minimum pump power, which maintains the plasma once it has been induced by the pump laser. The data points correspond to the annotated values of Fig. 5.20, when taking the temperature dependence of the Rb vapor density into consideration. The corresponding temperatures are annotated. This plot can be interpreted as a phase-diagram, where the borderline separates the laser-induced plasma phase from the normal uncharged Rb vapor phase.

Furthermore, the data reveal a remarkable relationship between the vapor cell temperature and the injected pump power along the plasma maintenance threshold. The annotated values of Fig. 5.20 can be interpreted as the minimum pump powers, which are required by the corresponding cell temperature in order to maintain an induced plasma. Plotting this laser power versus the Rb vapor density, which depends on the cell temperature (cf. appendix A), leads to Fig. 5.21. The plot reveals a clear correlation between the Rb vapor density N_0 and the injected pump power P_{Pump}. The induced plasma is maintained by the pump laser, as long as

$$P_{Pump} > \frac{\tilde{P}_0}{N_0} \tag{5.42}$$

can be satisfied; $\tilde{P}_0$ represents a constant. By changing the greater-than sign into an equals sign, it is possible to fit

$$P_{Th}(N_0) = \frac{\tilde{P}_0}{N_0} \tag{5.43}$$

to the data along the plasma maintenance threshold, where $P_{Pump} = P_{Th}$ applies. $P_{Th}(N_0)$ corresponds to the solid line in Fig. 5.21 and the fit yields $\tilde{P}_0 = 5.79(8) \times 10^{13}$ W/cm^3. Shifting N_0 to the left side and multiplying both sides of Eq. 5.43 by the volume V yields

$$P_{Th}N = P_{Th}N_0V = \tilde{P}_0V = P_0. \tag{5.44}$$

As the plasma extends the whole vapor cell, it is reasonable to insert $V = V_{Cell} = 4.9$ cm^3 (10 mm length and 25 mm in diameter) into Eq. 5.44, which yields $P_0 = 2.84(4) \times 10^{14}$ W.

However it has to be emphasized, that although Eqs. 5.43 and 5.44 fit well, they represent an empirical fit to the data. A more thorough theoretical description of the underlying couplings between the pump laser and the plasma phase, which comprises the interactions between neutral atoms, ions and hot electrons, is required for an accurate prediction of this threshold. Based on the theoretical framework of Ref. [180] Measures *et al.* derived a rate equation model, which allows to estimate the absorbed pump intensity [204, 205]. These highly nonlinear coupled rate equations have to be solved numerically, in order to extract the desired threshold behavior. Certainly, this is not the purpose of this thesis and is left for further discussions.

5.4 Vapor Cell II: 500 mT

The employment of vapor cell II results in a substantially increased magnetic field strength along the symmetry axis of the cell. The field reaches a maximum value of 530 mT (cf. appendix C) and considerably shifts the ESFADOF transmission edges towards the outside of the spectrum. In spite of the small inner diameter of this specific cell design, it was possible to guide $\kappa_P = P_{Out}/P_{In} = 69.6(7)\%$ of the available pump radiation through the cold ($T_{Cell} = 25^\circ$C) vapor cell II. Fig. 5.22a shows an ESFADOF spectrum recorded with the same experimental setup and employing the same data acquisition and evaluation procedure as it was the case for vapor cell I. The data prove that the adapted design of vapor cell II delivers ESFADOF transmission spectra, which overlap with the spectral region of interest of the Brillouin-lidar. In addition, Fig. 5.22b shows the corresponding standard deviation after averaging 200 individual spectra. The cell temperature was 150°C and the linearly polarized pump beam has been placed on the center of the $5S_{1/2} \rightarrow 5P_{3/2}$ transition ($\Delta\nu_P = 0$ GHz). It was possible to inject an effective pump power of $P^{Eff}_{Pump} = \kappa_P P_{Pump} = 278(3)$ mW.

Examining Fig. 5.22 reveals:

1. The spectrum shows a triple peak structure, with a maximum transmission of 5.94(8)%, 300(10) MHz red shifted from the center of the $5P_{3/2} \rightarrow 8D_{5/2}$ transition.
2. Two other peaks appear almost symmetrically red and blue shifted with respect to the first one. The red shifted peak is located at -6.70(1) GHz and shows a

maximum transmission of 3.78(7)% and the blue shifted peak is located at 6.55(1) GHz and shows a maximum transmission of 3.38(7)%.

3. The point of symmetry lies red shifted by 75(10) MHz, when considering only the red and blue shifted peak transmission.
4. The outer edge of the red shifted transmission peak rises by 2.16(6)% between -10.54(1) GHz and -7.47(1) GHz, when considering a transmission change from 10% to 90% of the red peak transmission.
5. The outer edge of the blue shifted transmission peak decreases by 1.84(6)% between 7.07(1) GHz and 10.67(1) GHz, when considering a transmission change from 90% to 10% of the blue peak transmission.
6. The outer edges of the ESFADOF spectrum overlap with the spectral region of interest of the Brillouin-lidar (marked by broken lines). The red edge shows a transmission change of 0.62(6)% between -7.8 GHz and -6.8 GHz and the blue edge shows a transmission change of 0.70(6)% within the 6.8 GHz–7.8 GHz range. When normalized to the maximum transmission, these values correspond to a relative change of 10(1)% and 12(1)% for the red and blue edges respectively.
7. Periodical dips appear in the ESFADOF transmission signal. The periodicity of 1 GHz indicates, that they originate from a crosstalk between the PMT signal, which delivers the etalonmarkers, and PD3, which records the ESFADOF spectrum. Due to technical issues and in contrast to former measurements, the signals of PD3 and PD4 have been recorded directly by the A/D-card and without any additional amplification, which explains the crosstalk and the increased measurement error.

The red and blue shifted peaks originate from the center of the permanent ring magnet, where the magnetic field strength reaches its maximum value of 530 mT. The middle peak adds up from the increasing and afterwards decreasing field strength along the probe beam path (cf. appendix C).

The standard deviation of the averaged ESFADOF transmission spectrum allows to roughly estimate the measurement accuracy, when employing the filter characteristics as an edge-filter: By relating the achieved transmission accuracy of 6×10^{-4} to the transmission change in the region of interest, a frequency discrimination of approx. 97 MHz and 86 MHz results for the red and blue shifted peak respectively. Relating the 97 MHz linearly to the Brillouin-lidar's temperature range of 40°C/GHz results in a temperature discrimination of at least 3.9°C.

Again, the symmetry of the ESFADOF transmission signal can be exploited in order to decrease the influence on arbitrary frequency jitter of the Brillouin-lidar's transmitter. By applying the same analysis as described in Sec. 5.2.3, Fig. 5.23 results and allows to investigate the symmetry more quantitatively: By minimizing $\int |\Theta_S(\Delta\nu, \Delta\nu_S)| \mathrm{d}\Delta\nu$ with respect to $\Delta\nu_S$, the symmetry point $\Delta\nu_S = -75$ MHz has been extracted (cf. also Eq. 5.10). The symmetry of the ESFADOF spectrum is clearly visible when overlaying the first derivative with its symmetric inversion, though the symmetry has not been experimentally optimized. In addition, the derivative reflects even more the already mentioned periodic crosstalk between

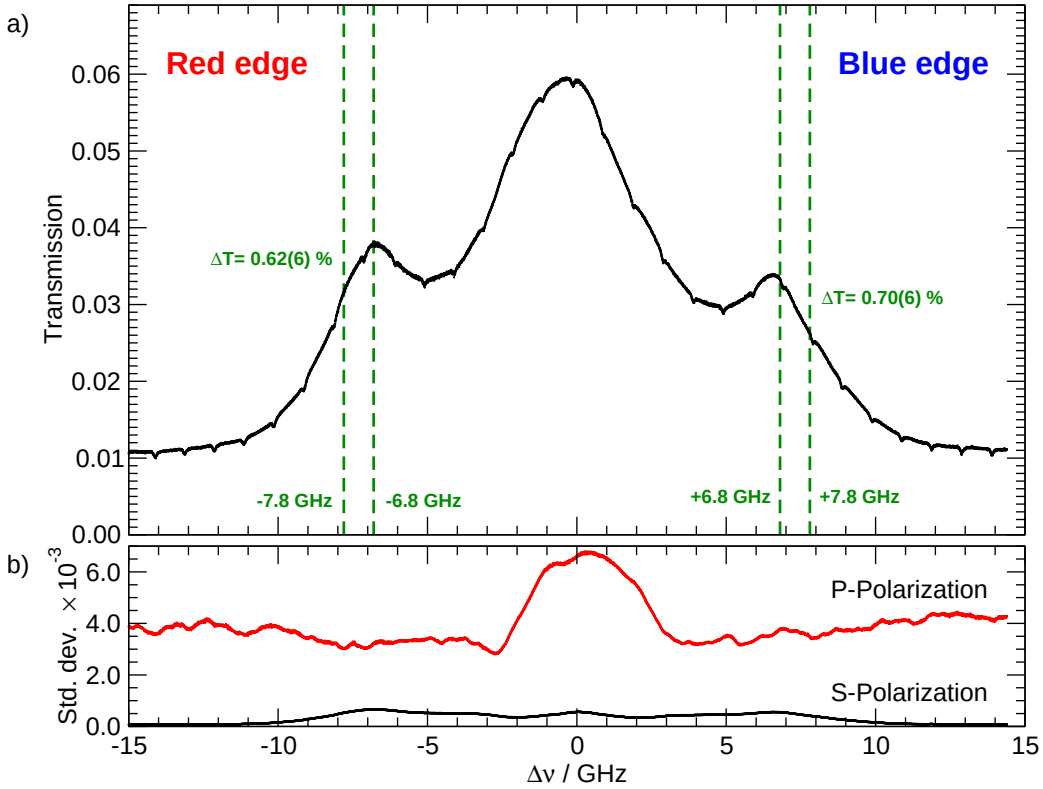

Fig. 5.22: ESFADOF spectra employing vapor cell II: The cell temperature was 150°C and an effective magnetic field strength of $B_z = 500$ mT has been applied. The linearly polarized pump beam has been placed on the center of the $5S_{1/2} \rightarrow 5P_{3/2}$ transition ($\Delta\nu_P = 0$ GHz) and an effective pump power of $P^{Eff}_{Pump} = 278(3)$ mW has been injected into the cell. a) ESFADOF transmission spectrum: The high magnetic field strength shifts the outer transmission edges towards the outside. The broken lines mark the spectral region of interest of the Brillouin-lidar. This spectrum clearly proves that the proposed setup delivers the required spectral overlap between the ESFADOF transmission edges and the Brillouin doublet. The annotated values refer to the transmission differences ΔT along the corresponding transmission edges inside the region of interest. The desired symmetrical shape has been almost achieved. This spectrum proves the general feasibility of the measurement principle and marks an important milestone. The periodical dips are artefacts. They originate from the crosstalk between the photomultiplier tube signal, which records the periodic etalonmarker and PD3, which records the ESFADOF signal. b) Corresponding standard deviation of the averaged transmission signal, which allows an error estimation of the transmission.

the PMT singal and the photodiodes. The first derivative shows a maximum absolute fluctuation of 1.1×10^{-5} MHz^{-1} within the region of interest. However, the currently discussed ESFADOF spectrum allows to take advantage of the symmetry of the Brillouin-doublet. The difference between the first derivative and its symmetric inversion (last row of Fig. 5.23) shows a maximum absolute fluctuation of 5×10^{-6} MHz^{-1} within the region of interest and proves again the outstanding advantage of a symmetric operation. On the one hand both Brillouin-peaks can be exploited, which increases the available signal by a factor of 2, and on the other hand this value increases the insensitivity to laser frequency jitter also by a factor of 2. By relating the achieved accuracy of 6×10^{-4} to the maximum tolerable intensity jitter of 5×10^{-6} MHz^{-1}, a tolerable frequency jitter of 120 MHz results. However, after resolving the above mentioned technical issues, it was possible to suppress the crosstalk and to optain the same accuracies as discussed for vapor cell I (cf. sec 4.4.4).

In addition, it has to be pointed out, that the ESFADOF spectrum of Fig. 5.22 does not represent the achievable optimum. It is rather the best spectrum, which has been possible to extract from the employed vapor cell II. Further measurements showed a constantly decreasing transmission over the course of time. Additionally, the spectra did not recover when decreasing the temperature again and a plasma phase has not been induced. The decrease of the ESFADOF transmission spectrum occurred in two steps: The maximum transmission decreased within one day below 10^{-2} and than within a week below 10^{-4} for the same experimental conditions. A degradation of the permanent ring magnet can be excluded, as the spectral characteristics of the ESFADOF transmission remained essentially unchanged. Hence, this dramatic decrease in absolute transmission indicates a strong consumption of the Rb atoms inside the cell. Furthermore, as no additional pressure broadening has been observed, intrusion of foreign gas from the outside can be excluded, e.g. O_2 would consume the Rb atoms, but N_2 would induce a strong pressure broadening. In conclusion, the Rb vapor has been consumed by other means. In view of these observations, the only reasonable explanations are the adhesion of the Rb atoms on the epoxy and/or the diffusion of the Rb atoms into the epoxy. These assumptions are corroborated by the fact that alkali-metals are known for their aggressivity and ability to diffuse into low melting glasses. For example, although Borosilicate glasses have a softening temperature of 821°C [150], they can not be used as alkali-metal vapor cells above 200°C. For a prolonged high temperature operation, fused silica cells are advantageous. The manufacturer of the employed epoxy quotes a glass transition temperature of $\geq$90°C, but guarantees long-term operation of up to 250°C without degradation [160]. However, due to this low glass transition temperature it is reasonable to assume, that the epoxy softens as much as the Rb atoms adhere and/or even diffuse into the epoxy. Unfortunately, it was not possible to find any comparable studies, which might have enlightened this issue. However, in this context it is reasonable to assume further that due to the small amount of epoxy, the consumption will saturate. However, due to technical reasons only a small amount of Rb has been sealed to vapor cell II. The Rb vapor has been almost fully consumed,

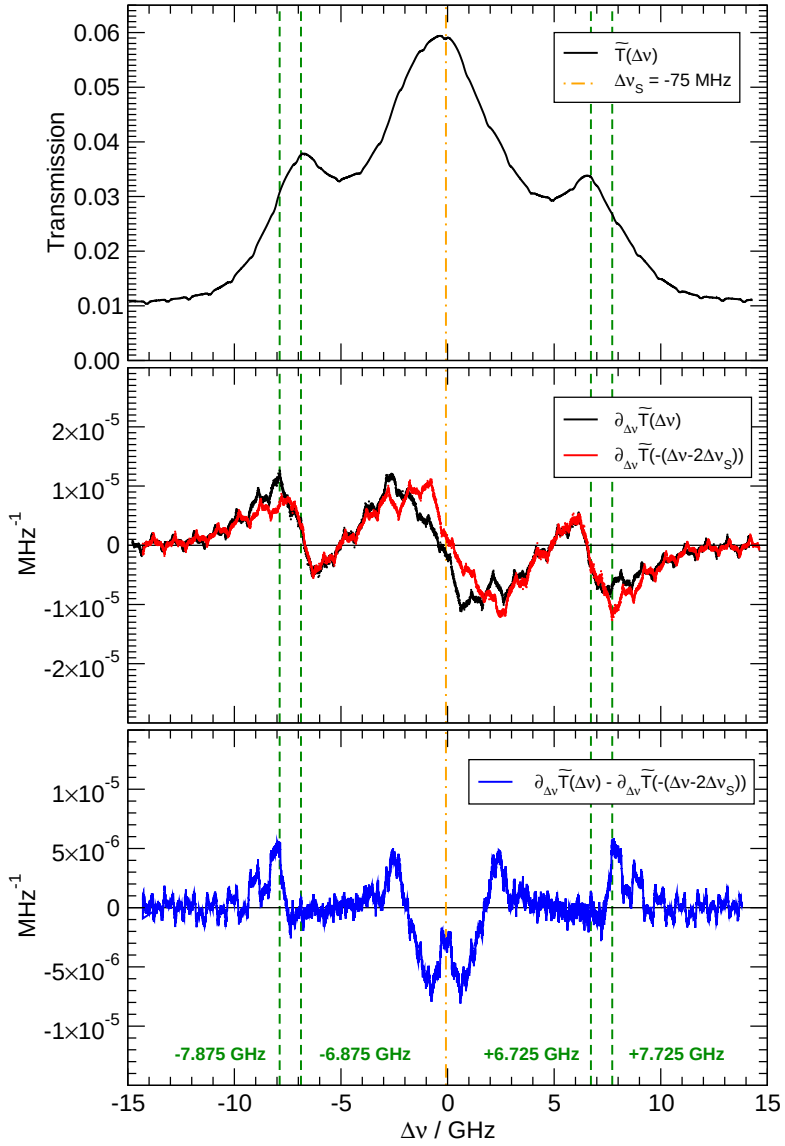

Fig. 5.23: Evaluating the symmetry according to the discussion of Sec. 5.2.3: The plot shows the ESFADOF transmission spectrum, which corresponds to Fig. 5.22, its first derivative, the symmetric inversion of the first derivative with respect to the symmetry point $\Delta\nu_S$ (dashed dotted line). The last row shows, similar to Figs. 5.10 and 5.11 , the difference between the derivative and its symmetric inversion and quantifies the increase in measurement accuracy when exploiting the symmetry. The broken lines indicate the spectral region of interest of the Brillouin-lidar with respect to the symmetry point. The derivative of the ESFADOF spectrum and its symmetric inversion exhibit in the region of interest already a high degree of congruence, though the symmetry has not been optimized. The periodic structures emerge from a crosstalk between the different signals on the A/D-card. Again, a very effective compensation of small frequency fluctuations of the Brillouin-lidar laser results.

such that a saturation has not been observed for this small amount. In order to verify this assumption and in order to guarantee a longer lifetime of vapor cell II, it is useful to increase the amount of sealed Rb. Unfortunately, the glass blowing facilities at the *Physikalisches Institut Heidelberg*, where vapor cell II has been filled, do not allow to increase the amount of sealed Rb. For future investigations a collaboration with the *5. Physikalisches Institut Stuttgart* has been initiated. Their facilities offer the possibility to considerably increase the amount of sealed Rb, as they do not need to evaporate the Rb prior to sealing the vapor cell.

Fig. 5.24 shows an ESFADOF spectrum, which has been recorded one day after the above spectum has been measured, directly after fixing the mentioned technical issues. In contrast to Fig. 5.22 the linear polarized pump beam has been placed 4.75 GHz red shifted from the center of the $5S_{1/2} \rightarrow 5P_{3/2}$ transition and an effective pump power of $P_{\mathrm{Pump}}^{\mathrm{Eff}} = 313(3)$ mW has been injected into the cell. The fact, that the absolute transmission decreased considerably, due to the discussed consumption of the Rb vapor, is striking. Nevertheless, the data reveals clearly that by red detuning the pump beam it is possible to suppress the middle peak. This can be understood as an effect of the inhomogeneous magnetic field. The red detuned pump beam reaches only Rb atoms which are influenced by high magnetic fields, i.e. it reaches only atoms which show a large Zeeman-splitting. The spectral overlap of Rb atoms, which are influenced by considerably lower magnetic fields, almost vanishes, such that they do not contribute any more to the ESFADOF spectrum.

Furthermore, a maximum transmission of only 1.58(5)% has been achieved due to the consumption of the Rb vapor. The transmission differences ΔT along the corresponding transmission edges inside the region of interest has been measured to 0.19(7)% and 0.18(7)% for the red and blue edge respectively. By relating these values to the maximum transmission, a relative transmission change of 12(1)% and 11(1)% results, which compares well with the above measurements. Hence, by increasing the Rb vapor density a considerable enhancement of the ESFADOF transmission can be expected.

In the final analysis, these measurement mark an important milestone towards an operational Brillouin-lidar. Even though the experiments have been limited due to the limited amount of Rb vapor sealed to vapor cell II, they prove the general feasibility of the ESFADOF device as high resolution edge-filter.

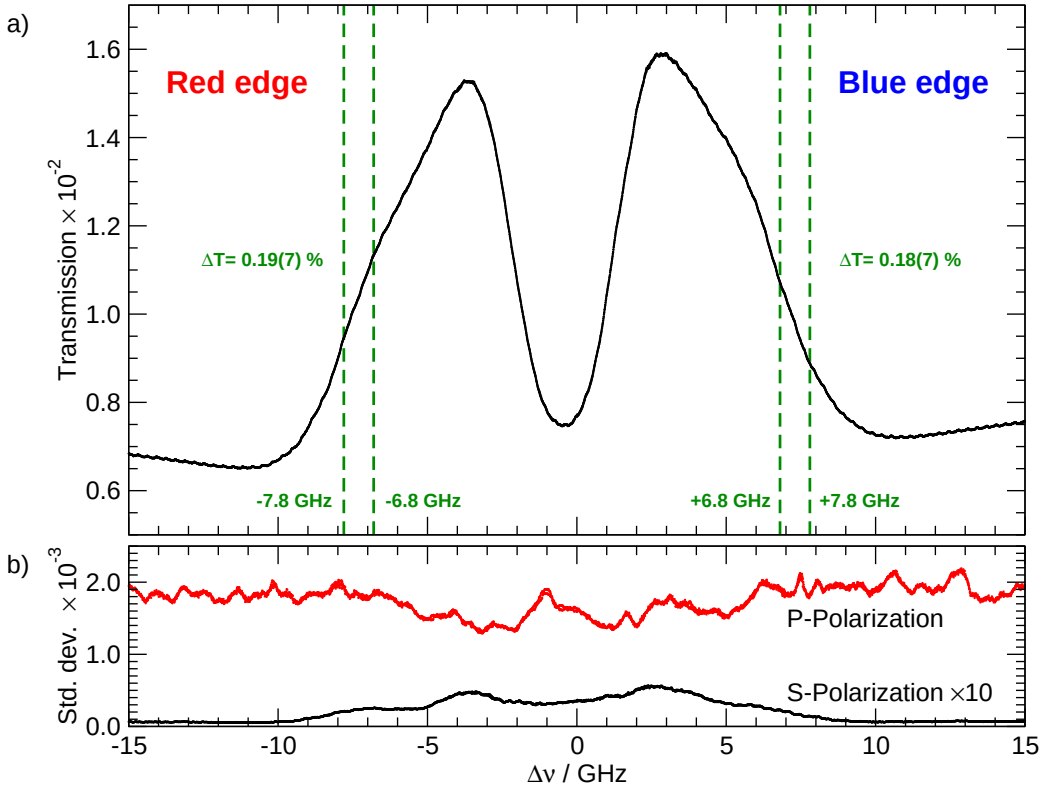

Fig. 5.24: ESFADOF spectrum employing vapor cell II one day after Fig. 5.22 has been measured: The cell temperature was $T_{ESFADOF} = 150°C$ and an effective magnetic field strength of $B_z = 500$ mT has been applied. The linear polarized pump beam has been placed 4.75 GHz red shifted from the center of the $5S_{1/2} \rightarrow 5P_{3/2}$ transition and an effective pump power of $P^{Eff}_{Pump} = 313(3)$ mW has been injected into the cell. a) ESFADOF transmission spectrum: The high magnetic field strength shifts the outer transmission edges towards the outside and allows the spectral overlap with the Brillouin-doublet. The region of interest of the Brillouin-lidar is marked by broken lines. In contrast to Fig. 5.22, a maximum transmission of only 1.58(5)% has been achieved due to the consumption of the Rb vapor. The annotated values refer to the transmission differences ΔT along the corresponding transmission edges inside the region of interest. The above encountered crosstalk between some A/D-channels has been resolved. b) Corresponding standard deviation of the averaged transmission signal: The accuracy has been singificantly increased due to the suppression of the crosstalk.

6

Conclusion and Outlook

The present work is dedicated to the development and the thorough assessment of Rubidium based excited state Faraday anomalous dispersion optical filters, which allow, when operating them as edge–filter receiver within a Brillouin–lidar remote sensing application, an area wide measurement of the temperature profile of the oceanic water column.

Chapter 2 discusses the working principle and the system requirements of this mobile remote sensing application. Emphasis is put on the Brillouin–scattering and in particular on the temperature and salinity dependence of its spectral profile, which is crucial for the implementation of the proposed lidar remote sensing technique. The working principle is based on a system of equations (cf. Eqs. 2.9, 2.12, 2.13, 2.23), whose known temperature and salinity dependence allows the deduction of both parameters by the measurement of the Brillouin–shift ν_{B} and the Brillouin–width $\delta\nu_{\mathrm{B}}$. The latter can be extracted from the spectral profile of the Brillouin–backscatter. Briefly speaking, a temperature range of 0°C to 40°C has to be resolved and salinities between 30 ‰ and 40 ‰ have to be expected. These values translate into a Brillouin–shift of $\pm 6.8 - 7.8$ GHz, when employing green laser pulses at a wavelength of 543 nm. The Brillouin–width varies between 1.66 GHz and 0.39 GHz for the same temperature range and wavelength. However, as the measurement of the Brillouin–width $\delta\nu_{\mathrm{B}}$ within a mobile remote sensing application is extremely challenging, the lack of this observable has to be compensated by the knowledge of the salinity parameter. Direct measurements of oceanic salinities are mostly restricted to fixed locations and hence not applicable for a remote sensing system. As Sec. 2.2.2 discusses and as extensive studies of Fry *et al.* show, the salinity parameter can be procured by relying on historical data, while including local and seasonal variations. As this data delivers the salinity parameter with an uncertainty of 1 ‰, a temperature accuracy of 0.5°C can be achieved. An increase of the knowledge of the salinity parameter, improves the temperature deduction. The precise knowledge of the salinity considerably decreases the temperature uncertainty by one order of magnitude to 0.06°C, when the Brillouin–shift is known with an accuracy of 1 MHz [72].

In addition, the discussion of Sec. 2.2.3 revealed that the temperature and salinity dependence of the Brillouin–width has to be included for a thorough assessment of the detection system. This is particularly important, when employ-

ing an edge–filter based direct detection scheme. As the resulting signal of an edge–filter receiver relies on a measurement of the filter transmission, this signal depends on both the Brillouin–shift ν_B and the Brillouin–width $\delta\nu_B$. The ideal edge–filter is the subject of Sec. 2.3, where the above mentioned dependencies of ν_B along with the ones of $\delta\nu_B$ on the temperature and the salinity parameter are simultaneously investigated for the first time. A clear dependency of the normalized transmitted intensity on the water temperature and the salinity is derived. It allows the deduction of one of these parameters, preferably the temperature, from the measurement of the filter transmission, when the other parameter is known. In view of the present discussion, the salinity can be extracted from historical data. Thus, it is possible to deduce the water temperature from the characteristic curves of the lidar receiver. Of course, these characteristic curves depend not only on the employed edge–filter characteristics, but also on the receiver technology and the signal acquisition chain. Thus, one has to perform a thorough calibration of the overall system. However, this procedure is straight forward, once the edge–filter characteristcs have been established [45]. Nevertheless, in view of the fact, that the Brillouin–width $\delta\nu_B$ decreases with increasing temperature, a considerable influence of the characteristic curves of the edge–filter receiver results. Thus, it is highly desireable that additional measurements of the temperature and salinity dependence of the Brillouin–width considerably improve the accuracy of the deduced empirical relation (cf. Eq. 2.23 and Tab. 2.3).

The requirements of an airborne compatible lidar–system, are rather stringent. The implementation of the overall system as well as that of the receiver is limited in space, weight and in power consumption. In addition, the receiver has to be insensitive to vibrations, has to offer a high light gathering power and must be able to resolve the temperature dependent Brillouin–scattering on a ns time scale.

Chapter 3 showed that Faraday anomalous dispersion optical filters are suitable edge–filters, which comply with the above mentioned requirements. As static devices, they are insensitive to vibration and their working principle provides a high light gathering power, steep transmission edges in the spectral region of interest and an excellent daylight supression. High penetration depths inside the water column require an operation close to the absorption minimum of water, i.e. between 380–550 nm [18]. Thus, an operation of the FADOF receiver on a transition line within this spectral band is highly desireable. The extension of this working principle to excited state Faraday anomalous dispersion optical filters, which operate between two excited states, increases the number of accessible atomic transition lines, such that a suitable line can be found. The central wavelength of the Rubidium $5P_{3/2} \rightarrow 8D_{5/2}$ transition (543.30 nm) falls within this band and the lower ESFADOF state can be pumped on the $5S_{1/2} \rightarrow 5P_{3/2}$ transition (780.24 nm) by efficient semiconductor devices. In addition, the employment of the alkali–metal Rubidium assures high vapor densities and hence high transmissions.

Furthermore, the Brillouin–lidar measurement principle in probing the temperature dependence of the spontaneous Brillouin–scattering requires probe laser

pulses which match the transition wavelength of the ESFADOF device. They can be provided by seeding a 3 stage Yb doped fiber amplifier with infrared radiation from a distributed feedback laser diode, which emits radiation at 1086.60 nm. This wavelength lies well within the gain spectrum of the Yb fibers, so that after amplification an important amount of radiation is transferred via second harmonic generation into 543.30 nm laser pulses. Currently, by operating the fiber amplifier at 1064 nm up to 131 μJ of converted, green pulse energy with a repetition rate of up to 5 kHz are available [43, 54]. Due to the broad emission spectrum of the Yb–ion an operation at 1086.60 nm is possible and similar output energies can be expected.

Equipped with this knowledge, two different Rubidium based excited state Faraday anomalous dispersion optical filter designs have been developed and investigated within this work: The geometry of vapor cell I restricted the magnetic field strength to 270 mT, such that the successive development of vapor cell II was required.

The transmission characteristics of these ESFADOF devices have been thoroughly investigated by the developed experimental setup and the measurement principle of chapter 4 has been employed. The sophisticated evaluation procedure assures the measurement of ESFADOF transmission spectra with the highest reported accuracies in transmission and frequency to date.

Vapor cell I allowed a systematic survey on the influence of the accessible experimental parameters. The outcome of this study demonstrates that:

1. Within distinct operational limits, stable and reliable ESFADOF operation is possible.
2. The absolute ESFADOF transmission is influenced by the number density of the atomic vapor, as well as by the injected pump power. Increasing the population of the lower ESFADOF state by means of increasing the density of the atomic vapor and/or the injected pump power results in an increase of the ESFADOF maximum transmission.
3. The ESFADOF spectral characteristics can be changed by detuning the wavelength of the pump laser from the center of the $5S_{1/2} \rightarrow 5P_{3/2}$ transition. This allows a symmetrization of the ESFADOF transmission edges with respect to the central wavelength of the Brillouin–lidar probe laser. By exploiting the symmetry of the Brillouin–backscatter, a potential increase in signal accuracy has been derived. This result allows to weaken the stability requirements on the lidar's probe laser wavelength.
4. Beyond a certain temperature threshold, which corresponds to a certain vapor density, or beyond a certain pump power the ESFADOF transmission collapses to a few percent. This collapse is caused by the onset of a laser induced plasma, which considerably consumes the population of the lower ESFADOF state and hence reduces the ESFADOF transmission.
5. The plasma state exhibits a hysteresis such that stable and reliable ESFADOF operation can be guaranteed below the plasma maintenance threshold only. Operations along this threshold reveal a maximum transmission of 25.01(1)%,

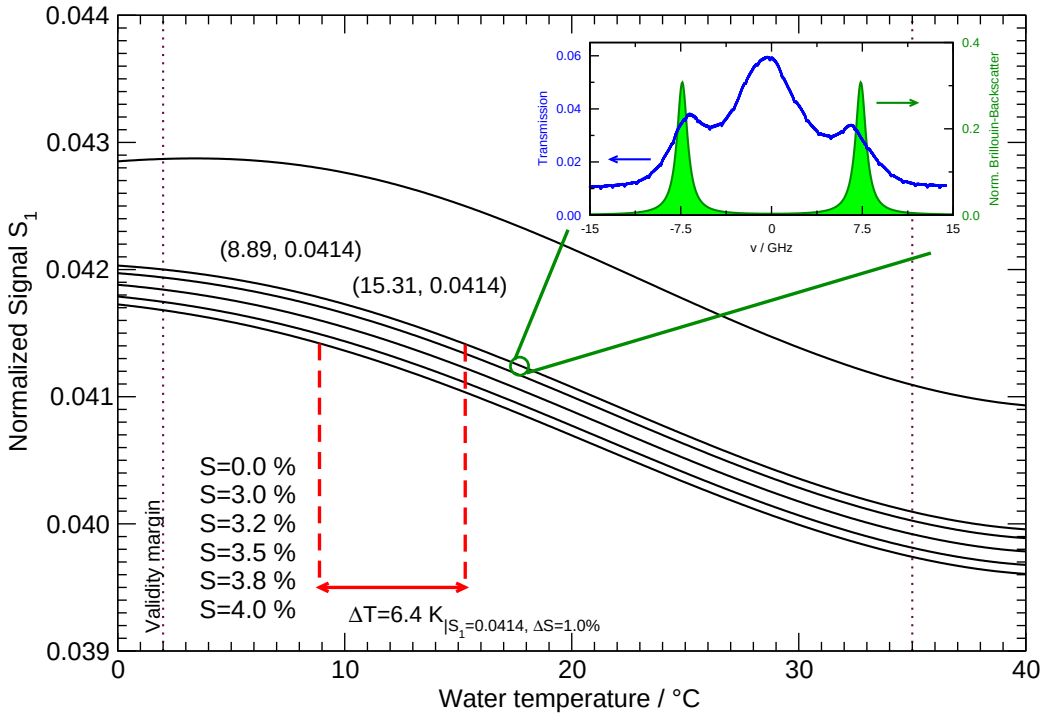

Fig. 6.1: Simulated characteristic curves of the Brillouin–lidar receiver, based on the measured ESFADOF transmission spectrum of Fig. 5.22: These characteristic curves result, when employing the measured ESFADOF transmission spectrum of Fig. 5.22 as edge–filter within the direct detection scheme. The inset shows the measured ESFADOF transmission spectrum and the simulated normalized Brillouin–backscatter, which corresponds to the circled data point. The characteristic curves have been achieved according to the discussion of Sec. 2.3. They reveal again the importance of the knowledge of the water salinity. The broken lines indicate the accuracy limitation of the temperature measurement, if the salinity is allowed to vary about 10 ‰. The resulting accuracy decreases compared to the result of the ideal square well edge–filter (cf. Fig. 2.7), due to the decreased slope.

when injecting a pump power of 147(2) mW into vapor cell I, which is held under a temperature of 179°C. This value is the highest realized ESFADOF transmission so far, which has been achieved with a continuously pumped ESFADOF device.

The special geometry of vapor cell II allowed to considerably increase the field strength to 500 mT. Only this high magnetic field strength shifts the ESFADOF transmission edges to the desired separation within the spectral region of interest of the Brillouin–lidar receiver. The employment of vapor cell II proved for the very first time, that the developed ESFADOF device provides transmission edges in the region of interest of the Brillouin–lidar, i.e. between $\pm 6.8 - 7.8$ GHz, nearly symmetrically located around the central wavelength of the $5P_{3/2} \rightarrow 8D_{5/2}$ ESFADOF transition. The symmetry has not been explicitly optimized. A de-

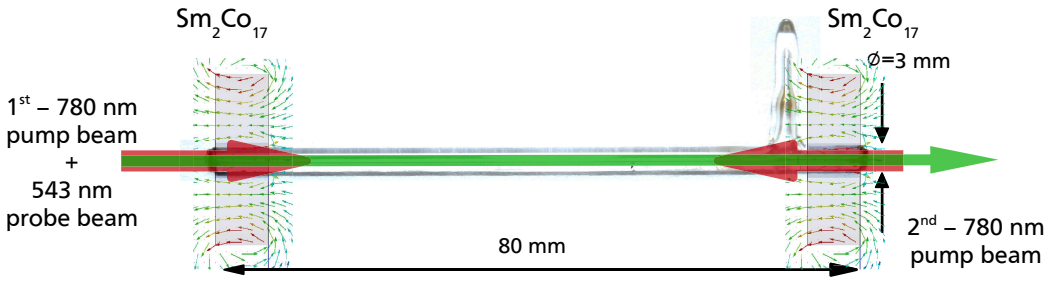

Fig. 6.2: Scalability of the ESFADOF device: By dublicating the active vapor cell volume, considerably higher ESFADOF transmissions result. The depicted case places a second permanent ring magnet at the opposite side of vapor cell II and injects a second pump laser. This procedure doubles the interaction length L and thus the Faraday rotation angle (cf. Eq. 3.7). According to Eq. 3.8 a considerably higher transmission results. This procedure can be repeated many times, as long as enough pump power is available. Particular care has to be spend on the position and orientation of the permanend ring magnets, in order to not allow them to cancel their contributions.

tuning of the pump laser frequency, as it has been done with vapor cell I, will symmetrize these spectra as well.

Although the current implementation of vapor cell II was limited in absolute transmission, the obtained results are very promising. They already allow a fundamental analysis of the Brillouin–lidar receiver. The same procedure, which leads to the characteristic curves of the ideal edge–filter (cf. Sec. 2.3 and Fig. 2.7), can be applied as well to the measured ESFADOF transmission spectrum (cf. Fig. 5.22). This evaluation results in the characteristic curves of Fig. 6.1 and in contrast to Fig. 2.7, they decrease when increasing the water temperature, due to the opposite slope of the ESFADOF transmission. Nevertheless, the figure demonstrates a clear correlation of the normalized lidar signal with the water temperature. Again, ignoring the salinity results in an increased uncertainty of the temperature derivation. A water temperature of 8.89°C and a salinity of 40 ‰ correspond to a signal amplitude of $S_1 = 0.0414$. Keeping this signal level constant, while decreasing the salinity to 30 ‰, changes the corresponding water temperature to 15.31°C. Hence an uncertainty of $\Delta T = 6.4$ K results. This increase in uncertainty is clearly a consequence of the flat slopes of the characteristic curves of Fig. 6.1, when compared to the ones of the ideal edge–filter Fig. 2.7, which are considerably steeper. However, the accuracy of the temperature assignment increases with the accuracy of the salinity parameter. These results mark an important mile stone towards an operational system, as it proves that the proposed detection–scheme is feasible.

An improvement of the ESFADOF device, which will lead to higher absolute transmission is currently under way. A maximum ESFADOF transmission of 10% has been achieved with vapor cell II. This is a consequence of the fact, that it was not possible to seal enough Rubidium inside the vapor cell, such that the

consumption of the Rubidium atoms by the employed epoxy saturates. Hence, the vanishing Rb vapor density considerably limited the maximum ESFADOF transmission. Future developments concentrate on improving the manufacturing process of vapor cell II. For that purpose a collaboration with Prof. Dr. Tilman Pfau from the *5. Physikalisches Institut Stuttgart* has been initiated. Their glass blowing facilities offer the possibility to increase the amount of sealed Rb, as they do not need to evaporate the Rb prior to sealing the vapor cell. In addition, a new manufacturing process of vapor cell II is currently under investigation. The glass blower of the *5. Physikalisches Institut Stuttgart* suggested to employ a special soldering technique in order to attach the fused silica front facets on the vapor cell, making the employment of the epoxy obsolete. It can be expected, that the employed solder reveals a much higher resistance against the Rb atoms than it was the case for the currently used epoxy. Thus, new results are to be expected in the near future.

Regardless of the employed technology in manufacturing the vapor cell, it is advantageous to exploit the scalability of the ESFADOF devices as well. FADOF and ESFADOF transmission spectra depend on the length of the active interaction volume L (cf. Eqs. 3.7 and 3.8). When regarding ground state FADOFs, this quantity corresponds to the vapor cell length, whereas the pumped vapor volume dominates this quantity, when regarding ESFADOFs. Depending on the available pump power, it is possible to increase the interaction length by a factor of two by simply inserting a second equally pumped vapor cell between the first vapor cell and the output polarizer. Fig. 6.2 illustrates this idea. By repeating this procedure several times, a significant increase of the maximum ESFADOF transmission can be expected. This possibility is also currently under way and is subject of the PhD–thesis of Andreas Rudolf [63].

In conclusion, this thesis succeeded in demonstrating the principal applicability of ESFADOF devices as high resolution edge–filter receivers, which comply with the needs of the direct detection scheme of the Brillouin–lidar project. The demonstrated maximum transmission of 25% marks the highest so far achieved value for a continuously pumped ESFADOF device. In addition, the presented research established distinct operational limits of these devices. These operational limits are based upon the formation of a laser induced plasma inside the alkali-metal vapor. However, by precisely considering these limits stable ESFADOF operations are possible.

Appendix

A

Rubidium Atom

1. Number density of the Rubidium vapor: A parameterization of the Rubidium vapor pressure can be found in Ref. [78]. By inserting it into the ideal gas law, the following relationship results:

$$n(T_{Cell}) = \frac{1}{k_B\, T_{Cell}} 10^{A_n + B_n/T_{Cell}} \text{ ,where} \tag{A.1}$$

$$A_n = 9.863 \text{ and } B_n = 4215 \text{ K for } 298 \text{ K} < T_{Cell} < T_{MP};$$
$$A_n = 9.318 \text{ and } B_n = 4040 \text{ K for } T_{MP} < T_{Cell} < 550 \text{ K}.$$

$T_{MP} = 312.46$ K marks the Rb melting point and Fig. A.1 is the graphical representation of Eq. A.1.

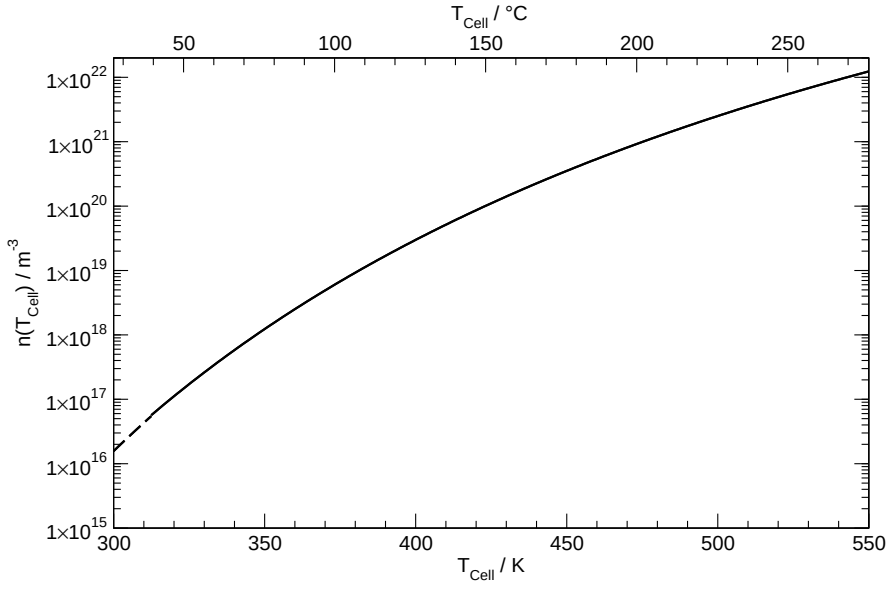

Fig. A.1: Temperature dependence of the Rubidium number density $n(T_{Cell})$: The Curves follow Eqs. A.1, where the dashed curve belongs to $T_{Cell} < T_{MP}$ and the solid one to $T_{Cell} > T_{MP}$. $T_{MP} = 312.46$ K is the Rubidium melting point [78].

2. Relevant atomic constants of the Rubidium isotopes: The constants follow the suggestions of Refs. [78, 144, 206–208].

^{85}Rb	^{87}Rb
Atomic Mass:	
$m_{^{85}Rb} = 84.911\,789\,732\,(14)$ u	$m_{^{87}Rb} = 86.909\,180\,520\,(15)$ u
Relative Natural Abundance:	
$a_{85} = 72.17\,(2)\%$	$a_{87} = 27.83\,(2)\%$
Decay Rates:	
$A_{5S_{1/2}\to 5P_{3/2}} = 38.117(11)$ MHz	
$A_{5P_{3/2}\to 8D_{5/2}} = 1.659$ MHz	
Transition wavenlegth (Vacuum): $5S_{1/2} \to 5P_{3/2}$	
$\lambda_{85} = 780.241\,368\,271\,(27)$ nm	$\lambda_{87} = 780.241\,209\,686\,(13)$ nm
Transition wavelength (Vacuum): $5P_{3/2} \to 8D_{5/2}$	
$\lambda_{85,87} = 543.3035$ nm	
Nuclear spin:	
$I = 5/2$	$I = 3/2$
Gyromagnetic factors of the nuclear spin momentum:	
$g_I = 0.000\,293\,640\,0\,(6)$	$g_I = 0.000\,995\,141\,4(10)$
Magnetic dipole (A) and electric quadrupole (B) constants,:	
$A_{5S_{1/2}} = 1\,011.910\,813\,0\,(20)$ MHz	$A_{5S_{1/2}} = 3\,417.341\,305\,452\,145\,(45)$ MHz
$A_{5P_{3/2}} = 25.002\,0\,(99)$ MHz	$A_{5P_{3/2}} = 84.718\,5\,(20)$ MHz
$B_{5P_{3/2}} = 25.790\,(93)$ MHz	$B_{5P_{3/2}} = 12.496\,5\,(37)$ MHz
$A_{8D_{5/2}} = -0.35\,(7)$ MHz	$A_{8D_{5/2}} = -1.20\,(15)$ MHz

A measured absorption spectrum of the $5S_{1/2} \to 5P_{3/2}$ transition is depicted in Fig. A.2.

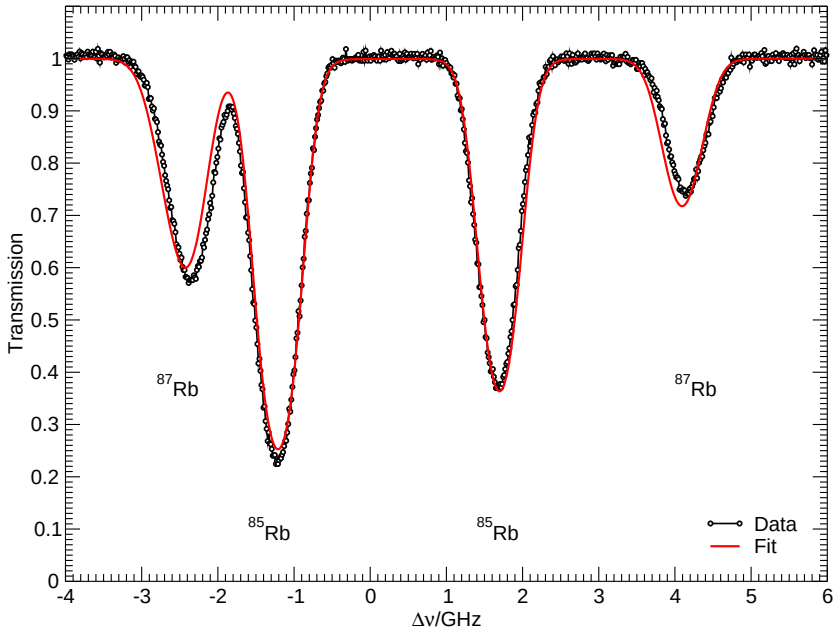

Fig. A.2: Measured absorption spectrum of the $5S_{1/2} \rightarrow 5P_{3/2}$ transition: The cell temperature was 41°C and the cell length L = 25 mm. The atomic hyperfine structure of both Rb isotopes is apparent. The data and the numerical fit have been extracted from Ref. [21].

B

Manufacturing process of Rb Vapor Cell II

The high demands on the geometry of the cell design makes the manufacturing process very difficult. Fig. B.1 shows the blueprint of vapor cell II. The preparation and glueing of the front facets are the main challenge. In addition to the performed vacuum tests, the scanning electron microscope pictures of Fig. B.2 prove the success of the following manufacuturing procedure:

1. Commercial hollow cylindrical raw glass tubes are cut into appropriate pieces. As the uncertainty of the outer diameter is more than ± 0.15 mm, which is the maximum allowed uncertainty of the permanent magnets' hollow core, the raw material has to be manually chosen. By carefully sliding the magnets over the tubes, appropriate pieces have been chosen for further treatment. The rest of the raw material serves for an additional filling extension.
2. The filling extension has been added by the glassblower. Briefly speaking, a hole is melted into the tube and another tube is melted perpendicular to the hole.
3. The tubes are cut by a diamond saw to their design length under an angle of 11°. After the cutting process, they are cleaned with ethanol and cooked in acetone.
4. The front facets have been cut with an ultrasonic drill from fused silica substrates. A diameter of 2.5 mm has been chosen in order to fully cover the angled front of the glass tubes, leaving enough surface for the glue within the maximum 3 mm diameter of the tube.
5. As already mentioned, a tapered form of the front facets is advantageous in preventing disturbing etalon effects. This tapered form has been achieved by an additional polishing process through several steps by a polishing machine. The angle of 2° has been chosen in order to keep the refraction of the beam small and to aviod the overlap with the reflected beam. In order to protect the polished sides, both facets have been covered with a thick film of First Contact [209]. First Contact is a commercially available polymer composite, protecting optical surfaces from dust and damages. The dissolved polymer can be applied on many different surfaces and seals them very efficiently after drying. When needed the film can be removed mechanically without any contamination of the surface. This procedure protects the facetes during the mechanical polishing process.

6. Gluing the facets on the tubes is a difficult task. In particular, applying too much glue results in a too small or completely covered aperture of the cell. The following procedure revealed the desired results: (1) A very thin film of glue (EpoTek 353ND [160]) is applied on the front of the cylinder. Then, a facet is positioned over the tube and dropped to its final place. This has to be done extremely careful in order to fully cover the aperture. As any correction is impossible, failed facets have to be replaced before curing the glue. Moving the facet once it sticks to the glue or applying to much glue results in a thin film of glue covering the aperture of the cell. (2) The glue cures at high temperatures beyond 60°C and is temperature resistant up to 300°C. Thus, placing the cell in an oven at 200°C proved to produce the best results. The high temperatures ensure a fast and uniform curing process leaving the aperture clear. (3) Once the facet is fixed a second film of glue around the facet has to be applied in order to ensure its impermeability. The second film is cured again in the oven at 200°C. This procedure is repeated for the second facet and for each cell.
7. All leak detector test proved to be negative. Therefore assuming leaks below the accuracy limit of the detector results in a half life of the vacuum of more than 6.5 days.

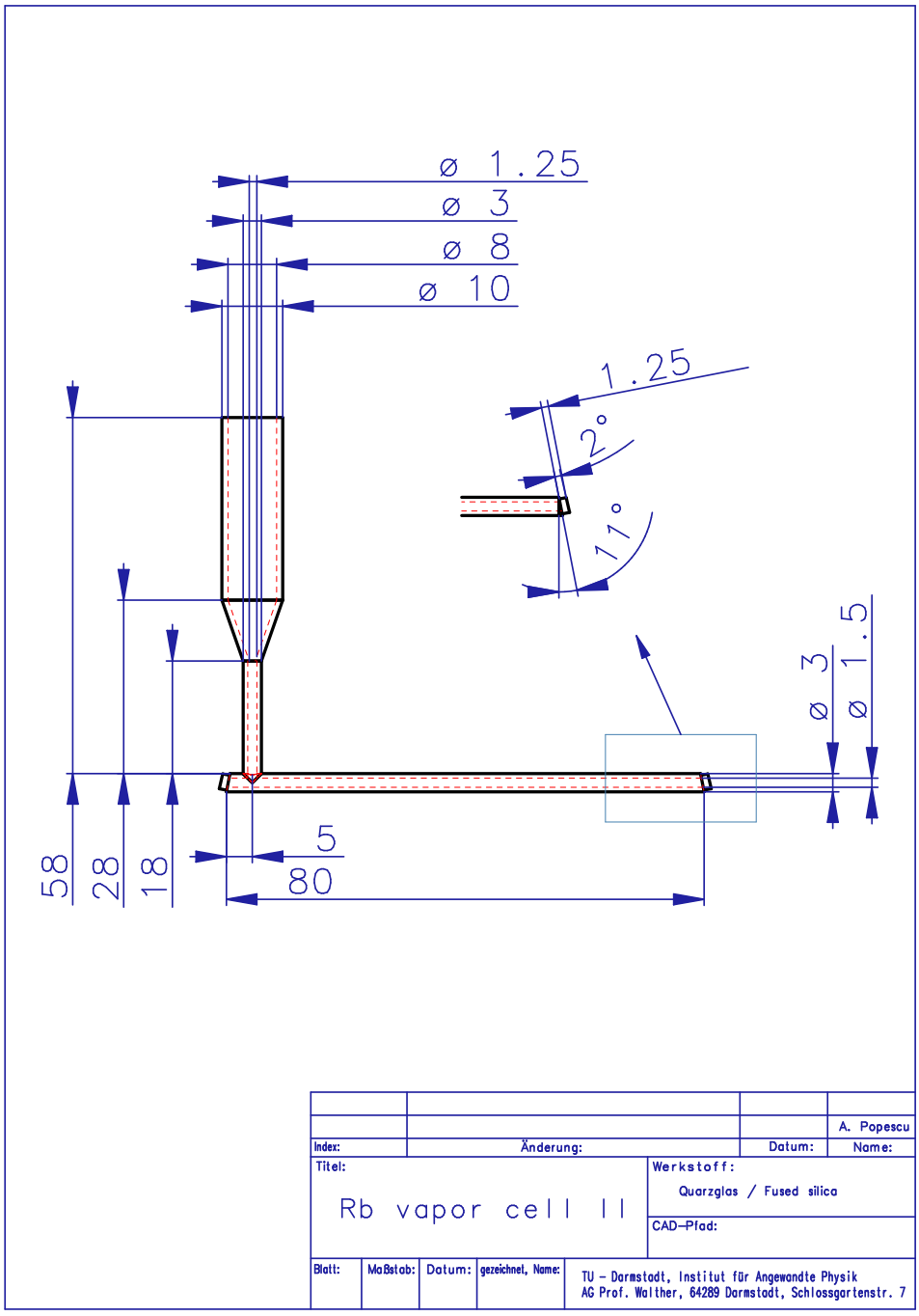

t!

Fig. B.1: Blueprint of vapor cell II: The front windows are glued with vacuum and temperature resistant glue (EpoTek 353ND [160]) on the cell tube. The cell front facets are glued under an angle of 11° and posses themselves a tapered shape of 2° inclination, inhibiting etaloning effects. The remaining optically accessible diameter is 1.5 mm, which is approx. 4 times of the pump laser diameter. The cell is made from fused silica, in order to inhibit the Rb diffusion into the cell walls.

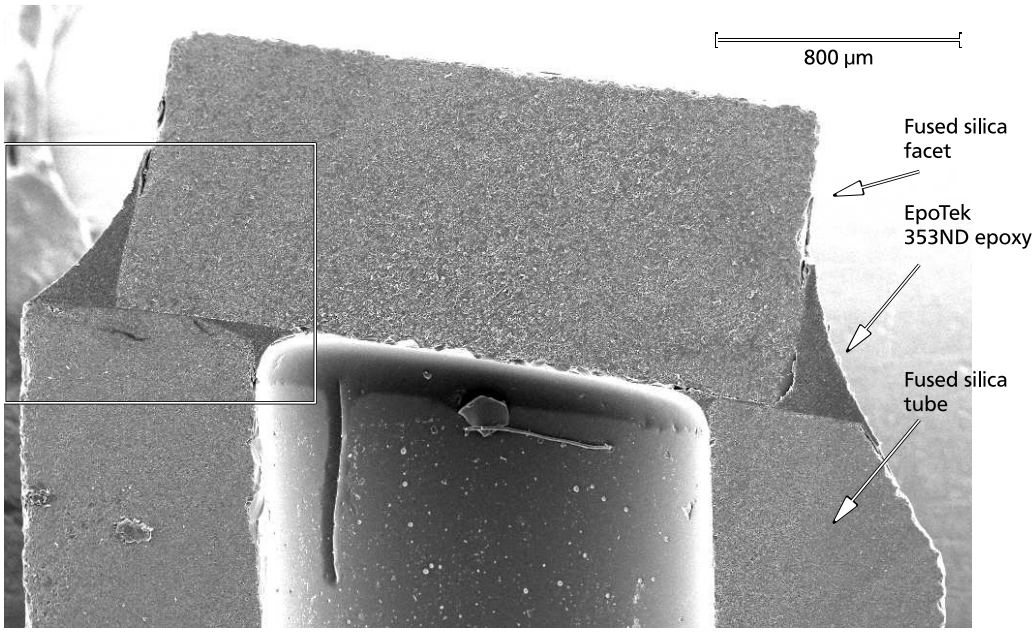

(a) Leak tight seal: The described manufacturing procedure of vapor cell II proves to be successful and seals the vapor cell very efficiently.

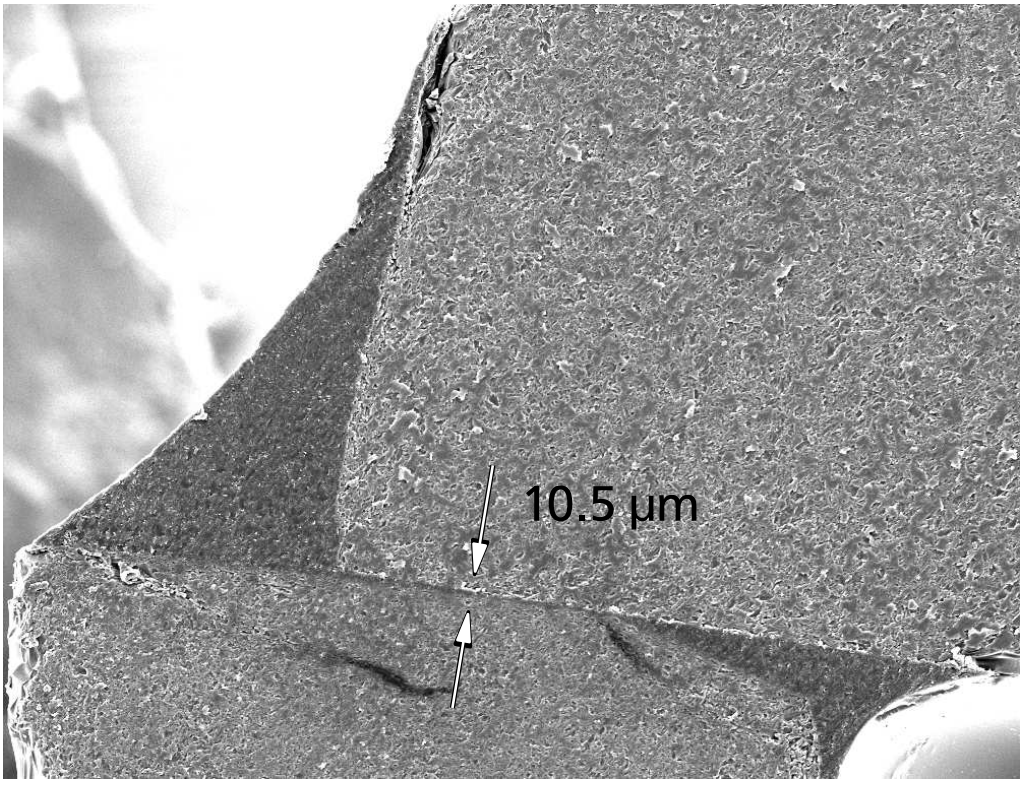

(b) Enlargement of the squared area of Fig. B.2(a): Applying only a thin film of glue is important. This prevents the glue from covering the narrow aperture.

Fig. B.2: Scanning electron microscope pictures of vapor cell II: This test sample has been cut along the symmetry axis and reveals a cross section of the glued front facet. The pictures have been taken by Arno Weick from the Institute of Applied Physics, Darmstadt.

C

Magnetic Field Strengths of the Employed Permanent Ring Magnets

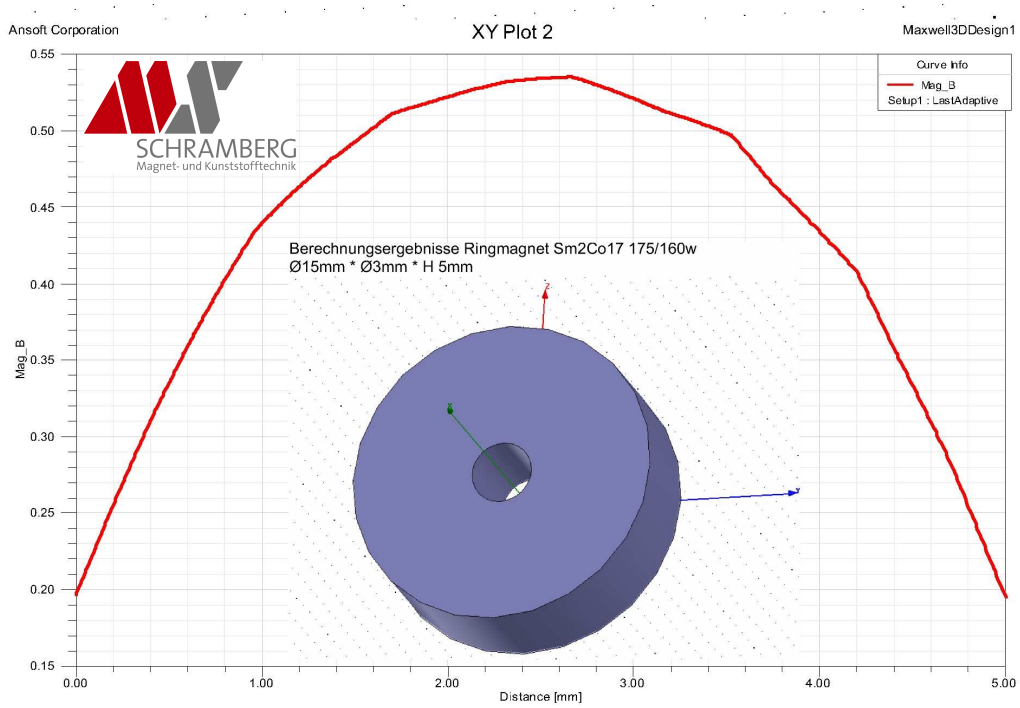

Fig. C.1: Finite element analysis of the magnetic field of the employed Sm_2Co_{17} ring magnet [151]; Courtesy of MS-Schramberg GmbH & Co. KG, Magnet- und Kunststofftechnik: The inset shows the geometry of the magnet. The outer diameter is 15 mm, the inner diameter is 3 mm and the length is 5 mm. The curve shows the magnetic field strength along the symmetry axis. The magnetic field strength reaches a maximum value of $B_z = 535$ mT. These simulations have been performed by A. Haberer.

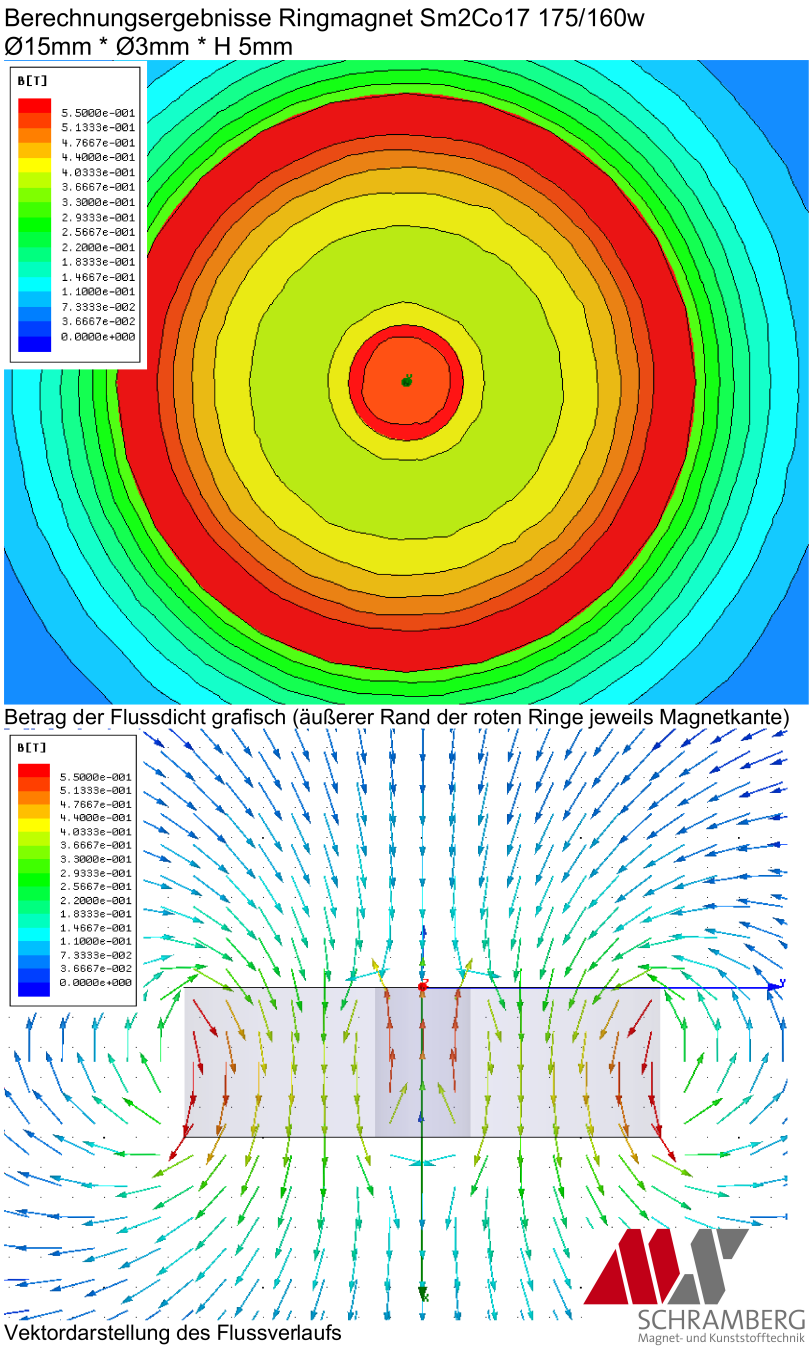

Fig. C.2: Finite element analysis of the same Sm_2Co_{17} ring magnet as depicted in Fig. C.1; Courtesy of MS-Schramberg GmbH & Co. KG, Magnet- und Kunststofftechnik: The upper part of the figure shows a top view cross section of the magnetic field strength as it penetrates the surface of the magnet. The outer margins of the red areas mark the rim of the ring magnet. The lower part is a vector plot of the magnetic field in the y,z–plane. These simulations have been performed by A. Haberer.

D

Tripod ECDL

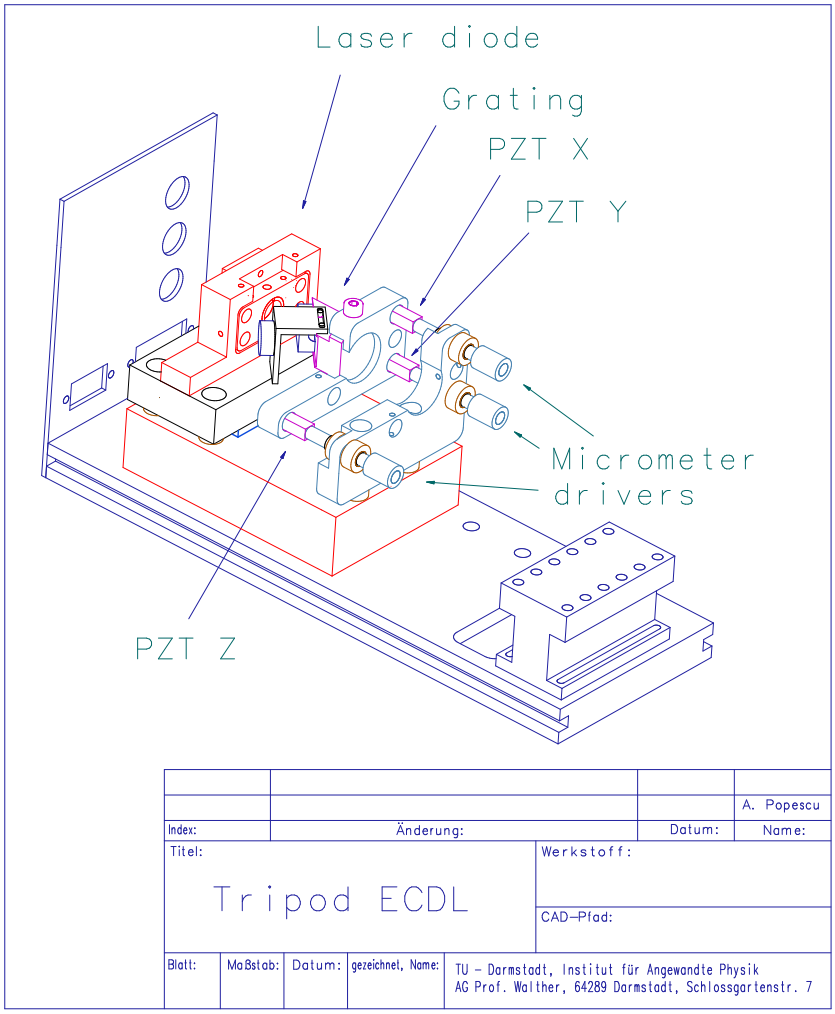

Fig. D.1: Schematic of the developed tripod ECDL: The employed piezo electric transducers (PZT X,Y and Z) offer an upstroke of 30 μm. A mode–hop free frequency tuning of up 89 GHz is achieveable with a 1086 nm laser diode [210].

References

[1] R.H. Stewart and A. Texas, Introduction to Physical Oceanography (Texas A & M University, 2005).

[2] G.R. Bigg, T.D. Jickells, P.S. Liss and T.J. Osborn, The role of the oceans in climate, *International Journal of Climatology*, **23** (2003) 1127–1159.

[3] S. Solomon, D. Qin, M. Manning, Z. Chen, M. Marquis, K.B. Averyt, M. Tignor and Miller H.L., Eds., Climate Change 2007: The Physical Science Basis: Contribution of Working Group I to the Fourth Assessment Report of the Intergovernmental Panel on Climate Change (Cambridge University Press, 2007).

[4] Gerald H. Haug, Detlef Gunther, Larry C. Peterson, Daniel M. Sigman, Konrad A. Hughen and Beat Aeschlimann, Climate and the Collapse of Maya Civilization, *Science*, **299** (2003) 1731–1735.

[5] Joel B. Smith, Stephen H. Schneider, Michael Oppenheimer, Gary W. Yohe, William Hare, Michael D. Mastrandrea, Anand Patwardhan, Ian Burton, Jan Corfee-Morlot, Chris H. D. Magadza, Hans-Martin Füssel, A. Barrie Pittock, Atiq Rahman, Avelino Suarez, and Jean-Pascal van Yperselen, Assessing dangerous climate change through an update of the Intergovernmental Panel on Climate Change (IPCC) (National Academy of Sciences of the United States of America, 2009) pp. 4133–4137.

[6] S. Levitus, J. I. Antonov, T. P. Boyer, R. A. Locarnini, H. E. Garcia and A. V. Mishonov, Global ocean heat content 1955–2008 in light of recently revealed instrumentation problems, *Geophysical Research Letters*, **36** (2009) L07608.

[7] Bjørn Lomborg, The Skeptical Environmentalist: Measuring the Real State of the World (Cambridge University Press, 2001).

[8] Michael Grubb, ENVIRONMENT: Relying on Manna from Heaven?, *Science*, **294** (2001) 1285–1287.

[9] Stephen Schneider, Misleading Math About the Earth, *Scientific American*, **286** (2002) 61–71.

[10] G.L. Mellor and P.A. Durbin, The Structure and Dynamics of the Ocean Surface Mixed Layer, *Journal of Physical Oceanography*, **5** (1975) 718–728.

[11] H.M. Stommel, The gulf stream: a physical and dynamical description (Univ. of Calif. Press, 1965).

[12] J.F. Price, Upper Ocean Response to a Hurricane, *Journal of Physical Oceanography*, **11** (1981) 153–175.

[13] K.A. Emanuel, The Maximum Intensity of Hurricanes, *Journal of the Atmospheric Sciences*, **45** (1988) 1143–1155.

[14] K.A. Emanuel, Thermodynamic control of hurricane intensity, *Nature*, **401** (1999) 665–669.

[15] H.E Willoughby, Hurricane heat engines, *Nature*, **401** (1999) 649–650.

[16] A. Popescu, K. Schorstein and Th. Walther, A novel approach to a Brillouin-LIDAR for remote sensing of the ocean temperature, *Appl. Phys. B*, **79** (2004) 955–961.

[17] E.S. Fry. Brillouin Lidar Receiver Based on Absorption in I_2 and Br_2. Tech. rep., Physics Department Texas A&M University, 1992.

[18] R.M. Pope and E.S. Fry, Absorption spectrum (380-800 nm) of pure water. II. integrating cavity measurements, *Appl. Opt.*, **36** (1997) 8710–8723.

[19] Kai-Matthias Schorstein, Aufbau eines Brillouin-LIDARs zur Messung des Temperaturprofils in Wasser basierend auf einem gepulsten Faserverstärker, Dissertation, Technische Universität Darmstadt, 2009.

[20] A. Popescu and Th. Walther, On the potential of Faraday anomalous dispersion optical filter as high-resolution edge filters, *Laser Phys.*, **15** (2005) 55–60.

[21] Alexandru Popescu, Untersuchung eines Faraday Filters als optisches Meßinstrument an der Rubidium $5s_{1/2} \rightarrow 5p_{3/2}$-Resonanz. Diplomarbeit, TU Darmstadt, 2004.

[22] A.P. Cracknell and L. Hayes, Introduction to Remote Sensing (CRC Press, Boca Raton, 2007).

[23] T. Fujii and T. Fukuchi, Eds., Laser Remote Sensing (CRC Taylor & Francis, Boca Raton, 2005).

[24] C. Weitkamp, Laser Remote Sensing, Kap. Lidar: Introduction (CRC Taylor & Francis, Boca Raton, 2005).

[25] G.E. Walrafen, Raman Spectral Studies of the Effects of Temperature on Water Structure, *The Journal of Chemical Physics*, **47** (1967) 114.

[26] D.A Leonard, B. Caputo and F.E. Hoge, Remote sensing of subsurface water temperature by Raman scattering, *Applied Optics*, **18** (1979) 1732–1745.

[27] L.I. Mandel'shtam, *Zh. Russk. Fiz.-Khim. Obshchestva Ch. Fiz.*, **58** (1926) 381.

[28] L. Brillouin, La Diffraction de la Lumière par des Ultrasons, *Annales de Physique (Paris)*, **17** (1921) 103.

[29] L. Brillouin, *Annales de Physique (Paris)*, **17** (1922) 88.

[30] J.L. Guagliardo and H.L. Dufilho, Range-resolved Brillouin scattering using a pulsed laser, *Rev. Sci. Instr.*, **51** (1980) 79–81.

[31] I.L. Fabelinskii, Molecular Scattering of Light (Plenum Press, New York, 1968).

[32] J.G. Hirschberg, A.W. Wouters, K.M. Simon, J.D. Byrne and C.E. Deverdun, Laser application to measure vertical sea temperature and turbidity, *NASA Report CR-144865*, (1976).

[33] Donald J. Collins, John A. Bell, Ray Zanoni, I. Stuart McDermid, James B. Breckinridge and Cesar A. Sepulveda, Recent progress in the measurement of temperature and salinity by optical scattering, *Ocean Optics VII*, **489** (1984) 247–269.

[34] J.G. Hirschberg, J.D. Byrne, A.W. Wouters and G.C. Boynton, Speed of sound and temperature in the ocean by brillouin scattering, *Appl. Opt.*, **23** (1984) 2624.

[35] G.D. Hickman, J.M. Harding, M. Carnes, A. Pressman, G.W. Kattawar and E.S. Fry, Aircraft laser sensing of sound velocity in water: Brillouin scattering, *Rem. Sens. Environ.*, **36** (1991) 165–178.

[36] J.D. Smith, C.D. Cappa, W.S. Drisdell, R.C. Cohen and R.J. Saykally, Raman Thermometry Measurements of Free Evaporation from Liquid Water Droplets, *J. Phys. Chem. B*, **109** (2006) 24391.

[37] G.D. Hickman and J.E. Hogg, Application of an airborne pulsed laser for near-shore bathymetric measurements, *Remote Sens of Env.*, **1** (1969) 47.

[38] G. C. Guenther, A. G. Cunningham, P.E. LaRocque and D.J. Reid, Meeting the accuracy challenge in airborne lidar bathymetry, *Proc. EARSeL-SIG-Workshop: LIDAR*, **1** (2000) 1–27.

[39] Y. Emery and E.S. Fry, Laboratory development of LIDAR for measurement of sound velocity in the ocean using Brillouin scattering, *Proc. SPIE, Ocean Optics XIII*, **2963** (1996) 210–215.

[40] E.S. Fry, J. Katz, R. Nicolaescu and Th. Walther, Remote sensing in the ocean: Measurement of sound speed and temperature, *Proc. SPIE, Ocean Optics XIV*, (1998).

[41] E.S. Fry, J. Katz, D. Liu and Th. Walther, Temperature dependence of the Brillouin linewidth in water, *J. of Mod. Opt.*, **49** (2002) 411–418.

[42] E.S. Fry, G. Xiao and J. Katz, Measurement of sound speed and temperature in the ocean via remote sensing of Brillouin scattering, *Proc. of Ocean Optics XV*, (2002).

[43] K. Schorstein, A. Popescu, M. Göbel and T. Walther, Remote Water Temperature Measurements Based on Brillouin Scattering with a Frequency Doubled Pulsed Yb: doped Fiber Amplifier, *Sensors*, **8** (2008) 5820–5831.

[44] K. Schorstein, E.S. Fry and Th. Walther, Depth-resolved temperature measurements of water using the Brillouin lidar technique, *Applied Physics B: Lasers and Optics*, **97** (2009) 4.

[45] S.W. Henderson, Laser Remote Sensing, Kap. Wind Lidar (CRC Taylor & Francis, Boca Raton, 2005).

[46] C.L. Korb, B.M. Gentry and C.Y. Weng, Edge technique: theory and application to the LIDAR measurement of atmospheric wind, *Appl. Opt.*, **31** (1992) 4202.

[47] A. Popescu, D. Walldorf, K. Schorstein and Th. Walther, On an excited state Faraday anomalous dispersion optical filter at moderate pump powers for a Brillouin-LIDAR receiver system, *Opt. Comm.*, **264** 475–481.

[48] Kai Schorstein, Gerrit Scheich, Alexandru Popescu, Thomas Walther and Edward S. Fry, A fiber amplifier and an ESFADOF: Developments for a transceiver in a Brillouin LIDAR, *Laser Physics*, **17** (2007) 975–982.

[49] J. Shi, G. Li, W. Gong, J. Bai, Y. Huang, Y. Liu, S. Li and D. Liu, A lidar system based on stimulated Brillouin scattering, *Appl. Phys. B*, **86** (2007).

[50] J. Shi, M. Ouyang, W. Gong, S. Li and D. Liu, A Brillouin lidar system using f-p etalon and iccd for remote sensing of the ocean, *Appl. Phys. B*, **90** (2008).

[51] W. Zirnig, M. Ulbricht, A. Fix and H. Klingenberg, Helicopter-borne laser methan detection system – A new tool for efficient gas pipeline inspection, *Proceedings 2004 International Gas Research Conference, Vancouver, Canada, November*, (2004).

[52] K. Schorstein, A. Popescu, G. Scheich, T. Walther and E.S. Fry, Towards a brillouin-lidar for remote sensing of the temperature profile in the ocean, *OCEANS 2006*, (2006) 1–6.

[53] Alexandru Popescu, Kai Schorstein, Gerrit Scheich, Ingo Massmann, Peer Fietzek, Thomas Walther and Edward S. Fry, Key developments for a brillouin-lidar for remote sensing of oceanic temperature profiles, in: 3rd EARSeL Workshop on the Remote Sensing of the Coastal Zone, ed. R. Reuter, 2007).

[54] K. Schorstein and Th. Walther, A high spectral brightness Fourier-transform limited nanosecond Yb-doped fiber amplifier, *Applied Physics B: Lasers and Optics*, **97** (2009) 591–597.

[55] L. Zenteno, High-power double-clad fiber lasers, *J. of Lightw. Techn.*, **11** (1993) 1435–1446.

[56] J. Limpert, T. Schreiber, T. Clausnitzer, K. Zöllner, H. Fuchs, E. Kley, H. Zellmer and A. Tünnermann, High-power femtosecond Yb-doped fiber amplifier, *Optics Express*, **10** (2002) 628–638.

[57] A. Galvanauskas, Mode-scalable fiber-based chirped pulse amplification systems, *IEEE J. of Selected Topics in QE*, **7** (2001) 504–516.

[58] J. Limpert, S. Höfer, A. Liem, H. Zellmer, A. Tünnermann, S. Knoke and H. Voelckel, 100-W average-power, high-energy nanosecond fiber amplifier, *Appl. Phys. B*, **75** (2002) 477–479.

[59] H.M. Pask, R.J. Carman, D.C. Hanna, A.C. Tropper, C.J. Mackechnie, P.R. Barber and J.M. Dawes, Ytterbium-doped silica fiber lasers: Versatile sources for the 1-1.2 μm region, *IEEE J. of Selected Topics in QE*, **1** (1995) 2–13.

[60] R. Nicolaescu, E.S. Fry and Th. Walther, Generation of near-fourier-transform-limited high-energy pulses in a chain of fiber–bulk amplifiers, *Opt. Lett.*, **26** (2001) 13–15.

[61] R.G. Smith, Optical power handling capacity of low loss optical fibers as determined by stimulated Raman and Brillouin scattering, *Appl. Opt.*, **11** (1972) 2489–2494.

[62] G.P. Agrawal, Nonlinear Fiber Optics (Academic Press, 1995).

[63] Andreas Rudolf, Dissertation, Technische Universität Darmstadt, to be published 2013.

[64] X. Quan and E.S. Fry, An empirical expression for the index of refraction of seawater, *Appl. Opt.*, **34** (1995) 3477–3480.

[65] B.J. Berne and R Pecora, Dynamic Light Scattering (Dover Publications, Inc., Mineola, New York, 2000).

[66] V.A Del Grosso, New equation for the speed of sound in natural waters (with comparisons to other equations), *The Journal of the Acoustical Society of America*, **56** (1974) 1084.

[67] Brian D. Dushaw, Peter F. Worcester, Bruce D. Cornuelle and Bruce M. Howe, On equations for the speed of sound in seawater, *The Journal of the Acoustical Society of America*, **93** (1993) 255–275.

[68] R.C. Millard and G. Seaver, An index of refraction algorithm for seawater over temperature, pressure, salinity, and wavelength, *Deep-Sea Research*, **37** (1990) 1090–1926.

[69] Claude C. Leroy, Stephen P. Robinson and Mike J. Goldsmith, A new equation for the accurate calculation of sound speed in all oceans, *The Journal of the Acoustical Society of America*, **124** (2008) 2774–2782.

[70] Claude C. Leroy and Francois Parthiot, Depth-pressure relationships in the oceans and seas, *The Journal of the Acoustical Society of America*, **103** (1998) 1346–1352.

[71] Claude C. Leroy, Erratum: "Depth-pressure relationships in the oceans and seas" [J. Acoust. Soc. Am. **103** (3), 1346–1352 (1998)], *The Journal of the Acoustical Society of America*, **121** (2007) 2447–2447.

[72] E.S. Fry, Y. Emery, X. Quan and J.W. Katz, Accuracy limitations on Brillouin LIDAR measurements of temperature and sound speed in the ocean, *Appl. Opt.*, **36** (1997) 6887–6894.

[73] R.W. Boyd, Nonlinear Optics (Academic Press Inc., San Diego, 1992).

[74] A.E. Siegman, Lasers (University Science Books, Mill Valley, 1986).

[75] L. Landau and G. Placzek, *Physik. Z.Sowjetunion*, **5** (1934) 172.

[76] D. H. Rank, Validity of the Landau Placzek Relationship in Brillouin Scattering in Liquids, *J. Opt. Soc. Am.*, **47** (1957) 103–104.

[77] J. Rouch, C. C. Lai and S. H. Chen, Brillouin scattering studies of normal and supercooled water, *The Journal of Chemical Physics*, **65** (1976) 4016–4021.

[78] CRC Handbook of Chemistry and Physics, 78th Edition (CRC Press, Boca Raton, 1997).

[79] A. I. Erokhin, Water Structure and Supergigahertz Phonons, *Journal of Russian Laser Research*, **23** (2002) 369–380.

[80] N. J. Tao and S. M. Lindsay, Coupling of acoustic phonons in lithium chloride aqueous solutions to a relaxation mode of the ionic hydration shell and observation of central peaks in inelastic light scattering, *The Journal of Physical Chemistry*, **92** (1988) 5855–5857.

[81] G. M. Gale, G. Gallot, F. Hache, N. Lascoux, S. Bratos and J-Cl. Leicknam, Femtosecond dynamics of hydrogen bonds in liquid water: A real time study, *Phys. Rev. Lett.*, **82** (1999) 1068–1071.

[82] Y. L. A. Rezus and H. J. Bakker, Orientational dynamics of isotopically diluted H_2O and D_2O, *The Journal of Chemical Physics*, **125** (2006) 144512.

[83] Huib J. Bakker, Water dynamics: Ion-ing out the details, *Nature Chemistry*, **1** (2009) 24–25.

[84] David E. Moilanen, Daryl Wong, Daniel E. Rosenfeld, Emily E. Fenn and M. D. Fayer, Ion–water hydrogen-bond switching observed with 2D IR vibrational echo chemical exchange spectroscopy, *Proceedings of the National Academy of Sciences*, **106** (2009) 375–380.

[85] Ulrike Paffrath, Performance assessment of the Aeolus Doppler wind lidar prototype, Dissertation, Technische Universität München, June 2006.

[86] Oliver Reitebuch, Christian Lemmerz, Engelbert Nagel, Ulrike Paffrath, Yannig Durand, Martin Endemann, Frederic Fabre and Marc Chaloupy, The Airborne Demonstrator for the Direct-Detection Doppler Wind Lidar ALADIN on ADM-Aeolus. Part I: Instrument Design and Comparison to Satellite Instrument, *Journal of Atmospheric and Oceanic Technology*, **26** (2009) 2501–2515.

[87] Ulrike Paffrath, Christian Lemmerz, Oliver Reitebuch, Benjamin Witschas, Ines Nikolaus and Volker Freudenthaler, The Airborne Demonstrator for the Direct-Detection Doppler Wind Lidar ALADIN on ADM-Aeolus. Part II: Simulations and Rayleigh Receiver Radiometric Performance, *Journal of Atmospheric and Oceanic Technology*, **26** (2009) 2516–2530.

[88] M.J. Kavaya, S.W. Henderson, J.R. Magee, C.P. Hale and R.M. Huffaker, Remote wind profiling with a solid-state Nd: YAG coherent lidar system, *Optics Letters*, **14** (1989) 776–778.

[89] Handbook of Mathematical Functions with Formulas, Graphs, and Mathematical Tables (Dover Publications, New York, 1972).

[90] J. I. Antonov, R. A. Locarnini, T. P. Boyer, A. V. Mishonov, and H. E. Garcia, World Ocean Atlas 2005, Volume 2: Salinity.

[91] B. Lyot, Optical apparatus with wide field using interference of polarized light, *C. R. Acad. Sci. (Paris)*, **197** (1933) 1593.

[92] B.E.A. Saleh and M.C. Teich, Fundamentals of Photonics (Wiley, New York, 1991).

[93] A. Popescu and Th. Walther, On an ESFADOF edge-filter for a range resolved Brillouin-lidar: The high vapor density and high pump intensity regime, *Applied Physics B: Lasers and Optics*, **98** (2010) 667–675.

[94] Cunyun Ye, Tunable External Cavity Diode Laser (World Scientific, New Jersey, USA, 2004).

[95] Lew Goldberg and J. F. Weller, Broad-area high-power semiconductor optical amplifier, *Applied Physics Letters*, **58** (1991) 1357–1359.

[96] J. N. Walpole, E. S. Kintzer, S. R. Chinn, C. A. Wang and L. J. Missaggia, High-power strained-layer ingaas/algaas tapered traveling wave amplifier, *Applied Physics Letters*, **61** (1992) 740–742.

[97] L. Goldberg, D. Mehuys, M.R. Surette and D.C. Hall, High-power, near-diffraction-limited large-area traveling-wave semiconductor amplifiers, *Quantum Electronics, IEEE Journal of*, **29** (1993) 2028–2043.

[98] E.S. Kintzer, J.N. Walpole, S.R. Chinn, C.A. Wang and L.J. Missaggia, High-power, strained-layer amplifiers and lasers with tapered gain regions, *Photonics Technology Letters, IEEE*, **5** (1993) 605–608.

[99] M. Mikulla, P. Chazan, A. Schmitt, S. Morgott, A. Wetzel, M. Walther, R. Kiefer, W. Pletschen, J. Braunstein and G. Weimann, High-brightness tapered semiconductor laser oscillators and amplifiers with low-modal gain epilayer-structures, *Photonics Technology Letters, IEEE*, **10** (1998) 654–656.

[100] S. B. Bayram and T. E. Chupp, Operation of a single mode external-cavity laser diode array near 780 nm, *Review of Scientific Instruments*, **73** (2002) 4169–4171.

[101] D. Macaluso and O.M. Corbino, *C.R. Acad. Sci.*, **127** (1898) 548.

[102] Robert W. Wood, Physical Optics (The Macmillan Company, New York, 1935).

[103] Yngve Öhman, *Stockholm Obs. Ann.*, **19** (1956) 3.

[104] T. H. Maiman, Stimulated Optical Radiation in Ruby, *Nature*, **187** (1960) 493–494.

[105] M. Cimino, A. Cacciani and N. Sopranzi, An Instrument to measure Solar Magnetic Fields by an Atomic-Beam Method, *Solar Physics*, **3** (1968) 618–622.

[106] S. Tomczyk, K. Streander, G. Card, D. Elmore, H. Hull and A. Cacciani, An instrument to observe low-degree solar oscillations, *Solar Physics*, **159** (1995) 1–21.

[107] G.J. Roberts, P.E.G. Baird, M.W.S.M. Brimicombe, P.G.H. Sandars, D.R. Selby and D.N. Stacy, The Faraday effect and magnetic circular dichroism in atomic bismuth, *J. Phys. B: Atom. Molec. Phys.*, **13** (1980) 1389.

[108] Pochi Yeh, Dispersive magnetooptic filters, *Appl. Opt.*, **21** (1982) 2069–2075.

[109] X. Chen, V.L. Telegdi and A. Weis, Magneto-optical rotation near the Cs D_2 line (Macaluso-Corbino effect) in intermediate fields, *J. Phys. B: Atom. Molec. Phys.*, **20** (1987) 5653.

[110] D. J. Dick and T. M. Shay, Ultrahigh-noise rejection optical filter, *Opt. Lett.*, **16** (1991) 867–869.

[111] B. Yin and T.M. Shay, Theoretical model for a Faraday anomalous dispersion optical filter, *Opt. Lett.*, **16** (1991) 1617.

[112] B. Yin, L.S. Alvarez and T.M. Shay, The Rb 780-nm Faraday anomalous dispersion optical filter: Theory and experiment, *TDA Progress Report*, **42** (1994) 71.

[113] H. Chen, C. Y. She, Paul Searcy and Eric Korevaar, Sodium-vapor dispersive Faraday filter, *Opt. Lett.*, **18** (1993) 1019–1021.

[114] H. Chen, M. A. White, David A. Krueger and C. Y. She, Daytime mesopause temperature measurements with a sodium-vapor dispersive Faraday filter in a lidar receiver, *Opt. Lett.*, **21** (1996) 1093–1095.

[115] T.M. Shay, A Rb 532 nm stark anomalous dispersion optical filter for doubled Nd:YAG lasers, in: Proceedings of the IEEE Lasers and Electro-Optical Society's Annual Meeting (1993) pp. 359–360.

[116] B. Yin and T.M. Shay, The Stark Anomalous Dispersion Optical Filter: The Theory, *TDA Progress Report*, **42** (1994) 14.

[117] R.I. Billmers, S.K. Gayen, M.F. Squicciarini, V.M. Contarino and W.J. Scharpf, Experimental demonstration of an excited-state Faraday filter operating at 532 nm, *Opt. Lett.*, **20** (1995) 106.

[118] Richard I. Billmers, Vincent Contarino, David M. Allocca, Martin F. Squicciarini, Martin F. Squicciarini and William J. Scharpf, Actively pumped faraday optical filter. 1996. United States Patent No. 5,513,032.

[119] S. K. Gayen, R. I. Billmers, V. M. Contarino, M. F. Squicciarini, W. J. Scharpf, Guangning Yang, P. R. Herczfeld and D. M. Allocca, Induced-dichroism-excited atomic line filter at 532 nm, *Opt. Lett.*, **20** (1995) 1427–1429.

[120] G. Yang, R.I. Billmers, P.R. Herczfeld and V.M. Contarino, Temporal characteristics of narrow-band optical filters and their application in LIDAR systems, *Opt. Lett.*, **22** (1997) 414.

[121] C. Fricke-Begemann, M. Alpers and J. Höffner, Daylight rejection with a new receiver for Potassium resonance temperature LIDARS, *Opt. Lett.*, **27** (2002) 1932.

[122] M. Alpers, R. Eixmann, C. Fricke-Begemann, M. Gerding and J. Höffner, Temperature LIDAR measurements from 1 to 105 km altitude using resonance, Rayleigh, and rotational Raman scattering, *Atmos. Chem. Phys.*, **4** (2004) 793–800.

[123] K.H. Fricke and U. von Zahn, Mesopause temperatures derived from probing the hyperfine structure of the D2 resonance line of sodium by lidar, *Journal of Atmospheric and Terrestrial Physics*, **47** (1985) 499 – 512.

[124] Norris R. Keeler, Reducing optical noise, 1992, GB Patent No. 2256766.

[125] Cord Fricke-Begemann, Lidar Investigations of the Mesopause Region: Temperature Structure and Variability, Dissertation, Universität Rostock, August 2004.

[126] J. Höffner and C. Fricke-Begemann, Accurate LIDAR temperatures with narrowband filters, *Opt. Lett.*, **30** (2005) 890.

[127] Fire Lidar (RL Associates Inc., UTP, Bldg. 2, Ste 2300 / 1350 Edgmont Ave / Chester, PA 19013 / USA, 2009). http://www.rlassociatesinc.com/index.html.

[128] Richard I. Billmers, Elizabeth J. Billmers, Vincent M. Contarino, Rudolph Lucente and Mary E. Ludwig, System for viewing objects at a fire scene and method of use. 2004. United States Patent No. 6,724,467.

[129] R.I. Billmers, S.K. Gayen, M.F. Squicciarini, V.W. Contarino, W.J. Scharpf and D.M. Alloca, Experimental demonstration of an excited-state Faraday filter operating at 532 nm, *Opt. Lett.*, **20** (1995) 106.

[130] I.I. Sobelman, Atomic Spectra and Radiative Transitions, 2nd Edition (Springer-Verlag, Berlin, 1992).

[131] B.W. Shore, The Theory of Coherent Atomic Excitation, Vol.1+2 (John Wiley & Sons, New York, 1990).

[132] R.D. Cowan, The Theory of Atomic Structure and Spectra (University of California Press, Berkeley and Los Angeles, California, USA, 1981).

[133] J. D. Jackson, Classical Electrodynamics, 3rd Edition (Wiley, New York, 1998).

[134] J.C. Slater, *Phys. Rev.*, **34** (1929) 1293.

[135] E.U. Condon and G.H. Shortly, The Theory of Atomic Spectra (University Press, Cambridge, 1935).

[136] Z. Michalewicz, Genetic Algorithms + Data Structures = Evolution Programs, Second, Extended Edition (Springer, 1994).

[137] D.W. Marquardt, *Journal of the Society for Industrial and Applied Mathematics*, **11** (1963) 431–441.

[138] T. Holstein, Imprisonment of resonance radiation in gases, *Physical Review*, **72** (1947) 1212.

[139] A.F. Molisch and B.P. Oehry, Radiation trapping in atomic vapours (Oxford Science Publications, Oxford, 1998).

[140] L Barbier and M Cheret, Energy pooling process in Rubidium vapour, *Journal of Physics B: Atomic and Molecular Physics*, **16** (1983) 3213–3228.

[141] William Happer, Optical pumping, *Rev. Mod. Phys.*, **44** (1972) 169–249.

[142] W.H. Press, B.P. Flannery, S.A. Teukolsky and W.T. Vetterling, Numerical Recipes in C : The Art of Scientific Computing (Cambridge University Press, 1992).

[143] N. W. Ressler, R. H. Sands and T. E. Stark, Measurement of Spin-Exchange Cross Sections for *Cs*133, *Rb*87, *Rb*85, *K*39, and *Na*23, *Phys. Rev.*, **184** (1969) 102–118.

[144] R.l. Kurucz and B. Bell, 1995 atomic line data, *Kurucz CD-ROM*, **23** (1995).

[145] C. van Trigt, Analytically Solvable Problems in Radiative Transfer. I, *Phys. Rev.*, **181** (1969) 97.

[146] C. van Trigt, Analytically Solvable Problems in Radiative Transfer. II, *Phys. Rev. A*, **1** (1970) 1298–1314.

[147] C. van Trigt, Analytically Solvable Problems in Radiative Transfer. III, *Phys. Rev. A*, **4** (1971) 1303–1316.

[148] C. van Tright, Analytically solvable problems in radiative transfer. IV, *Phys. Rev. A*, **13** (1976) 726–733.

[149] A. B. Matsko, I. Novikova, M. O. Scully and G. R. Welch, Radiation trapping in coherent media, *Phys. Rev. Lett.*, **87** (2001) 133601.

[150] Korning, 2002, Technical Data Sheet: Glass Code 7740.

[151] MS-Schramberg GmbH & Co. KG, Magnet- und Kunststofftechnik, Max-Planck-Str. 15, 78713 Schramberg-Sulgen, Germany, 2005, Technical Data Sheet: Sm_2Co_{17} 175/160w.

[152] L. Ricci, M. Weidenmüller, T. Esslinger, A. Hemmerich, C. Zimmerman, V. Vuletic, W. König and T.W. Hänsch, A compact grating-stabilized diode laser system for atomic physics, *Opt. Comm.*, **177** (1995) 541.

[153] D. Mehuys, D.F. Welch, R.G. Waarts, R. Parke, A. Hardy and W. Streifer, Analysis of monolithic integrated master oscillator power amplifiers, *Quantum Electronics, IEEE Journal of*, **27** (1991) 1900–1909.

[154] R. Nicolaescu, Th. Walther, E.S. Fry and M. Muendel, Ultranarrow-linewidth, efficient amplification of low-power seed sources by a fiber amplifier, *Appl. Opt.*, **38** (1999) 1784–1787.

[155] G.D. Boyd, A. Ashkin, J.M. Dziedzic and D.A. Kleinman, Second harmonic generation of light with double refraction, *Phys. Rev.*, **137** (1965) A1305–1320.

[156] A. Ashkin, G.D. Boyd and J.M. Dziedzic, Resonant optical second harmonic generation and mixing, *IEEE J. Quant. Elect.*, **2** (1966) 109–124.

[157] Texas Instruments Incorporated, 12500 TI Boulevard, Dallas, Texas 75243, USA, 2003, Technical Data Sheet: Opt 101.

[158] Triad Technology, 3131 Indian Road, Suite B, Boulder CO. 80301, USA, 2005, Technical Data Sheet: Rb vapor cells.

[159] Calibrated Hall probe, 2005, Courtesy of Prof. M. Roth, Institut für Kernphysik, Technische Universtät Darmstadt.

[160] Epoxy Technology Inc., 14 Fortune Drive, Billerica, MA 01821, USA, 2007, Technical Data Sheet: EPO-TEK 353ND.

[161] P.C. Becker, N.A. Olsson and J.R. Simpsoni, Erbium-Doped Fiber Amplifiers (Academic Press, 1997).

[162] Th. Führer and Th. Walther, Extension of the mode-hop-free tuning range of an external cavity diode laser based on a model of the mode-hop dynamics, *Opt. Lett.*, **33** (2008) 372–374.

[163] LIMO Lissotschenko Mikrooptik GmbH, Bookenburgweg 4-8, 44319 Dortmund, Germany, 2007, Technical Data Sheet: LIMO30-F200-DL808.

[164] N.G.R. Broderick, H.L. Offerhaus, D.J. Richardson, R.A. Sammut, J. Caplen and L. Dong, Large mode area fibers for high power applications, *Opt. Fiber Techn.*, **5** (1999) 185–196.

[165] J.D. Bierlein and H. Vanherzeele, Potassium titanyl phosphate: properties and new applications, *J. Opt. Soc. Am. B*, **6** (1989) 622–633.

[166] A.V. Smith, 2002, SNLO nonlinear optics code available from Sandia National Laboratories, Albuquerque, NM 87185-1423 through http://www.sandia.gov/imrl/XWEB1128/xxtal.htm.

[167] National Instruments, 2003, Technical Data Sheet: NI-PCI-6031E 64-Analog-Input Multifunction DAQ.

[168] P. Cancio, P. Zeppini, P. De Natale, S. Taccheo and P. Laporta, Noise characteristics of a high-power Ytterbium-doped fibre amplifier at 1083 nm, *Applied Physics B: Lasers and Optics*, **70** (2000) 763–768.

[169] Nabeel A. Riza and Nicholas Madamopoulos, High signal-to-noise ratio birefringence-compensated optical delay line based on a noise-reduction scheme, *Opt. Lett.*, **20** (1995) 2351–2353.

[170] C.E. Shannon, Communication in the presence of noise, *Proceedings of the IEEE*, **86** 447.

[171] T. Scholz, M. Schiffer, J. Welzel, D. Cysarz and W. Lange, Spatial effects of radiation trapping in an optically thick atomic vapor excited by a laser beam, *Phys. Rev. A*, **53** (1996) 2169–2172.

[172] T. Stacewicz, T. Kotowski, P. Wiewiór and J. Choräzy, Diffusion of resonance radiation in optically saturated Sodium vapour, *Opt. Comm.*, **100** (1993) 99.

[173] J. Choräzy, T. Kotowski and T. Stacewicz, Investigation of resonance radiation trapping for optically saturated $3^2S_{1/2} \rightarrow 3^2P_{1/2}$ transition in Sodium vapour, *Opt. Comm.*, **125** (1996) 65.

[174] T. Scholz, J. Welzel and W. Lange, Experiments on nonlinear radiation trapping in a saturable atomic vapor, *Phys. Rev.*, **64** (2001) 1.

[175] K. Yonehara, T. Yamagata, Y. Arimoto, T. Takeuchi and M. Tanaka, Relaxation mechanism of optically pumped Rb vapor of high density in strong magnetic fields, *Nuclear Instruments and Methods in Physics Research Section B: Beam Interactions with Materials and Atoms*, **184** (2001) 391 – 405.

[176] A. Gourevitch, G. Venus, V. Smirnov and L. Glebov, Efficient pumping of Rb vapor by high-power volume Bragg diode laser, *Opt. Lett.*, **32** (2007) 2611–2613.

[177] D. Tupa, L. W. Anderson, D. L. Huber and J. E. Lawler, Effect of radiation trapping on the polarization of an optically pumped alkali-metal vapor, *Phys. Rev. A*, **33** (1986) 1045–1051.

[178] D. Tupa and L. W. Anderson, Effect of radiation trapping on the polarization of an optically pumped alkali-metal vapor in a weak magnetic field, *Phys. Rev. A*, **36** (1987) 2142–2147.

[179] TOPTICA Photonics AG, Lochhamer Schlag 19, 82166 Graefelfing, Germany, 2005, Technical Data Sheet of the 1086.6 nm DFB Laser Diode: LD-1086-0030-DFB-1, S/N: 160/3-11.

[180] R. M. Measures, Electron density and temperature elevation of a Potassium seeded plasma by laser resonance pumping, *Journal of Quantitative Spectroscopy and Radiative Transfer*, **10** (1970) 107 – 125.

[181] M. A. Mahmoud, Electron energy distribution function in laser-excited Rubidium atoms, *Journal of Physics B: Atomic, Molecular and Optical Physics*, **38** (2005) 1545–1556.

[182] Mohamed A. Mahmoud, Kinetics of Rb_2^+ and Rb^+ formation in laser-excited Rubidium vapor, *Central European Journal of Physics*, **6** (2008) 530–538.

[183] T. B. Lucatorto and T. J. McIlrath, Efficient laser production of a Na^+ ground-state plasma column: Absorption spectroscopy and photoionization measurement of Na^+, *Phys. Rev. Lett.*, **37** (1976) 428–431.

[184] T. B. Lucatorto and T. J. McIlrath, Laser excitation and ionization of dense atomic vapors, *Appl. Opt.*, **19** (1980) 3948–3956.

[185] Raymond M. Measures, Efficient laser ionization of Sodium vapor—a possible explanation based on superelastic collisions and reduced ionization potential, *Journal of Applied Physics*, **48** (1977) 2673–2675.

[186] M. Cheret, L. Barbier, W. Lindinger and R. Deloche, Penning and associative ionisation of highly excited Rubidium atoms, *Journal of Physics B: Atomic and Molecular Physics*, **15** (1982) 3463–3477.

[187] L. Barbier and M. Cheret, Experimental study of penning and hornbeck-molnar ionisation of Rubidium atoms excited in a high s or d level (5d≤nl≤11s), *Journal of Physics B: Atomic and Molecular Physics*, **20** (1987) 1229–1248.

[188] L. Barbier, A. Pesnelle and M. Cheret, Theoretical interpretation of Penning and associative ionisation in collisions between two excited Rubidium atoms, *Journal of Physics B: Atomic and Molecular Physics*, **20** (1987) 1249–1260.

[189] J. T. Bahns, M. Koch and W. C. Stwalley, Laser-induced plasmas in metal vapors, *Laser and Particle Beams*, **7** (1989) 545–550.

[190] William C. Stwalley and John T. Bahns, Atomic, molecular, and photonic processes in laser-induced plasmas in alkali metal vapors, *Laser and Particle Beams*, **11** (1993) 185–204.

[191] Andrew C. Tam, Plasma formation in alkali metal vapors by quasi-resonant laser excitation, *ACS Symposium Series*, **179** (1982) 447–459.

[192] Dimitri Pappas, Benjamin W. Smith, Nicolo Omenettó and James D. Winefordner, Formation of a Cesium plasma by continuous-wave resonance excitation, *Applied Spectroscopy*, **54** (2000) 1245–1249.

[193] T.C. Killian, T. Pattard, T. Pohl and J.M. Rost, Ultracold neutral plasmas, *Physics Reports*, **449** (2007) 77 – 130.

[194] T. Ackemann, A. Heuer, Yu. A. Logvin and W. Lange, Light-shift-induced level crossing and resonatorless optical bistability in Sodium vapor, *Phys. Rev. A*, **56** (1997) 2321–2326.

[195] Hyatt M. Gibbs, Optical Bistability: Controling Light with Light (Academic Press Inc., Orlando, 1985).

[196] M. Möller and W. Lange, Radiation trapping: An alternative mechanism for chaos in a nonlinear optical resonator, *Phys. Rev. A*, **49** (1994) 4161–4169.

[197] M. Lindberg, S. W. Koch and H. Haug, Structure, formation, and motion of kinks in increasing-absorption optical bistability, *Phys. Rev. A*, **33** (1986) 407–415.

[198] Boris M. Smirnov and A. S. Yatsenko, Properties of dimers, *Physics-Uspekhi*, **39** (1996) 211–230.

[199] C.-J. Lorenzen and K. Niemax, Quantum defects of the n2P1/2,3/2 levels in 39K I and 85Rb I, *Physica Scripta*, **27** (1983) 300–305.

[200] Indrajit Saha, Panayiotis Nikolaou, Nicholas Whiting and Boyd M. Goodson, Characterization of violet emission from Rb optical pumping cells used in laser-polarized Xenon NMR experiments, *Chemical Physics Letters*, **428** (2006) 268 – 276.

[201] T. Ban, D. Aumiler, R. Beuc and G. Pichler, Rb_2 diffuse band emission excited by diode lasers, *The European Physical Journal D - Atomic, Molecular, Optical and Plasma Physics*, **30** (2004) 57–64.

[202] A. Ekers, M. Glodz, V. Grushevsky, J. Klavins and J. Szonert, Energy transfer between the 2s and 2d states in alkalis: experiments and theory, *Can. J. Phys.*, **79** (2001) 1039–1053.

[203] Michał Gryziński, Classical theory of electronic and ionic inelastic collisions, *Phys. Rev.*, **115** (1959) 374–383.

[204] R. M. Measures, N. Drewell and P. Cardinal, Laser interaction based on resonance saturation (libors): an alternative to inverse bremsstrahlung for coupling laser energy into a plasma, *Appl. Opt.*, **18** (1979) 1824–1827.

[205] R. M. Measures, N. Drewell and P. Cardinal, Electron- and ion-beam transportation channel formation by laser ionization based on resonance saturation—libors, *Journal of Applied Physics*, **50** (1979) 2662–2669.

[206] E. Arimondo, M. Inguscio and P.Violino, Experimental determinations of the hyperfine structure in the alkali atoms, *Reviews of Modern Physics*, **49** (1977) 31–75.

[207] Daniel A. Steck, Rubidium 85 D Line Data, 12. August 2009, available online at http://steck.us/alkalidata (revision 2.1.2).

[208] Daniel A. Steck, Rubidium 87 D Line Data, 12. August 2009, available online at http://steck.us/alkalidata (revision 2.1.2).

[209] Photonic Cleaning Technologies LLC, 1895 Short Lane Rd, Bldg 1, Platteville, WI 53818, USA, 2007, Technical Data Sheet: First Contact.

[210] Denise Stang, Weiterentwicklung eines ECDLs mit grossem modensprungfreien Abstimmbereich. Diplomarbeit, Technische Universität Darmstadt, Germany, September 2008.

Curriculum Vitae

Alexandru Lucian Popescu
Born 03.02.1977 in Bucharest/Romania

Education

01/2005–02/2010	PhD program at the Technische Universität Darmstadt, within the research group of Prof. Dr. Thomas Walther, Project: "A Brillouin-Lidar for the Measurement of Oceanic Temperature Profiles"; Associated member of the graduate college GRK 1114: "Optical Techniques for Measurement of Interfacial Transport Phenomena"
12/2004	Diploma in physics, Technische Universität Darmstadt Thesis: "Untersuchung eines Faraday Filters als Optisches Meßinstrument an der Rubidium $5s_{1/2} \rightarrow 5p_{3/2}$ – Resonanz"
09/2000–08/2001	Studies of physics within the ERASMUS program at the Univertsité Bordeaux 1, Sciences et Technologies, France
10/1997–12/2004	Studies of physics at the Technische Universität Darmstadt
08/1989–06/1996	Leibnizschule (Gymnasium), Offenbach, Germany

Work Experience

01/2005–Present	Scientific assistant at the Institute for Applied Physics, Technische Universität Darmstadt, Germany
03/2004–07/2004	Young scientific assistant at the DaimlerChrysler AG, Research Electronics and Mechatronics Group, Frankfurt, Germany
05/2001–06/2001	Internship at the Centre Physique Moleculaire Optique et Herzienne, Université Bordeaux 1, Sciences et Technologies, France
04/1998–08/2000	Young scientific assistant at the Institute for Computer Graphics Research (IGD), Darmstadt, Germany
07/1996–08/1997	Alternative civilian service at the Arbeiter Samariter-Bund e.V., Offenbach, Germany

Publications

Papers in Refereed Journals

A. Popescu and Th. Walther, On an ESFADOF edge-filter for a range resolved Brillouin-lidar: The high vapor density and high pump intensity regime, Applied Physics B: Lasers and Optics, 98, p. 667–675 (2010).

K. Schorstein, A. Popescu, M. Göbel and Th. Walther, Remote Measurements of water temperature based on Brillouin Scattering with a frequency doubled pulsed Yb:doped fiber amplifier, Sensors 8, p. 5820-5831 (2008)

K. Schorstein, G. Scheich, A. Popescu and Th. Walther, E. S. Fry, A Fiber Amplifier and an ESFADOF: Developments for a Transceiver in a Brillouin-LIDAR, Laser Physics 17, p. 975-982 (2007)

A. Popescu, D. Walldorf, K. Schorstein and Th. Walther, On an Excited State Faraday Anomalous Dispersion Optical Filter at Moderate Pump Powers for a Brillouin-LIDAR Receiver System, Opt. Comm., 264, p. 475-481 (2006)

A. Popescu and Th. Walther, On the Potential of Faraday Anomalous Dispersion Optical filter as High-Resolution edge Filters, Laser Physics, 15, p. 55–60 (2005)

A. Popescu, K. Schorstein and Th. Walther, A novel approach to a Brillouin-LIDAR for remote sensing of the ocean temperature, Appl. Phys. B, 79, p. 955–961 (2004)

E. Hugonnot, A. Popescu, S. Hanifi-Kadi and J.-P. Delville, Kinetic control of surface patterning by laser-induced photochemical deposition in liquid solutions. II. Experimental investigations, Phys. Rev. E 69, 051606 (2004)

Conference Proceedings

A. Popescu, K. Schorstein and Th. Walther, Proof of concept of a Brillouin-LIDAR for Remote Sensing of Oceanic Temperature Profiles, Proceedings of the 4th EARSeL Workshop on the Remote Sensing of the Coastal Zone, Chania, Greece (2009)

A. Popescu, K. Schorstein, G. Scheich, I. Massmann, P. Fietzek, Th. Walther and E. S. Fry, Key Developments for a Brillouin-LIDAR for Remote Sensing of Oceanic Temperature Profiles, Proceedings of the 3rd EARSeL Workshop on the Remote Sensing of the Coastal Zone, Lake Garda, Italy (2007)

K. Schorstein, A. Popescu, G. Scheich, Th. Walther, and E. S. Fry, Towards a Brillouin-LIDAR for remote sensing of the temperature profile in the ocean, IEEE Conference OCEANS 2006, Boston, USA (2006)

Talks and Posters presented at the annual meetings of the German Physical Society (DPG)

A. Popescu, K. Schorstein und Th. Walther, Ein Brillouin-LIDAR zur Messung von Temperaturprofilen des Ozeans: Erste Tiefenaufgelöste Messungen, Verhandl. DPG (VI) 44, 1/Q36.1, (2009)

K. Schorstein, A. Popescu, P. Fietzek, I. Maßmann, G. Scheich und Th. Walther, Ein Brillouin-LIDAR zur Messung von Temperaturprofilen in Wasser: Status der Strahlquelle, Verhandl. DPG (VI) 42, 3/Q32.4, (2007)

P. Fietzek, I. Maßmann, A. Popescu, K. Schorstein und Th. Walther, Tiefenaufgelöste Temperaturmessung in Wasser - Auf dem Weg zu einem Brillouin-LIDAR, Verhandl. DPG (VI) 42, 3/Q39.4, (2007)

I. Maßmann, A. Popescu und Th. Walther, Die Auswirkungen von Puffergas auf FADOF-Systeme, Verhandl. DPG (VI) 42, 3/Q68.5, (2007)

A. Popescu und Th. Walther, Charakterisierung eines Rubidium EFADOF Kantenfilter unter moderaten Pumpleistungen, Verhandl. DPG 41 2/Q60.4 (2006)

A. Bungert, A. Popescu, K. Schorstein und Th. Walther, Brillouin-LIDAR zur Messung von Temperaturprofilen in Wasser: Entwicklung der Systemkomponenten, Verhandl. DPG 41 2/Q73.3 (2006)

D. Walldorf, A. Popescu and Th. Walther, Ein Rb 5p3/2 ESFADOF zur Messung von Temperaturprofilen im Ozean, DPG Verhandlungen, Q 25.4 7/2005, (2005)

A. Popescu und Th. Walther, Untersuchungen zur Realisierung eines Brillouin-LIDARs für die Aufnahme von Temperaturprofilen im Ozean, DPG Verhandlungen, Q 61.2 7/2005, (2005)

A. Popescu und Th. Walther, Design und Test eines FADOF-Systems zur Messung von Temperaturprofilen von Wasser, DPG Verhandlungen, Q 46.9 7/2004, 157 (2004)

Summer School

A. Popescu, D. Walldorf, K. Schorstein and Th. Walther, Investigations of a FADOF System as an Edge-filter Receiver for a Brillouin-LIDAR for Remote Sensing of the Ocean Temperature, International School of Atomic and Molecular Spectroscopy - 22nd Course: New Developments in Optics and Related Fields: Modern Techniques, Materials and Applications, A NATO Advanced Study Institute, Erice, Sicily, Italy, June 6 – 21, 2005

Supervised Theses

Denise Stang, Weiterentwicklung eines ECDLs mit grossem modensprungfreien Abstimmbereich. Master thesis, Technische Universität Darmstadt, Germany, September 2008.

Simon Mieth, Weiterentwicklung und Untersuchung eines Nd:YAG basierten FADOF-Systems. Bachelor thesis, Technische Universität Darmstadt, Germany, September 2007.

Thorsten Führer, Aufbau eines ECDLs mit großem modensprungfreien Abstimmbereich. Diploma thesis, Technische Universität Darmstadt, Germany, July 2007.

Tobias Beck, Aufbau und Untersuchung eines festkörperbasierten FADOF-Systems. Bachelor thesis, Technische Universität Darmstadt, Germany, June 2007.

Ingo Massmann, Charakterisierung eines atomaren Faraday-Filters unter Einfluss von Xenon-Puffergas und Realisierung eines Alkali-Ethan-Lasers. Diploma thesis, Technische Universität Darmstadt, Germany, June 2007.

Peer Fietzek, Temperature-Dependent Properties of the Brillouin Doublet in Water. Diploma thesis, Technische Universität Darmstadt, Germany, May 2007.

Andreas Bungert, Brillouin-Streuung in Wasser. Diploma thesis, Technische Universität Darmstadt, January 2006.

Daniel Walldorf, On a $5p_{3/2} \rightarrow 8d_{5/2}$ Excited-state Faraday Anomalous Dispersion Optical Filter (EFADOF). Diploma thesis, Technische Universität Darmstadt, June 2005.

Danksagung

Es ist mir ein besonderes Anliegen allen Leuten, die an dem Gelingen dieser Arbeit beteiligt waren, an dieser Stelle meinen allerherzlichsten Dank auszusprechen:

Prof. Dr. Thomas Walther danke ich für die freundliche Aufnahme in seiner Arbeitsgruppe. Er versteht es stets notwendige Freiheiten mit einer exzellenten Betreuung zu kombinieren. Dabei schafft er es immer wieder, nicht unbedingt Selbstverständliches möglich zu machen. Dafür und für die mir von Anfang an übertragene Verantwortung gegenüber dem Lidar–Projekt, der Sensorgruppe und den betreuten Studenten, die ich als große Wertschätzung empfunden habe, gilt mein großer Dank.

Prof. Dr. Gerhard Birkl danke ich für die freundliche Übernahme des Zweigutachtens.

Dr. Mathias Sinther danke ich für seinen großen Einsatz. Er versteht es wie selbstverständlich als zuverlässiger Stützpfeiler der Arbeitsgruppe alle wissenschaftlichen und organisatorischen Fragen zu meistern.

Danken möchte ich den vielen Studenten, die ich während der letzten Jahre betreuen durfte. Durch ihre engagierten und exzellenten Arbeiten haben sie viele Ergebnisse erst möglich gemacht. Besonderer Dank geht an: Daniel Walldorf, Andreas Bungert, Peer Fietzek, Ingo Massmann, Tobias Beck, Simon Mieth und Denise Stang.

Der Feinmechanikwerkstatt des Instituts für Angewandte Physik bin ich zu größtem Dank verpflichtet: Besonders Herrn Kalbfleisch, Herrn Jeretzki, Herrn Wagenknecht, Herrn Hoffmann, sowie den zahlreichen Lehrlingen. Ihrer überaus exzellenten Arbeiten und Beratungen flossen nicht nur in diese Arbeit, sondern stellen eines der unentbehrlichsten Eckpfeiler des Instituts für Angewandte Physik dar.

Bei Herrn Arno Weick, der mit bei der Herstellung der atomaren Gaszellen behilflich war, möchte ich mich ganz herzlich bedanken. Durch seine Ausdauer und Geduld wurde die schwierige Herstellung überhaupt möglich.

Herrn Rainer Stadler von der Glasbläserei des Physikalischen Instituts Heidelberg bin ich ebenfalls zu großem Dank verpflichtet. Er hat für mich in großer Geduld die Quarzglasrohlinge präpariert und die fertigen Glaszellen befüllt.

Bei Herrn Baumann und Herrn Kringel bedanke ich mich für die Hilfe bei vielen elektronischen Problemen.

Dr. Joachim Holzfuss und Herrn Schmutzler möchte ich für die zuverlässige EDV-Betreuung danken und Frau Christiane Walther für ihre Professionalität und Durchsetzungskraft in allen Verwaltungsfragen.

Prof. Dr. Tilman Pfau vom 5. Physikalischen Institut der Universität Stuttgart möchte ich für die freundliche Kollaboration danken, sowie Thomas Baluktsian für seine Zeit, die er mir geopfert hat.

Prof. Dr. Markus Roth gilt mein Dank für die freundliche Überlassung einer Hall–Sonde.

Der gesamten Arbeitsgruppe Laser und Quantenoptik danke ich für die entspannte und konstruktive Arbeitsatmosphäre. Insbesondere danke ich meinen Kollegen: Cornelia Lengler, Thorsten Führer, Alexander Bertz, Daniel Depenheuer, Patrick Villwock und Kai Schorstein. Andreas Rudolf danke ich besonders für die sehr konstruktive Auseinandersetzung mit meiner Arbeit.

Den Mitgliedern des Graduiertenkollegs 1114 danke ich für die sehr vielen konstruktiven Veranstaltungen und der schönen Zeit.

Ein besonders herzlichen Dank geht an meine Freundin Ute Förster. In ihr finde ich allen erdenklichen Rückhalt in jeder Lebenslage.

Meinen Eltern und meiner Schwester gebührt ganz spezieller Dank. Sie haben schon früh meinen Hang zur Naturwissenschaft erkannt und bestärkten mich zu jeder Zeit diesen Weg zu gehen.